Kinematics and Metallicity of RGB Stars in the Triangulum (M33) Galaxy

This dissertation is submitted for the degree of Master of Science

David Trethewey

Institute of Astronomy
&
Robinson College

University of Cambridge

April 28, 2011

Preface

Declaration

This dissertation is the result of my own work and includes nothing which is the outcome of work done in collaboration except where specifically indicated in the text. No part of this dissertation has been submitted for any other degree or qualification. This dissertation does not exceed 60,000 words.

Figure 1: An image of the sky centred on M31 (upper right) and M33 (lower left), taken by the author using a Nikon D50 (at 70mm focal length) piggybacked on the Thorrowgood telescope mount at the Institute of Astronomy, Cambridge. 10 mins exposure, a background flattening routine is applied using MaxIm DL to reduce the visual impact of light pollution.

Acknowledgements

I thank my supervisors, Scott Chapman and Mike Irwin for guiding me in my research during my time at the Institute, and other members of the Institute of Astronomy who have also helped me in my academic life. I thank my office mates in O26 (and the now demolished SPO13) at the Institute of Astronomy; Scott Brown, Tim Staley, Duncan Hanson, Christopher Berry, Jonathan Crass, and other fellow graduate students I have known during my time here. I would also like to thank all of the IoA support staff, for everything from computing to morning coffee at the Institute. I thank the students, fellows and staff of Robinson College for the role they have played in the last nine years of my life, one third of my time on this Earth to date. One of them, Matt Davis as a PhD student in Geophysics always said he was more "down to earth" than me. I would like to thank the editors of Astronomy Now, noting that my interest in astronomy really began at the age of eight, with the January 1993 issue of that magazine. I also thank others who have been important in guiding me through my time as a graduate student. I thank Tony James, Peter Squibb, Mick Harvey and other members of the Cornwall Astronomical Society, through which my interest in astronomy developed. I also thank the people of the IAYC (International Astronomical Youth Camp) who I enjoyed spending time with in the forests of Central Europe.

Finally I thank my family, for encouraging me and supporting me at every stage.

Abstract

Kinematics and Metallicity of RGB Stars in the Triangulum (M33) Galaxy

David Trethewey

Eleven Keck DEIMOS (DEep Imaging Multi Object Spectrometer) fields around the Triangulum Galaxy (M33) are analysed in this work in combination with CFHT (Canada France Hawaii Telescope) photometry taken as part of the PAndAS (Pan-Andromeda Archaeological Survey) survey (McConnachie et al., 2009), containing a total of $\sim$ 2000 targets. A stellar population of candidate M33 RGB (Red Giant Branch) stars that is not rotating with the M33 disk is detected in most fields. The relative contribution of this population is estimated using kinematic windowing, both using a method of hard "disk" and "halo" kinematic windows in radial velocity and a Bayesian method taking account of priors for the expected disk and halo radial velocity distributions and relative contributions. The "disk" component has an exponential scale length of $\sim$ 1.7 kpc, agreeing with previous photometric work. If the non-disk population is assumed to be a "true" smooth halo, and fit by an exponential, it would contribute far more (9% of the disk luminosity integrated at 1% Bayesian halo prior and 17% integrated using simple windowing) than is indicated by photometric surveys (such as the INT-WFC (Isaac Newton Telescope Wide Field Camera) survey as published in Ferguson et al. 2007) and theoretical expectations, which constrain the contribution of a smooth stellar halo to the overall luminosity to less than a few percent.

The metallicity properties of both the "disk" and "halo" samples are analysed. Photometric metallicities are derived using the Dartmouth isochrones (Dotter et al., 2008), and spectroscopic metallicities are derived from the equivalent widths of the Ca II triplet of stacked spectra. The "disk" shows a downward metallicity trend with radius on the major axis of a magnitude 0.02-0.04 dex kpc^{-1} consistent between the photometric and spectroscopic analyses, which in the photometric analysis is significant at the 2σ level. The "halo" sample shows a downward metallicity trend with radius on the major axis of a magnitude 0.04-0.05 dex kpc^{-1} in the photometric analysis, but this is not significant at 2σ level, and can be taken to be consistent with constant [Fe/H]. In the spectroscopic analysis, the metallicity trend of the halo is stronger, being of magnitude 0.11-0.14 dex kpc^{-1} and significant at a 2σ level. The overall weighted mean [Fe/H]s of the "halo" sample across all fields, are -1.37 and -1.07 in the spectroscopic (CaT2 only) and photometric analyses respectively, and for the "disk" sample, -0.93 and -0.97. It is likely that the "halo" sample is largely the result of tidal stripping during a past interaction with M31 rather than a "true" primordial halo.

Contents

List of Figures

List of Tables

Chapter 1

Introduction

1.1 Andromeda and Triangulum historically

The Andromeda and Triangulum galaxies have been known from ancient times, since they are visible to the naked eye. Andromeda is the brighter of the two at around third magnitude ($V = 3.44$ in Roman et al. 1991), and can be seen by the naked eye under a reasonably dark sky. Triangulum is only marginally visible to the naked eye due to it being fainter ($V = 5.72$ in Roman et al. 1991) and having lower surface brightness and requires a very dark moonless night with an absence of significant light pollution. In the 18^{th} century, Messier included both in his catalogue of "nebulae", in order to better distinguish them from comets, which can look very similar in a small telescope. Andromeda and Triangulum received the designations M31 and M33 respectively. Through a typical amateur telescope, it is possible to see the central region of M31, including a dust lane in the disk[1]. It is also possible to see the dwarf elliptical satellite galaxy M32 and the spheroidal M110 (NGC 205). A further two satellites (NGC 185 and NGC 147) are visible although these are somewhat further away from M31 itself. The remaining satellites are faint or of low surface brightness and were not discovered until the 20^{th} century.

M33 is also a spiral galaxy, but the low surface brightness means that visually only the central region is visible through a typical amateur telescope, although in larger instruments the supergiant HII complex NGC 604 can be seen. There are three further NGC objects and 10 IC objects contained in M33.

In the mid 19^{th} century, Lord Rosse, using what was at the time the world's largest telescope, a 72-inch reflector located in Birr, Ireland, observed both M31 and M33 and characterised them as "spiral nebulae" due to the apparent spiral structure. Drawings based on these observations are shown in figure 1.1. (Rosse, 1850). In 1864, William Huggins made some spectroscopic studies of various "nebulae" (Huggins & Miller, 1864). Some nebulae had emission line spectra, others had continuous spectra with absorption lines. M31 was observed to fall into the latter category. Conclusive evidence that M31 and other "spiral nebulae" were stellar in nature had to wait until better quality spectra were produced (Scheiner, 1899). Pioneering photographic work was done by Isaac Roberts (Roberts, 1893, 1899) and later by J.E. Keeler of the Lick Observatory (Keeler, 1908). Isaac Roberts' photographs of M31 and M33 are shown in figure 1.2.

An understanding of their nature had to wait until later, and a full consensus on their nature as galaxies

[1] According to the Oxford English Dictionary, although *disc* is now the more usual form in British English, the earlier and better spelling is *disk*.

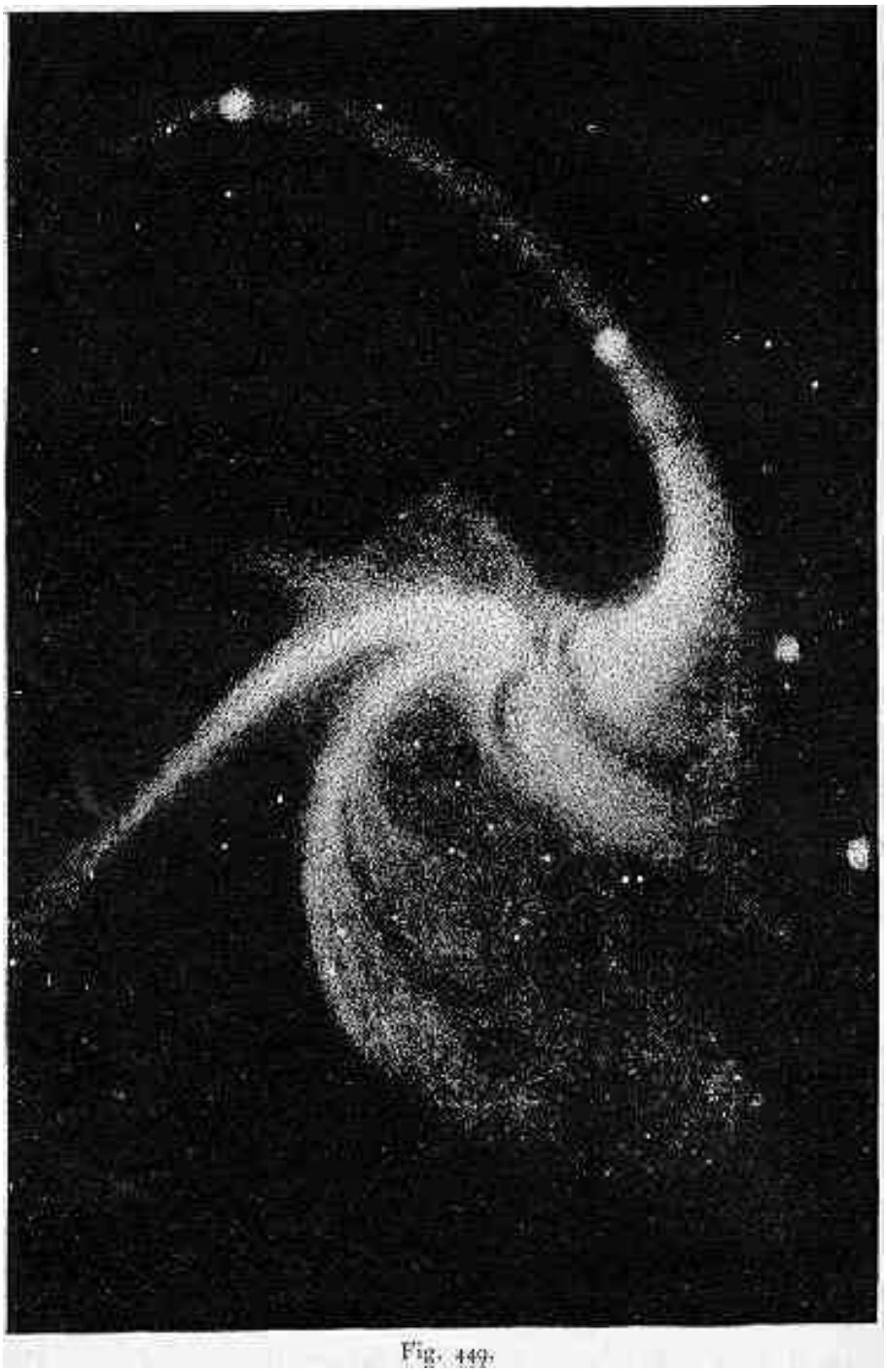

Figure 1.1: A drawing by R.J. Mitchell based upon Lord Rosse's observations of M33. (Rosse, 1850)

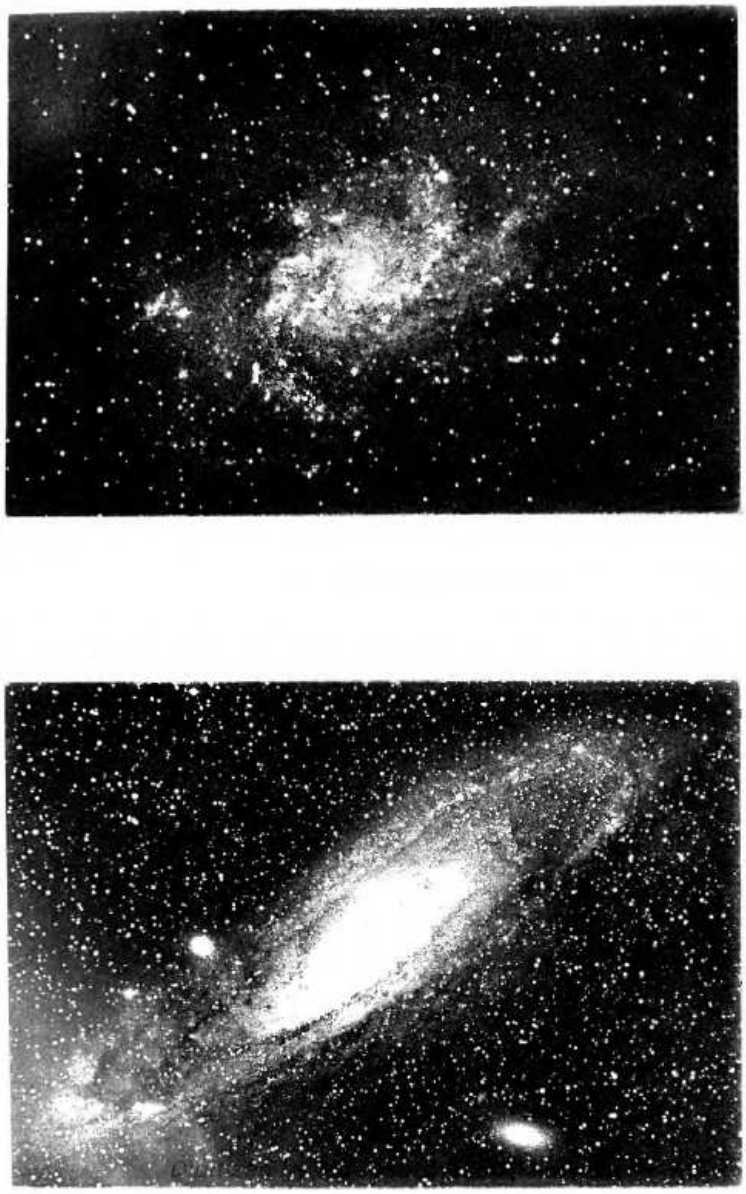

Figure 1.2: Early photographs of M33 (top) and M31(bottom). Reproduced from "A selection of photographs of stars, star-clusters and nebulae" Volume 2, Isaac Roberts 1899. Taken using a 20 inch reflector with exposure times of 135 and 90 minutes respectively on photographic plates.

like our own did not emerge until the 20^{th} century.

1.1.1 Distances to galaxies in the Local Group

One of the fundamental ways that the nature of external galaxies was realised was by determining their distance. This made it clear that these "spiral nebulae" were not part of our own galaxy. Until accurate astrometric measurements were made beginning in the 19^{th} century, the distances to the stars remained very uncertain. Nearby stars were observed to exhibit small changes in position relative to other stars, in a regular pattern over the course of the year. This is caused by our observing position moving depending on which side of the Sun the Earth is. This effect is known as "trigonometric parallax". Once the distance to a star is known, the apparent brightness can be converted to an absolute luminosity.

It was observed that some stars vary in brightness measurably. There is a specific class of variable stars known as Cepheid variables that vary in a regular way with a well defined period. These are a form of giant star in what is known as the "instability strip". The instability strip is a region in the Hertzsprung-Russell diagram occupied by pulsating variable stars. Most stars more massive than the Sun enter the instability strip at some point in their evolution. In the outer layers of these stars, there are layers in which helium is either in a singly or doubly ionised form. This tends to make the star pulsate, due to the effect of the ionisation on opacity. Explanations of the physics of the pulsation of stars in the instability strip are given in section 5.1.10 of Galactic Astronomy (Binney & Merrifield, 1998) and in chapter 39 of Stellar Structure and Evolution (Kippenhahn & Weigert, 1994). It was realised that for these Cepheid variables, there was a correlation between the absolute luminosity of these stars, and the period of variation. This enabled the distances of the Cepheid variables to be known at distances much greater than had been possible through parallax, which can only measure the distances to the most nearby stars.

When telescopes became powerful enough, Cepheid variables became observable in the Andromeda and Triangulum galaxies. Pioneering work was done by Edwin Hubble (Hubble, 1925), who derived a distance of 285 kpc for M33. Although initially the estimate was not very accurate (a modern value of the distance to M33 is 809 kpc (McConnachie et al., 2005)), these studies made it clear that the Andromeda and Triangulum systems are in fact external to our own galaxy. The reason for the error of Hubble's initial estimate was that no Cepheid variable was close enough for the distance to be measurable by direct trigonometric parallax, and instead statistical parallaxes were used to estimate the distances to Cepheids. Interstellar absorption was not taken account of, so the estimated Cepheid luminosities were too small.

This is an example of how our cosmological understanding has come forward through studies of individual stars in the Local Group. Our understanding of the Local Group is still incomplete, although in recent years it has expanded considerably.

1.2 Galaxy formation and motivation for the present study

The study of galactic structure can be used to investigate galaxy formation, an important area of astrophysics where there are still many open questions. The study of galactic structure and formation also interacts with overarching cosmological and gravitational theories.

Galactic structure and kinematics provides evidence for the existence of dark matter. It was originally suggested by Zwicky in the 1930s based on evidence from the kinematics of galaxy clusters that there is

greater mass in and around galaxies than can be accounted for by the stellar luminosity (Zwicky, 1933, 1937).

More evidence for the existence for dark matter comes from observations of the rotation curves of galactic disks. The enclosed mass within a given radius can be determined by the rotation speed assuming the Newtonian inverse square law of gravity (general relativistic effects being important only in the extreme strong field case as found in the vicinity of compact objects such as black holes and neutron stars). The rotation speed can be determined using the Doppler shift of the 21cm emission line of neutral hydrogen (H I) gas. It eventually became clear that there is approximately 10 times as much "dark matter" as ordinary or "baryonic matter". The rotation curve of M33 was studied in Corbelli & Salucci 2000.

According to modern estimations such as in Spergel et al. 2007, 85% of the matter density of the Universe is contributed by "non-baryonic" matter (which has no strong or electromagnetic interactions). Further information on the distribution of dark matter can be gleaned from the study of the stellar halos of galaxies. The halos of galaxies in the Local Group have such a low surface brightness that they need to be studied via resolved stellar populations, since integrated light measurements are limited by sky brightness. Observations of galactic halos are vital to provide evidence for comparisons with theories of galaxy formation, and by extension cosmology.

The emergence of stars, galaxies, groups and clusters of galaxies, and other inhomogeneities from the nearly homogeneous early universe is a process known as "structure formation". The density inside a luminous galaxy at a radius of a few kpc is around 10^5 times the critical density ρ_c, that is, the density at which the Universe contains just enough matter to be geometrically flat. Galaxy formation therefore involves highly non-linear density fluctuations. This means that the outcome of galaxy formation cannot be predicted exactly in an analytic fashion, and theoretical work must rely on simulations. Observations are therefore important to constrain simulations by comparison of their results with observable properties of galaxies.

1.2.1 The structure of galaxies

For a more detailed discussion of the below, see Chapter 4 of Galactic Astronomy (Binney & Merrifield, 1998) or Chapter 1 of Galactic Dynamics (Binney & Tremaine, 2008).

Galaxies are divided into four main types according to the Hubble classification system (Sandage & Bedke, 1994). See figure 1.3 for a visual representation of the main galaxy types.

Elliptical galaxies are smooth, apparently featureless stellar systems containing little or no cool interstellar gas or dust and little or no stellar disk. They are mostly composed of old stars, since there is little gas to form new stars. They are so named because the contours of constant surface brightness (isophotes) form approximately concentric ellipses. In the Hubble classification system, they are denoted by the symbols E0-E7 where a galaxy of type En has axis ratio of $\frac{b}{a} = 1 - \frac{n}{10}$. Elliptical galaxies are found in a wide range of sizes. The effective radius R_e is defined as the radius of the isophote containing half of the total luminosity. For the giant elliptical M87 found in the Virgo Cluster, this is 20 kpc, whereas for the dwarf elliptical M32 (a satellite of Andromeda) this is 0.2 kpc. Most luminous elliptical galaxies exhibit little or no rotation, although among dimmer elliptical galaxies, rotation and flattening appear to be correlated (Faber et al., 1997). The luminosity, velocity dispersion and size of elliptical galaxies are correlated in what is called the fundamental plane.

$$\log_{10} R_\mathrm{e} = 1.24 \log_{10}(\sigma_{||}) - 0.82 \log_{10}(\overline{I}_\mathrm{e}) + \text{constant}$$

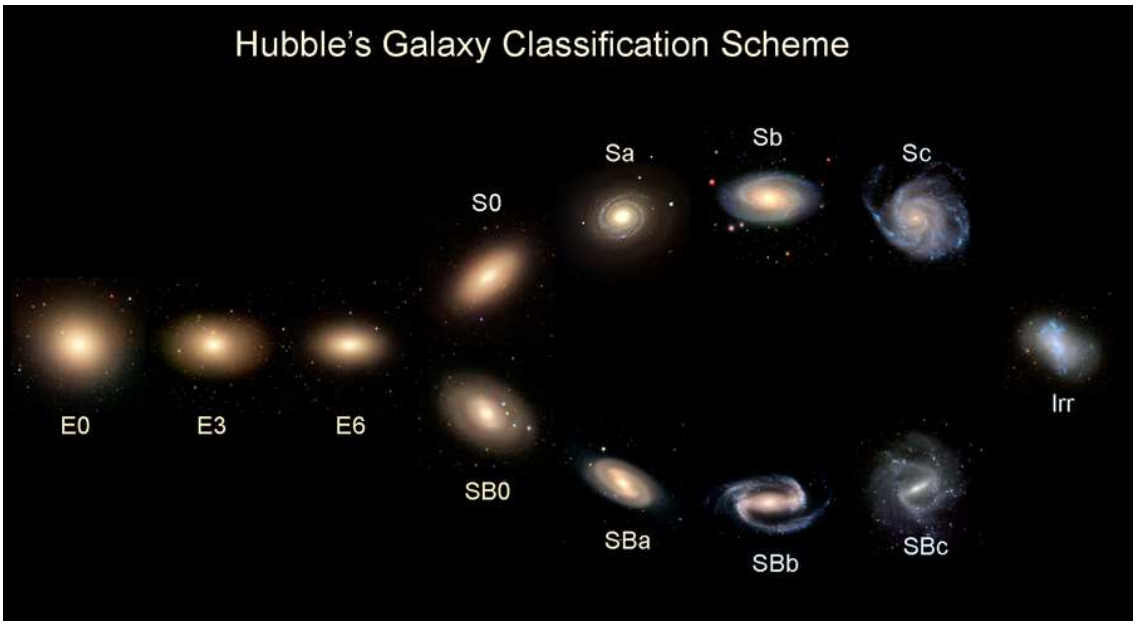

Figure 1.3: A visual representation of the Hubble "tuning fork" classification of galaxies. (Figure from Galaxy Zoo project website (Simpson, 2010))

where $\sigma_{||}$ is the velocity dispersion and $\overline{I}_e$ is the average surface brightness within the effective radius.

At luminosities $< 10^9 L_\odot$ a distinct family of dwarf spheroidal galaxies appears. These are more diffuse than would be expected for an elliptical galaxy of the same luminosity (Mateo, 1998). They are difficult to detect since they have very low surface brightness, and are known from counts of individual stars in nearby galaxies.

Spiral galaxies are galaxies which like the Milky Way, M31 and M33 contain a prominent disk composed of stars, gas and dust. The disk contains spiral arms, filaments in which stars are continuously being formed. Like the Milky Way, most spiral galaxies contain a bulge, a centrally concentrated stellar system that has a smooth or amorphous appearance. The luminosity of the bulge relative to that of the disk is correlated with many other properties of the galaxy, such as the fraction of the disk mass in gas, the colour of the disk, and how tightly the spiral arms are wound.

M31 has a large and prominent bulge component, however M33 does not. See Bothun 1992; Minniti et al. 1993; McLean & Liu 1996 for discussion of M33's lack of a significant bulge component.

The Hubble classification breaks spirals down into Sa, Sb, Sc and Sd types. Along this sequence, the relative luminosity of the bulge decreases, the spiral arms become more loosely wound, the relative mass of gas increases, and the spiral arms become more clumpy. The Milky Way is a spiral galaxy of Hubble type Sbc, M31 is a spiral of type SA(s)b and M33 is a spiral of type SA(s)cd (Roman et al., 1991). The capital A is simply to denote that the galaxy does not exhibit a bar, the letter B is added for barred spiral galaxies. There are also lenticular galaxies, that exhibit a disk and a bulge, yet do not have significant cool gas or recent star formation and do not exhibit spiral structure. They are labelled by the notation S0, or SB0 if barred. The transition from ellipticals to lenticulars to spirals is continuous and smooth. Lenticular galaxies are rare in low density regions but comprise almost half of galaxies in high density regions of rich

clusters. It is thought this may be because lenticulars are spirals that have been depleted of interstellar gas by interactions with the hot cluster gas. For example, see the article by van Gorkom, van Gorkom 2003.

Irregular galaxies exhibit recent star formation and cool gas, but the gas and young stars are arranged chaotically rather than in a spiral structure. They are denoted by the notation Sm or Im, which are so named after the Large and Small Magellanic Clouds which form the prototype for galaxies of this type.

1.3 Near-field cosmology in the Local Group

There are two ways to study the process of galaxy formation. One is to observe galaxies in the process of formation. This takes advantage of the fact that when we observe an object at a distance, we see it at an earlier cosmic time, due to the light travel time, since light travels at a finite speed. For very distant objects this light travel time can be a significant fraction of the age of the Universe. The downside of this approach is that distant objects are harder to observe. Distant objects appear smaller (angular diameter distance), and fainter (luminosity distance). In everyday life on terrestrial (and somewhat larger) scales, these two definitions of distance are equivalent, however in a cosmological context, due to cosmic expansion these definitions of distance diverge. An article explaining the different measures of distance in cosmology was written by Hogg 1999.

The alternative is to observe the present day galaxies in the local universe and look for the remnants of the process of formation in the present day structure of the galaxies. Focusing on the Local Group has the advantage that individual stars can be observed both photometrically and spectroscopically. The Local Group in this way can be used as a laboratory for studying galaxy formation and cosmology.

1.3.1 Review of the study of galaxy formation and near-field cosmology.

Eggen, Lynden-Bell and Sandage wrote a much cited paper in 1962 (Eggen et al., 1962), referred to below as ELS62, which detailed observations of stars in the solar neighbourhood. They argued that it is possible to detect a correlation between metallicity (as measured by the proxy measure of ultraviolet excess) and eccentricity (essentially a proxy for being a halo rather than a disk star) which they argued was an evidence for a monolithic collapse of the Galaxy as it formed. They found that the stars with a larger ultraviolet excess (and hence a lower metallicity), tended to have higher eccentricities e, and smaller angular momenta L_z. Both e and L_z are 'adiabatic invariants' in that their values for a given star change negligibly provided that the potential in which the star moves changes slowly. This means that either low metallicity stars formed on orbits with high e, or that the potential of the Milky Way has changed rapidly in the time since they formed. See section 3.6 of Galactic Dynamics for detail (Binney & Tremaine, 2008). They also found a correlation between the UV excess and W-velocity, that is the velocity perpendicular to the galactic plane. This led the authors to suggest that the old, metal-poor population was formed at various heights above the galactic plane, whereas the younger stars were formed very near the plane. They also argued that the collapse of the protogalactic cloud occurred relatively rapidly, in the space of a few $\times 10^8$ years.

In the review article Gilmore et al. 1989, ELS62's results were reviewed. They pointed out that ELS62 made two crucial assumptions in their interpretation, firstly that a pressure supported, primarily gaseous galaxy is stable against star formation and secondly that stellar orbits cannot be modified to become more radial after the formation of the star. Chiba & Beers 2000 found in a non-kinematically selected sample

of 1203 solar neighbourhood stars no correlation between eccentricity and metallicity. They state that the ELS62 result was influenced by the fact that ELS62 selected their sample kinematically and in so doing biased their result. ELS62 used two catalogues of stars, firstly the approximately 4000 stars for which accurate proper motions and radial velocities were available, and secondly a catalogue of all the stars for which the data available at the time indicated a total space motion in excess of 100 km s^{-1}. Of the 221 stars that ELS62 used in their analysis, 108 were from the first catalogue (Eggen, 1961), and 113 from the second (Eggen, 1964).

Searle & Zinn 1978 studied a series of 19 galactic globular clusters, and argued that the galactic halo had been formed by a process of hierarchical merging, since they found that there are globular clusters with a large range of ages and compositions in the Milky Way's halo but no clear radial abundance gradient. This variation in composition and age they took as evidence that the single monolithic collapse model was untenable, and that at least the more loosely bound clusters had a broad range of ages and originated in protogalactic fragments that continued to fall into dynamical equilibrium with the Galaxy for some time after its initial collapse.

Simulations of gravitational clustering find that the potential of the forming Galaxy to be far from axisymmetric, and therefore the angular momenta of individual stars is not conserved. Therefore the assumptions made by ELS62 about the modification of stellar orbits may not be realistic.

Subsequent studies have been made in the light of these two models. Recent work by such observational surveys as the Sloan Digital Sky Survey (SDSS) has greatly expanded our knowledge of the structure of the Milky Way's halo, and stellar population studies have recently been extended to other Local Group galaxies. One of the evidences for the hierarchical model is that the Milky Way studies using the SDSS have seen many "stellar streams". For example, Belokurov et al. detail a "Field of Streams", in which SDSS photometry of a wide area around the north Galactic cap is used to discover several wraps of the Sagittarius stream (Belokurov et al., 2006a,b, 2007a,b). The Sagittarius stream was discovered to have originated in the Sagittarius dwarf galaxy via tidal disruption by the Milky Way's gravitational potential, the galaxy itself having been discovered in 1994 (Ibata et al., 1994). There were also other streams observed including the Monoceros Ring (Newberg et al., 2002; Belokurov et al., 2006a,b) and the Orphan Stream (Belokurov et al., 2007a), some of which had identifiable progenitors, others including the Orphan Stream did not. See figure 1.4 where the map of the spatial density of SDSS stars around the north Galactic cap is reproduced from Belokurov et al. 2006a.

1.4 Introduction to the Local Group

1.4.1 The Local Group in context

Many galaxies are found in bound systems called groups or clusters of galaxies. Rich clusters of galaxies can be several Mpc in radius and contain thousands of galaxies. Galaxies are found in a hierarchical structure, which includes small groups, voids where very few galaxies are found, filaments and walls stretching for tens of Mpc and rich clusters containing thousands of galaxies. Eke et al. 2004 found that approximately 55% of the galaxies observed in the 2dfGRS (Two-Degree Field Galaxy Redshift Survey) were in groups of at least two members. Thus slightly less than half of galaxies are field galaxies, in relative isolation, and slightly more than half in some form of group or cluster. Approximately 10% of galaxies are found in rich clusters.

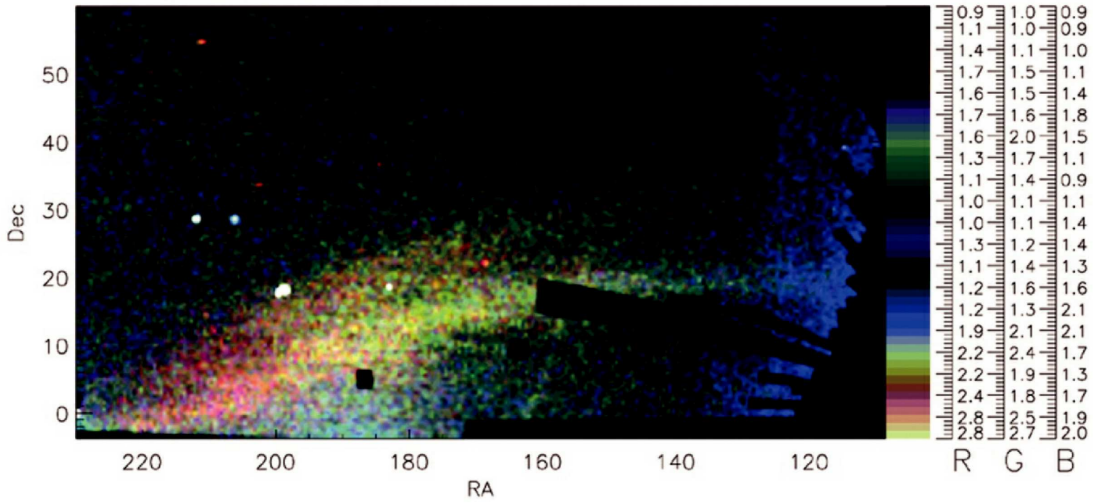

Figure 1.4: Spatial density of SDSS stars with $g - r < 0.4$ around the north Galactic cap in equatorial coordinates, binned $0^\circ.5 \times 0^\circ.5$. The colour plot is an RGB composite with blue for stars with $20.0 < r \leq 20.66$, green for stars with $20.66 < r \leq 21.33$ and red for the stars with $21.33 < r \leq 22.0$. The Sagittarius stream can be observed to bifurcate starting at $\alpha \approx 180^\circ$. Also visible is the Monoceros Ring at $\alpha \approx 120^\circ$ and a thin stream at $150^\circ \leq \alpha \leq 160^\circ$ and $0^\circ \leq \delta \leq 30^\circ$. The colour bar shows a palette of 50 representative colours labelled according to the stellar density (in units of 100 stars per square degree) in each of the red, green and blue components. Figure from Belokurov et al. 2006a.

Thus a large fraction of galaxies are found in small groups.

The environment in which galaxies are found correlates with the relative numbers of galaxies of different type. Galaxies in clusters are more likely to be elliptical or lenticular (S0) than field galaxies, and the elliptical fraction $f(E)$ has been found to vary between different clusters from around 15% to 40% (Oemler, 1974). Oemler found that $f(E)$ was correlated with the morphology of the cluster, a cluster with a high $f(E)$ tending to have a symmetrical appearance, with clusters with lower $f(E)$ appearing less symmetrical. The observed spiral fraction $f(Sp)$ in the centres of the clusters was found to be consistent with there being no spirals in the centres of rich clusters (given that only the projected density of galaxies is measured rather than the 3D density). It was also found that the ratio of S0 galaxies to spirals was observed to decrease with radius (Melnick & Sargent, 1977). It was concluded by Dressler 1980a,b that the key variable was the local density of galaxies, if there are more elliptical and lenticular galaxies the cluster is more dense. Giovanelli et al. 1986 discuss the morphology-density relation in the Pisces-Perseus supercluster. This probes a wide range in density down to that of field galaxies. They find that the "field" population has population fractions of 0.045:0.11:0.77 for E:S0:Sp and that broadly speaking, the same morphology-density relation applies in this lower density regime as in the rich cluster regime.

Our galaxy, the Milky Way belongs to a loose collection of galaxies known as the Local Group. The Local Group consists of all the galaxies within ~ 1 Mpc. The two dominant members of this group are the Galaxy and M31, both spiral galaxies, and most of the dozens of other members are satellites of the two dominant ones, although there are some which follow more isolated orbits. The spiral galaxy M33, the primary topic of this dissertation, is part of the M31 subgroup, and depending on its precise distance and kinematics, may

or may not be the largest satellite of M31 (Loeb et al., 2005; van der Marel & Guhathakurta, 2008). The Local Group is one of a number of small groups of galaxies in the nearby Universe, others including the Antlia-Sextans group at $D_{LG} = 1.7$ Mpc, the Sculptor group at $D_{LG} = 2.4$ Mpc, the IC342/Maffei group at $D_{LG} = 3.2$ Mpc, and the M81 group at $D_{LG} = 3.5$ Mpc. Since most galaxies in the field and in small groups are spiral galaxies, the Local Group is fairly representative of field populations of galaxies in the nearby Universe, hence it is useful to study the properties of Local Group galaxies to learn about the properties of galaxies in general.

Groups and clusters of galaxies may be regarded as assemblies of masses orbiting under their mutual gravitational attraction. It must be remembered however that groups and clusters of galaxies are dynamically young; a typical galaxy even in a rich cluster has completed only a few orbits since the cluster formed, and in many smaller groups including the Local Group, galaxies are still falling towards the group centre for the first time. This is the case for the Milky Way and M31. Collisions between galaxies in groups and clusters are much more frequent than collisions between stars in a stellar system, since the ratio between the size of a typical galaxy and the size of a cluster or group is very much larger than that of a star relative to the size of a stellar system.

The Local Group offers an opportunity to observe three large spiral galaxies. This dissertation primarily focuses on the Triangulum galaxy (M33), which is the third largest galaxy in the Local Group after Andromeda (M31) and the Milky Way.

1.4.2 Basic parameters of the Milky Way, Andromeda and Triangulum galaxies

Detailed information concerning the various members of the Local Group can be found in reviews such as van den Bergh 1999 and Mateo 1998.

In van den Bergh 1999 it is stated that there are a total of 35 certain or probable members of the Local Group. This number has increased somewhat in recent years with the discovery of a number of dwarf spheroidal satellites of both the Milky Way and Andromeda following large scale CCD surveys such as the SDSS in the case of the Milky Way and the INT (Isaac Newton Telescope) and CFHT (Canada-France-Hawaii-Telescope) surveys in the case of Andromeda. Figure 1.6 shows the overall distribution of the major Local Group galaxies.

The total mass of the Local Group is $M_{LG} = (2.3 \pm 0.6) \times 10^{12} M_{\odot}$ and the total luminosity is $M_V = -22.0$, implying a mass to light ratio of $\frac{M}{L_V} = 44 \pm 12$ in solar units (van den Bergh, 1999). The timing argument in regards to the mass of the Local Group has been used to estimate the total mass, or at least provide a lower limit on it. It was noted by Kahn & Woltjer 1959 that the Local Group is dominated by the two large spiral galaxies (the Milky Way and Andromeda) and they are approaching each other at approximately 100 km s^{-1}. The Local Group was modelled very simply as two point masses on a radial orbit, with a pericentre at the beginning of cosmic time (the Big Bang) and an apocentre at some point before the present time in order for the galaxies to be in approach today. This required an apocentric separation larger than the current one and an orbital period less than twice the age of the Universe. For current estimates of the distance scale, velocity and age of the Universe, this argument estimates the total mass at $5 \times 10^{12} M_{\odot}$ (Li & White, 2008). The transverse velocity is poorly constrained, and any transverse velocity means a larger present kinetic energy, and therefore a larger required mass to reverse the initial expansion, so this is a lower limit on the mass. Li & White 2008 used data from the Millennium Simulation of the ΛCDM cosmogony

to estimate the error distribution of the timing argument estimation of the Local Group and Milky Way mass. The interquartile range of their mass estimate is $\log\frac{M_{LG}}{M_\odot}$ in the range [12.58, 12.83], and the 5% and 95% points in the distribution are [12.26,13.01] with their median likelihood estimate of the true mass being 5.27 $\times 10^{12} M_\odot$. This is approximately double the figure given in van den Bergh 1999. They also estimate the virial mass of the Milky Way itself at 2.43 $\times 10^{12} M_\odot$ based on a timing argument with reference to the recession velocity of the distant satellite Leo I, although there are large systemic uncertainties, and the 95% lower confidence limit is 0.80 $\times 10^{12} M_\odot$.

Watkins et al. 2010 estimate the masses of the Milky Way and Andromeda galaxies using the kinematics of satellite galaxies. The mass of the Milky Way and Andromeda within 300 kpc of each is given as $0.9 \pm 0.3 \times 10^{12} M_\odot$ and $1.4 \pm 0.4 \times 10^{12} M_\odot$ respectively, although this analysis assumes velocity isotropy. Plausible ranges of velocity anisotropy can give masses from 0.7 $\times 10^{12} M_\odot$ to 3.4 $\times 10^{12} M_\odot$ for the Milky Way, and 1.3 $\times 10^{12} M_\odot$ to 1.6 $\times 10^{12} M_\odot$ for M31. The best estimate for the mass of the Milky Way increases to $1.4 \pm 0.3 \times 10^{12}$ if proper motion data for the six satellites for which it was available is taken into account.

Therefore there is no definitive determination of which of the Milky Way and Andromeda are the more massive. It is clear however, that both galaxies contain a substantial dark matter halo, since their masses are considerably more than can be accounted for by stars and gas.

The Milky Way galaxy

A detailed discussion of the components of the Milky Way galaxy can be found in Chapter 10 of Galactic Astronomy (Binney & Merrifield, 1998).

Most of the stars in the Milky Way galaxy lie in a flattened, approximately axisymmetric structure known as the Galactic disk. This is visible to the naked eye as a luminous band stretching across the sky, and is the source of the name "Milky Way" for our Galaxy. An early study of the shape of the Milky Way was conducted by Sir William Herschel (Herschel, 1785). Although it was realised that the Milky Way is a flattened system, the full extent of the system was not, due to the distances (and therefore the stellar luminosity function) being unknown, and the effect of interstellar extinction in the plane of the Galactic disk not being accounted for.

The midplane of the Galactic disk defines the equator of Galactic coordinates. The Sun is located at a distance R_0 from the centre of the Galaxy, the best current estimate $R_0 = (8.0 \pm 0.5)$ kpc is derived from the orbits of stars near the black hole that exists at the centre of the Galaxy.

In disk galaxies generally, the surface brightness is approximately an exponential function of radius, $I(R) = I_d \exp(-\frac{R}{R_d})$ where R_d is the disk scale length. See for example de Jong 1996 for an observational review of this in a number of nearby face-on disk galaxies. The disk scale length is estimated to be between 2 and 3 kpc for the Milky Way Galaxy (Freudenreich, 1998). Thus the Sun is located further from the Galactic centre than about 75-90% of disk stars. This concentration of the disk towards the centre of the Galaxy is not very apparent in visible light due to interstellar dust extinction, however in infrared images the concentration of light in the direction of Sagittarius is obvious. This is shown in the all-sky panoramas in figure 1.5. The density of stars also falls off exponentially with the "vertical" distance z, which is the distance perpendicular to the Galactic plane. The disk stars are predominantly found in nearly circular orbits.

As well as the disk, the Galaxy contains a bulge, which is a centrally located stellar system that is thicker

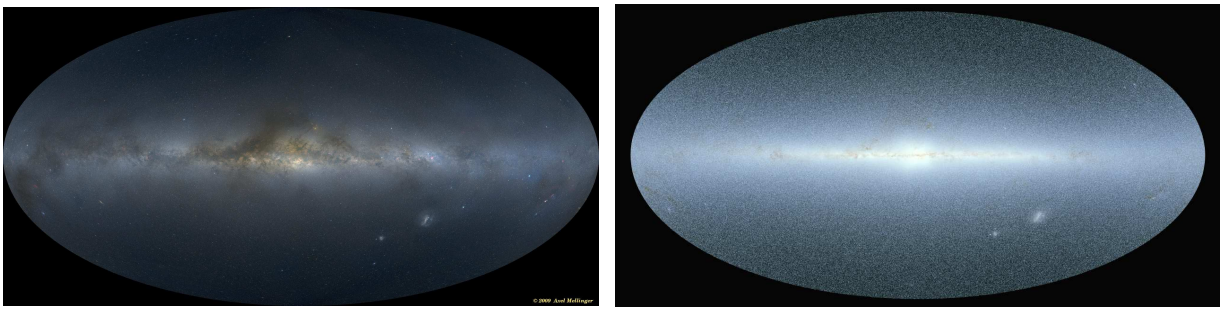

Figure 1.5: Visible light (left) and near-IR (right) all-sky panoramas. Visible light panorama from Mellinger 2009. Near-IR from Two Micron All Sky Survey (Skrutskie et al., 2006).

than the disk and in the Milky Way comprises $\sim$ 15% of the luminosity of the whole galaxy. It is clearly visible in infrared images, where dust extinction is greatly reduced. The bulge is estimated to have formed early in the history of the Galaxy, and is comprised of old stars. It has a wide distribution of [Fe/H] from -1.25 to +0.5 with a mean value $<$ [Fe/H] $>$ = -0.25 (McWilliam & Rich, 1994). It is somewhat triaxial, and may in fact consist of more than one structure with some studies indicating a long bar structure as well as a bulge (Babusiaux & Gilmore, 2005; Cabrera-Lavers et al., 2008).

About 1% of the stellar mass in the Galaxy is contained in the stellar halo, which contains old stars of low metallicity. The halo has little or no mean rotation (although see a recent paper by Deason et al. 2010 which discusses the matter), and a density distribution that appears to be to first order spherical and following a power law $\rho \propto r^{-3}$, although triaxiality is fairly likely. The stellar halo contains a population of globular star clusters.

Fellhauer et al. 2006 state the Milky Way halo is close to spherical, based on study of the Sagittarius stream, Helmi 2004 stated the data is consistent with simulations that favour an oblate or prolate halo with an axial ratio of about 0.6. Johnston et al. 2005 use the Two Micron All Sky Survey to trace debris associated with the Sagittarius dwarf, this dataset preferring an oblate halo, with a flattening q in the range 0.90-0.95. Law et al. 2009 including all well-established phase space data for the Sagittarius stream state that a triaxial model with $\frac{c}{a} \approx 0.67$, $\frac{b}{a} \approx 0.83$ and triaxiality parameter $T \sim 0.56$ is preferred. However Peñarrubia et al. 2010 consider the possibility that the Sagittarius stream progenitor was a disk galaxy, i.e. having its own rotation, and go on to state that this would affect constraints on the Milky Way halo shape derived from the Sagittarius stream. Carollo et al. 2007, 2010 argue for a two-component halo, based on Sloan Digital Sky Survey data.

The total size and mass of the Galaxy's halo can be constrained by the kinematics of distant globular clusters and nearby galaxies. Wilkinson & Evans 1999 find a best-fit mass of $2 \times 10^{12} M_{\odot}$ although the uncertainties are large and allow masses between $2 \times 10^{11} M_{\odot}$ and $5 \times 10^{12} M_{\odot}$. Li & White 2008 estimate the Milky Way mass at $2.43 \times 10^{12} M_{\odot}$, and Watkins et al. 2010 estimate it at $1.4 \pm 0.3 \times 10^{12} M_{\odot}$. See earlier in this subsection for a discussion.

Our understanding of the structure of the Milky Way itself has improved greatly in recent years due to more observations of stellar populations, notably via the Sloan Digital Sky Survey. (Belokurov et al., 2006a,b, 2007a,b). See figure 1.4.

Complementary studies of the Andromeda and Triangulum systems have also been made, recently par-

ticularly with the PAndAS and SPLASH surveys.

Andromeda and Triangulum

The M31 thin disk scale length is 5.9 kpc (Walterbos & Kennicutt 1988, adjusted for our assumed distance of 785 kpc). By comparison the Milky Way's thin disk scale length is 2.3 ± 0.6 kpc (Hammer et al., 2007), with a scale height of 300 pc (in the solar neighbourhood). Thus, the M31 disk scale length is more than twice as large as the Milky Way's. Hammer et al. 2007 estimate it as a factor of 2.5 ± 0.8 times larger. M33's disk scale length is 1-2 kpc, being estimated by Ferguson et al. 2007 from INT survey data at 1.8 kpc. A much shorter scale length was estimated in Teig 2008 of 0.92 kpc.

Both the Milky Way and M31 contain a significant central bulge. There is some evidence that the Milky Way's central bulge exhibits a bar (McWilliam & Rich, 1994).

The M31 bulge component is quite large, old and metal rich. Brown 2009 reviews the M31 and M33 spheroid (bulge and halo) components. A recent study of the M31 bulge component is Saglia et al. 2010. The M31 bulge was modelled by Widrow et al. 2003 as having a mass about 30% that of the disk, with their preferred value for the bulge mass being 3.5 $\times 10^{10} M_{\odot}$. Davidge et al. 2005 using near-IR imaging with adaptive optics on Gemini North of two fields in the M31 bulge resolved the upper 4-5 mag of the RGB and AGB. The resulting H and K CMDs are consistent with a population dominated by stars at an age of $\sim$ 10 Gyr and a near-solar metallicity.

M33 does not appear to possess a classical bulge, although there is a small nucleus (Bothun, 1992; Stephens & Frogel, 2002). Stephens & Frogel 2002 find this nuclear component has a wide range of ages and a mean metallicity of [Fe/H] = -0.26.

The stellar halo components in the Local Group have also been studied recently. A recent review of the Milky Way halo is Helmi 2008. The local halo metallicity distribution peaks at [Fe/H] $\sim$ -1.6, which a tail to very metal poor stars of [Fe/H] $<$ -3.

Being large, bright and nearby galaxies, M31 and M33 have been extensively studied over the decades, however it is only fairly recently that large-format CCD detectors have been available, the advent of which has transformed astronomers' ability to conduct large photometric surveys of these galaxies.

Mould & Kristian 1986 pioneered CCD based work on the halos of Andromeda and Triangulum. They observed a field 7 kpc out on the minor axis of M31, and a similar field in M33 (see section 1.5.2), using a 800 × 800 pixel CCD, with V and I band filters. They estimated a high mean metallicity for the M31 halo of $<$[M/H]$>$ = -0.8, albeit with a large dispersion (not quantified accurately in that work). Later studies continued to appear to indicate a high metallicity of the M31 halo, for example Durrell et al. 2004 found a wide metallicity dispersion peaking at [M/H] $\sim$ -0.5. Chapman et al. 2006; Ibata et al. 2007 pointed out that what had been measured as M31 "halo", was on closer study either substructure including various stellar streams, or the extended disk, and that the "true" halo is substantially more metal poor at around [Fe/H] = -1.5.

Between 2000 and 2004, the Isaac Newton Telescope was used to make a survey of the area around the Andromeda galaxy. This led to the discovery of the Giant Southern Stream (discovery paper Ibata et al. 2001) and other substructures. See figure 2.1 for the INT survey coverage of M31, and 2.2 for the INT survey's coverage around M33. More extensive work was done under the aegis of the PAndAS and SPLASH surveys, using both photometric and spectroscopic information. For detail on the PAndAS survey

Galaxy	Hubble Type	Total Mass	Total Luminosity (M_V)	Bulge fraction (luminosity)	Halo fraction (luminosity)	Disk scale length
Milky Way	Sbc	$0.9 \pm 0.3 \times 10^{12} M_\odot$	-20.9	12 %	$\sim 1\%$	2.3 kpc
M31	SA(s)b	$1.4 \pm 0.4 \times 10^{12} M_\odot$	-21.2	25 %	$\sim 2.5 - 5\%$	5.9 kpc
M33	SA(s)cd	$\sim 10^{11} M_\odot$	-18.9	negligible	$<$ few %	1.8 kpc

Table 1.1: Comparative properties of the major Local Group galaxies.

see McConnachie et al. 2009; Martin et al. 2009 and papers referenced therein. See figure 2.3 for the PAndAS survey coverage. A more detailed description of the INT and PAndAS surveys can be found in section 2.1.

Wide field imaging surveys of M31 have shown an active merger history for M31, and deep ACS observations at 21 kpc (in the transition between bulge and halo) and 35 kpc (where the surface brightness profile and metallicity are characteristic of a halo population) have shown that although the population is dominated by old stars, there are $\sim$ 30% of stars there younger than 10 Gyr, and only $\sim$ 10% of the stars are ancient and metal-poor (age $\geq$ 12 Gyr and [Fe/H] $\leq$ -1.5) (Brown et al., 2007, 2008, 2009). Ibata et al. 2007 fit the metal-poor M31 halo with a Hernquist model with a large scale length of 55 kpc.

The M33 halo component is not well constrained, although recent wide-field imaging surveys have detected a component which appears to be a tidal substructure from a possible interaction with M31 (McConnachie et al., 2010). Sarajedini et al. 2000 observed a number of halo clusters, and Sarajedini et al. 2006 studied a population of RR Lyrae stars in M33 which was interpreted as a field halo component.

1.4.3 Satellites of the major Local Group galaxies

The satellite system of the Milky Way

The Large and Small Magellanic Clouds are satellite galaxies of the Milky Way, the LMC being a barred irregular galaxy of type Ir III-IV, located at a distance of 50 kpc and having a luminosity M_V = -18.5. The SMC is a dwarf irregular galaxy of type Ir IV-V. A recent review of the Magellanic Clouds is Westerlund 1997.

There are also a number of dwarf spheroidal satellites of the Milky Way, including the Sagittarius dwarf spheroidal, which is in the process of being disrupted by tidal forces producing the Sagittarius stream. There are also many fainter dwarf spheroidal satellites, the number of which are known has increased in recent years through surveys such as the SDSS. A summary of some structural properties of local dwarf galaxies is given in figure 1.7 (from Tolstoy et al. 2009).

The satellite system of Andromeda

The M31 satellite M32 is arguably the only 'true' elliptical galaxy in the Local Group, with a luminosity profile that can be represented by an $R^{\frac{1}{4}}$ law, whereas the profiles of most spheroidal/dwarf spheroidal galaxies are best represented by an exponential profile. However it is not a pristine example of an elliptical galaxy, since as a close satellite of M31, it has experienced gravitational interaction with M31 itself. M32 is a close companion of M31, separated by only 5.3 kpc. It is peculiar in surface brightness and size, being classed as a compact (cE) galaxy, cE2, due to its low luminosity, compactness and high surface brightness. It has been argued that it may be a 'true' elliptical galaxy at the lower extreme of the mass sequence, or alternatively a former spiral galaxy whose concentrated bulge, unlike its disk, has survived tidal interactions

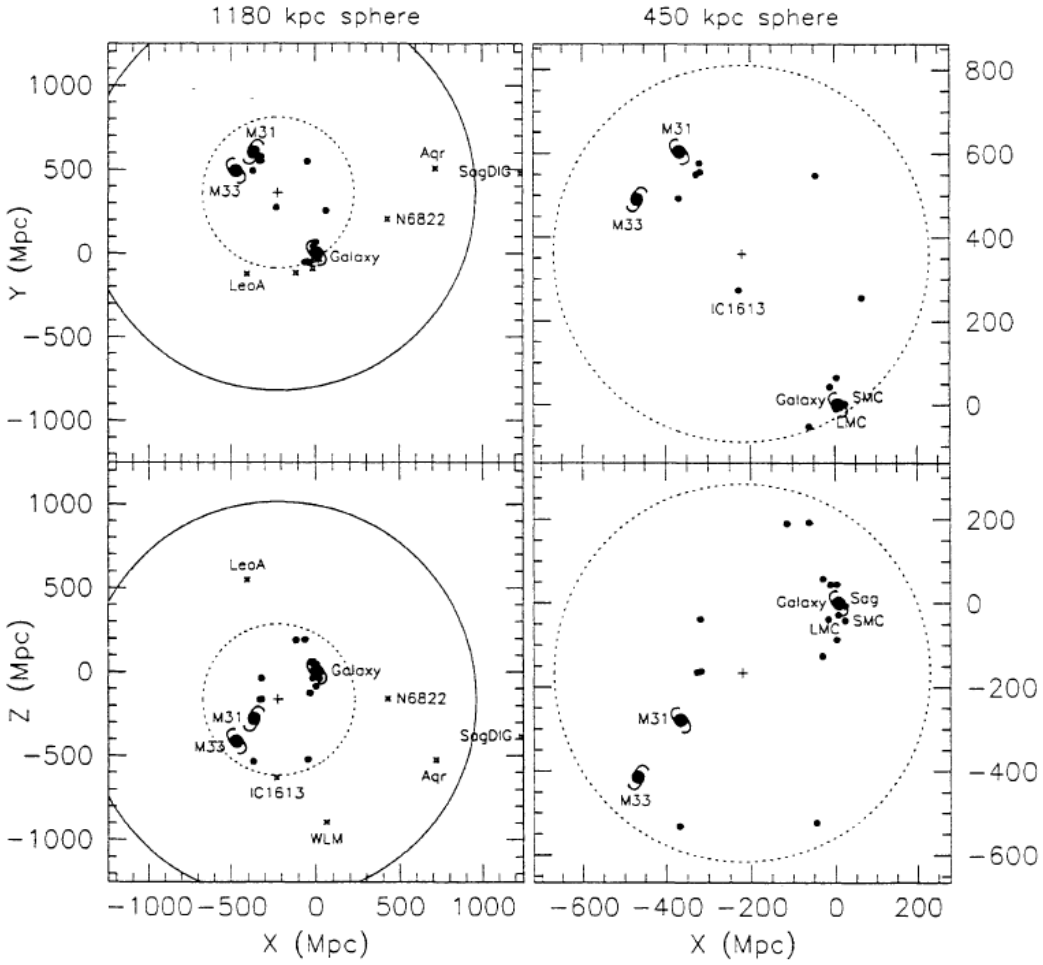

Figure 1.6: The distribution of Local Group members, as viewed from two orthogonal directions. The X, Y and Z axes point towards the Galactic centre (l=0°, b = 0°), the direction of rotation (l=90°, b = 0°) and the north Galactic pole (b=+90°), respectively. The majority of Local Group members are concentrated in two subgroups centred on the Galaxy and Andromeda. The circle of radius 1180 kpc corresponds to the zero-velocity surface of the Local Group. The dashed circle of radius 450 kpc shows the radius of the sphere that contains half of all Local Group galaxies. Figure from van den Bergh (1999).

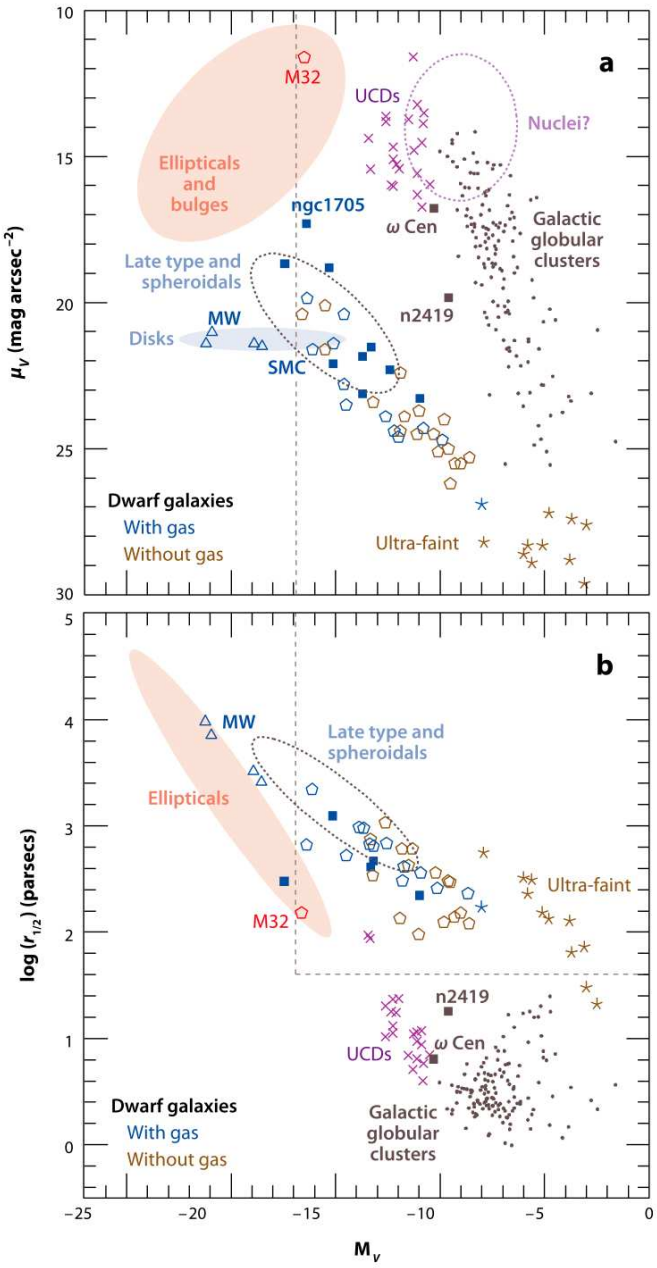

Figure 1.7: This is a figure from Tolstoy et al. 2009 detailing relationships between structural properties for different types of galaxies. (a) the absolute magnitude, M_V, versus central surface brightness μ_V plane; (b) the M_V versus half-light radius, $r_{\frac{1}{2}}$ plane. Marked with coloured ellipses are the typical locations of elliptical galaxies and bulges (light red), spiral galaxy disks (light blue), galactic nuclei (dashed purple), and large early-(spheroidals) and late-type systems (dashed grey). Galactic globular clusters are plotted individually as small grey points. M31, the Milky Way, M33 and the LMC are shown as blue open triangles. Some of the blue compact dwarfs are marked as blue solid squares. The peculiar globular clusters ω Cen and NGC 2419 are marked, M32 in the region of elliptical galaxies and the SMC near the border of the dwarf class. The ultracompact dwarfs (UCDs) studied in the Virgo and Fornax clusters are marked with purple crosses. Local Group dwarf galaxies are plotted as open pentagons, blue for systems with gas, and yellow for systems without gas. The ultrafaint dwarfs are given star symbols and the same colour code.

with M31. (Kormendy et al., 2009; Bekki et al., 2001). There are also a number of bright spheroidal galaxies associated with M31, including NGC 205, NGC 185 and NGC 147. A number of dwarf spheroidal satellites of M31 have been discovered in recent years. For example Martin et al. 2009 and papers referenced therein. See also Richardson et al. 2011 for an update based on the full PAndAS survey coverage.

A possible satellite of Triangulum?

There is only one known dwarf galaxy which may be a satellite of Triangulum. This is Andromeda XXII, which is a faint (M_V = -6.5 ± 0.8) dwarf spheroidal. It is not certain whether it is bound to Andromeda or Triangulum since its heliocentric distance is uncertain to a large degree. See Martin et al. 2009 for more information.

1.5 The Triangulum Galaxy

The Triangulum galaxy is the third largest galaxy in the Local Group, and it characterised as a late-type spiral of Hubble type SA(s)cd, with two open spiral arms and no evidence for a bulge component (Bothun, 1992; Minniti et al., 1993; McLean & Liu, 1996). The great majority of the luminosity is distributed in an exponential disk component (de Vaucouleurs, 1959), and the optical disk is tilted at nearly 30° to the strongly warped H I envelope (Rogstad et al., 1976). This indicates that the gas disk has been disrupted to a degree, implying some level of interaction perhaps with Andromeda. The small mass to light ratio of the nucleus ($\frac{M}{L}$ <0.4 indicates there is no supermassive black hole at its centre (Kormendy & McClure, 1993; Lauer et al., 1998). M33 is a fairly low surface brightness object, with an integrated V band surface brightness of μ_V = 23.0 mags/arcsec^2 (based on the parameters from NASA/IPAC Extragalactic Database 2011). By comparison M31 has an integrated surface brightness of μ_V = 22.2 mags/arcsec^2. The distribution of galaxy surface brightnesses is discussed in Impey & Bothun 1997. M33 has approximately $\frac{1}{10}$ of the mass of the Andromeda galaxy. (perhaps $\sim 10^{11} M_\odot$). An image of M33 (from the 2nd Palomar Digitised Sky Survey) is reproduced in figure 1.8.

1.5.1 Context of its relation to Andromeda

The argument has been advanced that the Triangulum galaxy has interacted quite strongly with the Andromeda galaxy, and may be gravitationally bound to it such that it can be described as Andromeda's largest satellite galaxy. (Loeb et al., 2005; van der Marel & Guhathakurta, 2008). The warping of the gas disk and its inclination with respect to the stellar disk provide support to this hypothesis. See section 4.4 for a more detailed discussion of this hypothesis.

1.5.2 Previous work on Triangulum

There has been less work studying the Triangulum galaxy than Andromeda, especially the stellar outer disk and halo regions. The literature is summarised below and a figure showing positions of fields in various studies overlaid onto the PAndAS map of M33 is displayed in figure 1.9. There is some further discussion of the literature regarding the M33 disk scale length and metallicity properties in Chapter 4.

Figure 1.8: An image of M33 from the 2nd Palomar Digitised Sky Survey (Blue), 1 degree $\times$ 1 degree centred on M33.

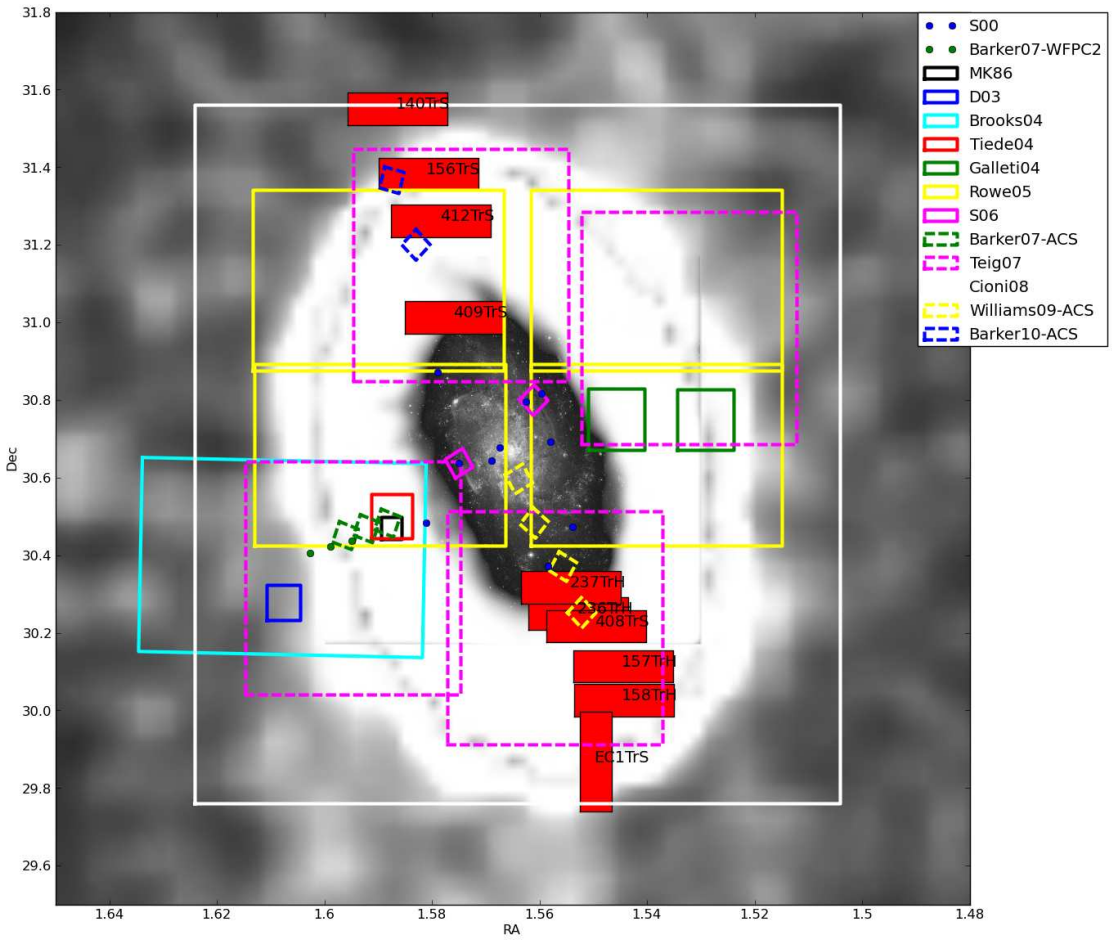

Figure 1.9: A diagram showing the positions of fields studied in various studies of M33 overlaid on the PAndAS survey map. The spectroscopic fields used in this dissertation are the red filled boxes. The field studied in Mould & Kristian 1986 is the black box, the locations of the Sarajedini et al. 2000 clusters are marked as blue dots, the Davidge 2003 field are shown as the blue box, the Brooks et al. 2004 field is the cyan box, the Tiede et al. 2004 field is the red box, Galleti et al. 2004 the two green boxes, Rowe et al. 2005 the large yellow boxes, Sarajedini et al. 2006 the two small magenta boxes, Barker et al. 2007a the green dotted boxes (ACS fields) and the green dots (WFPC2 fields). The Teig 2008 photometric fields are the four magenta dashed boxes, the Cioni et al. 2008 infrared survey area is the large white box, the Williams et al. 2009 ACS fields are the four small dashed yellow boxes, and finally the ACS fields analysed in Barker et al. 2010 are the blue dashed boxes. A Palomar DSS image of M33 is overlaid.

Pioneering work on the stellar populations in M33 was undertaken by Mould & Kristian 1986. They observed a field at a projected radius of 7 kpc on the minor axis of M33, in a southeasterly direction. By producing a colour-magnitude diagram, and comparing to fiducials from galactic globular clusters, they estimate a metallicity of <[M/H]> = -2.2 ± 0.8 for the M33 halo. This is in comparison to their value of -0.6 for a field at a similar location with respect to M31, although this sampled an "extended disk" component rather than the halo.

Kim et al. 2002 used VI photometry of 10 HST/WFPC2 fields located at M33 radii between 2′.6 and 17′.8 projected, and estimated a metallicity gradient among RGB stars in the inner disk following a trend -0.55(±0.02) - 0.05(±0.01)R_{dp}.

Tiede et al. 2004 studied stellar populations in the outer regions of M33, finding a metallicity of [Fe/H] ∼ -1.0 in a field ranging in deprojected radius from around 8.5 to 12.5 kpc. They concluded this was predominantly a disk population. Davidge 2003 studied a field on the minor axis of M33 at a radius in the disk of between 14 and 17 kpc (the distance of Kim et al. 2002 of 916 kpc is adopted). They detect bright AGB (asymptotic giant branch) stars as well as RGB stars, indicating an intermediate age population occurring outside the young star-forming disk of M33. Based on the colour of the stars on the upper RGB, they derive a metallicity of [Fe/H] = -1.0 ± 0.3(random) ± 0.3 (systematic) in their field. Rowe et al. 2005 study AGB stars in a large mosaic of fields in M33. As well as V and I photometry, narrowband filters (TiO and CN) were used to divide the AGB population into C (carbon star) and M types. The C/M star ratio was used to investigate the metallicity gradient, finding that the disk becomes more metal poor at larger radii. Barker et al. (Barker, 2007; Barker et al., 2007a,b; Barker & Sarajedini, 2008) wrote a series of papers focused on M33 which follow up this paper, again focusing on the region from 9-13 kpc in deprojected radius, also considering the population to be predominantly disk related although a halo component is not ruled out. Barker et al. 2007a estimate by their own and other studies the halo/disk transition at around 50′ (12.3 kpc). Matthew Teig wrote a PhD thesis which included surface brightness profiles of the M33 disk and halo (Teig, 2008), his work indicated a scale length of 0.92 kpc in the disk. This scale length is much shorter than any other work (cf. Barker et al. 2007a 4′.7 or Ferguson et al. 2007 1.8 kpc), with the disk dominant in Teig's work to about 8 kpc. Cioni et al. 2008 use UKIRT wide-field JHK_s near-infrared observations covering an area of 1.8° × 1.8° around M33 to study the population of AGB stars. They confirm a metallicity gradient, finding a spread in [Fe/H] of at least 0.6 dex, the most metal poor regions having [Fe/H] = -1.54 and the most metal rich having [Fe/H] = -0.91 dex.

Sarajedini et al. 2006 studied RR Lyrae variables in M33, finding two populations which they identify as disk and halo components. A previous study, Sarajedini et al. 2000 had focused on halo clusters for which they derived a metallicity of <[Fe/H]> = -1.27 ± 0.11. The peak of the metallicity distribution of the supposed field halo RR Lyrae stars is consistent with this. Brooks et al. 2004 constructed a radial stellar density profile out to 1 degree from the centre of M33. They determine a peak metallicity for the halo of M33 of [Fe/H] = -1.24 ± 0.04. McConnachie et al. 2006 presented initial spectroscopic work in this galaxy finding 11 candidate halo stars which exhibited an average [Fe/H] ∼ -1.5, distinct in both velocity and colour from the strongly peaked disk populations in the same spectroscopic fields. Ibata et al. 2007 and McConnachie et al. 2009 present wide field photometry of this galaxy taken with the CFHT-MegaCam, showing faint extended emission and possible tidal tails dominating the radial profile of M33 at large radius, implying the presence of an extended stellar halo in M33. McConnachie et al. 2010 show the presence of a large substructure around M33, which they take as evidence that the Triangulum galaxy has interacted with

Study	Method	Distance Modulus	Distance (kpc)	Reddening
U et al. (2009)	BSG	24.93 ± 0.11	968.3	$< E(B-V) >= 0.083$
U et al. (2009)	TRGB	$24.82^{+0.10}_{-0.06}$	920.4	$E(B-V) = 0.04$
Scowcroft et al. (2009)	Cepheids	24.53 ± 0.11	805.4	See note 1
Bonanos et al. (2006)	DEB	24.92 ± 0.12	963.8	$E(B-V) = 0.09 \pm 0.01$
Sarajedini et al. (2006)	RR Lyrae	24.67 ± 0.08	859.0	$\sigma_{E(V-I)} = 0.30$
Brunthaler et al. (2005)	Water masers	24.32 ± 0.45	731.1	N/A
Ciardullo et al. 2004	PNe	$24.86^{+0.07}_{-0.11}$	937.6	$E(B-V) = 0.04$
Galleti et al. (2004)	TRGB	24.64 ± 0.15	847.2	$E(B-V) = 0.04$
McConnachie et al. (2004)	TRGB	24.50 ± 0.06	794.3	$E(B-V) = 0.042$
Tiede et al. (2004)	TRGB	24.69 ± 0.07	867.0	$E(B-V) = 0.06 \pm 0.02$
Kim et al. (2002)	TRGB	$24.81 \pm 0.04(r)^{+0.15}_{-0.11}(s)$	916.2	$E(B-V) = 0.04$
Kim et al. (2002)	RC	$24.80 \pm 0.04(r) \pm 0.05(s)$	912.0	$E(B-V) = 0.04$
Lee et al. 2002	Cepheids	$24.52 \pm 0.14(r) \pm 0.13(s)$	801.7	$E(B-V) = 0.20 \pm 0.04$
Freedman et al. 2001	Cepheids	24.62 ± 0.15	839.5	$E(B-V) = 0.27$
Pierce et al. 2000	LPVs	24.85 ± 0.13	933.3	$E(B-V) = 0.10$
Sarajedini et al. (2000)	HB	24.84 ± 0.16	929.0	$< E(V-I) >= 0.06 \pm 0.02$

Table 1.2: A review of recent distance determinations to M33. DEB: Detached eclipsing binary, TRGB: tip of the red giant branch, PNe: planetary nebulae, RC: the red clump, LPVs: long period variables, HB: horizontal-branch stars, BSG: Blue Supergiants. Note 1: The Wesenheit reddening-free period-luminosity relation is used in this work.

Andromeda, and that this substructure has its origin in tidal interactions. It is possible that the original halo of Triangulum may have been stripped off entirely, and studies of the "halo" of Triangulum are sampling this substructure population. See section 4.4 for a discussion of this hypothesis.

1.5.3 Distance to M33

The distance to the M33 galaxy has been determined by a range of different methods. However they do not all agree. See Bonanos et al. 2006 for a review of a number of different measurements, and Scowcroft et al. 2009 and U et al. 2009 for a couple of more recent results.

We have assumed a distance to M31 of 809 kpc ($M - m = 24.54 \pm 0.06$) (McConnachie et al., 2005).

The TRGB result from U et al. 2009 is $M - m = 24.82^{+0.10}_{-0.06}$. A number of other distance determinations quote a value near to this, so it is worth examining the consequences for our work if the distance modulus was say, 0.3 magnitudes larger (approximately 100 kpc more distant). The first obvious consequence is that the halo and disk scale lengths will change by approximately 13%, however this is only important when comparing to other work, since the main topic of interest is the relative contribution of the halo compared to the disk.

The other consequence is for the metallicities. The photometric metallicities are measured by the star's position in the colour-magnitude diagram, in comparison to isochrones. The distance assumption also affects the spectroscopic metallicities, by way of the calibration of the Ca II triplet equivalent width to [Fe/H] relation. Discussions of the effect of distance assumptions and errors therein on our photometric and spectroscopic metallicities respectively can be found in sections 3.5.1 and 3.6.2.

Chapter 2

Context - The INT and PAndAS surveys and DEIMOS spectroscopic observations

2.1 Photometric studies

2.1.1 The INT WFC survey

The Isaac Newton Telescope has a 2.54 metre diameter primary mirror with focal ratio f/2.94. It is located at the Observatorio del Roque de los Muchachos, La Palma, Canary Islands.

A survey of the area of the sky around M31 and M33 was conducted using this telescope with the Isaac Newton Telescope Wide Field Camera, which is a 4-chip EEV 4k × 2k CCD mosaic , which coupled with the Isaac Newton Telescope images ≈ 0.29 square degrees. Between September 2000 and January 2004 163 fields were imaged corresponding to ≈ 40 square degrees in the disk and halo of M31. The coverage extends over an elliptical region of semi-major(minor) axis 4(2.5)° or ≈ 55(34) kpc, with an additional ∼ 10 square degree extension towards the south. Images were taken in the Johnson V and Gunn i bands, and the exposure time of 800-1000s per passband allowed a depth of $i = 23.5$, $V = 24.5$ (signal/noise ≈ 5) to be reached. At the M31 distance this allowed RGB stars to be detected to $M_V \approx 0$ and main sequence stars to $M_V \approx$ -1. Further information about the survey observations can be found in Irwin et al. 2005; Ferguson et al. 2002; Ibata et al. 2001. The foreground contamination increases smoothly from around ≈ 13000 stars per square degree to ≈ 20000 stars per square degree from the southern to northern extremities of the survey area respectively. The extent of the coverage of the INT survey in M31 is shown in Figure 2.1 and around M33 in Figure 2.2.

2.1.2 PAndAS - the Pan-Andromeda Archaeological Survey

More extensive work was done under the aegis of the PAndAS and SPLASH surveys, using both photometric and spectroscopic information. For detail on the PAndAS survey see McConnachie et al. 2009; Martin et al.

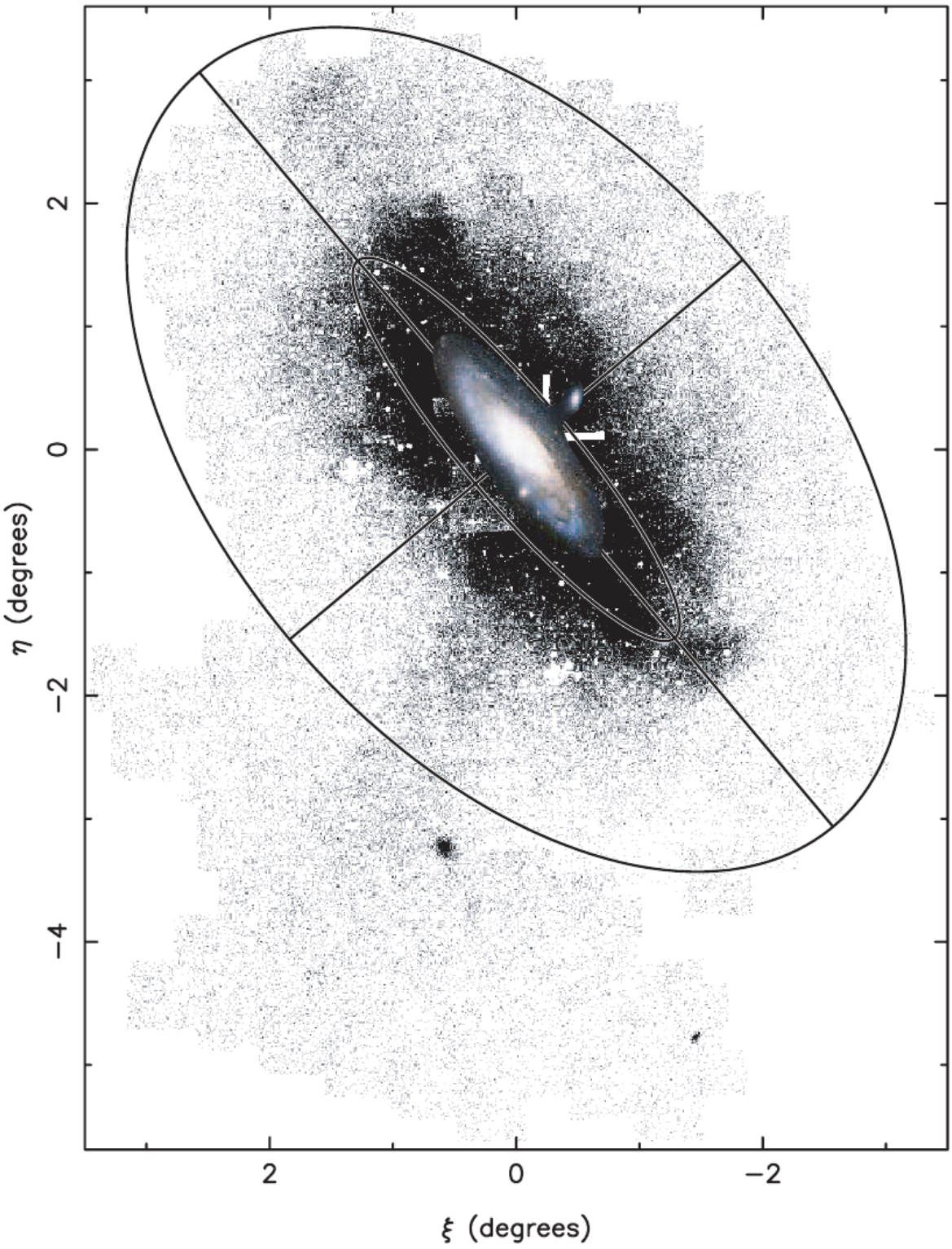

Figure 2.1: A diagram showing the coverage of the INT survey, the outer ellipse shows a segment of a 55 kpc radius ellipse flattened to $\frac{c}{a} = 0.6$, and the major and minor axes are indicated with straight lines. M31 is located at the centre of the coordinate system. Figure from Ibata et al. 2005.

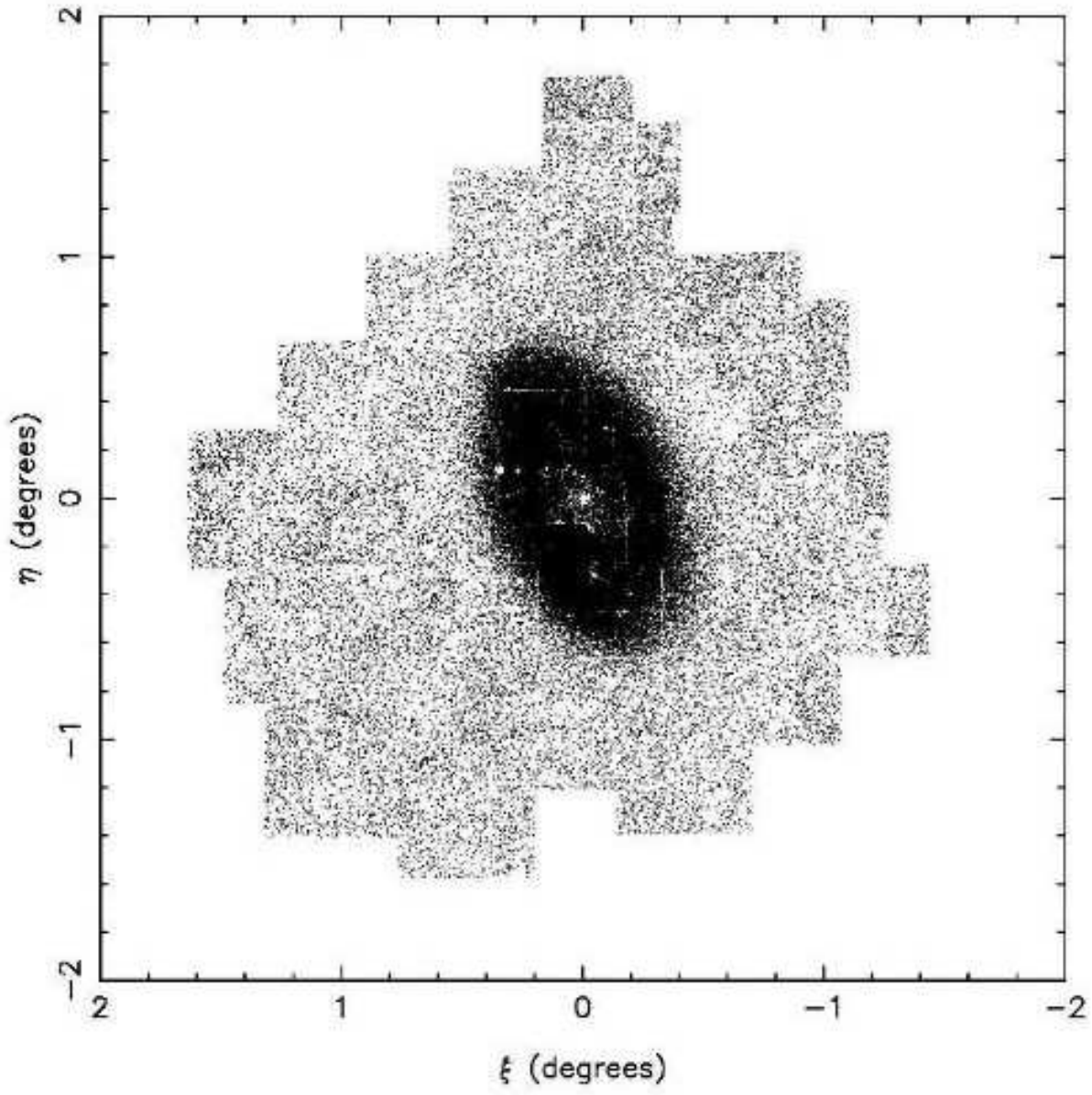

Figure 2.2: A diagram showing the coverage of the INT survey around M33. M33 is located at the centre of the coordinate system. Figure from Ferguson et al. 2007.

2009 and papers referenced therein. The extent of the coverage of the PAndAS survey can be seen in Figure 2.3.

The PAndAS (Pan-Andromeda Archaeological Survey) is a programme using the 1-square degree field of view MegaPrime/MegaCam camera on the 3.6m Canada France Hawaii Telescope (CFHT). The survey area covers a wide area around M31 and M33. Completed in January 2011, the survey covers more than 300 square degrees (over 70,000 kpc^2) and extends to a maximum projected radius from the M31 centre of $r_p \approx 150$ kpc. This is the largest contiguous imaging survey of a massive galaxy and spans the stellar halo out to extremely large radii. PAndAS surveys in the g and i bands and resolves stars in M31 to depths of $g = 26.5$, $i = 25.5$ at signal/noise = 5.

Another group led by Guhathakurta has conducted the SPLASH (Spectroscopic and Photometric Landscape of Andromeda's Stellar Halo) survey, which also used the DEIMOS instrument to cover a different range of fields. In this case targets were selected based on photometric data from either the CFHT MegaCam or KPNO (Kitt Peak National Observatory) 4m/Mosaic data. For some more detail on the SPLASH survey see for example, Gilbert et al. 2009; Kalirai et al. 2009.

The target population of stars is the red giant branch (RGB). The red giant branch is an evolutionary phase late in a star's life, during which the star expands and brightens to perhaps a few hundred to a few thousand times the Sun's luminosity. Red giants are common, since although the red giant branch phase is much briefer than the main sequence, lasting only perhaps a few million or tens of millions of years, the vast majority of stars go through this phase. The high luminosity means that they can be seen at the distance of M31 and M33 .

2.2 Spectroscopic work with DEIMOS

DEIMOS is an acronym for DEep Imaging Multi-Object Spectrometer. Mounted on the 10m Keck II telescope on Mauna Kea, Hawai'i, it is arguably the best instrument for medium and high resolution multi-object spectroscopy in the world at the present time. It has a field of view of $16'.7 \times 5'$ and can be used in a number of modes. Chapman et al. 2006 describes how it was used to gather spectroscopic data around Andromeda. Technical information concerning the DEIMOS instrument design can be found in Davis et al. 2003.

2.2.1 Technical detail about the DEIMOS instrument and its operation

Light is directed to the DEIMOS instrument using a tertiary mirror tilted at 45°. A diagram of how DEIMOS is mounted on the Keck II telescope is shown in figure 2.4. The light comes to focus at the focal plane, which is covered by a smooth sheet of metal into which small slits are cut, forming a "slitmask". The slits are located precisely to accept light from targeted objects.

Light passes through the slitlets into the body of the spectrograph to a collimator mirror, then via a flat mirror to the grating, which spreads it into a spectrum, then a camera which focuses the dispersed light onto the CCD detectors. A diagram of the optics of DEIMOS is shown in figure 2.5. There are eight CCDs each with 2000 × 4000 pixels. DEIMOS also incorporates a flexure control system which compensates for shifts in optical alignment, reducing difficulties in the calibration and data reduction. In the observations detailed in Chapman et al. 2006 (and subsequent observations of M31 and M33), several different modes of operation

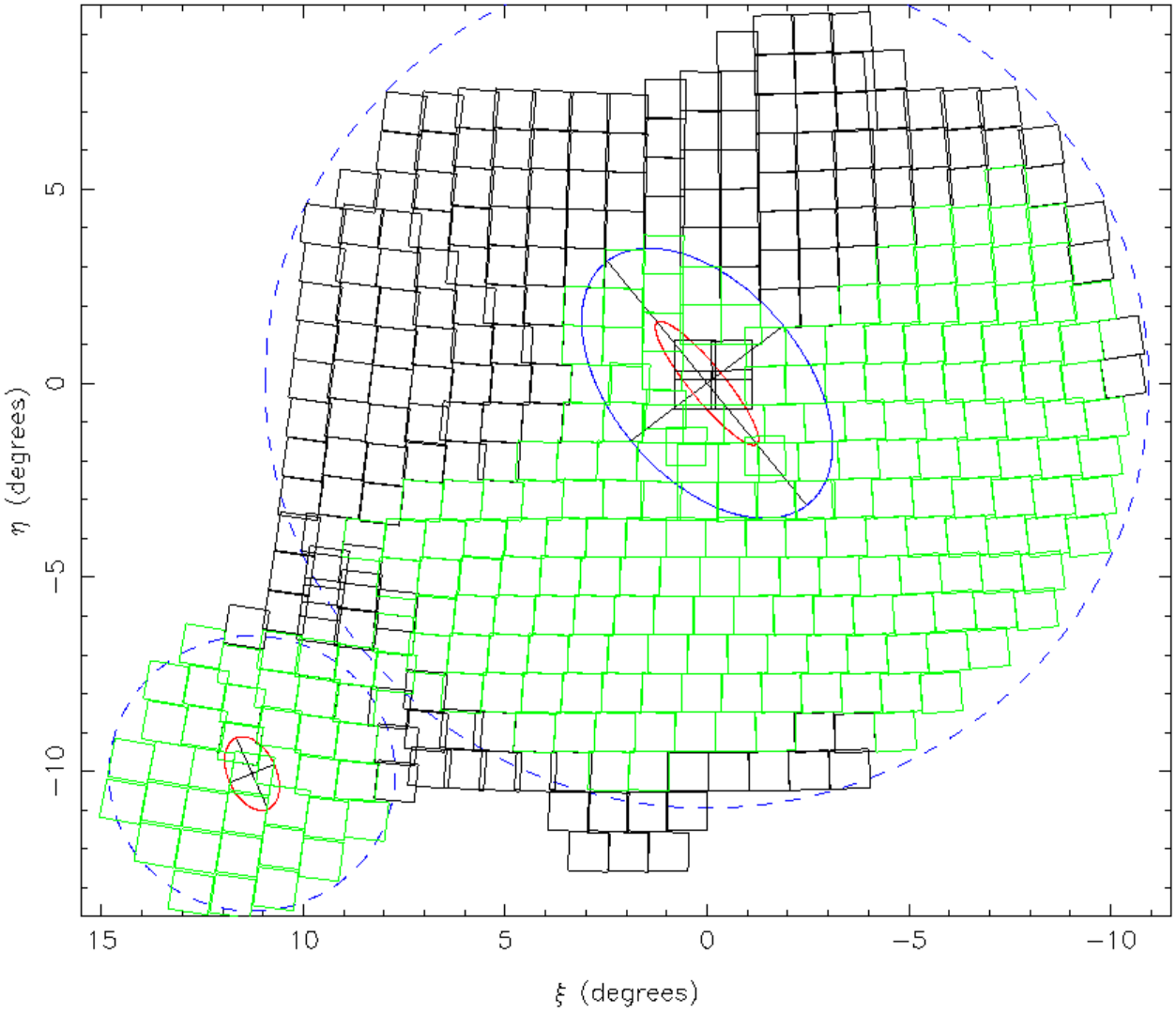

Figure 2.3: A diagram showing the coverage of the PAndAS survey. M31 is located at the centre of the coordinate system. M33 is shown in the lower left. Dotted blue lines indicated projected distances of 150 kpc from M31 and 50 kpc from M33. Fields in green are those published in Martin et al. 2009, those in black since then.

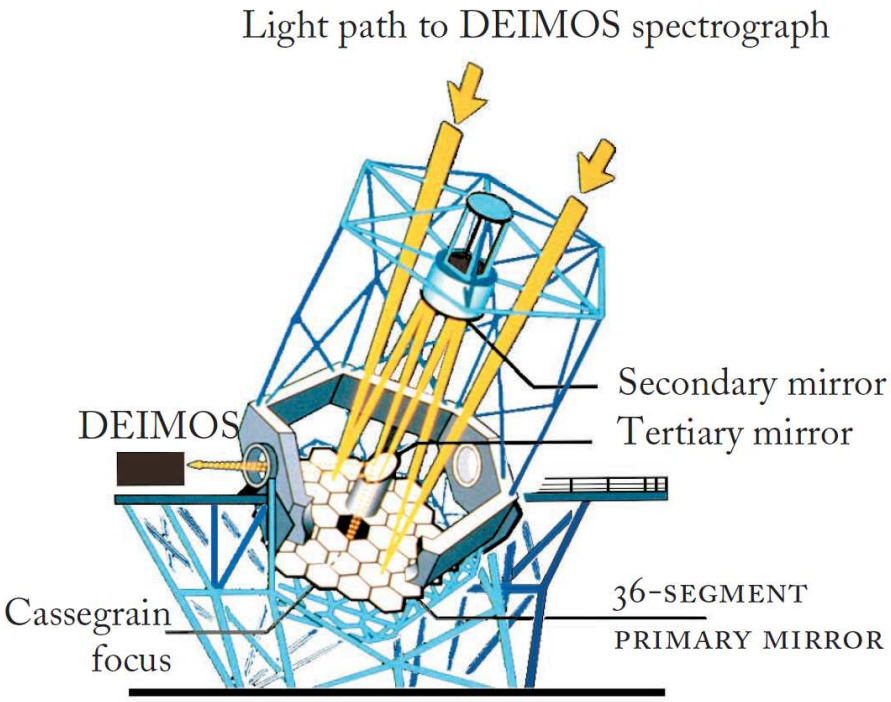

Figure 2.4: A diagram showing the mounting of DEIMOS on Keck II. (From DEEP survey brochure, Faber et al. 2000)

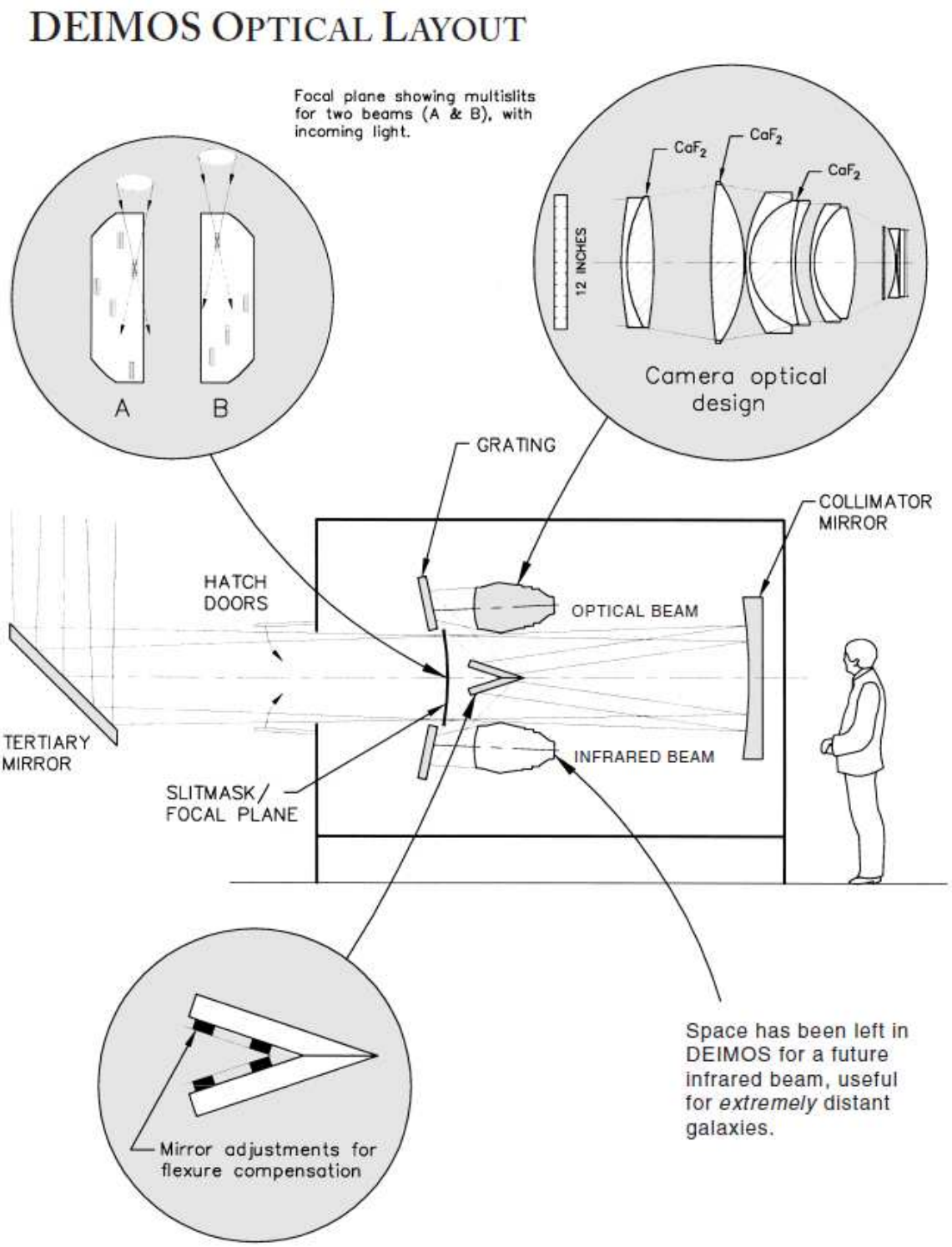

Figure 2.5: A diagram showing the optics of the DEIMOS instrument. (From DEEP survey brochure, Faber et al. 2000)

of the DEIMOS instrument were used. In lower density fields the standard DEIMOS multislit approach was used as for the DEEP2 survey (see Davis et al. 2003 for example) but in the high density inner fields, two different approaches were used. These were a band-limiting ~ 300 $\mathring{A}$ Ca II triplet filter to multiplex $\sim 4''$ slitlets in the spectral direction yielding as many as 800 slits per mask, and a "fiber-hole" approach using $0.7''$ slitlets packing ~ 600 holes per mask. The fiber-hole approach proved to be very successful, giving Poisson-limited sky subtraction (down to $i = 21.5$) by assigning holes to monitor the sky spectrum. The $0.7''$ hole diameter was chosen to match the median seeing.

2.2.2 The use of DEIMOS to observe Andromeda and Triangulum

In total to date, DEIMOS has been used to measure spectra of a total of over 16000 stars in over 90 masks around Andromeda and Triangulum. Of these about 14000 are located in fields distributed around Andromeda and about 2000 around Triangulum. Approximately half to two-thirds are likely to be RGB stars within the Andromeda and Triangulum systems.

The DEIMOS spectra (where the standard high-resolution DEEP2 slit-mask approach is used - see Davis et al. 2003) cover a range from 6400 to 9000 $\mathring{A}$, which covers the region around the Ca II triplet (CaT) lines. The spectral resolution is ~ 0.6 $\mathring{A}$. These spectra were processed using the DEEP2 (Deep Extragalactic Evolutionary Probe) pipeline, to yield radial velocities, and spectroscopic [Fe/H] metallicities based on the equivalent width of the three CaT lines. The DEEP2 data reduction pipeline was developed by the DEEP2 survey team at the University of California, Berkeley (UCB). It is based on the SDSS spectral reduction package. In addition, Rodrigo Ibata has re-processed the data using his own pipeline.

2.2.3 Target selection

For each field (except the M31 stream fields), the highest priority targets were selected from the photometric surveys within a colour-magnitude box with I-band magnitudes in the range $20.5 < i < 22.0$ (without reddening correction) and colours $1.0 < (V - i)_0 < 4.0$. This broad selection was designed to pick out both metal-poor and metal-rich RGB stars. Other nonsaturated targets brighter than $i = 22$ were also chosen by an automated selection algorithm at lower priority to fill in available space on the spectrograph detector. In addition to spectroscopic metallicities based on the measurement of CaT lines of individual stars, the spectra have also been stacked within each field to get a more reliable measurement for each field as a whole (there is a wide scatter in the individual stellar metallicity measurements due to low signal to noise).

2.2.4 Accuracy of radial velocity and metallicity measurements.

DEIMOS used in the above way produces radial velocities accurate to a typical error of 5-10 km s^{-1}, for Andromeda or Triangulum RGB stars at magnitude $I = 21.0$. The spectroscopic metallicities are not very accurate for individual RGB stars, however can be useful either used statistically comparing different groups of stars, or using co-added spectra.

2.2.5 Summary of scientific work using DEIMOS on M31

The DEIMOS masks are located in a range of settings around M31 and M33. There are masks covering areas around the M31 disk, Giant Southern Stream, other M31 halo substructure, the Ibata et al. 2007 tangential

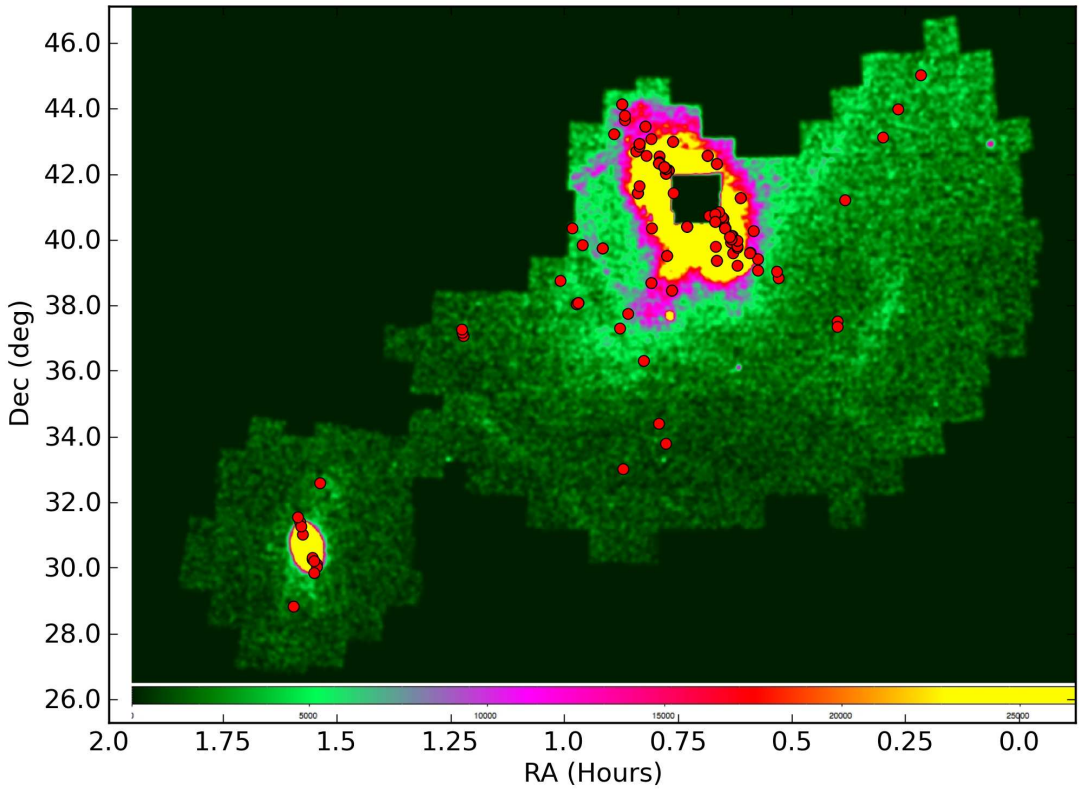

Figure 2.6: A tangent plane projection of RGB stars in M31 and M33 with $I < 23$, from the CFHT MegaCam *PAndAS* survey (McConnachie et al. 2009). The locations of the Keck/DEIMOS fields are indicated by the red dots.

Field	RA	Dec	Total N Targets	Observing run
156Tri	$01^h34^m50^s.46$	$31°23'00''.0$	105	2005 Sep
157Tri	$01^h32^m39^s.91$	$30°06'48''.0$	224	2005 Sep
158Tri	$01^h32^m39^s.62$	$30°01'36''.0$	156	2005 Sep
236Tri	$01^h33^m10^s.00$	$30°15'00''.0$	306	2006 Sep
237Tri	$01^h33^m15^s.00$	$30°19'00''.0$	283	2006 Sep
408TrS	$01^h32^m58^s.26$	$30°13'02''.4$	196	2008 Oct
409TrS	$01^h34^m33^s.02$	$31°00'48''.3$	193	2008 Oct
412TrS	$01^h34^m42^s.05$	$31°15'42''.7$	152	2008 Oct
M33EC1	$01^h32^m58^s.51$	$29°52'03''.0$	110	2008 Sep
M33EC2	$01^h35^m41^s.78$	$28°49'15''.5$	50	2008 Sep
511TrS	$01^h32^m13^s.00$	$32°35'18''.0$	47	2009 Oct
140Tri	$01^h35^m11^s.06$	$31°33'00''.0$		

Table 2.1: Table showing the field positions and numbers of stars in each field in the DEIMOS masks around M33. The field 140Tri had some problems in the data reduction, so is not used in this dissertation.

streams, M33 disk and halo substructure. See Figures 2.6 and 2.7, table 2.1 and table A.1.

The DEIMOS spectrograph has been used to study the disk and halo of M31. Work has been done on the Giant Stream and other substructure in the M31 halo in order to better characterise the kinematics of the M31 Giant Stream, and ascertain whether there is any evidence that any of the other substructure found in the M31 halo is related to the Giant Stream (see Ibata et al. 2007; McConnachie et al. 2009 for descriptions of what has been observed photometrically in the M31 halo by the PAndAS survey).

Fardal et al. have tried to model the Giant Stream as the consequence of the accretion of a dwarf galaxy progenitor (the core of which has not been identified) in Geehan et al. 2006; Fardal et al. 2006, 2007. The SPLASH survey group have also published observational work on the Giant Stream (Guhathakurta et al., 2006; Gilbert et al., 2009). The tangential streams observed in Ibata et al. 2007 were followed up spectroscopically in Chapman et al. 2008 as well as extended clusters (Collins et al., 2009). The M31 disk has also been a topic of investigation, with work by Collins et al. 2011 characterising the "thick disk" population. Dwarf satellite galaxies have also been a subject of investigation using the DEIMOS spectra (Martin et al., 2006, 2009; Kalirai et al., 2009; Collins et al., 2010; Kalirai et al., 2010).

2.2.6 The DEIMOS data in M33

The M33 DEIMOS masks are located in regions covering the outer disk and halo of the Triangulum galaxy (M33) from a (projected) distance from the centre of M33 of 5.2 to 28 kpc. There are 11 masks used in this work, with a total of 1822 stars observed spectroscopically. There are masks on both the northern and southern sides of the centre of M33. The locations of the M33 DEIMOS fields are shown superimposed on a RGB star density map of the M33 disk in Figure 2.7. The red boxes show the footprints of the $16'.7 \times 5'$ DEIMOS masks.

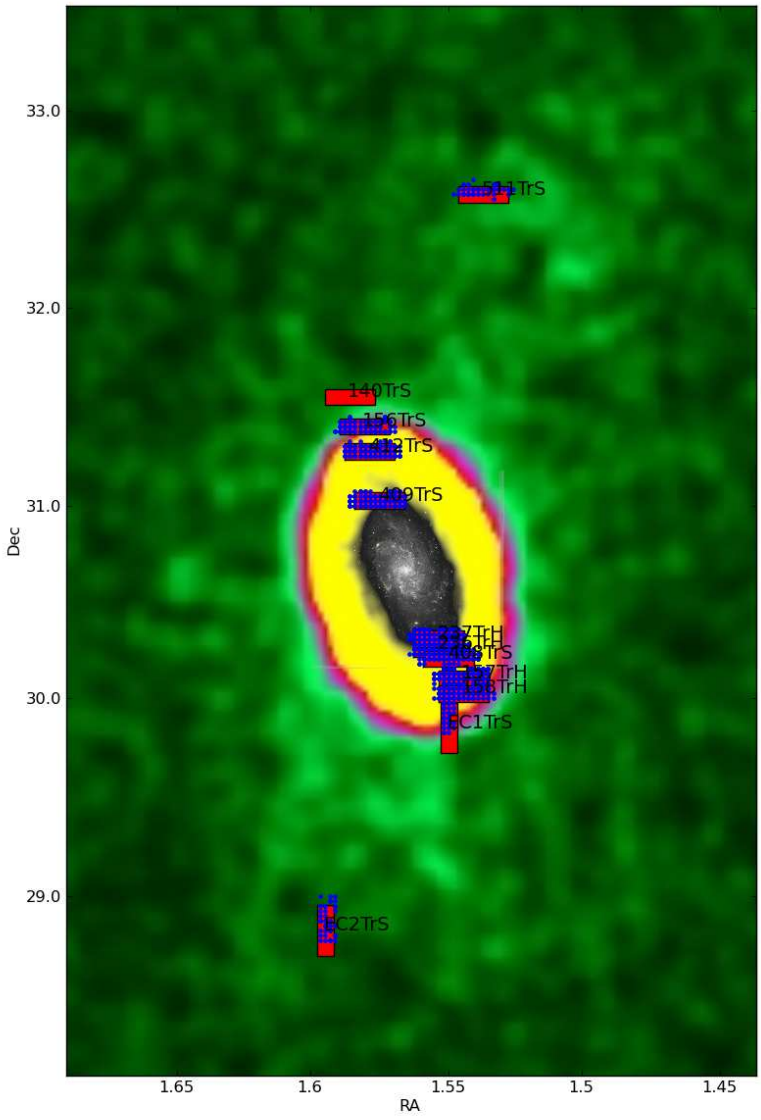

Figure 2.7: A tangent plane projection of RGB stars in M33 with $I < 23$, from the CFHT MegaCam *PAndAS* survey (McConnachie et al. 2009). The locations of the Keck/DEIMOS fields are indicated.

Chapter 3

M33 disk and halo in the DEIMOS data

3.1 Processing of the pipelined data

Programs were written in Python to process the pipelined data. One program simply reads the pipelined data in from the tabulated catalogue files. Another program applies the quality cuts (discussed later) and generates the velocity histograms. This outputs the "disk" and "halo" samples into various data files, either using simple or Bayesian kinematic windowing as described in section 3.1.5.

A further program was written to read in the spectra using the PyFITS library, again apply quality cuts, and stack the spectra based on their membership of particular fields and kinematic windows, and measure the Ca II triplet equivalent widths by the fitting of Gaussians. This program weights the spectra using the following scheme: any spectra which fail the quality cuts are ignored entirely, and the remaining spectra are normalised and then weighted by their signal to noise ratio. For the Bayesian samples, the spectra are also weighted by the probability of being in the "halo" or "disk" population.

Further programs produce summary plots of various quantities, such as the disk and halo profiles, the metallicity distributions, and metallicity as a function of radius.

3.1.1 Kinematic summary plots

Figures 3.1 and 3.2 show heliocentric velocity histograms of the various M33 DEIMOS fields. Figure 3.1 shows the fields which are located to the south of the centre of M33 on the sky, which means that the M33 disk population is at higher velocities than the M33 systemic velocity of -179 km s^{-1}. The velocities are in a heliocentric frame. Following the usual convention in astronomy, a negative velocity indicates an object is moving towards the Sun. In Figure 3.2, the velocity histograms of the 4 fields to the north of the centre of M33 are shown. Here the M33 disk population is visible at more negative velocities than M33 systemic. The systemic velocity of M33 is indicated on the histograms using a dotted line. In Figures 3.3 and 3.4 the overall velocity distribution is illustrated by stacking all of the southern, and northern fields respectively. Figure 3.5 shows contour plots of the density in velocity-photometric [Fe/H] space. See section 3.5 where

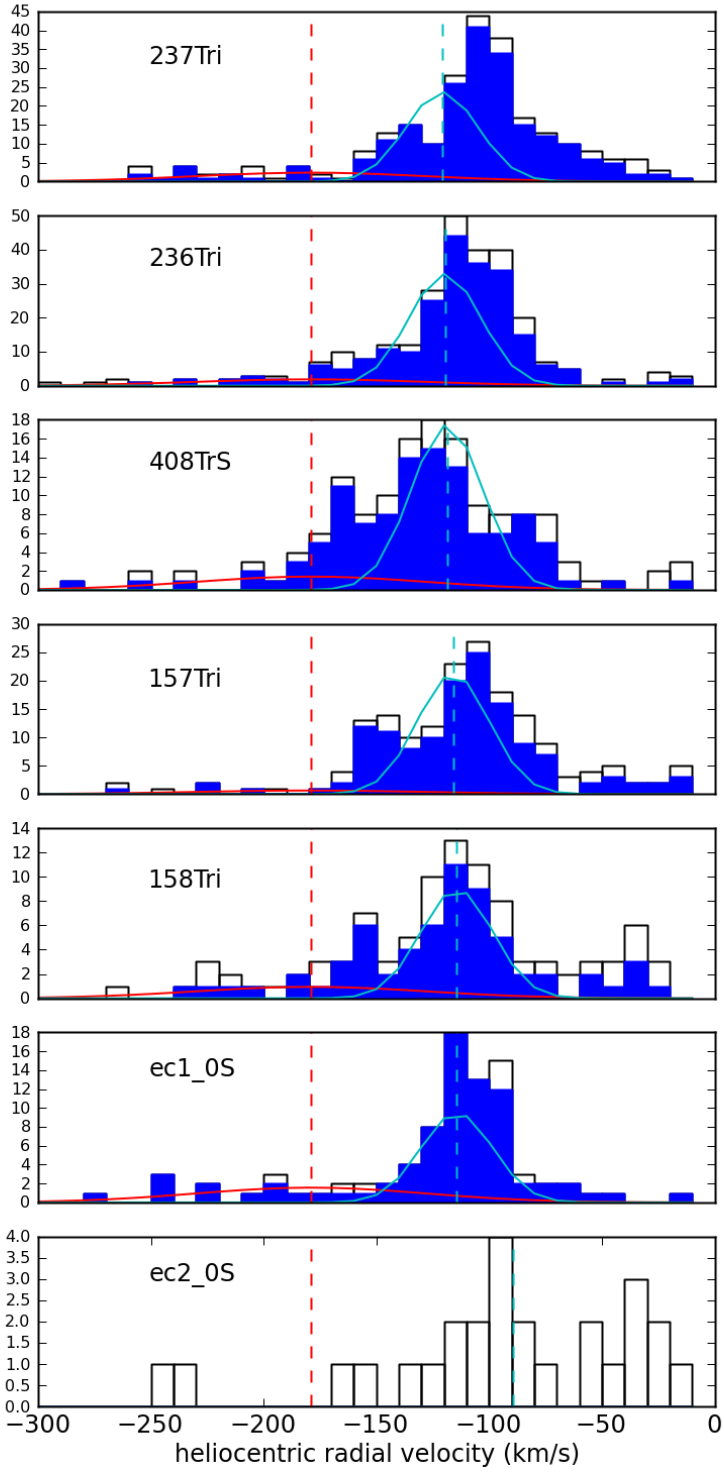

Figure 3.1: Velocity histograms for the 7 southern fields. The filled bars show the stars passing all quality cuts, the unfilled ones show all stars. An expected velocity distribution for the disk (light blue line) based upon the Corbelli et al. 2000 rotation curve and the McConnachie et al 2006 figure of $\sigma = 16$ km s^{-1} for the disk is overlaid. A halo velocity dispersion around -179 km s^{-1} is overlaid in red.

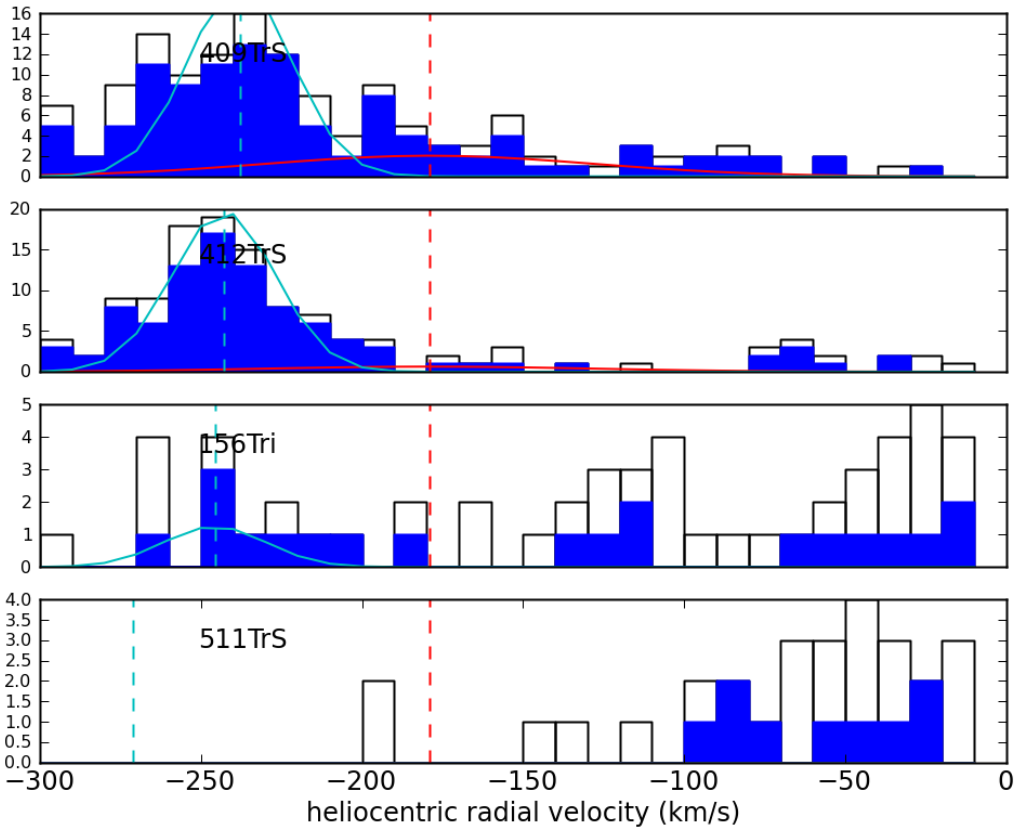

Figure 3.2: Velocity histograms for the 4 northern fields. The filled bars show the stars passing all quality cuts, the unfilled ones show all stars. An expected velocity distribution for the disk (light blue line) based upon the Corbelli et al. 2000 rotation curve and the McConnachie et al 2006 figure of $\sigma = 16$ km s^{-1} for the disk is overlaid. A halo velocity dispersion around -179 km s^{-1} is overlaid in red.

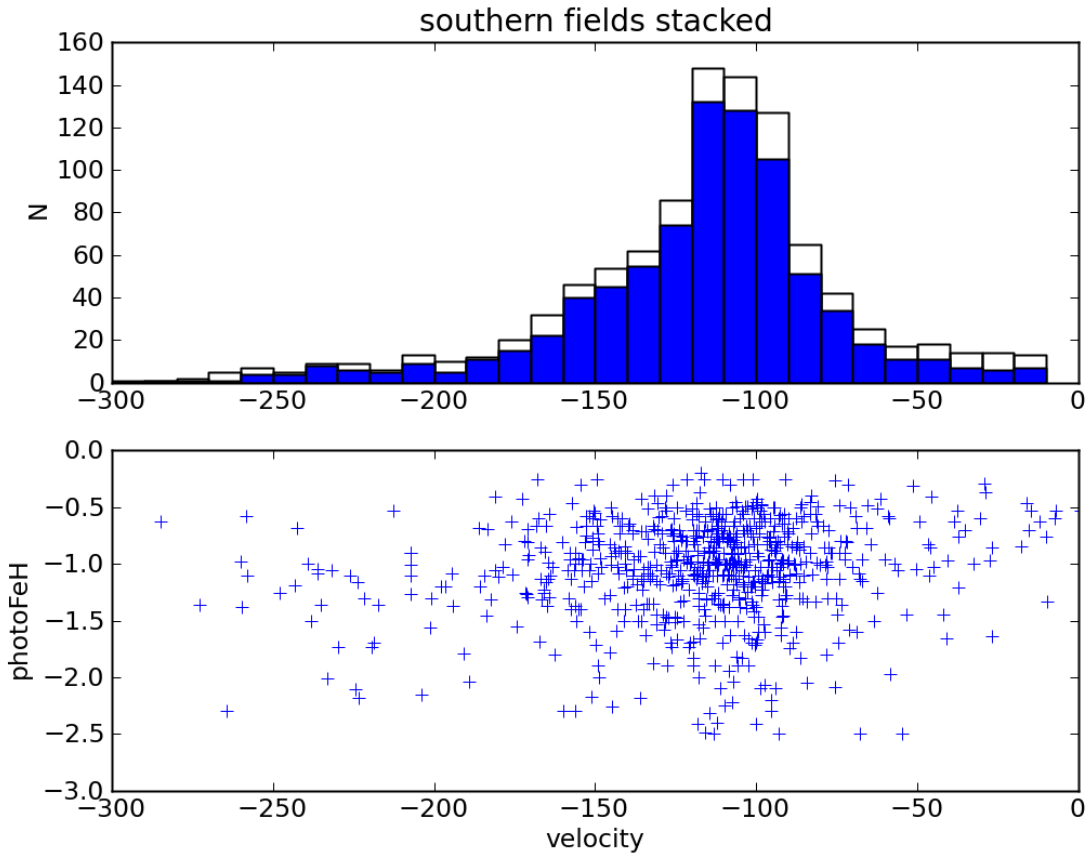

Figure 3.3: Heliocentric velocity histogram for the 7 southern fields stacked. Below this the scatter plot of velocity against photometric metallicity is shown (Dartmouth isochrones (Dotter et al., 2008), age = 8 Gyr, $\alpha = +0.2$).

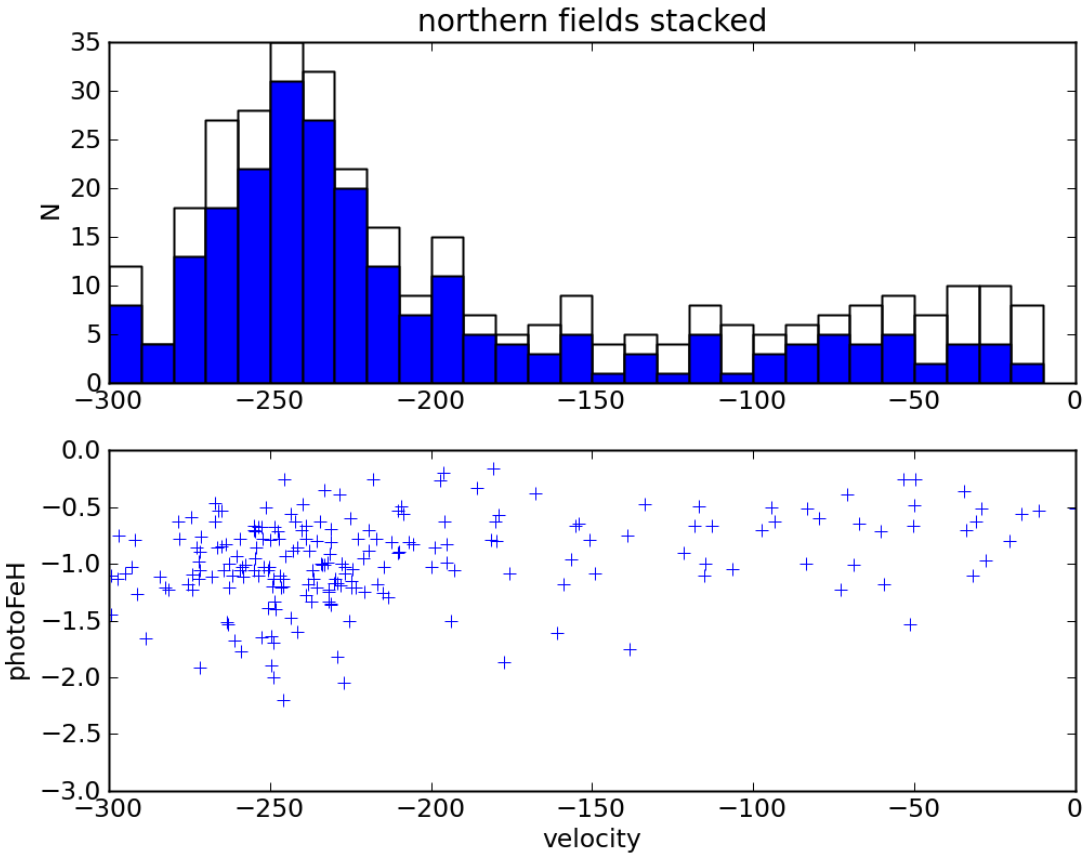

Figure 3.4: Heliocentric velocity histogram for the 4 northern fields stacked. Below this the scatter plot of velocity against photometric metallicity is shown (Dartmouth isochrones (Dotter et al., 2008), age = 8 Gyr, $\alpha = +0.2$)

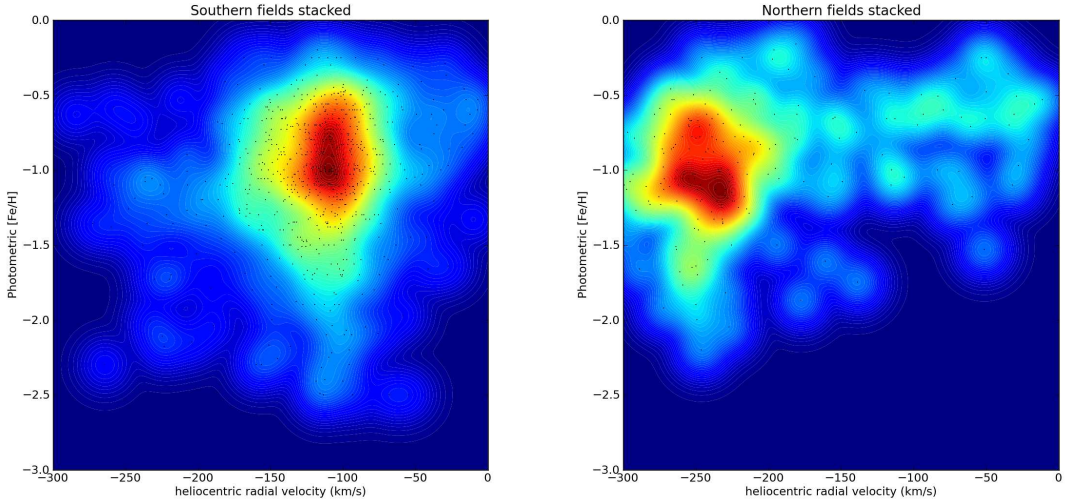

Figure 3.5: In this figure, the velocity and photometric [Fe/H] (Dartmouth isochrones, 8 Gyr, $\alpha = +0.2$) data had been used to create a contour plot of the density of points for the stacked southern fields (left) and northern fields (right). Each point is used to generate a 2D Gaussian (sigmas 10km s^{-1}, 0.1 dex) and these Gaussians are added together. The colours from blue through green, yellow to red indicate increasing density (there is a square root scaling used). There is a metal poor component that follows the disk kinematically.

the procedure for calculating the photometric [Fe/H] is explained.

3.1.2 Disk rotation

The M33 disk is at an inclination of 56°, (with the convention being 0° being face on, and 90° edge on). The rotation curve has been studied using the radial velocities of H I gas, for example Corbelli & Salucci 2000. A figure from this paper is reproduced in figure 3.6 showing the rotation curve of M33 according to their model. In the range of the majority of our observations (which are on the major axis) that is, 5-12 kpc in projected radius, the rotation curve approximates to a straight line with the equation $v = 90 + \frac{8}{3}$r. Note that this is the velocity in the disk plane, which must be adjusted to get the radial velocity. However on the major axis, this is simply multiplying the disk velocity by the cosine of the inclination and adding the M33 systemic velocity. McConnachie et al. 2006 observed a velocity dispersion of 16km s^{-1} for the stellar disk. The M33 disk has been observed to have a warp in H I. This is shown in figure 3.7. This warp means that the inclination is not constant with radius, especially beyond a projected radius of about 4-5 kpc. This means that the rising rotation curve may not reflect reality but instead the change in inclination, so that in fact the real rotation curve could be flat. In our analysis we have removed their inclination correction in Figure 3.8 and this results in a much flatter curve. The Corbelli et al. inclination varies between 50 and 58 degrees, and this varying inclination correction is removed.

For comparison purposes, a rotation curve from our own stellar velocities was generated, which can be found in figure 3.8. Here, the magnitude of the rotation based on the velocity dispersions of the "disk" sample in individual fields appears smaller, and the data is consistent with a flat rotation curve. There is an indication that the H I gas velocity is greater than that of the stellar disk, which may indicate the stellar

disk is tilted with respect to the gas disk. The Corbelli & Salucci 2000 results may also be compared to the work by Putman et al. 2009. See figure 4.5 for the intensity weighted velocity map of the H I gas from Putman et al. 2009. It can be seen that the Putman et al. 2009 velocities agree with the Corbelli & Salucci 2000 that the gas rotational velocity is $\sim$ 100 km s^{-1}, i.e. greater than our stellar velocities.

Another possible explanation for the tendency of the stellar velocities to lag the gas disk, is the phenomenon known as *asymmetric drift*. This is explained in section 4.4.3 of Binney & Tremaine 2008. The stars in a galactic disk such as that of the Milky Way travel on nearly circular and coplanar orbits. Consequently, distribution functions that generate cool disks in which random velocities are much smaller than the circular speed are central to understanding disk galaxies. One such distribution is the Schwarzschild distribution (equation 4.156 in Binney & Tremaine 2008). Binney & Tremaine 2008 examine the consequences of such a model on the distribution of azimuthal velocities $\tilde{v}_\phi$, showing that for a broad velocity distribution, the distribution of azimuthal velocities becomes extremely skew, with a long tail to negative values of $\tilde{v}_\phi$ and a sharp cutoff for $\tilde{v}_\phi > 0$. The reasons for this are the exponential decline of the disk density with radius, and the decline of the velocity dispersion σ_R with radius. The combined effect, is that there are more stars in the solar neighbourhood that have less angular momentum than the local standard of rest than those that have more, there being more stars reaching the Sun with eccentric orbits that come from radii interior to the solar neighbourhood than stars reaching the Sun from radii exterior to the solar neighbourhood. This effect will also apply in M33, its disk being approximately axisymmetric, and exponential like the Milky Way. The effect known as *asymmetric drift* is the fall of the mean rotation rate further below the circular speed with increasing "temperature" $\overline{v_R^2}$. The difference between the stellar and gas disks arises because the stellar population is an effectively collisionless system, whereas the gas disk is not. A further possible effect is the geometric effect caused by some stars not being precisely on the major axis, the DEIMOS fields having a size on the sky of $16' \times 5'$.

3.1.3 Milky Way dwarf contamination

In front of M33, there is a foreground component of dwarf stars within the Galaxy. The expected contribution from Galactic stars that lie in the same part of the colour-magnitude diagram (CMD) used to select candidate RGB stars can be estimated using models. The Besançon star count model (Robin et al., 2003) estimates 3 Galactic stars per M33 DEIMOS field of view ($16'.7 \times 5'$) with $v_{hel} <$ -179 km s^{-1} if all available candidates were observed. We have typically observed $< 50\%$ of the stars which are consistent with M33 RGB colours available in the region covered by a DEIMOS mask. Within the disk of M33 there is a choice of $\sim$ 1000 targets per field and a maximum multiplexing of $\sim$ 300 stars per DEIMOS mask with our mega-slitlets approach (see Ibata et al. 2005).

The Galactic contamination is estimated to be less at smaller radius, where the targets were selected from a larger number of candidates, the smaller selection fraction meant that the Galactic contamination, which is similar across all fields contributes less towards the DEIMOS counts. See tables 3.2 and 3.3.

Contamination may be more of an issue in the N fields "halo" sample, where we are looking at stars with velocities between -179 km s^{-1} and -100 km s^{-1} closer to the main part of the distribution of Galactic stars. To assess the level of Galactic contamination, we can compare the observed star counts to predictions using the Besançon models. The best fields to assess this are 409TrS and 412TrS, which are located to the north of the M33 centre. In the range above the M33 systemic velocity, -179 km s^{-1} $< v_{hel} <$ 0 km s^{-1}, we should see

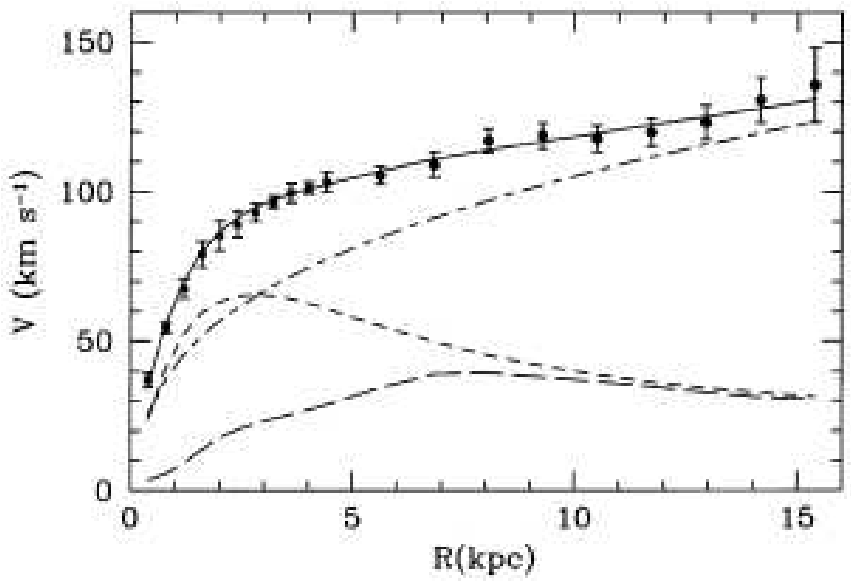

Figure 3.6: The Corbelli et al. 2000 rotation curve for M33. (Corbelli et al. 2000, fig 6) The observed M33 rotation curve is shown by the points. The best-fitting model is shown by the continuous line. Also shown are the halo contribution (dot-dashed line), the stellar disk (short-dashed line) and the gas contribution (long-dashed line).

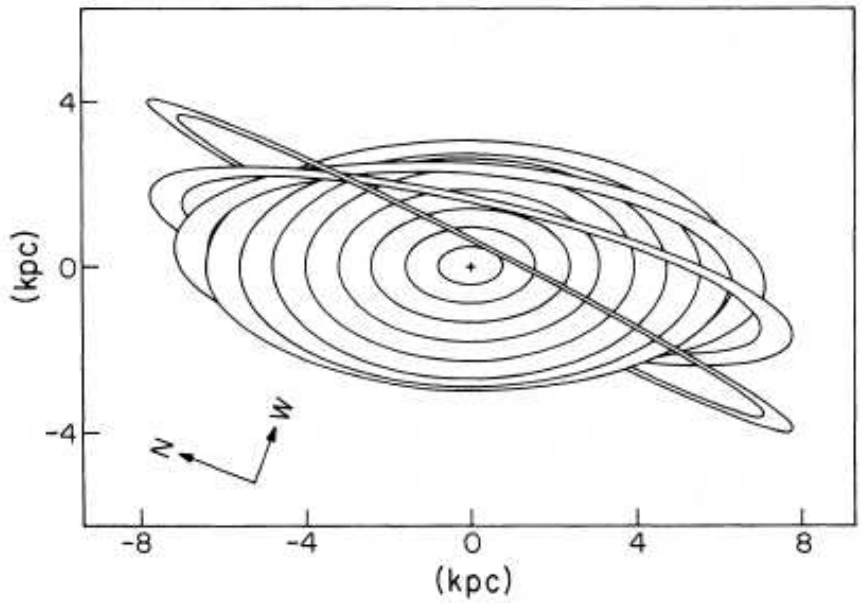

Figure 3.7: A diagram of the warp in the M33 H I disk. (Reproduced from Rogstad et al. 1976 (their figure 14))

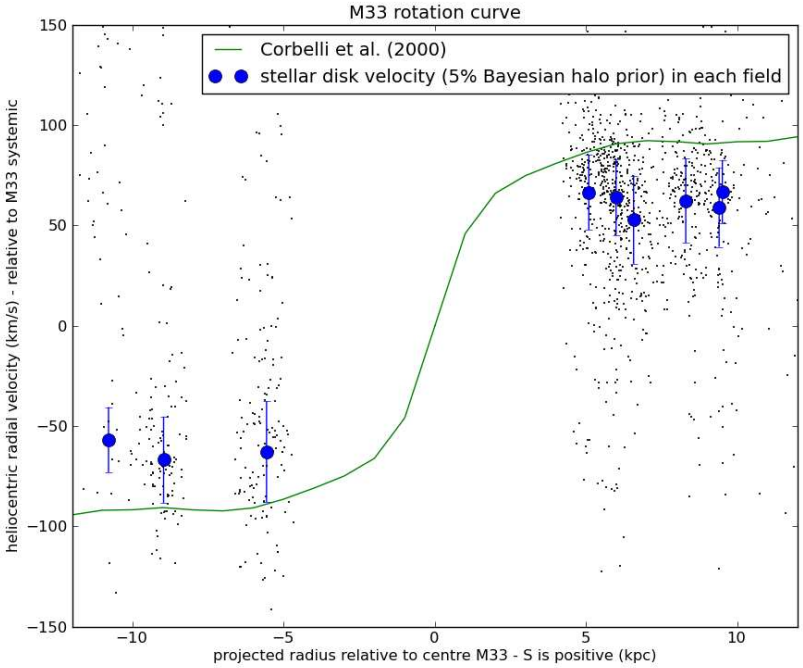

Figure 3.8: A rotation curve based on our own stellar heliocentric velocities, derived from the mean and standard deviation of the Bayesian (5% halo prior) disk sample in each DEIMOS field. Individual stars (quality cut) are plotted with black dots. The velocities are relative to M33 systemic for comparison with figure 3.6. The Corbelli et al. (2000) rotation curve is overplotted, with the inclination correction removed. The error bars displayed are the size of the disk dispersion. It appears that the H I gas rotation velocity is higher than the stellar. This may be due to asymmetric drift (see section 4.4.3 of Binney & Tremaine 2008), or it is possible the stellar disk is tilted with respect to the H I at the radii we are observing it ($\sim$ 5-12 kpc).

a mix of Galactic contaminants, and M33 halo stars. In tables 3.2 and 3.3 the numbers of stars observed by DEIMOS in the various fields are presented in comparison to the Besançon predictions. For the field 409TrS the fraction of available targets that are selected for DEIMOS is 0.065. This would mean that the expected numbers of Galactic stars that should actually be observed by DEIMOS in the ranges -179 km s^{-1} $< v_{hel} <$ 0 km s^{-1} and -179 km s^{-1} $< v_{hel} <$ -100 km s^{-1} are 7.5 and 0.8. If the Besançon predictions are accurate, this would indicate that the majority of stars observed by DEIMOS in both ranges are genuine M33 stars. In the range -179 km s^{-1} $< v_{hel} <$ 0 km s^{-1} the expected Galactic fraction is about one-quarter, and in range -179 km s^{-1} $< v_{hel} <$ -100 km s^{-1} the fraction is 0.042. For the field 412TrS the fraction of available targets that are selected for DEIMOS is 0.22. This means that the numbers of Galactic stars that should be observed by DEIMOS in the ranges -179 km s^{-1}$< v_{hel} <$ 0 km s^{-1} and -179 km s^{-1}$< v_{hel} <$-100 km s^{-1} are 27 and 1.3. In this case we expect to see more Galactic stars in the -179 km s^{-1}$< v_{hel} <$0 km s^{-1} range than the total number of stars actually observed. However in the restricted range -179 km s^{-1}$< v_{hel} <$ -100 km s^{-1} we only predict a Galactic fraction of 0.16.

When considering the range -100 km s^{-1} $< v_{hel} <$ 0 km s^{-1}, in 409TrS we have 12 stars observed, and predict 7 Galactic stars, and in 412TrS we have 14 stars observed and predict 26 Galactic stars. It appears that the numbers of stars observed in 409TrS in this velocity range are in line with the Besançon predictions, and the predictions overpredict the numbers of Galactic stars by a factor of two in 412TrS, although this overprediction may not be statistically significant. It would appear that the use of the cut at -100km s^{-1} is a wise move, because in the range above this velocity, it appears that the majority of what is observed with DEIMOS will be Galactic in origin.

Na I doublet observations

A way in which contamination can be combated is using the Na I doublet (λ = 8183, 8195 $\mathring{A}$) observations. The Na I doublet information was used in work such as Guhathakurta et al. 2006; Gilbert et al. 2006 as part of a procedure to differentiate between RGB stars and foreground dwarfs. We have this data for all fields except 157Tri, 158Tri, 236Tri and 237Tri where a mini-slitlets approach was used. This absorption line is stronger in dwarfs than in red giant stars, since it is surface gravity dependent.

The sample is cut by requiring that the Na I doublet equivalent width is less than 4.5 $\mathring{A}$. In figures 3.9 and 3.10 the Na I doublet equivalent width is plotted against heliocentric radial velocity. The relationship is not clear, it may be observed that in the range -150 km s^{-1} $< v_{hel} <$ -100 km s^{-1}, there seems to be a distinct population of stars with a high Na I doublet equivalent width, however in the region -100 km s^{-1} km s^{-1} $< v_{hel} <$ 0 km s^{-1} where the greatest number of Galactic dwarf stars are expected, there are few stars with high Na I EW. Indeed it looks as though the trend is in the opposite direction to the expected. For this reason, it was decided not to cut by Na I EW in the final analysis. A reason for the failure of the Na I equivalent width cut to clearly reject Galactic dwarf stars may be that the Na I doublet is not only surface gravity sensitive, but also temperature and [Fe/H] sensitive. It was found by Guhathakurta et al. 2006 that the Na I doublet EW was only a useful piece of information for the redder RGB stars, our results confirm this finding. Although cooler dwarfs than T$_{eff}$ $\sim$ 4000 K, which corresponds to $(V-I)_0 > 1.8$ have a strong Na I doublet, hotter dwarfs have weaker lines, i.e. the Na I doublet is not only surface-gravity dependent but also temperature dependent. It was found in Gilbert et al. 2006 that there is only a clean separation between dwarfs and giants at $(V-I)_0$ colours redder than $\sim$ 2.5. It can be observed from figures

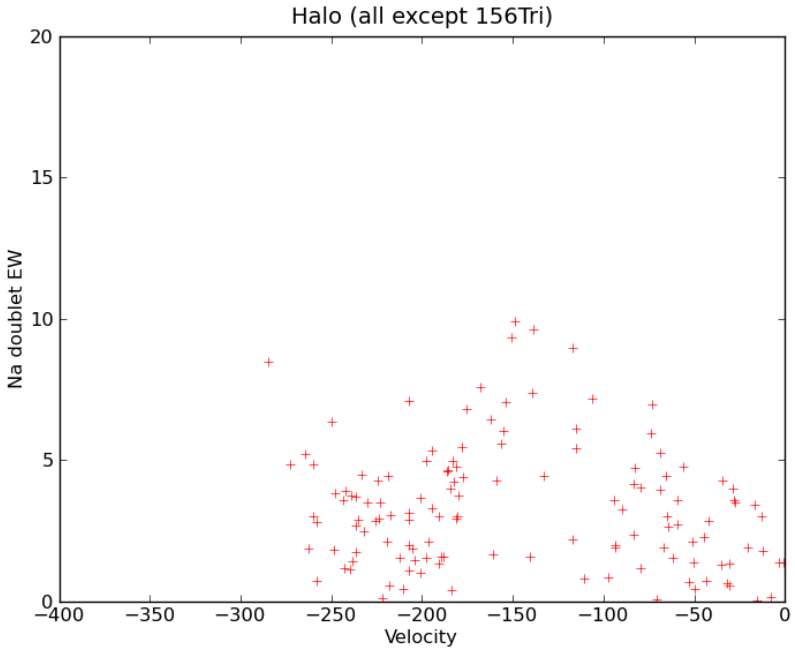

Figure 3.9: For the (simple windowing) "halo" sample, a scatter plot of heliocentric radial velocity against Na I doublet equivalent width.

3.27 and 3.28 that the majority of the stars in our sample are not this red.

Guhathakurta et al. 2006 also used DDO51 photometry (a passband of width $\Delta\lambda \approx 100\mathring{A}$ centred around $\lambda \sim 5150\mathring{A}$ which covers the surface gravity sensitive Mg I triplet and MgH absorption features) to preselect their sample. These features are strong in dwarf stars but weak in RGB stars. Gilbert et al. 2006 use the Na I doublet as part of a likelihood-based method using five criteria (radial velocity, DDO51 photometry, Na I doublet EW, location in $(I,\ V-I)$ colour-magnitude diagram and comparison of photometric and spectroscopic (Ca II triplet) metallicity) to assess whether a given star is a foreground dwarf or a giant.

In the field 408TrS there are 14 stars that pass all other quality cuts but fail on Na I EW, of which 10 have velocities v_{hel} < -100 km s^{-1}. The total passing quality and Na I EW cuts is 104. All except one of these 10 are in the "disk" range -179 km s^{-1}< v_{hel} < -100 km s^{-1}. In EC1 there are 7 stars in this category with only 3 with velocities v_{hel} < -100 km s^{-1} of a total of 88 passing all quality and Na I EW cuts. These 3 are all in the disk range -179 km s^{-1} to -100 km s^{-1}. In 409TrS there are 9 (7 with velocities in range -300 km s^{-1} to -100 km s^{-1}) out of 112 passing all quality and Na I EW cuts. All of these 7 stars are within the "disk" range -300 km s^{-1} < v_{hel} < -179 km s^{-1}. In 412TrS there are 11 (8 with velocities < -100 km s^{-1}) out of 91 passing all quality and Na I EW cuts. Again all of these 8 are in the "disk" range -300 km s^{-1} < v_{hel} < -179 km s^{-1}. All other fields have no stars that pass all other quality cuts but fail on the Na I EW cut. This indicates that it does not actually matter, if one is considering the contamination of the (simple windowing) "halo" sample, whether the Na I equivalent width cut is used or not.

Looking at the velocity histograms in figure 3.2, the fields 156Tri and 511TrS appear to have a significant Galactic component. The Besançon models predict 126 and 109 Galactic stars in each field respectively in

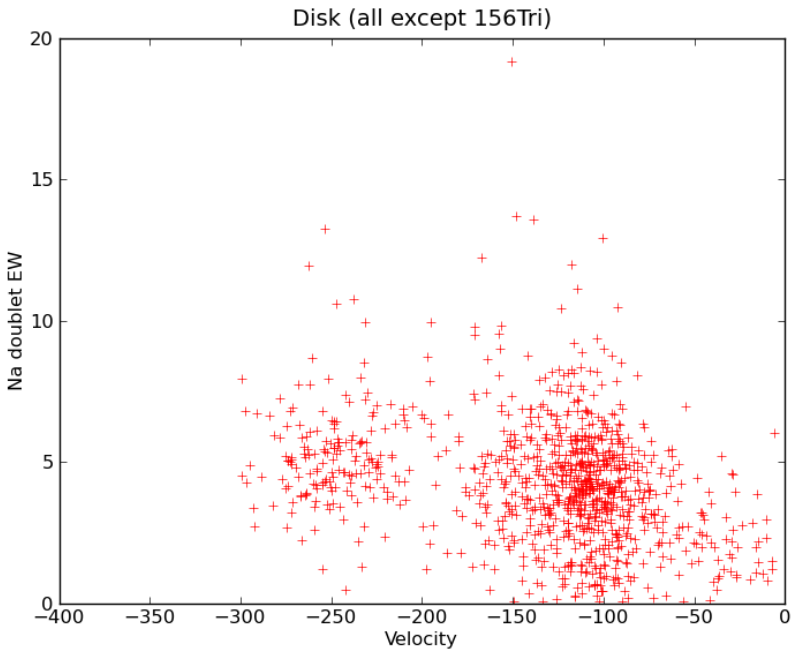

Figure 3.10: For the (simple windowing) "disk" sample, a scatter plot of heliocentric radial velocity against Na I doublet equivalent width.

the velocity range -179 km s^{-1} $< v_{hel} <$ 0 km s^{-1}. For field 156Tri this means that we can expect about 44 Galactic stars in this velocity range to be observed by DEIMOS. In fact, we observe 45 stars in this range, a large number of which (about three-quarters in 156Tri) fail the quality cuts. It would appear from these numbers that the majority of what is observed in 156Tri above -179 km s^{-1} is Galactic in origin.

When considering the range -179 km s^{-1} $< v_{hel} <$ -100 km s^{-1}, in the field 156Tri, Besançon predicts 3 Galactic stars (about 1 after selection) and 15 are observed, which indicates that with the -100 km s^{-1} cut, most of the sample is not likely to be Galactic in origin. This would appear to indicate that when the -100 km s^{-1} cut is used, the bulk of the Galactic component is successfully rejected. However only 4 of these stars pass the quality cuts, so it is possible that in 156Tri at least, many of the observed DEIMOS stars are there in the velocity window because of spurious velocities, and that once these are weeded out by the quality cuts, the Galactic component may still be large enough to dominate the sample. The effect of DEIMOS selection for all fields can be found in tables 3.2 and 3.3.

3.1.4 Quality cuts to the data

The following quality cuts were applied to the data to reduce spurious datapoints. These are cross-correlation maxima > 0.02, in order to remove datapoints with an unreliable velocity, signal to noise ratio > 2.0 to remove very poor spectra, Tonry-Davis coefficient > 2.0, velocity error < 25.0 km s^{-1} and I band magnitude > 20.5. The Tonry-Davis r coefficient is a measure of the height of the true peak in the cross-correlation function versus the rest of the correlation function (Tonry & Davis, 1979). The effect of the quality cuts can be seen in figures 3.1 and 3.2, where the unfilled bars show the total sample, and the filled ones show the sample

Field	Number of stars in window				Estimated contribution			
	"halo"		"disk"		"halo"		"disk"	
	No cuts	After cuts	No cuts	After cuts	No cuts	After cuts	No cuts	After cuts
237Tri	22	15	121	110	44.7	30.5	96.6	93.3
236Tri	17	12	166	142	34.6	24.4	147.1	128.7
408TrS	13	9	95	79	26.4	18.3	80.6	69.0
157Tri	7	4	104	89	14.2	8.1	96.2	84.6
158Tri	12	6	54	42	24.4	12.2	40.7	35.3
M33ec1	11	10	50	48	22.4	20.3	37.8	36.9
M33ec2	2	0	8	0	4.1	0.0	5.8	0.0
409TrS	19	13	110	89	42.9	29.4	92.9	77.3
412TrS	8	4	99	82	18.1	9.0	91.8	78.4
156Tri	15	4	16	9	33.9	9.0	2.5	5.4
511TrS	3	0	2	0	6.8	0.0	-0.7	0.0

Table 3.1: The second to fifth columns give the numbers of observed stars within the "halo" and "disk" kinematic windows. Numbers are given before and after the quality cuts that are described in the text. The right hand four columns give estimated numbers of "halo" and "disk" stars (simple windowing) after adjusting for stars outside the velocity bounds and "halo" stars hidden "under" the disk, again before and after the quality cuts described in the text.

that passes the quality cuts, and also in the distributions of the parameters plotted in figure 3.11.

3.1.5 Kinematic windowing

"Simple" windowing process

Using the heliocentric velocity measurement, for the southern fields, a population is selected with kinematics consistent with being a halo population, (-300 km s^{-1} to -179 km s^{-1}), and a disk population (-179 km s^{-1} to -100 km s^{-1}), where -179 km s^{-1} is the M33 systemic velocity. This allows the magnitude of the halo contribution to be estimated. The portion of the halo that is not hidden "under" the disk or at severe risk of Milky Way contamination is sampled. These windows are reversed for the northern fields, where the disk is at more negative velocities than M33 systemic. The disk is cut off at -100 km s^{-1} in order to reject the likely Milky Way contamination at more positive velocities. The "raw" numbers produced by this process are detailed in the second to fifth columns of table 3.1, before and after the quality cuts.

Assuming that the "halo" stars are symmetrically distributed in a Gaussian around the systemic velocity, by dividing the numbers of stars in the halo window by the proportion of the halo that we theoretically observe, it can be estimated what the total halo contribution is within a particular field. The procedure for this is as follows. For the southern fields we integrate the (normalised) Gaussian from -300 km s^{-1} to -179 km s^{-1}, which gives a value of 0.492. For the northern fields we integrate from -179 km s^{-1} to our cut-off at -100 km s^{-1} which gives a number of 0.443. So by dividing the observed number of "halo" stars by this number we estimate the total "halo" population. We then multiply this number by the proportion of the Gaussian within the -300 km s^{-1} and -100 km s^{-1} bounds if we are interested in the number of "halo" stars that would be observed if we had been able to cleanly separate the "halo" and the disk.

Similarly the halo count is subtracted from the disk count to estimate the number of "true" disk stars. For the southern fields we multiply the "halo" count by 0.443/0.492 before doing this, for the northern fields

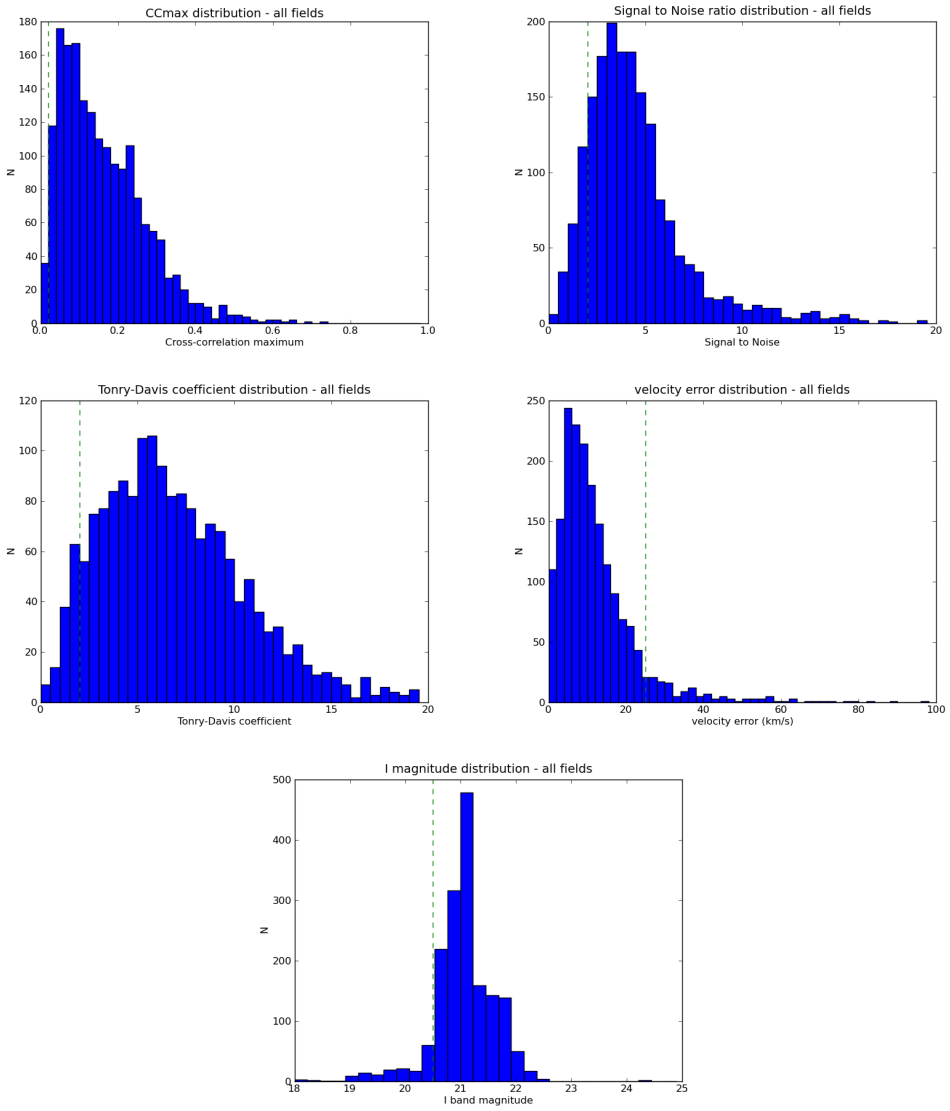

Figure 3.11: A set of histograms showing the distributions of the parameters including cross-correlation maximum, signal to noise ratio of the spectrum, Tonry-Davis coefficient, velocity error and I band magnitude. The dotted lines show the location of the quality cut.

we multiply by 0.492/0.443 in order to adjust for the cuts at -300 km s^{-1} and -100 km s^{-1}. Tables of the resulting numbers of "halo" and "disk" stars within each field are presented in the right hand four columns of table 3.1.

Overall, before quality cuts, 954 stars have velocities below -100 km s^{-1}, of these 129 have velocities in the "halo" window. This would indicate that there are about 691 "disk" stars and 263 "halo" stars in the sample, which would indicate a halo contribution of over 25%.

After quality cuts, 767 stars have velocities below -100 km s^{-1}, of these 77 have velocities in the halo window. This would indicate that there are about 628 "disk" stars and 158 "halo" stars in the sample, which would indicate a halo contribution of approximately 20%.

Bayesian counting of halo and disk populations

A second method, using Bayesian statistics, was also used to count up the likely numbers of halo and disk stars.

Using the heliocentric velocity measurement, a population of stars is windowed out by requiring that the velocity is between -300 km s^{-1} and 0 km s^{-1}. The systemic heliocentric radial velocity of M33 is $v_{hel} = -179$km s^{-1}. This windowing removes stars with extreme measured velocities that are likely to be spurious, in regions of velocity space where there are likely to be few genuine M33 stars.

Then it is assumed that the halo, disk and Milky Way dispersions have specific properties, i.e. that they are Gaussian distributions, with dispersions $\sigma = 51$ km s^{-1} for the halo (from our data) and $\sigma = 16$km s^{-1} for the disk (McConnachie et al., 2005). The location of the disk peak in velocity space varies with distance from the centre of M33, in this work the work of McConnachie et al. 2006 is used to quantify this. It is input as a prior that the halo contribution is 5%, 3%, 1%, 0.5%, or 0.1% that of the disk. See table 4.1 for the observed integrated halo contributions at various input halo priors. The Milky Way contaminants are assumed to be as numerous as the M33 disk stars (this is about what the Besançon model indicates), and distributed around 0km s^{-1} with a dispersion of $\sigma = 50$km s^{-1}. In fact, Milky Way halo stars will be distributed about zero in a galactocentric, not heliocentric frame. Triangulum is located at galactic $l = 134$ ° and $b = 31$ °. This means that Milky Way halo stars will be located around a velocity of -140 km s^{-1}, however the majority of contaminants are likely to be Milky Way disc stars which are likely to have velocities centred between -100 and 0 km s^{-1} depending on distance.

For each star with velocity between -300 km s^{-1} and 0 km s^{-1}, the halo, disk and Milky Way fractions at that location in velocity space are estimated by the Bayesian formulae. The halo, disk and Milky Way fractions represent the probability that a star observed at this velocity is a halo, disk or Milky Way star respectively.

$$f_{\rm halo} = \frac{\rm P(data|halo)P(halo)}{\rm P(data|halo)P(halo) + P(data|disk)P(disk) + P(data|MW)P(MW)}$$

$$f_{\rm disk} = \frac{\rm P(data|disk)P(disk)}{\rm P(data|halo)P(halo) + P(data|disk)P(disk) + P(data|MW)P(MW)}$$

$$f_{\rm MW} = \frac{\rm P(data|MW)P(MW)}{\rm P(data|halo)P(halo) + P(data|disk)P(disk) + P(data|MW)P(MW)}$$

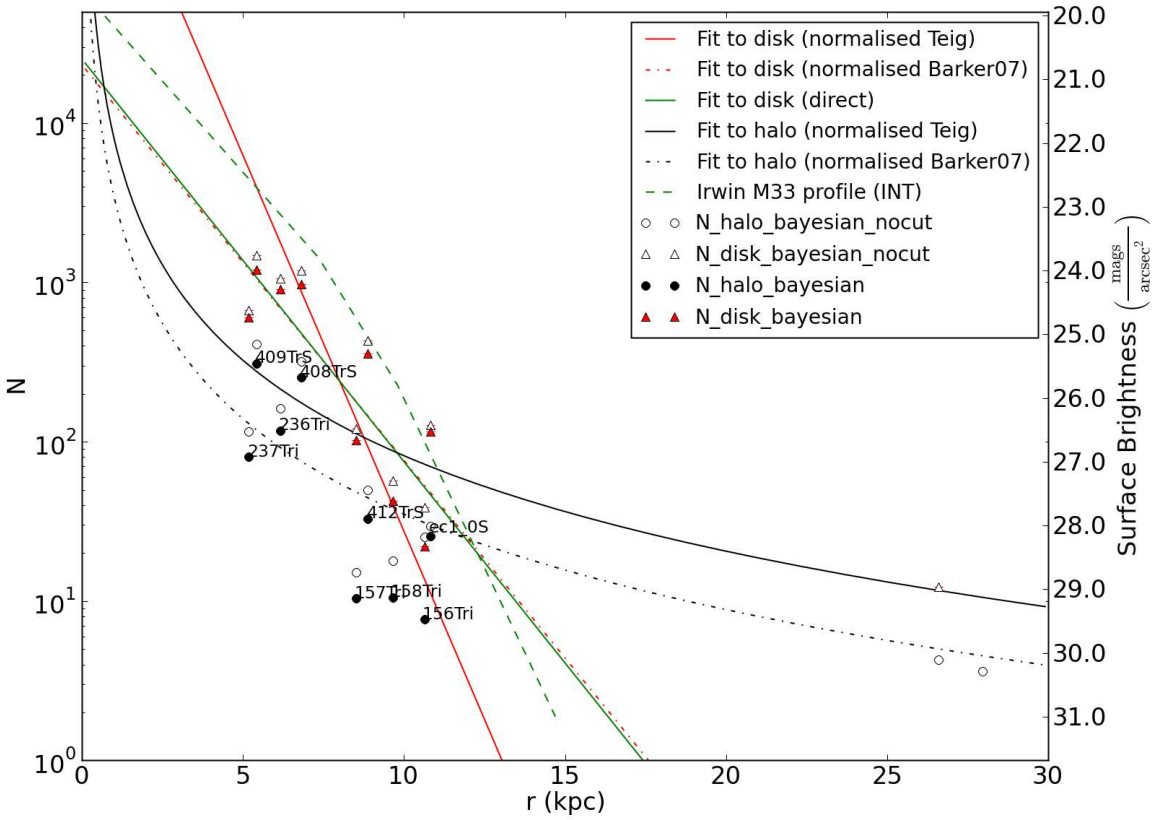

Figure 3.12: Halo and disk radial profiles - using Bayesian counting method, 5% halo prior, with the DEIMOS selection effect compensated for. This figure uses the quality cuts as described in the text, with the pre quality cut numbers being overplotted using open symbols.

What is the "halo" population?

In Chapter 4, the alternative hypothesis that we are dealing with a stripped disk or other substructure population rather than a "true" smooth halo population is discussed.

3.2 Halo and disk profiles

3.2.1 Bayesian selection

Figure 3.12 shows the numbers of stars in each field that have been categorised by the Bayesian process as being either "halo" and "disk", after DEIMOS selection effects are compensated for. In this figure a power-law profile has been overplotted (with exponent $\alpha = -1.99 \pm 0.78$) with a scale length of $r_0 = 8.99 \pm 0.78$ kpc as fitted by Teig 2008 for the "halo", and the Teig exponential profile has been plotted for the disk, these being normalised to the observed disk population. A profile based on the Barker et al. 2007a disk scale

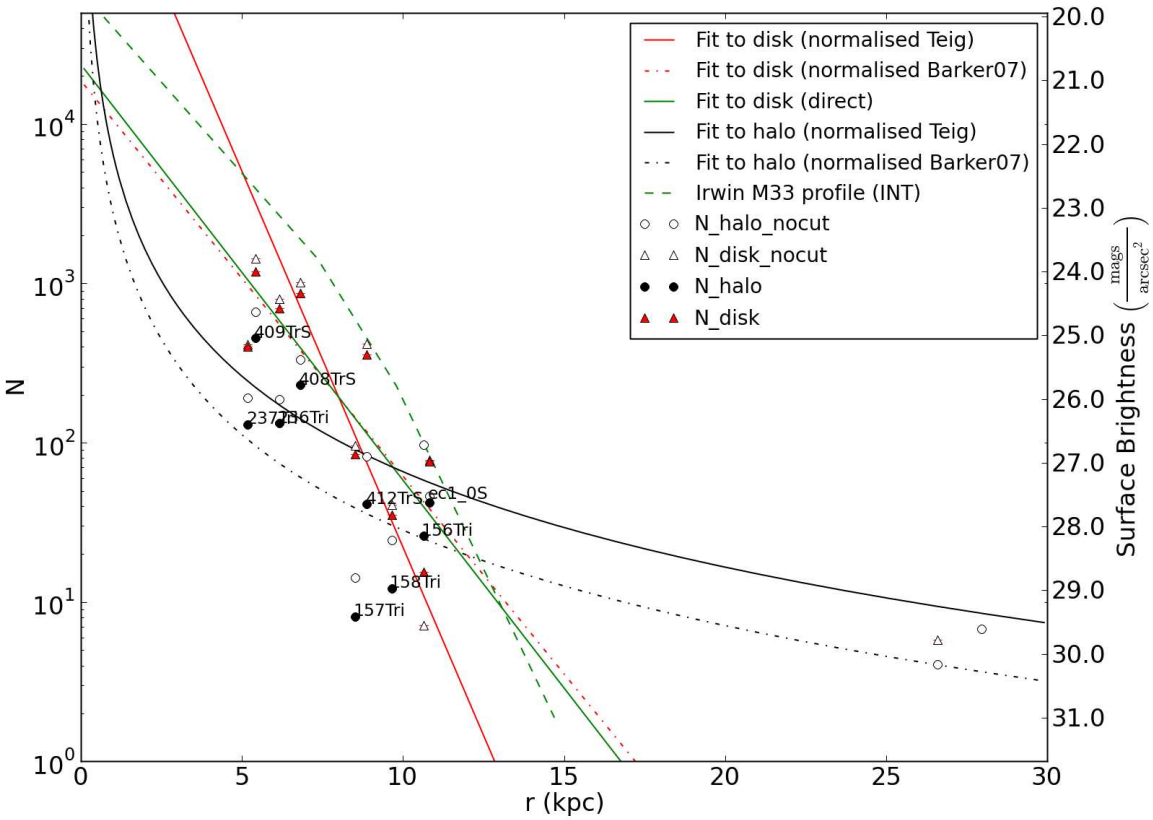

Figure 3.13: Halo and disk radial profiles - using simple kinematic windowing method with the DEIMOS selection effect compensated for. This figure uses the quality cuts as described in the text, with the pre quality cut numbers being overplotted using open symbols.

Field	Available stars	Observed by DEIMOS	Observed by DEIMOS -179< v_{hel} <0	Besançon -179< v_{hel} <0	Besançon (-179< v_{hel} <0) (after DEIMOS selection)
M33EC1	229	111	78	91	44
156Tri	328	114	45	126	44
157Tri	367	367	166	69	69
158Tri	377	377	86	101	101
236Tri	2289	422	247	108	20
237Tri	1831	428	224	92	22
408Tri	2861	227	129	116	9
409Tri	3456	224	31	116	8
412Tri	762	167	22	124	27
511TrS		47	28	109	
M33EC2		50	24	95	

Table 3.2: Numbers of available versus selected stars in each DEIMOS mask in M33. A comparison is made to the Besançon predictions. The counts of stars observed with DEIMOS are the total number of targets in each field, and the number with velocities in range -179 km s^{-1} < v_{hel} < 0 km s^{-1} before any quality cuts. It can be seen that in M33EC1, 156Tri, 157Tri and 412Tri, the Besançon prediction after the DEIMOS selection means that a large proportion of the stars observed between -179 km s^{-1} < v_{hel} <0 km s^{-1} are likely to be Galactic in origin. The problem is less severe in the more crowded fields 236Tri, 237Tri and 408Tri but is still not insignificant. In the outer fields 511TrS and M33EC2, if DEIMOS observed all or most available stars in the CMD selection box, it is likely that most are Galactic in origin.

length (and a model for the halo based on halo/disk crossover at 12 kpc, and a halo scale length of 12 kpc, with the same power-law exponent as for the Teig profiles) is also overplotted. The normalisation excludes the outer two fields M33EC2 and 511TrS. It is uncertain how many (if any) genuine M33 stars are in the "halo" and "disk" samples in these fields so they are omitted from the analysis.

A direct linear regression (of log(number in disk sample)) is also used, which in the case where quality cuts are used and DEIMOS selection effects compensated for produces a scale length of 1.72 kpc (measured in our fields along the major axis) in the Bayesian case (5% halo prior). Varying the halo prior or indeed switching to simple windowing does not change this scale length significantly. This scale length agrees with the determination of 1.8 kpc in Ferguson et al. 2007 and 1.75 kpc (normalised to our distance assumption of 809 kpc) from Barker et al. 2007a, as can be seen by the fact the direct fit follows the normalised Barker et al. 2007a profile closely.

3.2.2 Simple kinematic windowing

Figure 3.13 shows the numbers of stars in each field that have been categorised by the simple kinematic windowing process as being either "halo" and "disk", adjusted for the DEIMOS selection effects.

3.2.3 Halo/disk ratios

Figure 3.14 shows the expected halo/disk ratio based upon the Teig and Barker et al. 2007a profiles and the observed ratio in each field based on the Bayesian selection process. Figure 3.15 shows the same for the simple windowing process.

Some studies have tried to at least place an upper limit on the contribution of the M33 stellar halo to the overall luminosity. Ferguson et al. 2007 limit the M33 halo contribution based on a fit to the disk population at "a few percent" of the disk luminosity. However this limit is in terms of the overall integrated profile,

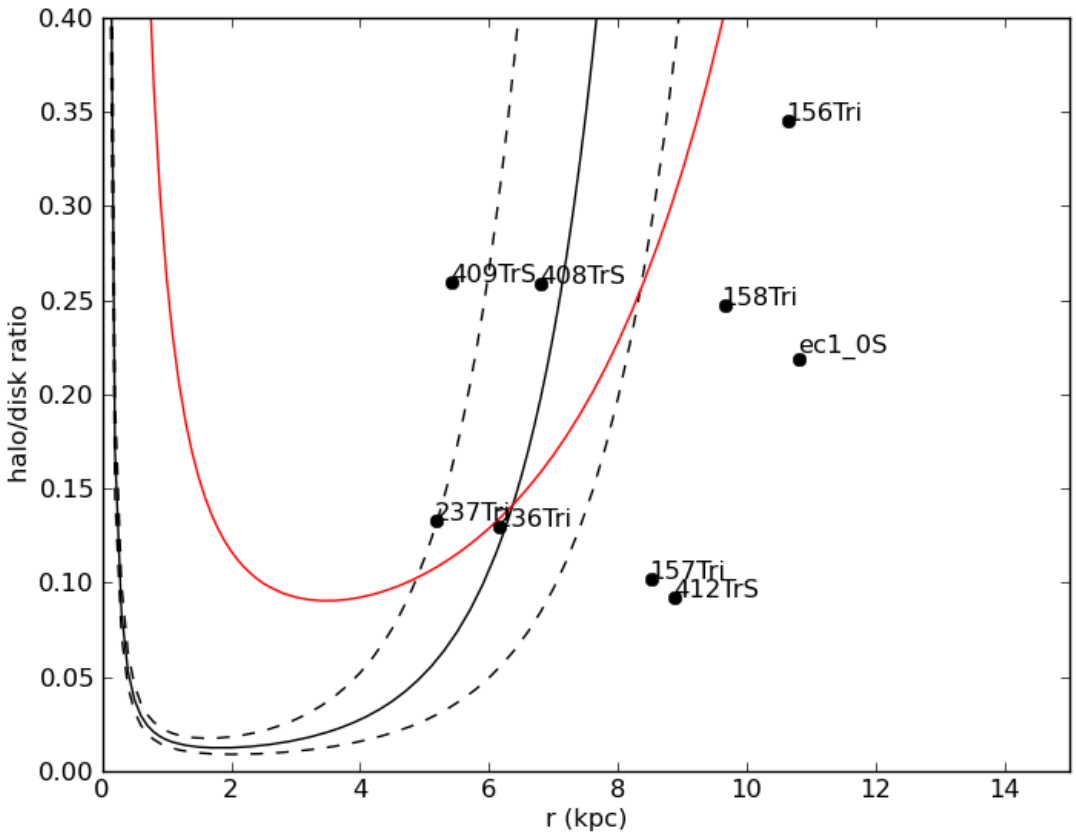

Figure 3.14: Halo to disk ratio (Bayesian selection - halo prior 5%). Teig relative normalisation overplotted (black), with maximum and minimum ranges (dashed lines) based on their quoted errors for their halo and disk scale lengths. A model using Barker et al. scale length (1.75 kpc) and halo scale length of 12 kpc, with halo disk equality assumed at 12 kpc is overplotted in red. Quality cuts have been used on the data for this figure.

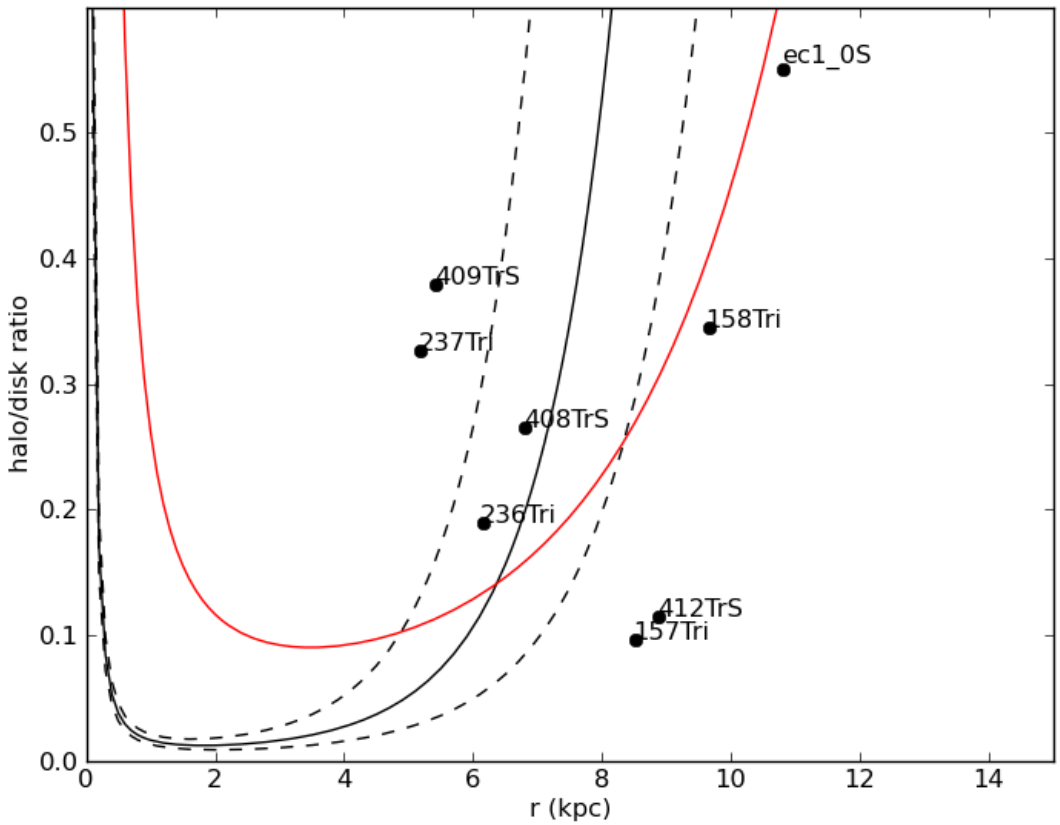

Figure 3.15: Halo to disk ratio (Simple kinematic windowing). Teig relative normalisation overplotted (black), with maximum and minimum ranges (dashed lines) based on their quoted errors for their halo and disk scale lengths. A model using Barker et al. scale length (1.75 kpc) and halo scale length of 12 kpc, with halo disk equality assumed at 12 kpc is overplotted in red. Quality cuts have been used on the data for this figure.

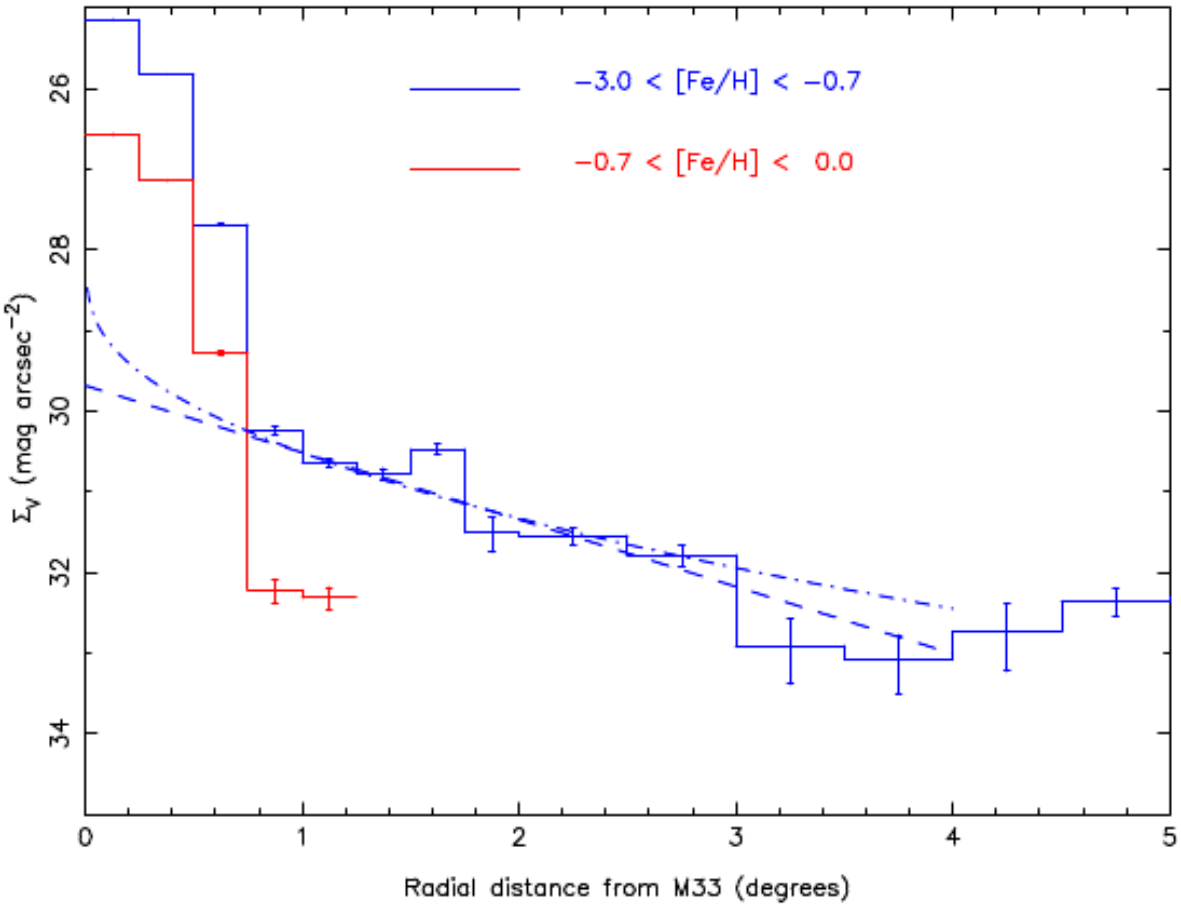

Figure 3.16: The M33 halo profile as published in Ibata et al. 2007. An exponential model with scale length 18 ± 1 kpc and a projected Hernquist model with scale radius 55 ± 2 kpc are displayed. Note that at the distance of M33 1 degree ≈ 14.1 kpc. This profile is very much affected by the tidal debris, the extent of which was not realised at the time of publication of Ibata et al. 2007, so does not measure a "true" halo scale length. Both the exponential and Hernquist models have a much larger scale length than is realistic for a smooth halo component in M33.

Field	Available stars	Observed by DEIMOS	Observed by DEIMOS -179< v_{hel} <-100	Besançon -179< v_{hel} <-100	Besançon (-179< v_{hel} <-100) (after DEIMOS selection)
M33EC1	229	111	50	8	3.9
156Tri	328	114	15	3	1.0
157Tri	367	367	104	4	4
158Tri	377	377	54	8	8
236Tri	2289	422	166	7	1.3
237Tri	1831	428	121	7	1.6
408Tri	2861	227	95	2	0.2
409Tri	3456	224	19	13	0.8
412Tri	762	167	8	6	1.3
511TrS		47	3	6	
M33EC2		50	2	10	

Table 3.3: Numbers of available versus selected stars in each DEIMOS mask in M33. In the fourth column the number of stars with heliocentric radial velocities in the range -179 km s^{-1} $< v_{hel} <$ -100 km s^{-1} (before any quality cuts) is given. In most fields, the likely numbers of Galactic stars is a small fraction (less than 10% except in 158Tri and 412Tri) of the numbers of stars observed by DEIMOS with heliocentric radial velocities between -179 km s^{-1} and -100 km s^{-1}. In the outer fields, 511TrS and M33EC2, if DEIMOS observed all or most of the stars available, it is likely that most of the stars observed are Galactic in origin.

however in the range at which our observations were made the halo contribution will be larger. The halo and disk profiles from the Teig thesis (Teig, 2008) when integrated between 5 and 12 kpc, approximately the region studied in our fields excluding M33EC2 and 511TrS, give a halo contribution of about 28% in this range. When integrated all the way to the centre, the Teig profiles suggest a total halo contribution of 5.5%. Taking exponential fits to our observed halo and disk profiles, we integrate these at all radii for the different Bayesian priors and simple windowing method, producing halo/disk fractions as detailed in table 4.1.

3.3 The outer two fields - EC2 and 511TrS

It is worth asking, since there are such a small number of stars found in the outer two fields, how many, if any genuine M33 stars are to be found in these fields. All of the stars currently fail the quality cuts, although in EC2 this is because the V and I magnitude data is missing from the catalogue files for most stars, and in 511TrS for some stars. The Besançon predictions predict at least as many Galactic stars in the -179 $< v_{hel} <$ -100 km s^{-1} range (where the EC2 disk sample and the 511TrS "halo" sample are located) as DEIMOS observed in this velocity range. It is likely, given that the fields are less crowded than the inner fields, that DEIMOS will have observed most or all of the available targets in the CMD window. It is therefore prudent to assume that the stars in these two fields are Galactic foreground dwarfs unless they can be shown to be likely M33 giants. Therefore the 511TrS and M33EC2 fields are excluded from the analysis. Tables of the individual stars including EC2 and 511TrS are located in Appendix C.

3.4 Halo velocity dispersions

Figures 3.17 and 3.18 show the velocity dispersion of the (Bayesian selected) "halo" and "disk" samples (at a halo prior of 5%). Figure 3.20 shows the same for the simple kinematic windowing method "halo" sample. It may be compared with the work of Chapman et al. 2006 for M31, which found a dispersion of

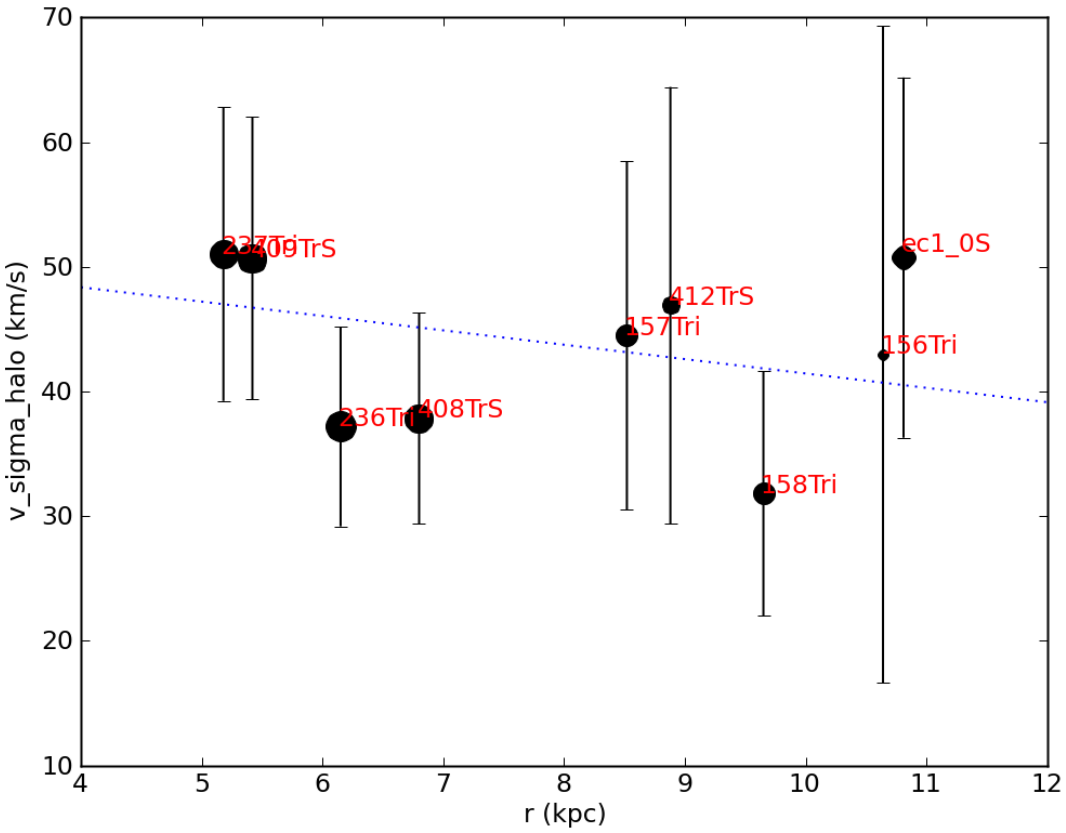

Figure 3.17: Halo velocity dispersion (fitted to fixed -179 km s^{-1} halo mean velocity). M33EC2 and 511TrS are excluded from the analysis, due to the small size and uncertain character of the sample in these fields. Quality cuts have been used on the data. The area of the plotting symbol corresponds to the number of stars in the (Bayesian) "halo" sample (5% prior). The dispersion is simply the standard deviation of the sample, weighted by the probability of each star being in the Bayesian halo sample. The error bars shown are the standard error, calculated by dividing the standard deviation by the sample size. At a 2σ level the data is consistent with a constant dispersion.

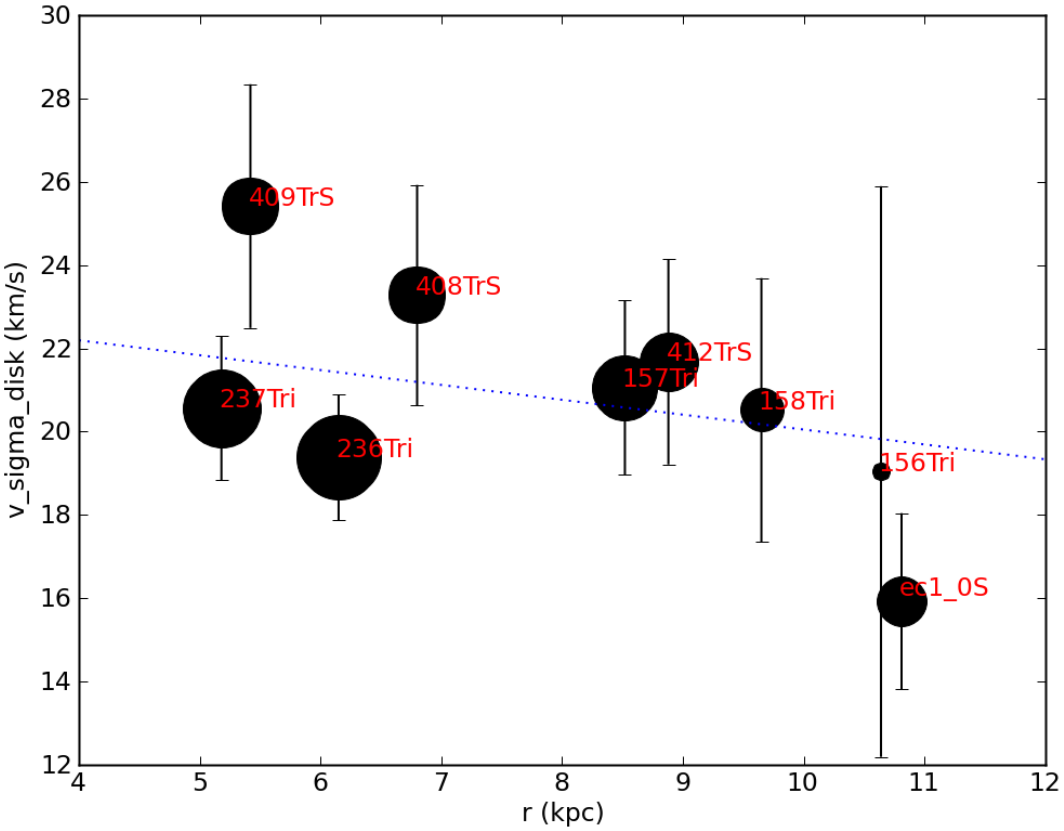

Figure 3.18: Disk velocity dispersion (fitted to the McConnachie et al. disk model mean velocity). Quality cuts have been used on the data. The area of the plotting symbol corresponds to the number of stars in the (Bayesian) "disk" sample (5% halo prior). Dispersion and errors are calculated in the same manner as for the halo dispersion. At a 2σ level the data is consistent with a constant dispersion.

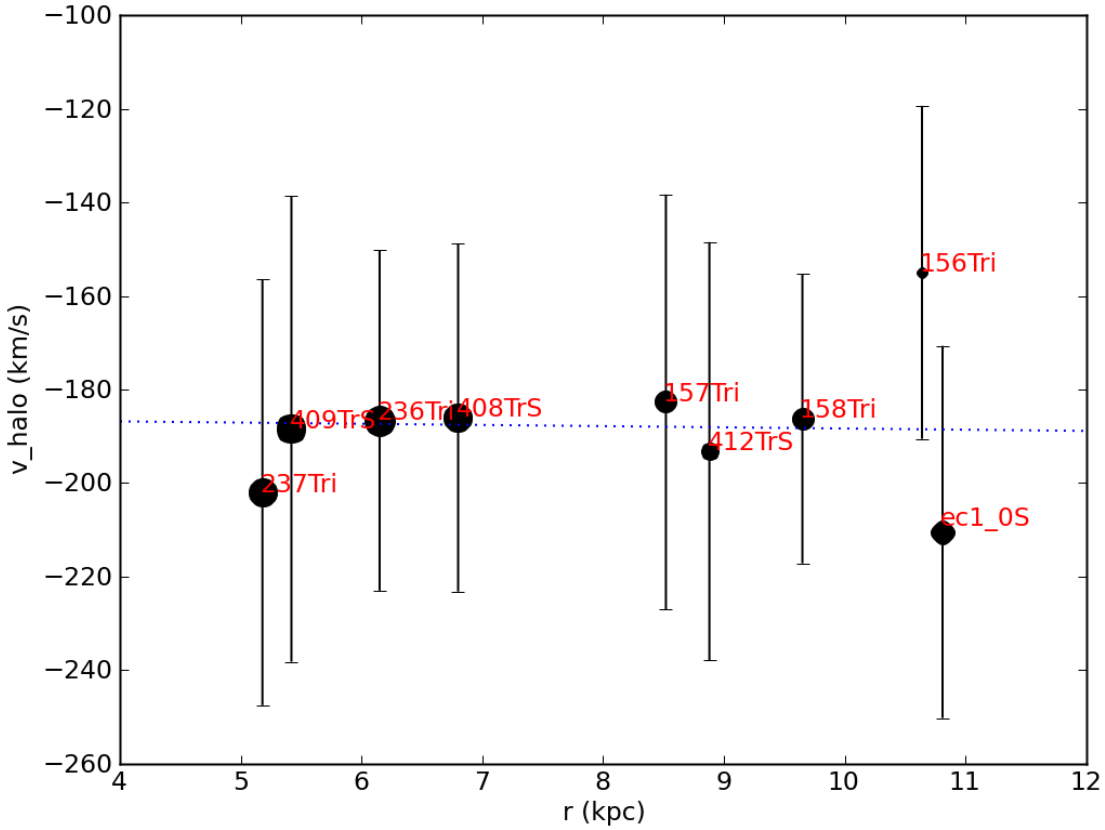

Figure 3.19: Halo velocity (mean halo velocity freely chosen by fitting process). M33EC2 and 511TrS are not plotted here. The "halo" sample for these fields is too small for the data to be meaningful. Quality cuts have been used on the data. The area of the plotting symbol corresponds to the number of stars in the (Bayesian) "halo" sample (5% halo prior).

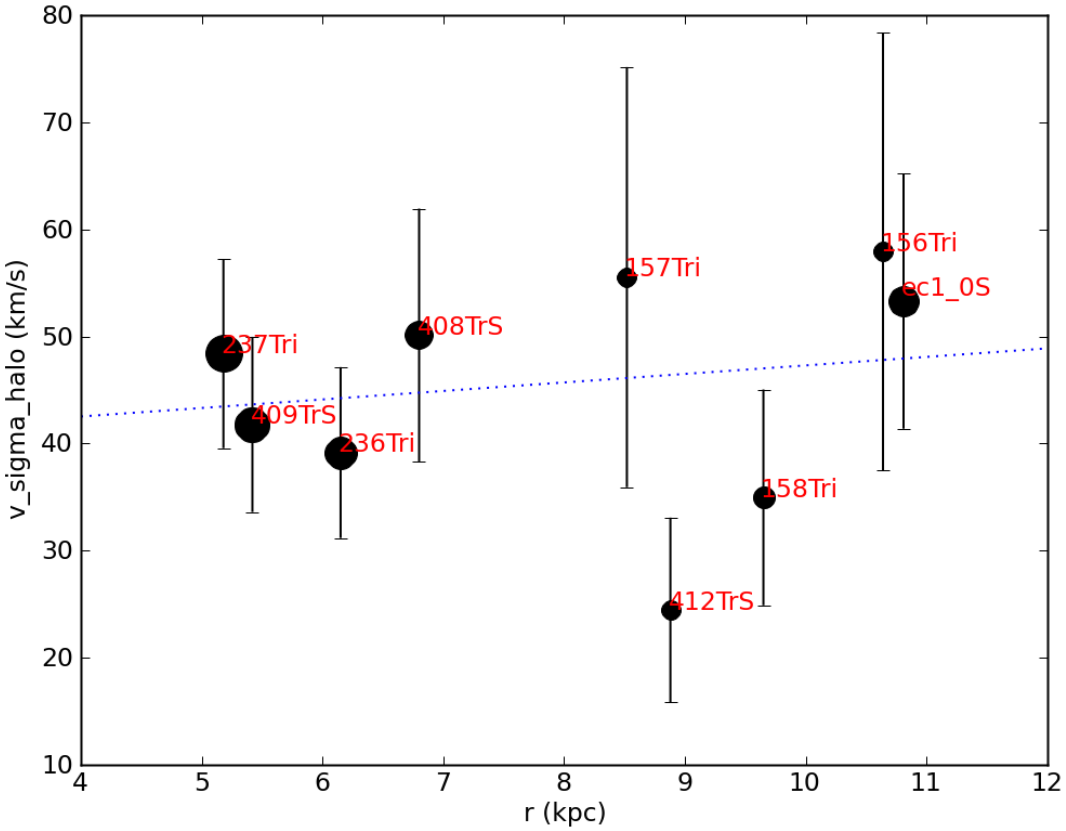

Figure 3.20: Halo velocity dispersion (fitted to fixed -179 km s^{-1} halo mean velocity). Quality cuts have been used on the data. The area of the plotting symbol corresponds to the number of stars in the (simple kinematical windowing) "halo" sample. The EC2 and 511TrS fields do not have any stars in the halo window after the quality cuts so are not plotted here. At a 2σ level the data is consistent with a constant dispersion.

$\sigma_V(R) = 152 - 0.90\frac{R}{1\text{kpc}}$ km s^{-1} using data at radii ranging from 10-70 kpc. This work shows a (weighted) mean dispersion of 44 km s^{-1} for M33 when the halo systemic velocity is fixed at -179 km s^{-1}.

For a 5% halo prior, the fit produces a gradient of -1.15 km s^{-1} kpc^{-1} in the dispersion of the "halo" population, and -0.36 km s^{-1} kpc^{-1} in the dispersion of the "disk" population. However, the 2σ (approx 95%) confidence intervals in this case are -4.64, +2.34 and -1.26, +0.54 respectively, so the observed gradient is not significant in either case at the 95% level, or even at a 1σ level. When the mean halo velocity is a free parameter of the fitting, the mean dispersion is 41 km s^{-1}. For the simple kinematic windowing method the result is 45 km s^{-1}. It is generally accepted that the mass of M33 is approximately $\frac{1}{10}$ of that of M31. See for instance work on rotation curves by Corbelli et al. 2000 which implied a dark halo mass of at least 5 $\times 10^{10} M_\odot$. If that is the case, then it can be expected that the velocity dispersion of its halo is $\sqrt{10}$ times smaller, which is what we observe. The work of Chapman et al. 2006 found a downward gradient of the dispersion with radius in M31. It is clear that these results do not provide any evidence for a gradient in the "halo" or "disk" dispersion in M33 with radius, the data being consistent with constant dispersion with radius. However the large range of the confidence intervals do not constrain the dispersion tightly enough to discriminate between the hypotheses of a gradient and a constant dispersion.

3.5 Photometric metallicities - how photometry in various colour bands can provide information on metallicity

Heavy elements (or "metals", i.e. not H, He) are found in small amounts in stellar atmospheres. This leads to greater opacity than would be the case in a metal-free star. Greater opacity means that the surface of last scattering (i.e. where the star's light that we see is emitted) is higher up in the star's atmosphere and therefore at a lower temperature, so the observed colour of the star is redder.

The properties of stars can be modelled, and there have been many attempts to predict the observable properties of red giant stars based on age, metallicity and α abundance. Samples of the Dartmouth isochrones (Dotter et al., 2008) are plotted in figures 3.21 and 3.23 showing that more metal poor stars are bluer, and younger stars are bluer.

The pipelined data uses the Girardi et al. 2000 (Padova) isochrones to generate the photometric metallicities. In order to ensure more accurate metallicities we decided to use Dartmouth isochrones instead, using variable age and alpha enhancement. Alpha enhancement is defined in section 3.5.2. A program written by Michelle Collins (personal communication) is used to reprocess the data using these isochrones.

3.5.1 Consequences of the distance assumption

Another issue with the "halo" sample, is the distance effects on halo stars. We assume a distance of 809 kpc to M33, however the "halo" sample will be widely spread along the line of sight with an error in the distance assumption. An approximate magnitude to this uncertainty can be gathered by assuming the line of sight uncertainty is of the same order as the projected distance (about 1 degree or 14 kpc at the distance of M33). This translates to a change of apparent magnitude of $\sim$ 0.03-0.04 mag. There is the question of the systemic distance to M33, which may be up to 0.3 magnitudes larger in distance modulus. (See review of distance determinations in section 1.5.3.

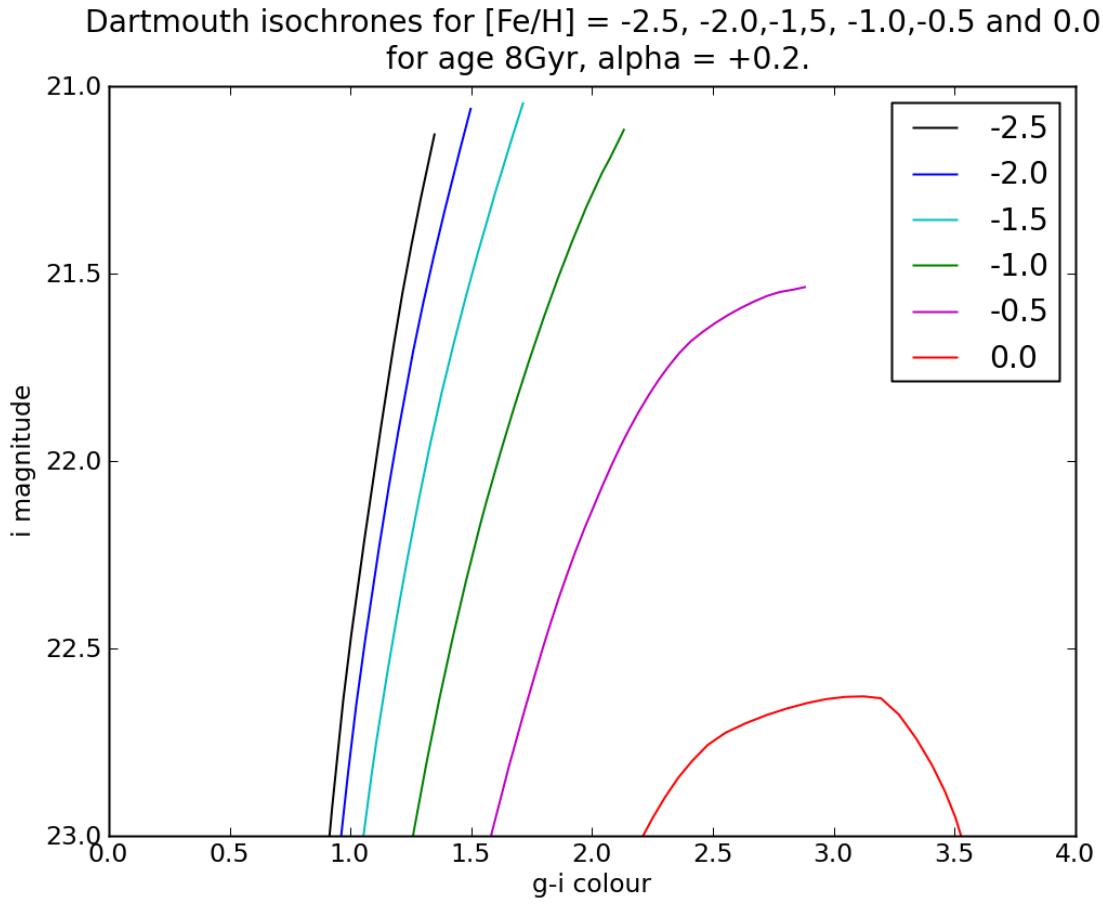

Figure 3.21: The Dartmouth (Dotter et al., 2008) isochrones showing the red giant branch at the M33 distance, for a range of metallicities, choosing an age of 8 Gyr and α enhancement of $[\alpha/\mathrm{Fe}] = +0.2$. These are plotted using the SDSS g and i bands, which are similar but not identical to the CFHT bands.

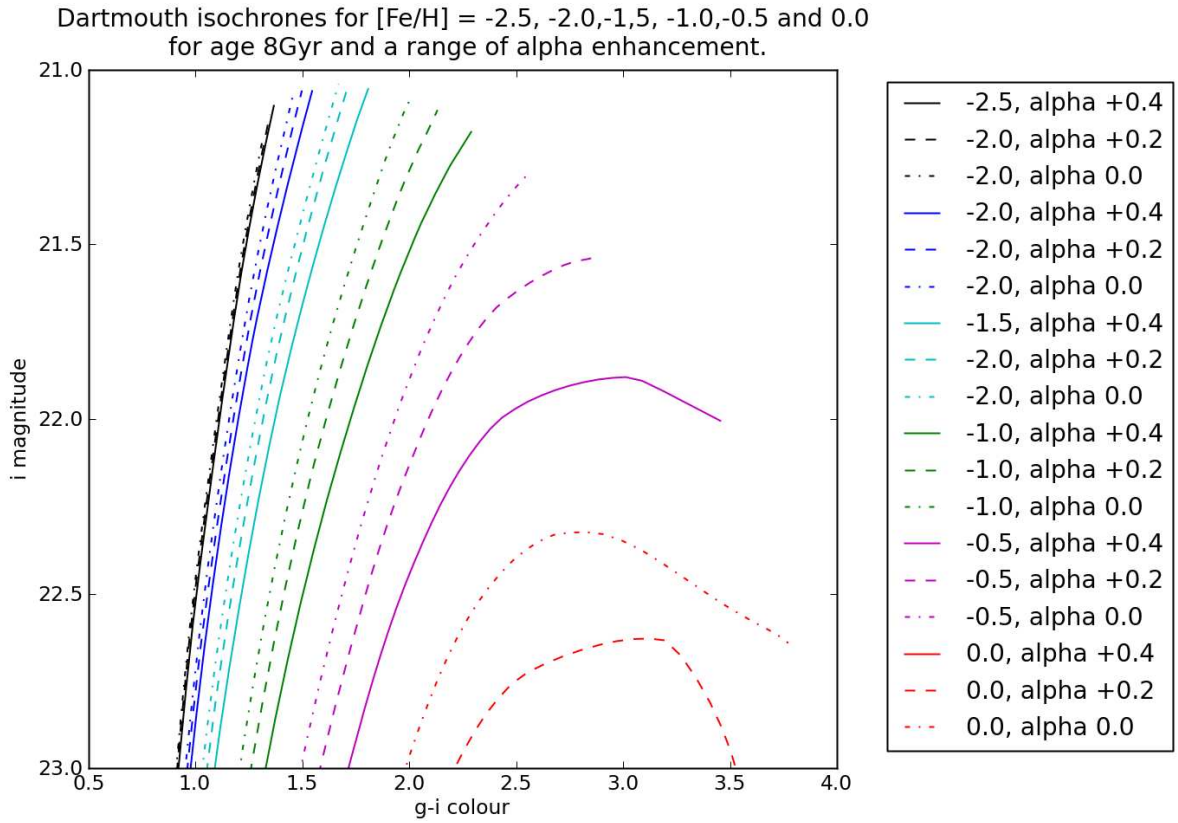

Figure 3.22: The Dartmouth (Dotter et al., 2008) isochrones showing the red giant branch at the M33 distance, for a range of metallicities, choosing an age of 8 Gyr and α enhancements of $\alpha = 0.0$, +0.2 and +0.4. These are plotted using the SDSS g and i bands, which are similar but not identical to the CFHT bands.

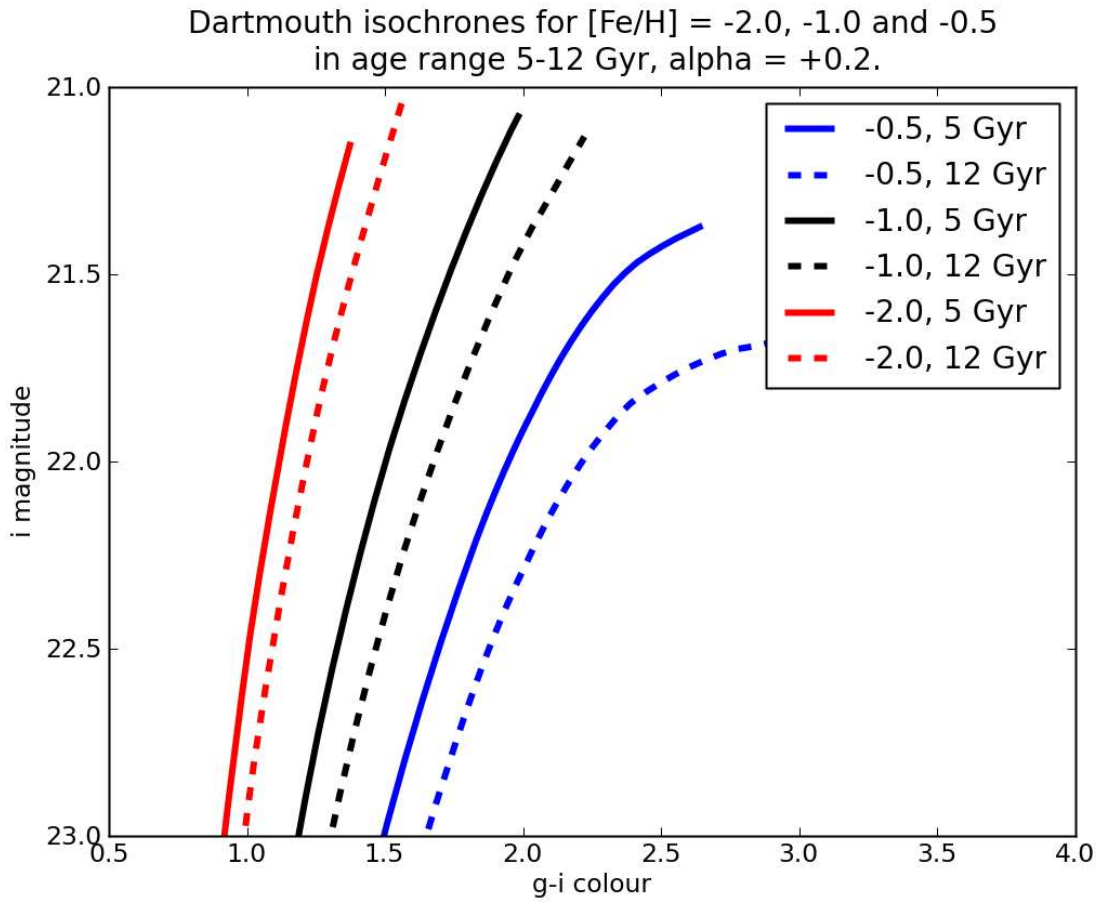

Figure 3.23: The Dartmouth isochrones, showing the RGB again for several metallicities, showing the effect of age (between 5 and 12 Gyr) upon the isochrones.

For a RGB star at i = 22.0, the Dartmouth isochrones have slopes of 3.6, 2.2 and 1.5 at [Fe/H] = -2.0, -1.0 and -0.5 respectively for α = +0.2. This means that for a change in apparent magnitude of 0.04 mag, at [Fe/H] = -2.0, -1.0 and -0.5, the possible changes in [Fe/H] are approximately 0.01, 0.02 and 0.03 dex respectively. This would mean that at higher metallicities, the observed metallicity distribution would be broadened by up to 0.03 dex, however it is pointed out that this is small compared with the existing error bars in Figures 3.34 to 3.37, even at the highest observed photometric metallicities. However at α = +0.4, the [Fe/H] = -0.5 isochrone has a shallower slope of $\sim$ 0.5, resulting in a larger change of metallicity of $\sim$ 0.08 dex.

If the systemic distance to M33 is 0.3 magnitudes larger, the changes in [Fe/H] are 0.08, 0.14 and 0.2 dex respectively. If the distance is larger than our assumption, our estimated [Fe/H]s will be more metal poor than the true values. The effect is more pronounced at higher metallicities, the result of which being that any metallicity gradients would be flattened somewhat. If there is a true gradient of 0.05 dex kpc^{-1}, between 5 and 15 kpc, and the [Fe/H] is -0.5 at 5 kpc and -1.0 at 15 kpc, the metallicity at 5 kpc will be measured at -0.7 and at 15 kpc -1.14, so a flatter gradient is observed, but the effect is not larger than the existing errors. However at a higher α of +0.4, a greater flattening is possible.

3.5.2 Effect of age and alpha assumptions on photometric metallicity results

The calibration of the photometric metallicity derived from a star's position in a colour-magnitude diagram is dependent on parameters such as age and α-abundance. The α-abundance is the ratio of α elements relative to the amount of iron in a star, in comparison with the solar value ([α/Fe]). The α nuclides are nuclides that can be formed by adding α particles to ^{16}O during C- and O-burning. They consist of the most common isotopes of Ne, Mg, Si, S, A and Ca. Since they are formed during C- and O-burning, they are related to the precursors of Type-Ib and Type-II supernovae, i.e. core collapse supernovae in massive stars at the end of their lives. In contrast the iron peak elements, although they are produced in core collapse supernovae, are also produced in Type-Ia supernovae, with the Type-Ia being the dominant mode of production. The Type-Ia supernovae, being caused by mass transfer onto a white dwarf from a giant star within a binary system, have progenitors among much older stellar populations than the core collapse supernovae, for which the progenitors are relatively young, massive stars.

Increasing [α/Fe] results in an increase in $V - I$ colour. The size of this effect is strongly dependent on metallicity, at the lowest metallicities, the effect is very small, and at high metallicity it becomes more significant. For a i=22 RGB star, the size of the change in colour for [Fe/H] = -1.5 between α = 0.0 and α = 0.4 is 0.09 mag. At [Fe/H] = -0.5 it is 0.49 mag. By comparison at this magnitude the $V - I$ colours of stars at [Fe/H] = -1.5, -1.0 and -0.5 and α = 0.2 are 1.31, 1.61 and 2.09. This means that a change in alpha of 0.1 dex, will affect the metallicity result by approximately 0.04 dex at [Fe/H] = -1.5, rising to 0.1 dex at [Fe/H] = -0.5. Thus an uncertainty of $\pm$ 0.2 dex in α will affect the metallicity by 0.08-0.2 dex respectively at these metallicities. This differential effect means that metallicity gradients are affected. A lower α mimics a lower metallicity and vice versa, the result of this being that if the α is lower than the assumed value, the measured [Fe/H] will be lower, both for low and high metallicity stars but more so for high metallicity stars, thus tending to flatten out metallicity gradients. A higher α than assumed would cause measured [Fe/H] to be higher, again both for low and high metallicity stars but more so for the high metallicity ones, thus tending to steepen any metallicity gradients.

Increasing age results in an increase in $V-I$ colour. At [Fe/H] = -1.0 and alpha = +0.2, the $V-I$ colour is 1.50 for a i=22 RGB star of age 5 Gyr. For a 12 Gyr old star, it is 1.67. At [Fe/H] = -0.5 and alpha = +0.2, the $V-I$ colour is 1.94 for a i=22 RGB star of age 5 Gyr. For a 12 Gyr old star, it is 2.21. Thus a change in age of 1 Gyr will affect the metallicity result by approximately 0.03-0.045 dex. With our age assumption of 8 Gyr, a 2Gyr difference from this could result in a different metallicity by $\sim$ 0.06-0.09 dex. Again, the effect is larger at high metallicity so metallicity gradients will be affected, although the differential effect is fairly small here.

We believe that 8 Gyr, $\alpha = +0.2$ are reasonable assumptions for the RGB population we are studying. Our choice of $\alpha = +0.2$ is based on the general range of α as observed in the Milky Way. α-abundance is observed to correlate with metallicity, and for metallicities typical of what we observe in M33, $\alpha = +0.2$ is a reasonable choice (see Beers et al. 2008 for a discussion of α-abundance in the Milky Way). The age assumption is a reasonable assumption in the middle of the potential range for the RGB star population (approximately 5-12 Gyr) and consistent with Barker et al. 2007a,b; Williams et al. 2009.

Overall histograms of the photometric metallicities for the (Bayesian) "disk" and "halo" populations can be seen in figures 3.30 and 3.31. In figures 3.24, 3.25, and 3.26, I show 3 panel figures showing photometric metallicity distribution function histograms, velocity histograms, and photometric metallicity-radial velocity scatter plots for individual fields. I also show CMDs for the selected stars (quality cut) in figures 3.27 and 3.28.

3.6 Spectroscopic metallicities

3.6.1 Stacking the spectra

The individual spectroscopic [Fe/H] measurements for the stars have a very wide scatter and a large number of catastrophic errors. In an effort to combat this problem, I stacked (first removing the Doppler shift caused by the radial velocity) the spectra within the Bayesian "disk" and "halo" subpopulations in each field. This was an effort to get a more reliable average spectrum, and the Ca II triplet equivalent widths were measured (by fitting a Gaussian to each of the three Calcium triplet absorption lines) on these spectra. Example figures showing the result of this are shown in Figures 3.32 and 3.33.

The procedure was as follows, as for the photometric analysis, each star is assigned a probability of being "halo" or "disk", and in each of the "halo" and "disk" samples, the spectrum is weighted by this probability. The spectra are also weighted by signal to noise ratio, with higher signal to noise ratio spectra being given greater weighting. In addition, any spectra from stars that fail quality cuts are not included, that is any star with a spectrum with signal to noise ratio < 3, cross-correlation maximum < 0.1, or velocity error $>$ 25 km s^{-1}, or I magnitude < 20.5. The spectra are normalised before stacking, this was originally done by dividing the spectrum by a coarsely (300 $\AA$) smoothed version of itself, however in some cases this smoothed spectrum was badly affected by sky lines. In some cases the sky subtraction had produced a large negative flux in the spectrum, which resulted in the smoothed spectrum crossing zero. This introduced error into the stacked spectra, particularly around CaT1. It was therefore decided to normalise in a different way, by dividing by the mean flux. Normalising by the median flux was also done, but using the mean produced slightly smaller quoted errors on the spectroscopic [Fe/H]s and tighter 2σ bounds on the [Fe/H] gradients.

The equivalent widths are fitted by Gaussians, and the errors in the equivalent widths are given by a

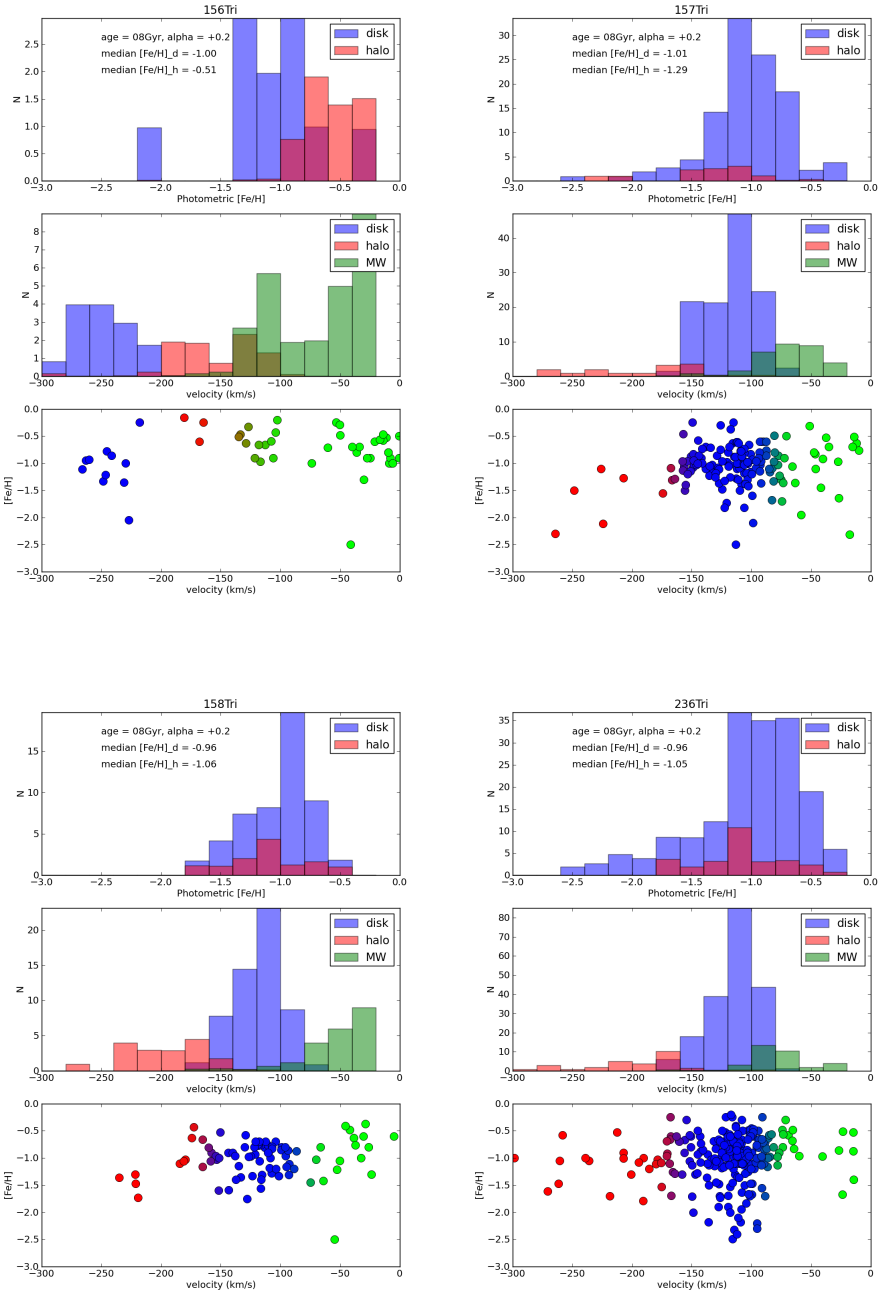

Figure 3.24: Photometric MDF, velocity histogram and scatter plot for stars from individual fields, using Dartmouth isochrones. Age 8 Gyr, $\alpha = +0.2$. The Bayesian "halo", "disk" and "MW" counting method is used (5% halo prior). The colours are used to specify the different populations. In the bottom panel, the halo, disk and MW probabilities are passed as a RGB (red, green, blue) tuple to specify the colour of the plotting symbol. Halo is coded red, disk blue, and Milky Way green. The photometric metallicities in the bottom panel for the Milky Way (green) datapoints are spurious since these are in fact dwarf stars.

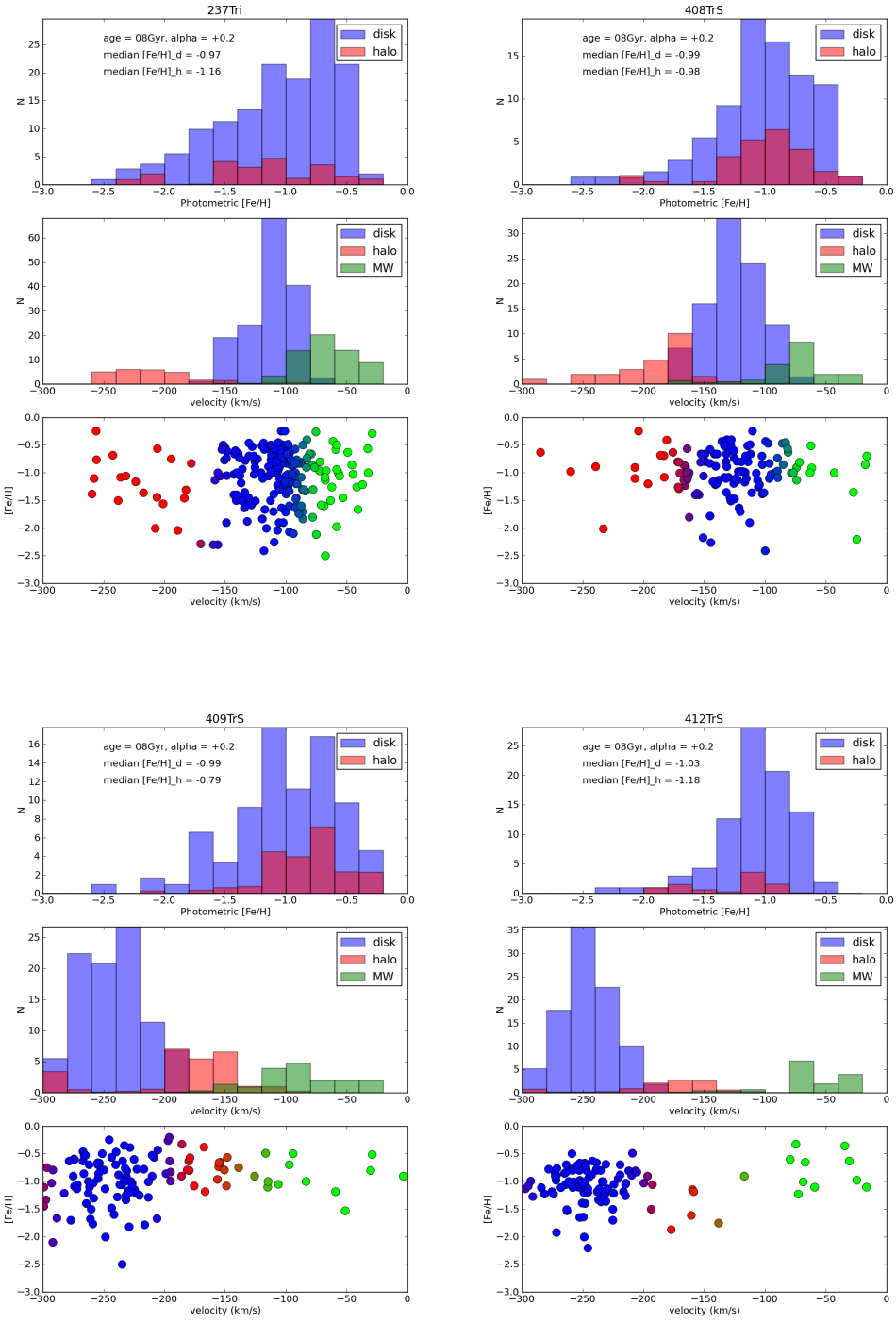

Figure 3.25: Photometric MDF, velocity histogram and scatter plot for stars from individual fields, using Dartmouth isochrones. Age 8 Gyr, $\alpha = +0.2$. The Bayesian "halo", "disk" "and "MW" counting method is used (5% halo prior). The colours are used to specify the different populations. In the bottom panel, the halo, disk and MW probabilities are passed as a RGB (red, green, blue) tuple to specify the colour of the plotting symbol. The photometric metallicities in the bottom panel for the Milky Way (green) datapoints are spurious since these are in fact dwarf stars.

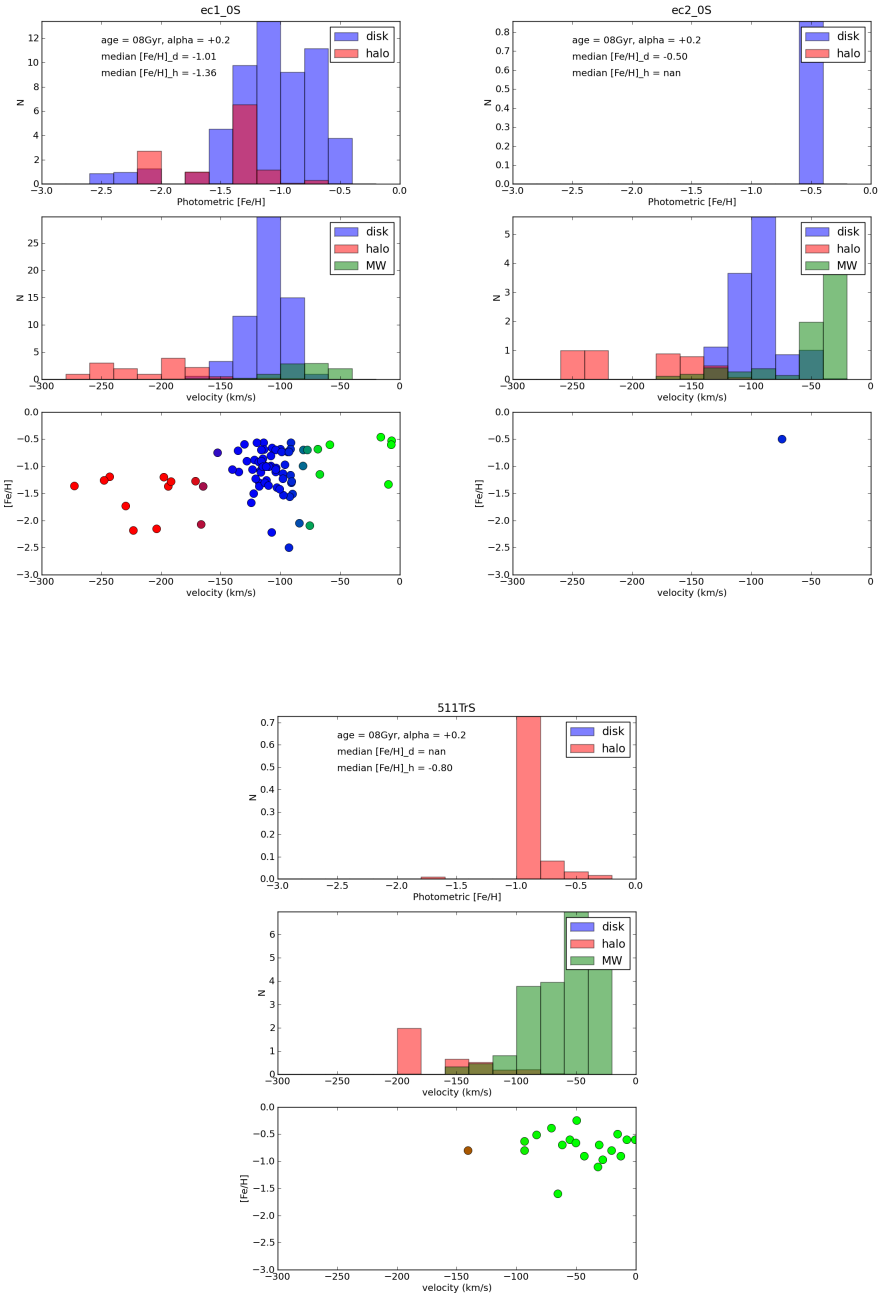

Figure 3.26: Photometric MDF, velocity histogram and scatter plot for stars from individual fields, using Dartmouth isochrones. Age 8 Gyr, $\alpha = +0.2$. The Bayesian "halo", "disk" and "MW" counting method is used (5% halo prior). The colours are used to specify the different populations. In the bottom panel, the halo, disk and MW probabilities are passed as a RGB (red, green, blue) tuple to specify the colour of the plotting symbol. The photometric metallicities in the bottom panel for the Milky Way (green) datapoints are spurious since these are in fact dwarf stars. The histograms for 511TrS and EC2 are affected by the fact that there is very little photoFeH data available due to the missing V and I data in EC2, and some of 511TrS.

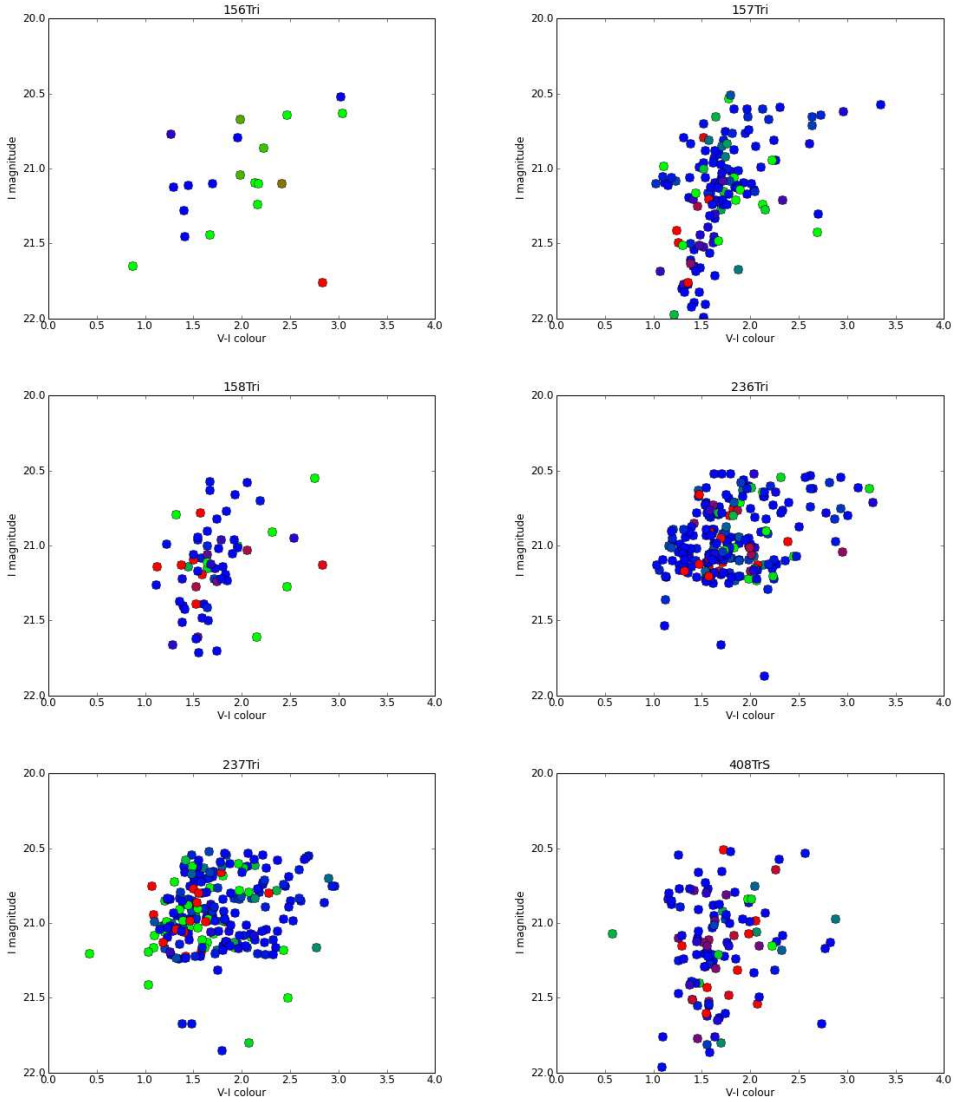

Figure 3.27: CMDs for stars from individual fields (quality cut data). The Bayesian "halo", "disk" and "MW" counting method is used (5% halo prior). The colours are used to specify the different populations. The halo, disk and MW probabilities are passed as a RGB (red, green, blue) tuple to specify the colour of the plotting symbol. Halo is coded red, disk blue, and Milky Way green.

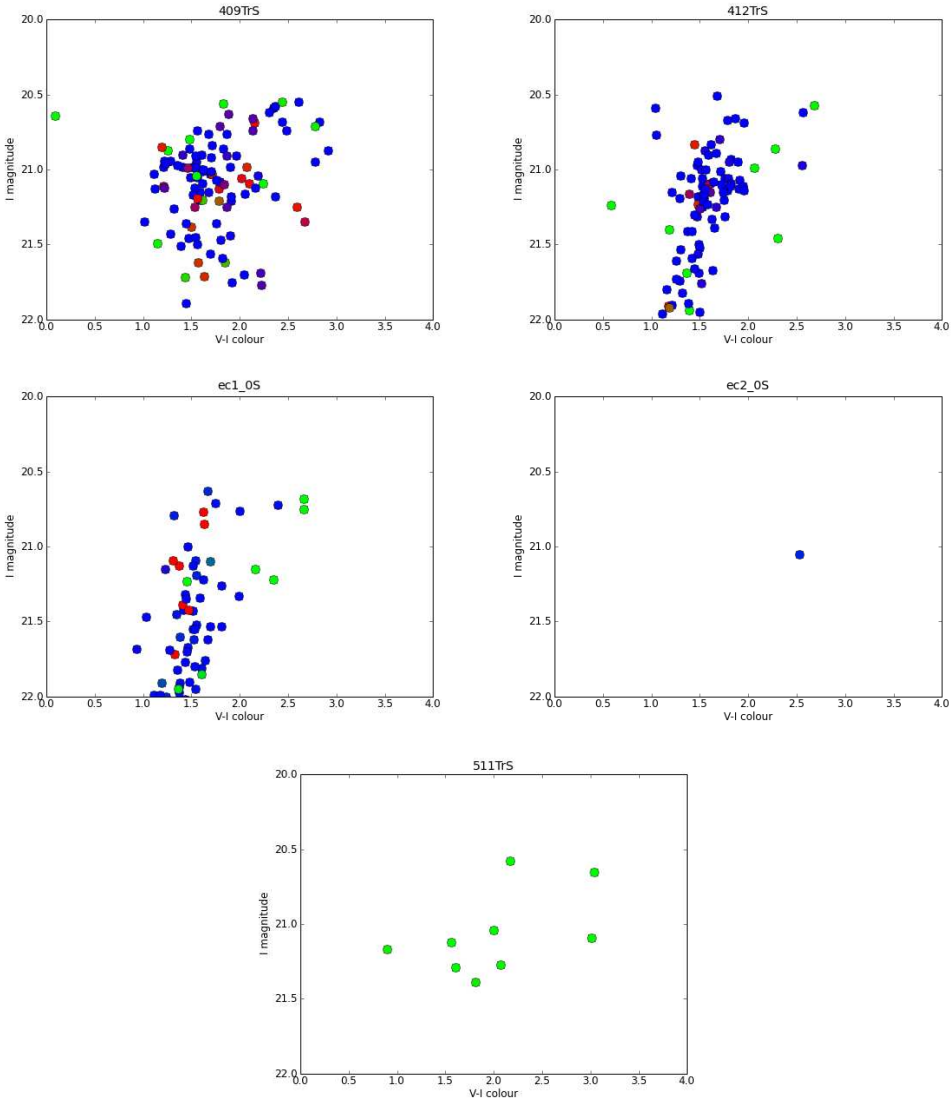

Figure 3.28: CMDs for stars from individual fields (quality cut data). The Bayesian "halo", "disk" and "MW" counting method is used (5% halo prior). The colours are used to specify the different populations. The halo, disk and MW probabilities are passed as a RGB (red, green, blue) tuple to specify the colour of the plotting symbol. Halo is coded red, disk blue, and Milky Way green. Note that there are some stars in EC2 and 511TrS that are missing V and I data in the catalogue files.

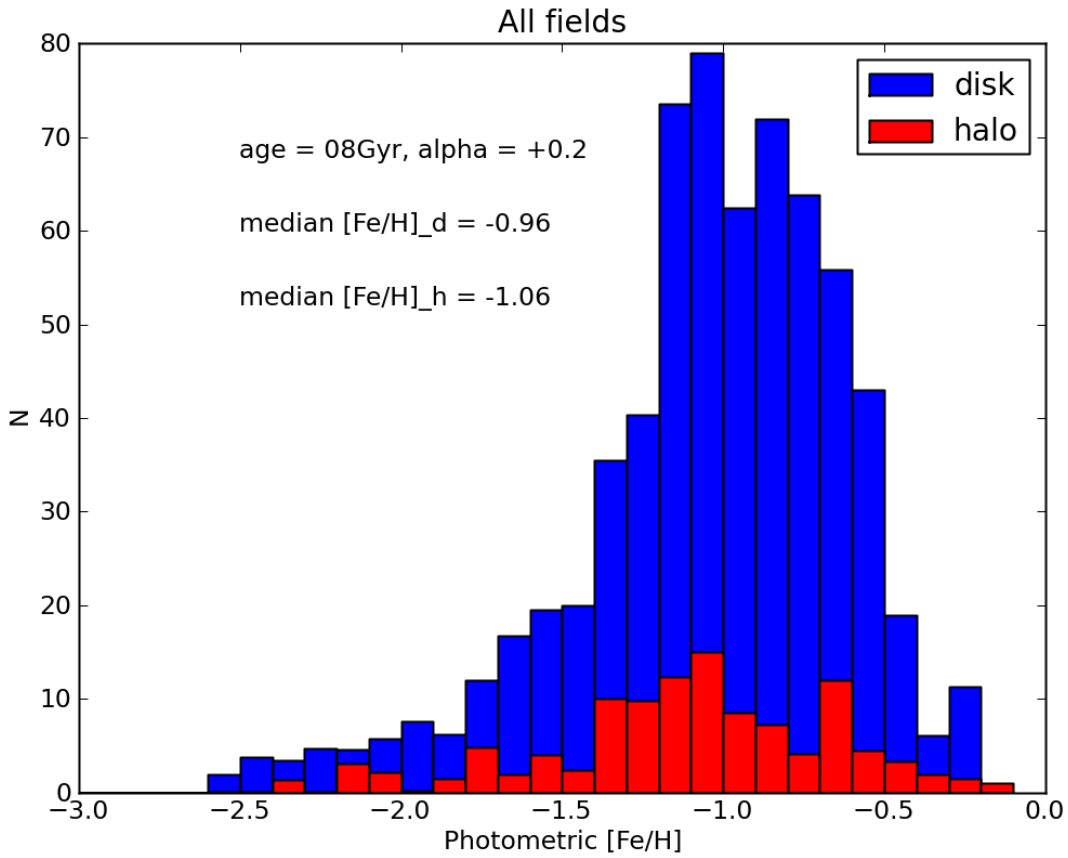

Figure 3.29: Photometric MDF, using Dartmouth isochrones. Age 8 Gyr, $\alpha = +0.2$. The Bayesian "halo", "disk" and "MW" counting method is used. Halo prior of 5%.

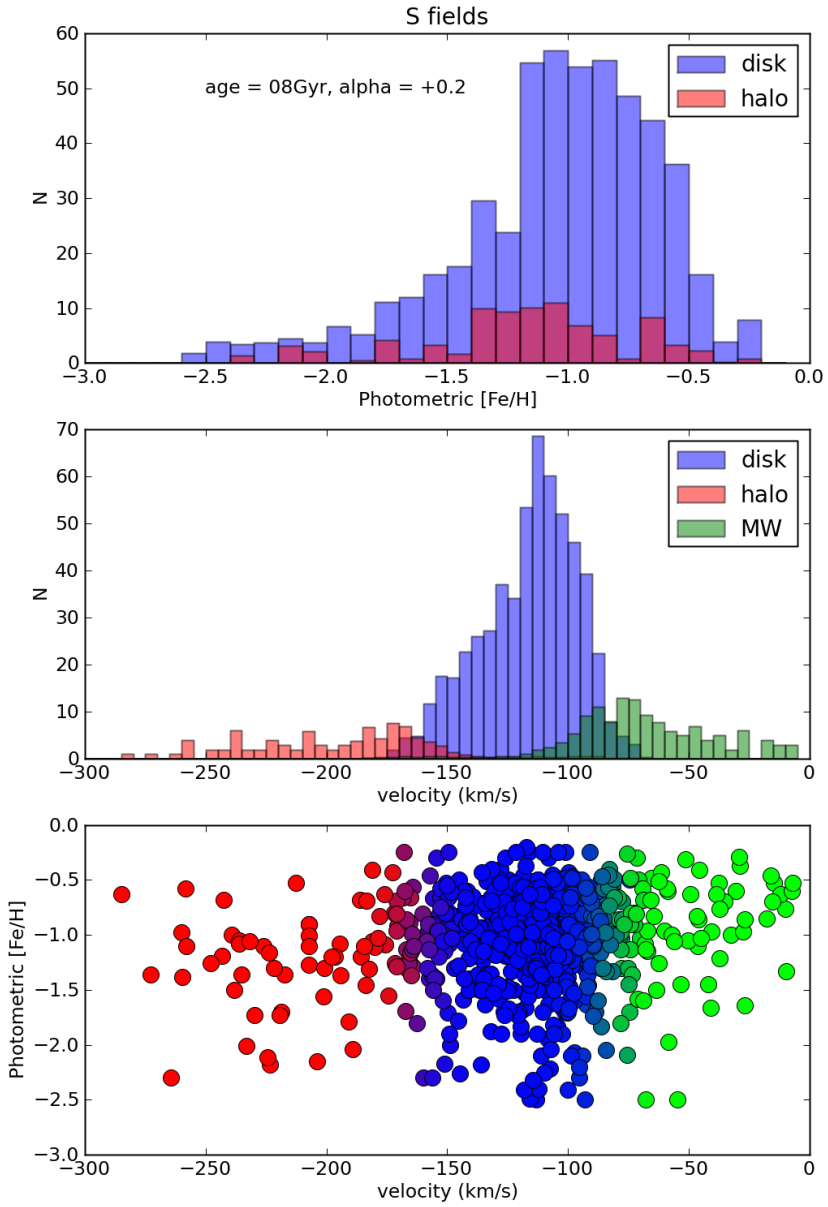

Figure 3.30: Photometric MDF, velocity histogram and scatter plot for stars from all fields to the south of the centre of M33, using Dartmouth isochrones. Age 8 Gyr, $\alpha = +0.2$. The Bayesian "halo", "disk" and "MW" counting method is used (5% halo prior). The colours are used to specify the different populations. In the bottom panel, the halo, disk and MW probabilities are passed as a RGB (red, green, blue) tuple to specify the colour of the plotting symbol.

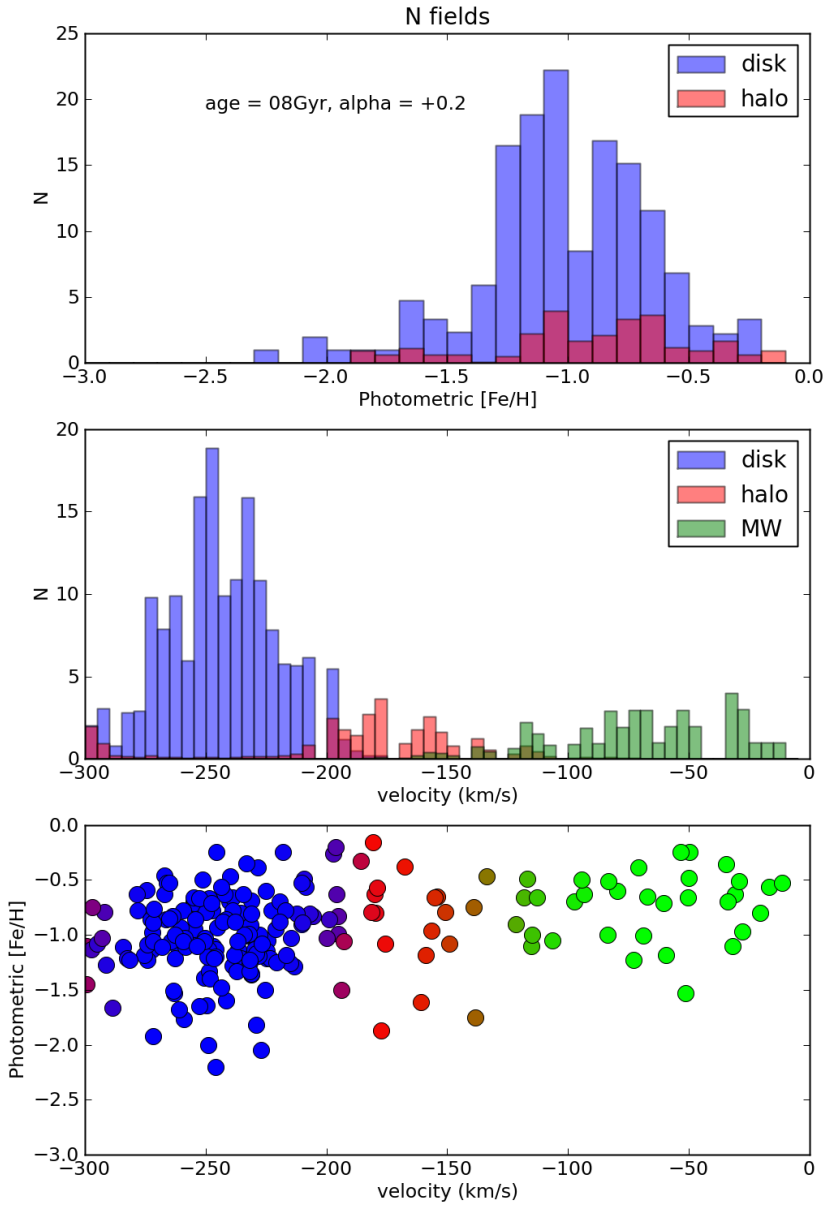

Figure 3.31: Photometric MDF, velocity histogram and scatter plot for stars from all fields to the north of the centre of M33, using Dartmouth isochrones. Age 8 Gyr, $\alpha = +0.2$. The Bayesian "halo", "disk" and "MW" counting method is used (5% halo prior). The colours are used to specify the different populations. In the bottom panel, the halo, disk and MW probabilities are passed as a RGB (red, green, blue) tuple to specify the colour of the plotting symbol.

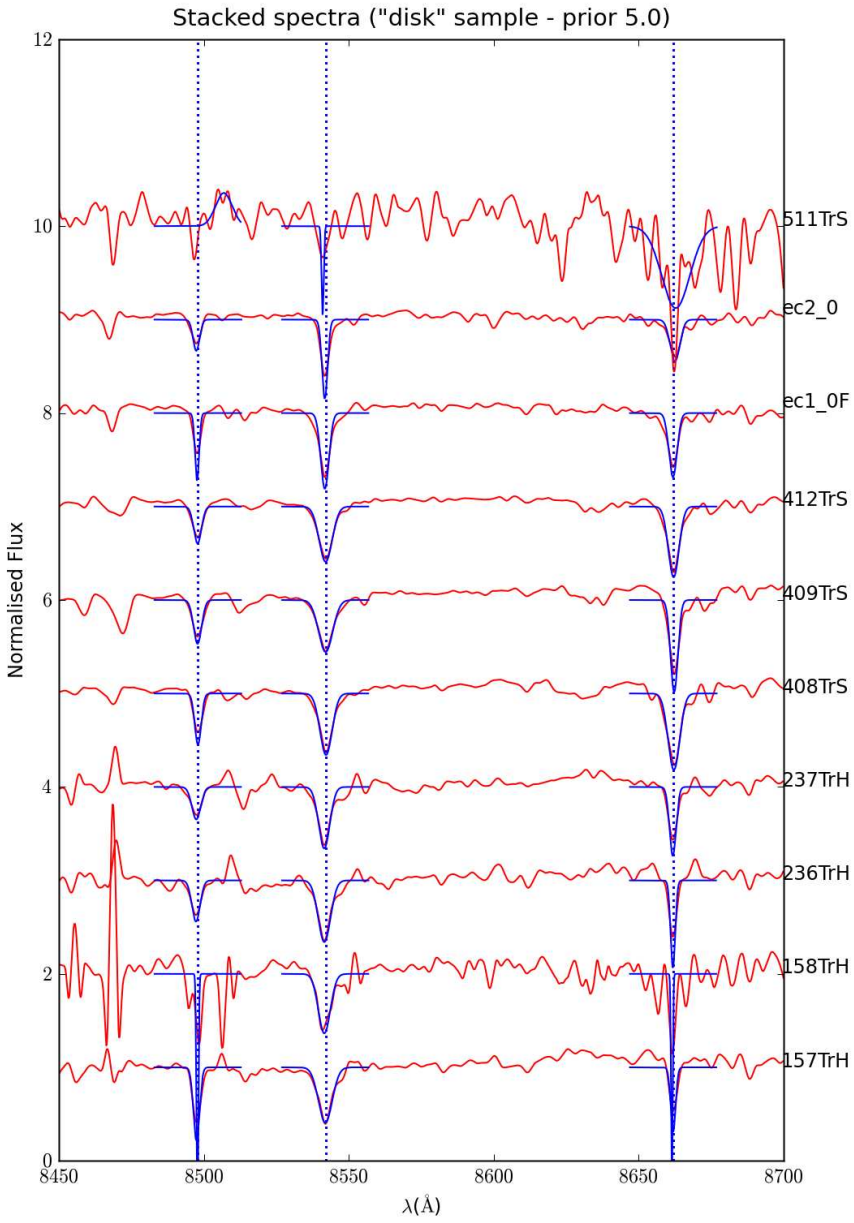

Figure 3.32: Stacked spectra of the "disk" samples with 5% halo Bayesian prior. The spectra have had their Doppler shift as a result of their radial velocity removed, interpolated to a fine 0.001$\AA$ grid, stacked and smoothed back down to the original instrumental resolution (in most cases 0.33$\AA$ per pixel) before the CaT equivalent widths are fit. For display purposes, the spectra plotted here are smoothed to 5$\AA$. The blue lines show Gaussian fits to the regions containing each Ca II triplet line.

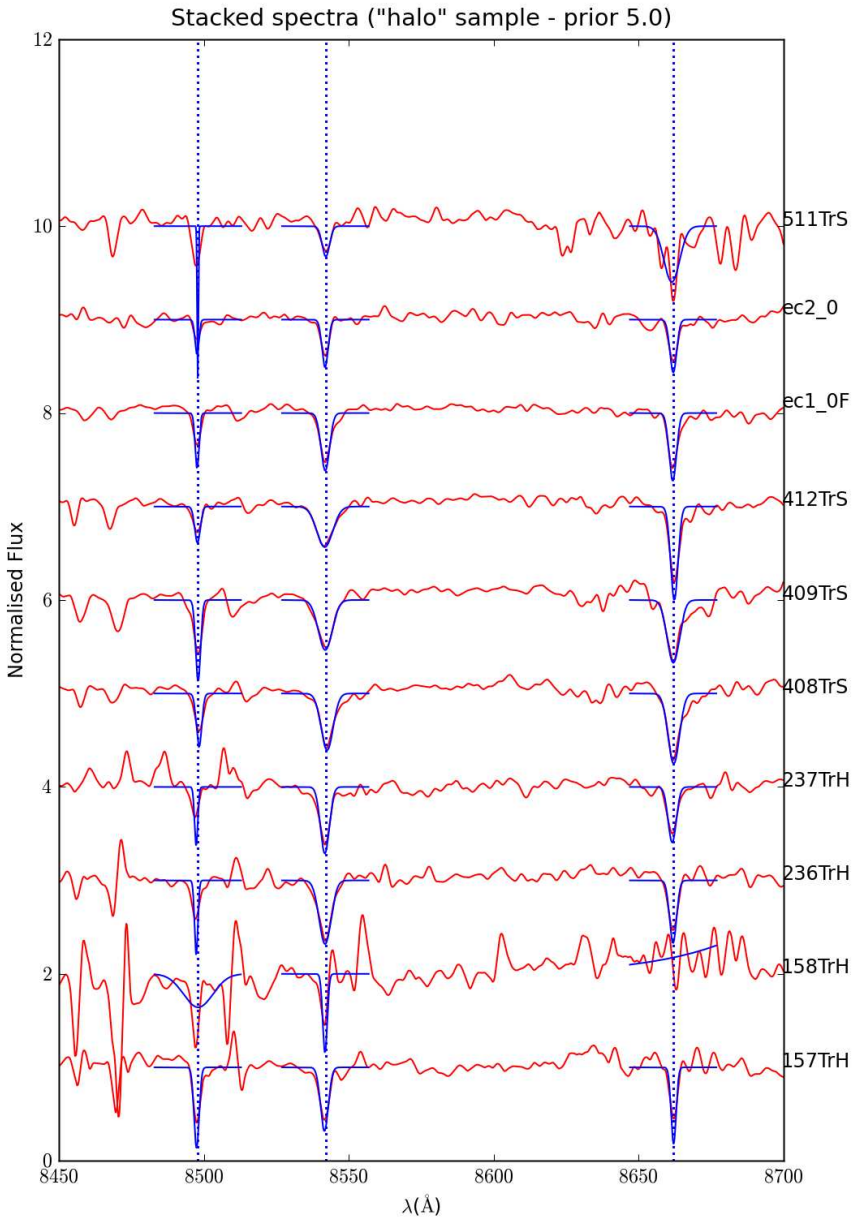

Figure 3.33: Stacked spectra of the "halo" samples with 5% halo Bayesian prior. The spectra have had their Doppler shift as a result of their radial velocity removed, interpolated to a fine 0.001$\AA$ grid, stacked and smoothed back down to the original instrumental resolution (in most cases 0.33$\AA$ per pixel) before the CaT equivalent widths are fit. For display purposes, the spectra plotted here are smoothed to 5$\AA$. The blue lines show Gaussian fits to the regions containing each Ca II triplet line.

formula found in Battaglia et al. 2008. Over any individual line C, the noise can be taken to be constant over the lines of interest, therefore the error in the equivalent width due to random noise ΔEW is given by $\Delta EW = \frac{\sigma_n \sqrt{w}}{C} = \frac{\sqrt{w}}{\frac{S}{N}}$ where $\frac{S}{N}$ is the signal to noise ratio, and w is the effective width ($\mathring{A}$) the line is integrated over. For a fitted Gaussian profile this is $w = \sqrt{4\pi}\sigma \approx 1.5$(FWHM).

The calibrations used follow the formulae from Battaglia et al. 2008.

Where only CaT2 and CaT3 are used, the equation used is [Fe/H] $= -2.81 + 0.44(EW2 + EW3 + 0.64 * (V - V_{HB}))$ (their equations 11 and 16), where all three lines are used, the equation used is [Fe/H] $= -2.966 + 0.362(EW1 + EW2 + EW3 + 0.73 * (V - V_{HB}))$. Where only CaT1 and CaT2 are used, the formula used for CaT2 and CaT3 is adapted using the figure 3:5:4 given for the typical ratios of the various CaT equivalent widths. These are reasonable calibrations to use except at very low metallicity (the Starkenburg et al. 2010 calibration begins to deviate from the standard calibration at [Fe/H]s < -2, and the difference becomes more significant at lower [Fe/H]s). Nonetheless, the Battaglia et al. 2008 calibration is applicable enough for the purposes of the current work down to $\sim$ [Fe/H] = -2.5, which is likely to be sufficient since most of the [Fe/H]s turn out to be at least -1.5.

It was later decided to revise the analysis to use the CaT2 line only, since the CaT3 line was also affected by sky lines distorting the fits. The calibration was adapted for this, using the estimate for the ratio CaT2/CaT3 in Appendix B of Starkenburg et al. 2010.

Summary plots were produced, and weighted linear regression was used to look for any trends with radius. The datapoints were weighted by the numbers of stars within each sample. 2σ confidence intervals (approximately 95%) were calculated for the gradient to see how significant any trends with radius are. κ-sigma clipping was used to exclude outliers that fall beyond 2σ of the mean value for the photometric and spectroscopic [Fe/H]s respectively.

3.6.2 Effect of distance of the [Fe/H] calibration

The calibration of the CaT-[Fe/H] relation includes a term that expresses the position in the CMD above the horizontal branch magnitude. This term is affected by the distance assumption to M33. We have assumed a distance to M33 of 809 kpc ($M - m = 24.54 \pm 0.06$, McConnachie et al. 2005), and an apparent magnitude of the horizontal branch of $M_V = 25.24$. For halo stars we have an uncertainty of $\sim$ 0.04 mag due to the varying line of sight distance to stars either in front or behind the centre of M33. Since the effect is small compared to existing errors, we have not adjusted the calibration for disk stars for the varying distance to different parts of the disk. There is also a possibility of systematic error due to the possibility that the distance modulus to M33 is up to 0.3 mag larger than our assumption of 809 kpc, (McConnachie et al., 2005) as suggested by some studies. See section 1.5.3 for a discussion of the range of distances for M33 in the literature. The change in dex as a result of the line of sight uncertainty is approximately $\pm$ 0.01 dex, which is much smaller than the σ on the [Fe/H] measurement for any given spectroscopic stack. Given the small size of this contribution to the uncertainty, it should not affect the significance of any observed metallicity trends by much.

The systemic distance uncertainty could mean that the spectroscopic [Fe/H] could be up to approximately 0.09 dex more metal poor than our calibration suggests if the distance to M33 was 0.3 mag larger in modulus. This however would affect each field equally, and would not affect any [Fe/H] gradients, although may be worth bearing in mind when comparing this work with other work, particularly where that other work has

Halo prior (%)	Sub-population	Method	Fit for [Fe/H](r)	Lower 2σ confidence	Upper 2σ confidence	(Weighted) mean [Fe/H]
5	halo	photometric	-0.8 - 0.044r	-0.131	0.043	-1.07
5	halo	spectroscopic	-0.35 - 0.137r	-0.234	-0.039	-1.37
5	disk	photometric	-0.8 - 0.024r	-0.038	-0.010	-0.97
5	disk	spectroscopic	-0.63 - 0.038r	-0.092	0.015	-0.93
3	halo	photometric	-0.75 - 0.042r	-0.133	0.049	-1.06
3	halo	spectroscopic	-0.37 - 0.136r	-0.231	-0.041	-1.40
3	disk	photometric	-0.8 - 0.024r	-0.039	-0.009	-0.97
3	disk	spectroscopic	-0.64 - 0.038r	-0.092	0.015	-0.93
1	halo	photometric	-0.82 - 0.048r	-0.128	0.032	-1.11
1	halo	spectroscopic	-0.45 - 0.128r	-0.216	-0.041	-1.46
1	disk	photometric	-0.78 - 0.026r	-0.042	-0.011	-0.97
1	disk	spectroscopic	-0.64 - 0.039r	-0.092	0.014	-0.93
0.5	halo	photometric	-0.87 - 0.045r	-0.120	0.030	-1.14
0.5	halo	spectroscopic	-0.5 - 0.122r	-0.204	-0.039	-1.49
0.5	disk	photometric	-0.77 - 0.028r	-0.046	-0.010	-0.97
0.5	disk	spectroscopic	-0.64 - 0.039r	-0.092	0.014	-0.94
0.1	halo	photometric	-0.82 - 0.053r	-0.103	-0.002	-1.16
0.1	halo	spectroscopic	-0.56 - 0.110r	-0.181	-0.038	-1.55
0.1	disk	photometric	-0.76 - 0.029r	-0.047	-0.011	-0.97
0.1	disk	spectroscopic	-0.65 - 0.040r	-0.092	0.013	-0.94
simple windowing	halo	photometric	-0.89-0.039r	-0.128	0.049	-1.14
simple windowing	halo	spectroscopic	-0.36 - 0.128r	-0.230	-0.025	-1.45
simple windowing	disk	photometric	-0.72 - 0.033r	-0.055	-0.011	-0.96
simple windowing	disk	spectroscopic	-0.79 - 0.019r	-0.077	0.038	-0.95

Table 3.4: The 2σ confidence intervals for the gradients in [Fe/H]. The spectroscopic [Fe/H] values are using the CaT2 line only, since this produced lower values of the quoted error on the [Fe/H] and the tightest bounds on the gradients. Results using CaT12, CaT23 and CaT123 are reproduced in Appendix B.

explicitly used a larger distance assumption.

3.7 Overall trends in metallicity

The overall trends in metallicity are shown in Figures 3.34 and 3.35 for a 5% Bayesian halo prior, and 3.36 and 3.37 for simple windowing. The 2σ ($\approx 95\%$) confidence intervals in the gradients for these and other Bayesian halo priors are shown in Table 3.4.

In the "disk" subsample, there is a downward metallicity trend with radius in both the photometric and spectroscopic measurements, although it is significant at 2σ level in the photometric method only, even if the trend is larger in the spectroscopic analysis. This result is the same qualitatively speaking irrespective of the Bayesian halo prior, or simple windowing.

In the "halo" subsample, a downward trend is indicated in the spectroscopic analysis for all Bayesian halo priors as well as simple windowing. Using the photometric analysis there is also a downward trend, albeit a weaker one. The trend is significant at the 2σ level in only the spectroscopic analysis. It may be noted, that in the "halo" sample of the field M33EC1, which is the outermost field with good data in our sample ($R =$ 10.8 kpc), there appears to be a difference in [Fe/H] between the spectroscopic and photometric analysis. No other field exhibits such a difference found both in the Bayesian (5% prior) and "simple" windowing.

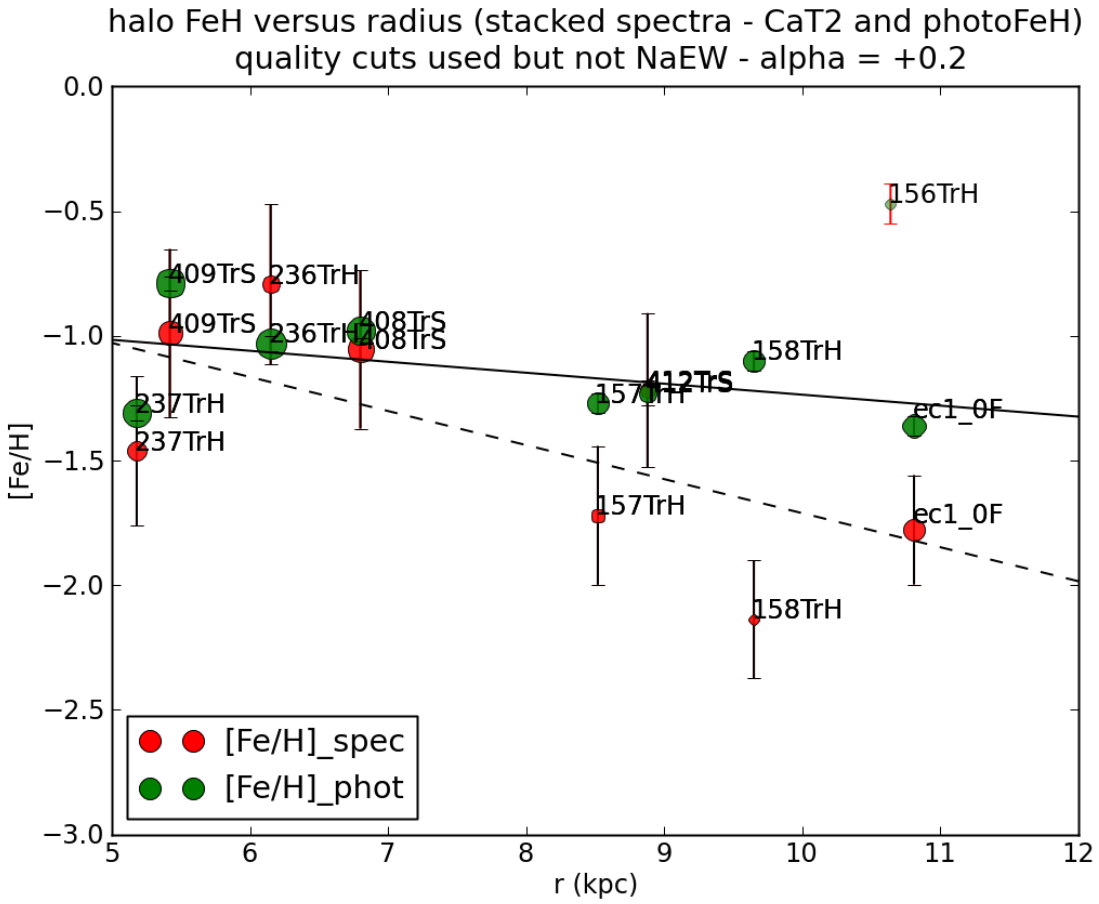

Figure 3.34: Comparing photometric and spectroscopic [Fe/H]s (based on stacked spectra) on a field by field basis - kinematic halo candidates (Bayesian selection method used - halo prior of 5%). Photometric [Fe/H]s use isochrones for age 8 Gyr, $\alpha = +0.2$. Spectroscopic [Fe/H]s use the CaT2 line only, since this gives the smallest quoted error on [Fe/H]. A change in age of the isochrones of $\pm$ 2 Gyr would result in the photometric metallicities being shifted by $\sim$ 0.1 dex with respect to the spectroscopic. Weighted linear regression is applied to derive a metallicity gradient, the equation of which is for the spectroscopic $[Fe/H]_s$ = -0.35 - 0.137r, with 2σ confidence ranges on the gradient being -0.234, -0.039 and photometric $[Fe/H]_p$ = -0.8 - 0.044r, with 2σ confidence ranges on the gradient being -0.131, 0.043. The dotted line is the spectroscopic [Fe/H] fit, the solid line the photometric. Points plotted as semi-transparent and with red error bars are not included in the fit ($\kappa\sigma$ clipping as described in the text)

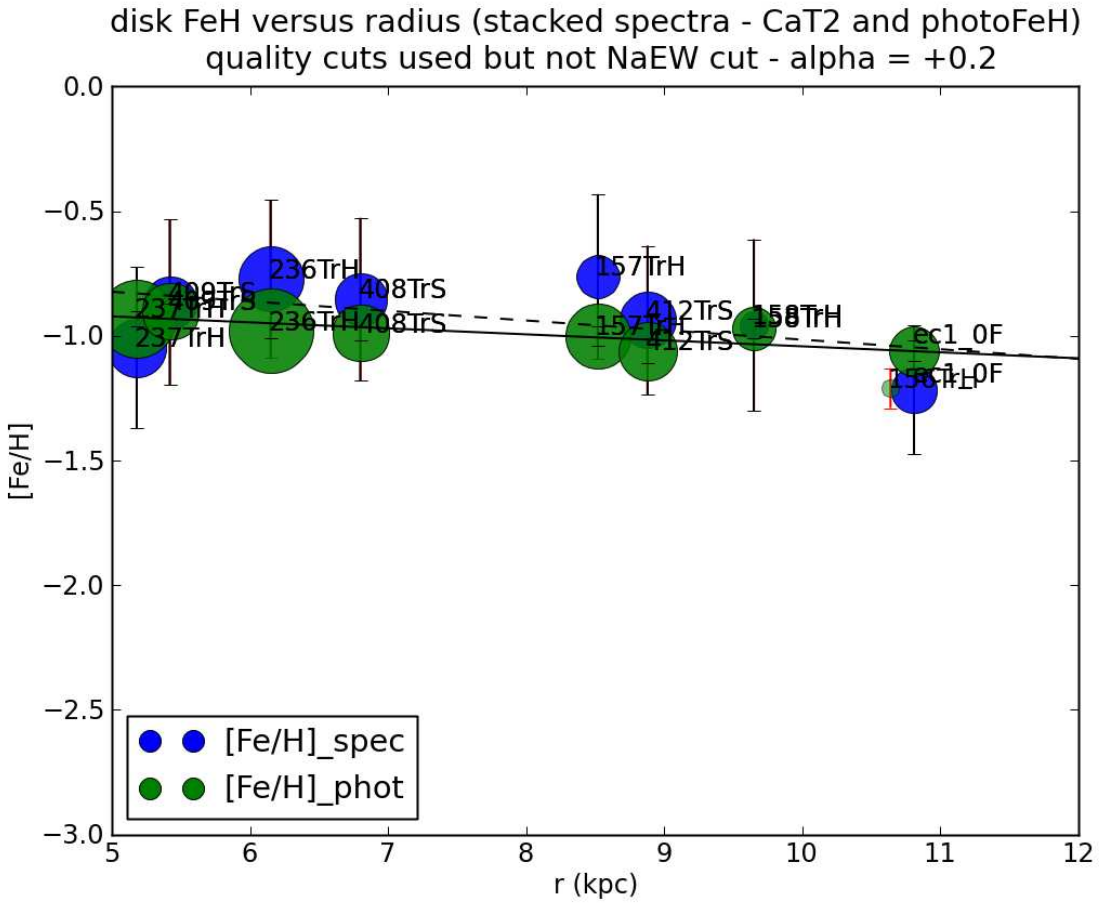

Figure 3.35: Comparing photometric and spectroscopic [Fe/H]s (based on stacked spectra) on a field by field basis - kinematic disk candidates (Bayesian selection method used - halo prior of 5%). Photometric [Fe/H]s use isochrones for age 8 Gyr, $\alpha = +0.2$. Spectroscopic [Fe/H]s use the CaT2 line only, since this gives the smallest quoted error in [Fe/H]. A change in age of the isochrones of $\pm$ 2 Gyr would result in the photometric metallicities being shifted by $\sim$ 0.1 dex with respect to the spectroscopic. Weighted linear regression is applied to derive a metallicity gradient, the equation of which is for the spectroscopic $[Fe/H]_s$ = -0.63 - 0.038r, with 2σ confidence ranges on the gradient being -0.092, 0.015 and photometric $[Fe/H]_p$ = -0.82 - 0.024r, with 2σ confidence ranges on the gradient being -0.038, -0.010. The dotted line is the spectroscopic [Fe/H] fit, the solid line the photometric. Points plotted as semi-transparent and with red error bars are not included in the fit ($\kappa\sigma$ clipping as described in the text)

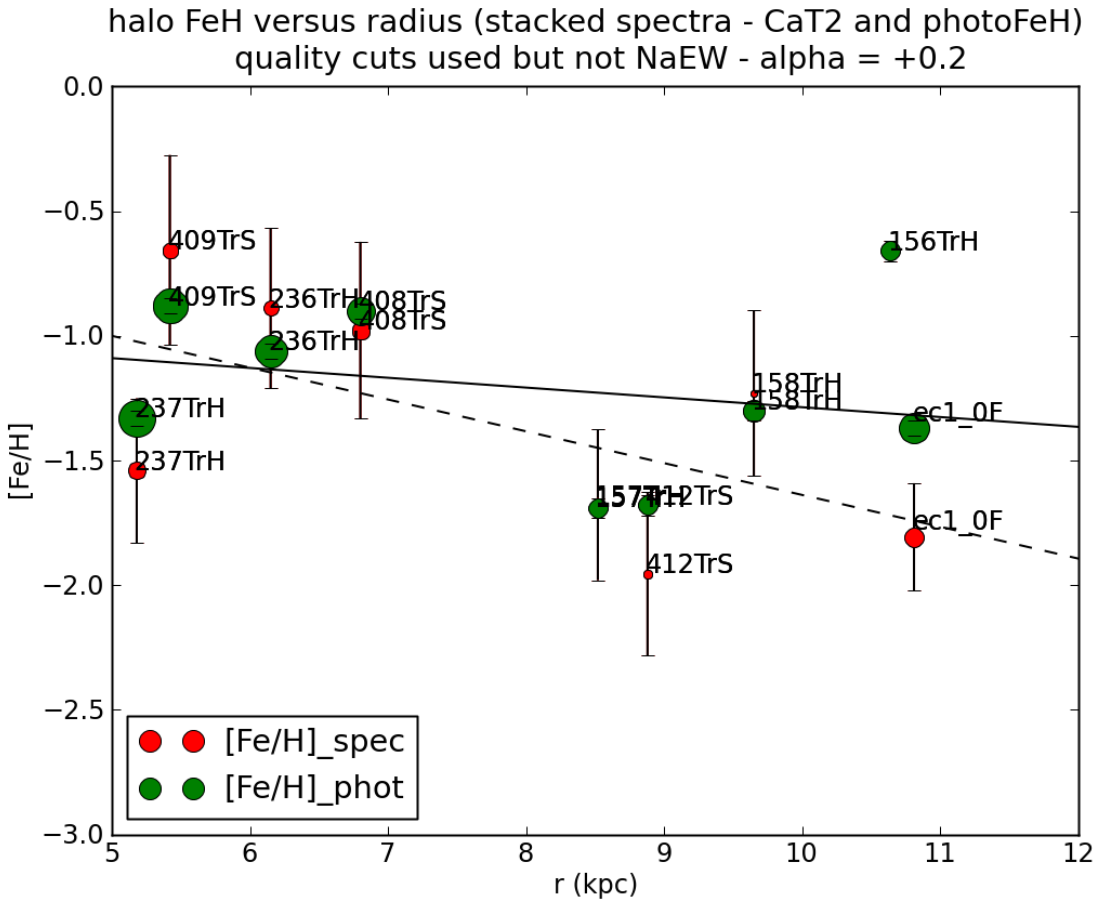

Figure 3.36: Comparing photometric and spectroscopic [Fe/H]s (based on stacked spectra) on a field by field basis - kinematic halo candidates. Simple kinematic windowing method used. Photometric [Fe/H]s use isochrones for age 8 Gyr, α = +0.2. Spectroscopic [Fe/H]s use the CaT2 line only, since this gives the smallest quoted error in [Fe/H]. A change in age of the isochrones of $\pm$ 2 Gyr would result in the photometric metallicities being shifted by $\sim$ 0.1 dex with respect to the spectroscopic. Weighted linear regression is applied to derive a metallicity gradient, the equation of which is for the spectroscopic $[Fe/H]_s$ = -0.36 - 0.128r, with 2σ confidence ranges on the gradient being -0.230, -0.025 and photometric $[Fe/H]_p$ = -0.89 - 0.039r, with 2σ confidence ranges on the gradient being -0.128, 0.049. The dotted line is the spectroscopic [Fe/H] fit, the solid line the photometric. Points plotted as semi-transparent and with red error bars are not included in the fit ($\kappa\sigma$ clipping as described in the text).

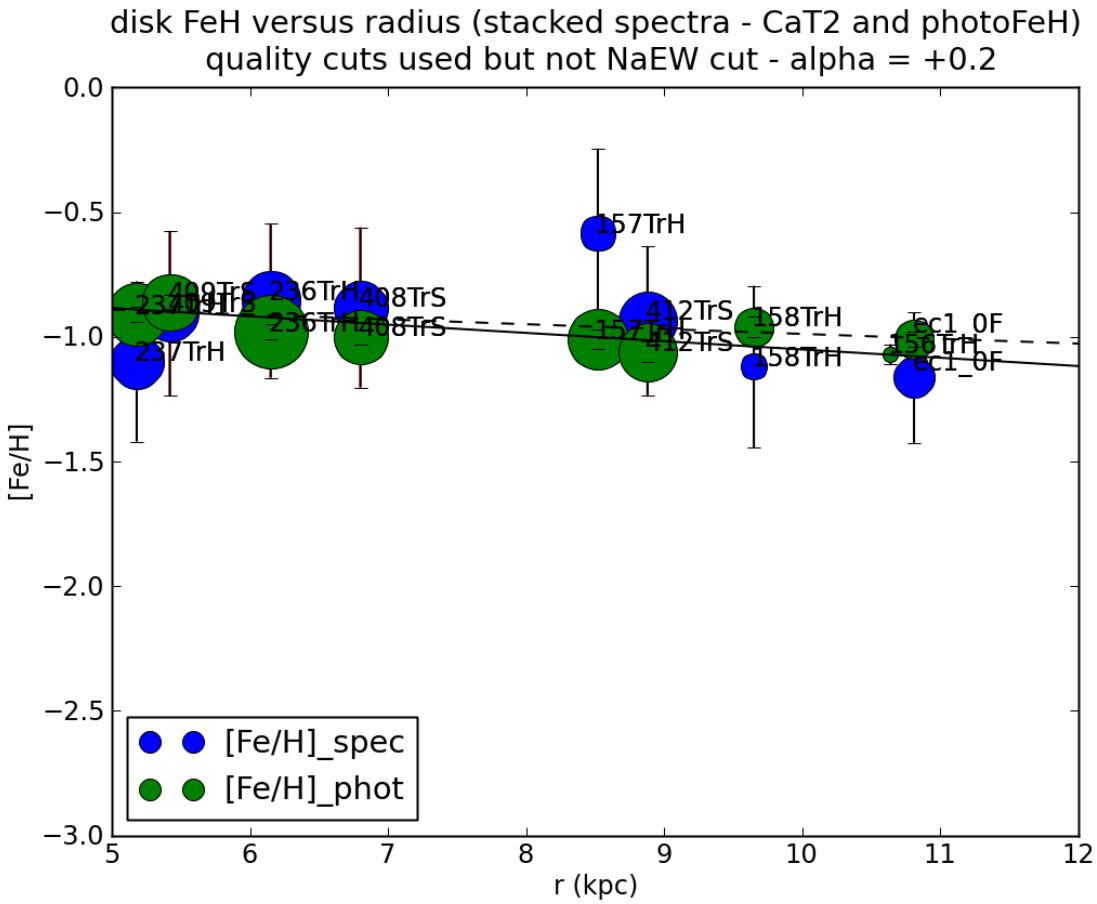

Figure 3.37: Comparing photometric and spectroscopic [Fe/H]s (based on stacked spectra) on a field by field basis - kinematic disk candidates. Simple kinematic windowing method used. Photometric [Fe/H]s use isochrones for age 8 Gyr, $\alpha = +0.2$. Spectroscopic [Fe/H]s use the CaT2 line only, since this gives the smallest quoted error in [Fe/H]. A change in age of the isochrones of $\pm$ 2 Gyr would result in the photometric metallicities being shifted by $\sim$ 0.1 dex with respect to the spectroscopic. Weighted linear regression is applied to derive a metallicity gradient, the equation of which is for the spectroscopic $[Fe/H]_s$ = -0.79 - 0.019r, with 2σ confidence ranges on the gradient being -0.077, 0.038 and photometric $[Fe/H]_p$ = -0.72 - 0.033r, with 2σ confidence ranges on the gradient being -0.055, -0.011. Points plotted as semi-transparent and with red error bars are not included in the fit ($\kappa\sigma$ clipping as described in the text).

Chapter 4

Discussion

4.1 The disk profile

4.1.1 General properties of the disk

General properties of the M33 disk were discussed in sections 1.4.2 and 1.5 and M33 is placed in the context of the other two major spiral galaxies of the Local Group, namely the Milky Way Galaxy and M31. The disk surface brightness for all of the spiral galaxies in the Local Group can be reasonably fitted by an exponential profile, this being a general property of disk galaxies. See for example de Jong 1996 for an observational review of a number of nearby face-on disk galaxies illustrating this.

The M33 galaxy being smaller than the two larger spirals of the Galaxy and M31, has a smaller thin disk scale length (1.8 kpc according to Ferguson et al. 2007) versus 5.9 kpc for M31 and 2.3 kpc for the Galaxy. (Walterbos & Kennicutt, 1988; Hammer et al., 2007). The rotation of the M33 disk in H I gas was studied by Corbelli & Salucci 2000, and their rotation curve for M33 is reproduced in figure 3.6. Our kinematic data is placed in the context of that rotation model in figure 3.8. The M33 disk in H I is also observed to contain a warp as discovered by Rogstad et al. 1976 and illustrated in Figure 3.7.

As well as a thin disk population, the Milky Way and M31 galaxies are also observed to contain a "thick disk". See Collins et al. 2011 for a kinematic study of a "thick disk" component in M31. It has been suggested that M33 may contain a thick disk component (Hood et al., 2007).

4.1.2 The disk scale length

Freeman 1970 gave a B band scale length of 1.6 kpc for the disk of M33, based on photometry by de Vaucouleurs 1959. Their distance assumption for M33 is 720 kpc, normalising to our distance assumption (809 kpc) their scale length is 1.8 kpc. Regan and Vogel derived a scale length of $5'.8$ (1.4 kpc for our assumed distance to M33 of 809 kpc) in the K-band (Regan & Vogel, 1994).

Ferguson et al. 2007 using RGB star counts from the INT survey of M31 and M33, find a scale length of ~ 1.8 kpc for M33, with a break at ~ 8 kpc beyond which the luminosity profile significantly steepens. They find that the steep outer component dominates the M33 radial light profile out to at least 14 kpc, limiting the contribution of any shallow power-law stellar halo component to "no more than a few percent of the disk

luminosity".

Barker et al. 2007a using ACS fields on the SE minor axis of M33, located $\sim 20'$ to $30'$ in projected distance SE of M33's nucleus (9-13 kpc deprojected in the disk), derive a scale length of $4'.7 \pm 0'.1$, which corresponds to 1.8 kpc, normalised to our distance assumption. They find that young populations have shorter scale lengths, ranging down to $1'.92$ at ages of 0.35 Gyr, and that there is a positive age gradient with older stars found at larger radii. This appears to contradict the inside-out formation scenario. Alternatively a transition between two distinct components is being observed (thin/thick disk? disk/halo?), or there is radial mixing whereby older stars are redistributed to larger radii. Barker et al. 2007a estimate from their own and other studies that the halo/disk transition is located at around $50'$ (12.3 kpc). This is substantially greater than Teig's estimate of 8-9 kpc. Matthew Teig produced a PhD thesis which included surface brightness profiles of the M33 disk and halo (Teig, 2008), his work indicated a scale length of 0.92 kpc in the disk. This scale length is much shorter than any other work (cf. Barker et al. 2007a or Ferguson et al. 2007).

Williams et al. 2009 use resolved stellar photometry of four fields along the major axis of the M33 disk from Hubble ACS images. They derive a scale length that varies with the age of the stars, evolving from $r_s = 1.0 \pm 0.1$ kpc at 10 Gyr to $r_s = 1.8 \pm 0.1$ kpc at times more recent than 5 Gyr. A couple of figures from that paper are reproduced in Figures 4.1 and 4.2. They concluded that there is a negative age gradient in the region of the disk studied, which is at smaller deprojected radii than the Barker et al. 07 work. They interpret the contrast between the age gradient in the inner and outer disk as evidence for radial mixing which tends to redistribute older stars to larger radii, producing the break in the exponential disk profile observed by Ferguson et al. 2007, and the reversal of the age gradient at large radii observed by Barker et al. Simulation work has been done that predicts this result (Roškar et al., 2008a,b).

Verley et al. 2009 show scale lengths in various IR bands (their table 2). The IR profiles show a scale length of ~ 1.55 kpc for old stellar populations and ~ 1.75 kpc for dust emission. They also derive ~ 2 kpc for tracers of recent star formation including Hα and UV emission. The youngest stellar components have longest scale length, supporting an inside-out disk growth scenario. This is because in the inside-out growth scenario, the scale lengths of galaxy disks are believed to increase with time due to late accretion of gas at large radii and exhaustion of gas in the centres of galaxies.

Observations from this work

The scale length of our spectroscopic "disk" sample is, when the DEIMOS selection effects are compensated for, 1.72 kpc. This scale length is in good agreement with values from the literature. Varying the halo prior or indeed switching to simple windowing does not change the observed scale length significantly.

4.2 The halo profile

4.2.1 Comparing the observed "halo" population to photometric surveys.

Photometric surveys such as the INT survey detailed in Ferguson et al. 2007 have to date failed to clearly detect a M33 halo population. The PAndAS survey detected what could have been interpreted as M33 halo in Ibata et al. 2007 but as the survey area was extended it became clear that what was being seen was a tidal substructure, potentially caused by interaction between M31 and M33. (McConnachie et al., 2009, 2010).

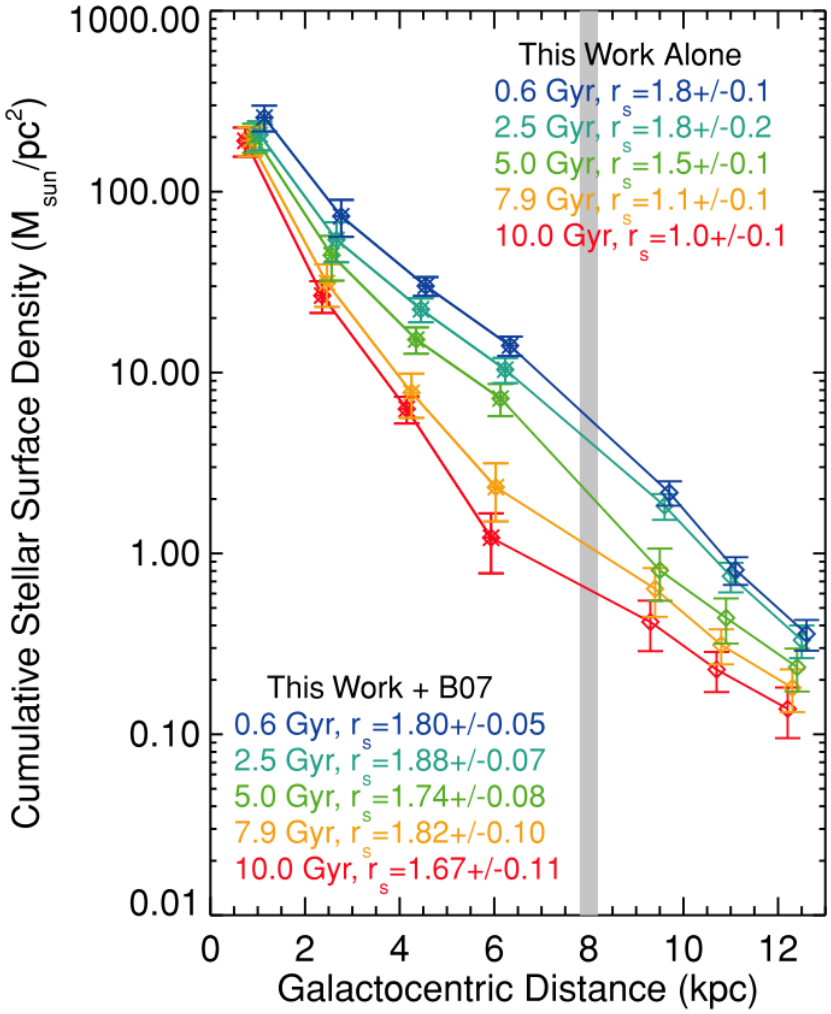

Figure 4.1: A figure reproduced from Williams et al. 2009 (their figure 4 left hand panel). M33 stellar surface densities are shown as a function of deprojected radius as computed from measured star formation histories (stars) and a reanalysis of the Barker et al. 2007a fields (diamonds). Different colours show the total stellar densities that would be observed at different lookback times, noted in the corners. The best-fit exponential scale length for each epoch using just the fields inside the disk break is listed in the upper right, and those using all of the fields are listed in the lower left. The young main sequence stars in M33 have a shorter scale length (Tiede et al., 2004; Teig, 2007). Data points have been offset from one another by 0.1 kpc to avoid overlapping error bars. The vertical grey line indicates the disk break measured by Ferguson et al. 2007. It may be noted that the disk break, a steepening of the profile is not seen in this work. The three datapoints outside the disk break are those from the Barker et al. 2007a work.

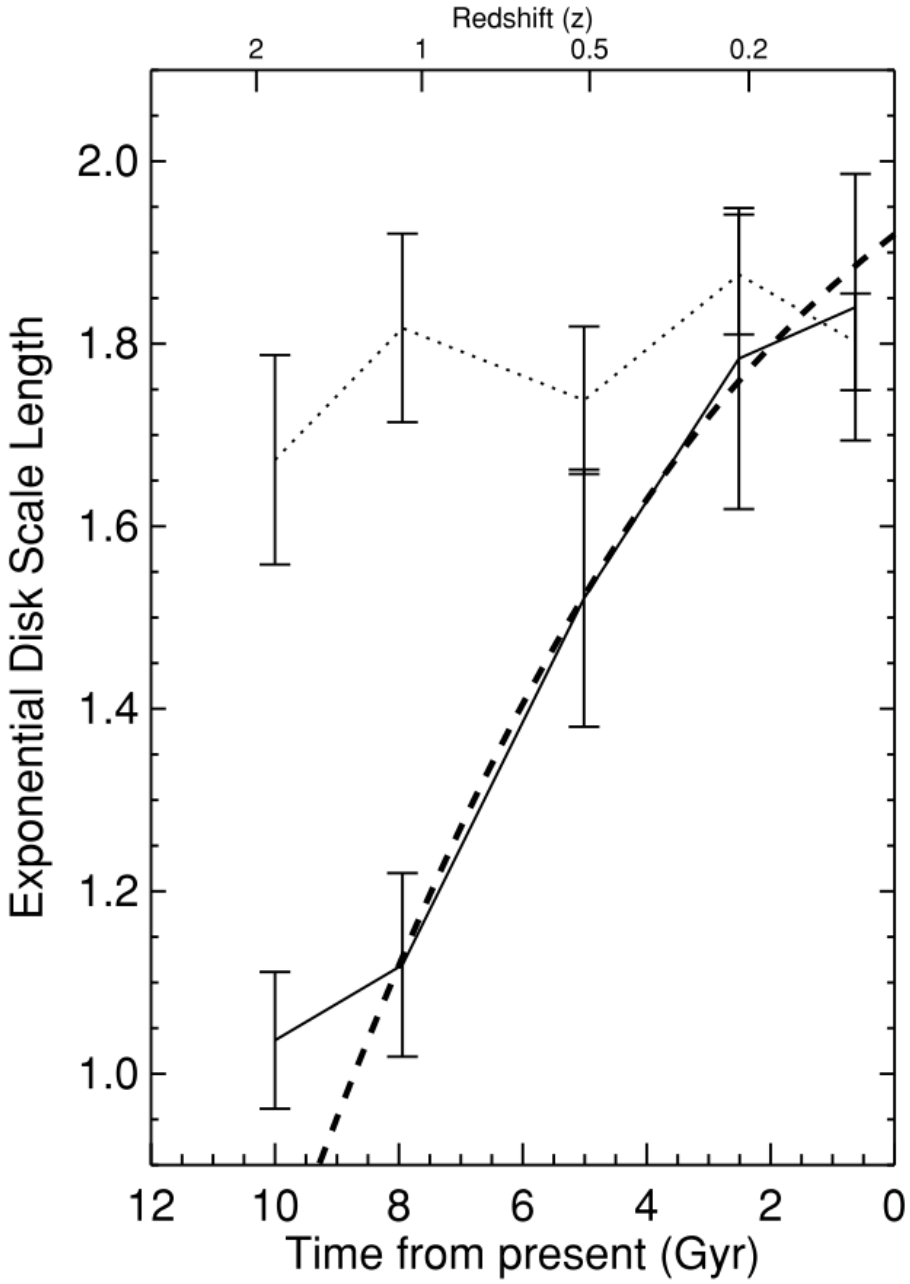

Figure 4.2: A figure reproduced from Williams et al. 2009 (their figure 4 centre panel). The disk scale length as a function of age inside the disk break (solid line) and from all fields (dotted line). The dashed line shows the scaling relation of Mo et al. 1998 normalised to their 5 Gyr measurement. The young main sequence stars in M33 have a shorter scale length.

Bayesian prior halo/disk	Output integrated halo/disk
0.1%	3.8 %
0.5%	6.9 %
1%	8.7 %
3%	12.2 %
5%	14.3 %
10%	18.1 %
15%	21.1 %
20%	23.8 %
25%	26.4 %
30%	28.8 %
simple windowing	17.0 %

Table 4.1: The exponential fits to the disk and halo DEIMOS counts are integrated and a total halo/disk figure is given for a range of Bayesian priors as well as the simple windowing method.

Photometric surveys limit the halo fraction to a few percent of the total luminosity of the galaxy, however in the fields observed spectroscopically by DEIMOS the fraction appears to vary between $\sim$ 10% and 30% in the region studied.

Teig 2008 claimed to detect the M33 halo photometrically. The profile in that work shows a single exponential disk, with a shallowing at 7-8 kpc projected which is interpreted as the halo becoming dominant. In contrast the work of Ferguson et al. 2007 shows a steepening at a radius of about 0.6 degrees (8 kpc projected) and the steep outer component dominating the profile out to at least 14 kpc.

The Teig profiles when integrated, produce a halo fraction of 5.5% overall and 28% in the range 5-12 kpc which is approximately the range of distances covered by our DEIMOS fields. This may be compared with the "halo" contribution observed in our DEIMOS fields in figures 3.14, 3.15 and the integrated "halo" in table 4.1. The Teig disk scale length is shorter than the general range of values given in the literature. The halo contribution obtained from integrating the profiles strongly depends on the disk scale length used. In any case, the tidal substructure observed by McConnachie et al. in the PAndAS survey means that the Teig work probably doesn't probe a "true" primordial halo.

Using the Bayesian method of classifying stars as "disk" or "halo", the halo contribution can be estimated by integrating exponential fits to the disk and halo counts in the DEIMOS fields. However the output halo contribution depends strongly on the priors that are put into the Bayesian formulae. The effect of changing the halo prior is shown in table 4.1. It is the case that all of these figures, are greater than the Purcell et al. theoretical expectation of 0.1%-1%. Most, excluding the 0.1% prior are greater than the "few percent" of Ferguson et al. 2007.

4.2.2 Theoretical expectations

Purcell et al. 2007 make theoretical predictions for the fraction of stellar mass in diffuse, intrahalo light. They predict, based on analytical models for subhalo infall and evolution that the stellar mass fraction in diffuse, intrahalo light should rise on average from $\sim$ 0.5% to $\sim$20% from small galaxy halos ($\sim 10^{11}M_{\odot}$) to poor groups ($\sim 10^{13}M_{\odot}$). This does not constitute a prediction for any individual galaxy, although it may be noted that M33's mass falls at the lower end of this range. The mass dependence of the diffuse light fraction is governed mainly by the fact that the mass to light ratio in galaxy halos varies as a function of

halo mass, galaxy halos having little diffuse light because they accrete most of their mass in small subhalos that themselves have high mass to light ratios.

The stellar halo of the Milky Way contributes $f_{\rm IHL} \sim 1\%$ of the Galaxy's total luminosity (references in Purcell et al. 2007), whereas the M31 halo may contribute somewhat more, perhaps $f_{\rm IHL} \sim 2.5\% - 5\%$. In M33, photometric data is consistent with a very low stellar mass fraction in the M33 diffuse halo, although a higher number of up to a few percent is not ruled out (Ferguson et al., 2007). Purcell et al. 2007 predict 0.1%-1% for halo contribution in a galaxy of M33's mass ($\sim 10^{11} {\rm M}_{\odot}$) (their figure 4).

Observations from this work

The integrated exponential fits to the "disk" and "halo" populations in table 4.1 all produce a halo fraction substantially greater than the 0.1% to 1% predicted by Purcell et al. 2007 for a galaxy of M33's mass. This would appear to indicate that if M33's halo is typical of galaxies of a similar size, the "halo" population in our DEIMOS fields is more dominated by a substructure population than a "true" primordial halo. Unless the substructure population can be somehow disentangled from the "true" halo, it is unlikely that the latter will be able to be constrained with any great accuracy.

4.3 Metallicity and age properties

As detailed in section 3.5 the position of a star in the colour-magnitude diagram (CMD) can be used, by comparison with isochrones, to estimate the metallicity of the star. However metallicity is not the only property that affects the star's position in the CMD. The age of the star, as well as the α-element abundance also are involved. In this work, we have assumed an age of 8 Gyr, [α/Fe] = +0.2 and used the Dartmouth isochrones (Dotter et al., 2008). The effect of the age and α assumptions on the photometric metallicity results are detailed in section 3.5.2. As stated in that section, a change in α of 0.1 dex will affect the metallicity result by approximately 0.04 dex at [Fe/H] = -1.5 and 0.1 dex at [Fe/H] = -0.5. A lower α mimics a lower metallicity and vice versa, the result of this being that if the α is lower than the assumed value, the measured [Fe/H] will be lower, both for low and high metallicity stars but more so for high metallicity stars, thus tending to flatten out metallicity gradients. A reasonable range for [α/Fe] may be 0.0 to +0.4 (see Beers et al. 2008 for a discussion of α-abundance in the Milky Way) in which case the metallicity may vary by 0.1-0.2 dex.

The effect of the age differing by 1 Gyr affects the metallicity by approximately 0.03-0.04 dex. A reasonable range for the age assumption of the RGB stars studied may be 5-12 Gyr, i.e. $\sim \pm$ 0.2 dex. A younger age mimics a lower metallicity, the effect being stronger for high metallicity stars, thus a younger age than assumed will tend to flatten observed [Fe/H] gradients and an older one to steepen them.

A couple of other factors that affect the [Fe/H] measurements are distance and reddening. The consequences for the observed [Fe/H]s of line of sight distance uncertainty and the possibility of variance of the systemic M33 distance are discussed in section 3.5.1 and for the spectroscopic [Fe/H]s section 3.6.2.

Reddening is caused by the differential absorption of light by interstellar dust (both within M33 and in our own Galaxy) of different wavelengths. Light from sight lines along which there is dust is preferentially absorbed at bluer wavelengths, thus causing the colour to be reddened. The reddening within our own Galaxy is relatively well known and M33 is not too close to the Galactic disk plane where the strongest

reddening occurs. See Schlegel et al. 1998 for maps of interstellar dust. A map of the extinction towards the M31 and M33 region of the sky is reproduced in Figure 3 of Ibata et al. 2007. Since the reddening is fairly well-known, it can be assumed that it is adequately corrected for by the pipeline used. It is however possible that internal reddening within M33 could have some effect, however this is hard to quantify because the extinction maps (e.g. Schlegel et al. 1998) are not fine enough in resolution to detect small scale variations in reddening. Hippelein et al. 2003 have published FIR maps of M33, but even these will not pick up small scale variations. Wilson et al. 1990 state there is some evidence for a radial gradient in the average internal reddening in M33, but the small scale variations remain unquantified.

In section 3.7 the observed metallicity of the various different fields was detailed and trends were plotted in Figures 3.34 and 3.35 for a 5% halo prior and 3.36 and 3.37 for simple windowing. The trends are also tabulated for these and other Bayesian halo priors in table 3.4.

There are negative metallicity trends in the disk population, significant at the 95% (2σ) level in photometric but not spectroscopic measurements. For the halo the trend is also negative, significant at the 2σ level in the spectroscopic but not photometric analysis. In both cases the trend is stronger in the spectroscopic analysis, although it is small enough in the disk population to not be significant at the 2σ level. These conclusions qualitatively hold regardless of the Bayesian prior and also in the case of simple windowing.

Chandar et al. 2002 analyse the kinematics of star clusters in M33, and find two distinct kinematic populations, which they argue represent the disk and halo populations, although individual stars belonging to a halo component in M33 had not been directly observed. Tiede et al. 2004 studied stellar populations in the outer regions of M33, finding a metallicity of [Fe/H] $\sim$ -1.0 in a field ranging in deprojected radius from around 8.5 to 12.5 kpc. They concluded this was predominantly a disk population. Barker et al. (Barker, 2007; Barker et al., 2007a,b; Barker & Sarajedini, 2008) wrote a series of papers focused on M33 which follow up this paper, again focusing on the region from 9-13 kpc in deprojected radius, also considering the population to be predominantly disk-related although a halo component is not ruled out.

4.3.1 Disk

Kim et al. 2002 from VI photometry in 10 HST/WFPC2 fields of RGB stars estimate there to be a metallicity gradient in the inner disk that follows the fit -0.55($\pm$0.02) - 0.05($\pm$0.01)R_{dp}. Their fields are located at radii between $2'.6$ and $17'.8$ projected ($3'.3$ and $18'.7$ deprojected, i.e. 0.8 kpc to 4.4 kpc with our distance assumption of 809 kpc). Teig, using the Padova isochrones (Girardi et al., 2000) constructed colour-magnitude diagrams including blue-plume main sequence and RGB/AGB stars. Teig concluded that in the inner disk of M33, the blue plume stars (i.e. young ($<$ 0.25 Gyr), bright main-sequence stars) must have metallicities of greater than [Fe/H] = -1.28 in order to avoid having a RGB that is too blue to fit the data, and the youngest (brightest) blue plume stars observed must have [Fe/H] $>$ -0.38. By discussing the slope of the isochrones, Teig estimates an upper bound on the metallicity of the blue plume of [Fe/H] = 0. Further out in the disk, Teig noticed that the brightest blue plume stars were fainter, and therefore older than in the inner disk. In the mid-disk, Teig estimates a metallicity range similar to the inner disk (-1.28 $<$ [Fe/H] $<$ 0) but a more even distribution compared to clustering at higher metallicities in the inner disk.

In the Teig "halo" field, very few blue plume stars were found, although Teig qualitatively argues that the blue plume that is found is older than further out in the disk. Teig argues that these are nevertheless halo stars, since at a projected radius of $>$ 7.3 kpc, their radius in the disk would be $>$ 12 kpc, which according

to the Teig scale length is 13 disk scale lengths. Nevertheless, even older blue plume stars would be very young for a halo population.

As far as the low mass RGB is concerned (more relevant for comparison to the current work), in the inner disk, Teig estimates the majority of red giants in M33 have metallicities -1.28 < [Fe/H]< -0.38. Although stars more metal-poor than [Fe/H] = -1.28 exist, such isochrones are not red enough even at old ages to cover the entire RGB. Stars at metallicities of [Fe/H] = -0.38 become too red to match the data at ages > 5 Gyr. In the mid-disk, the CMDs show a slightly narrower RGB, and therefore a narrower age and metallicity range than in the inner disk. In Teig's "halo" field , he finds a predominantly blue RGB, i.e. metal-poor, that spans a range between -2.02 < [Fe/H] < -0.78 according to globular cluster fiducials, with stars more likely to occupy the metal-poor end of the range.

Teig estimates the median metallicity of the mid-disk at [Fe/H] = -1.0, and the "halo" at [Fe/H] = -1.2, and states that this corresponds to a metallicity gradient of -0.027 dex kpc^{-1}.

The work by Barker et al. 2007a summarises the work done by themselves and others previously on the metallicity gradient of the M33 disk in their figure 20 (reproduced here as Figure 4.3). The size of the gradient in the M33 disk metallicity was estimated in that work as 0.01875/1′ (deprojected). 1′ (deprojected) $\sim$ 0.25 kpc (with their distance assumption of 867 kpc). Therefore they estimated a metallicity trend of 0.074 dex kpc^{-1} (deprojected). Barker et al. 2007b estimate, by CMD modelling by linear combinations of individual synthetic populations that in the fields they studied the mean age increases with radius from $\sim$ 6 Gyr to $\sim$ 8 Gyr and mean metallicity decreases from [M/H] $\sim$-0.7 to $\sim$ -0.9. This would represent a metallicity gradient of -0.05 dex kpc^{-1} (deprojected), -0.08 dex kpc^{-1} projected. Thus the outer disk shows a metallicity gradient consistent with that found by Kim et al. 2002 in the inner disk. Williams et al. 2009 used stellar photometry from four Hubble ACS fields along the major axis of the M33 disk and detailed CMD modeling, and found that the percentage of stellar mass formed prior to $z = 1$ (i.e. more than a lookback time of 7.7 Gyr in the concordance cosmology) changes from 71 $\pm$ 9% in the innermost field to 16 $\pm$ 6% in the outermost one. In their work, the estimated the disk scale length has grown from $r_s = 1.0 \pm 0.1$ kpc 10 Gyr ago to $r_s = 1.8 \pm 0.1$ at times more recent than 5 Gyr ago. Barker et al. 2010 present work on two further ACS fields located at 9.1 kpc and 11.6 kpc along M33's northern major axis. In the inner field S1, the mean age is $\sim 3 \pm 1$ Gyr and the mean metallicity is [M/H] $\sim -0.5 \pm 0.2$ dex. In the outer field S2, the mean age is $\sim 7 \pm 2$ Gyr and mean [M/H] $\sim -0.8 \pm 0.3$ dex. S2 contains $\sim$ 30 times less stellar mass. This shows that the "inside-out" disk growth that was previously measured for the inner disk of M33 extends out to the disk edge at $\sim$ 9 kpc.

Our photometric and spectroscopic results both show a smaller gradient than the Barker et al. 2007a result. For the 5% halo prior, the photometric disk metallicity trend is [Fe/H] = -0.8 - 0.024r and the spectroscopic is [Fe/H] = -0.63 - 0.038r. The spectroscopic trend is not significant at the 2σ level, i.e. is consistent with constant, although the photometric trend is significant at that level. The overall median photometric [Fe/H] for the "disk" sample in all fields is -0.96 (at 5% Bayesian prior - quality cut data). The weighted mean of the spectroscopic [Fe/H] (CaT2 only) of the stacked spectra is -0.93 for the same prior.

Tiede et al. 2004 and the Barker et al. papers have assumed an M33 distance of 867 kpc, Chandar et al. 2002 have assumed 847 kpc, Kim et al. 2002 determine one of 916 kpc, and Teig 2008 assume 809 kpc (the same as in this work). Due to the change in the slope of the isochrones with metallicity, a differential effect on the photometric metallicities exists that modifies metallicity gradients depending on the distance assumption. This is a stronger effect at the highest metallicities and α-abundances. Therefore if a larger

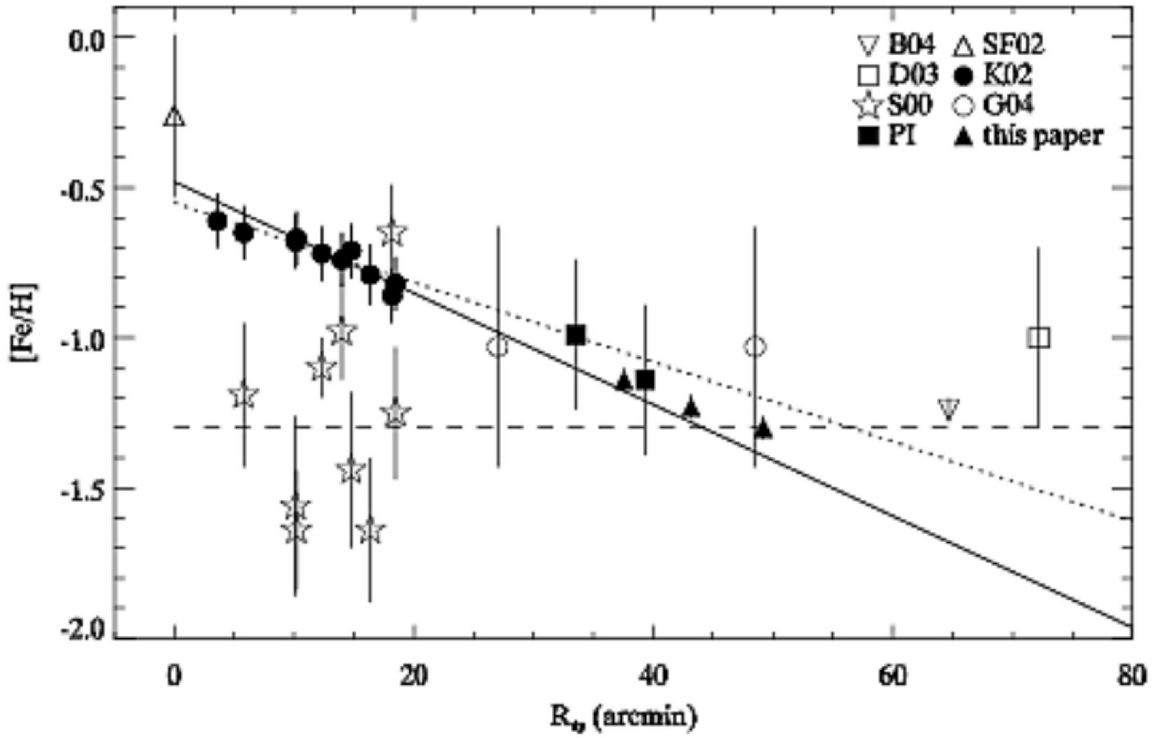

Figure 4.3: A figure reproduced from Barker et al. 2007a (their Figure 20). This figure shows the RGB metallicity gradient based on their own work along with other work from the literature. S00 = Sarajedini et al. 2000, K02 = Kim et al. 2002, SF02 = Stephens & Frogel 2002, D03 = Davidge 2003, B04 = Brooks et al. 2004, G04 = Galleti et al. 2004, PI = Tiede et al. 2004 (referred to as Paper I).

distance modulus is assumed, the tendency will be to measure a steeper metallicity gradient. It is possible that the M33 distance modulus may be up to 0.3 mag larger than our assumption, if this were the case, at a metallicity of -0.5 and α of +0.2, the change in metallicity due to the change in distance assumption is 0.2 dex, where at [Fe/H] = -2.0 it is 0.08 dex. See also section 3.5.1.

The mass metallicity relation was measured for SDSS galaxies by Vale Asari et al. 2009.M33 has approximately $10^{10}M_{\odot}$ of stellar mass, according to their figure 2 showing the mass-metallicity relation it would be expected to have a disk metallicity of about -0.1, which is rather higher than is observed by ourselves and others. Thus M33 may be considered a low-metallicity galaxy.

4.3.2 Halo

Sarajedini et al. 2006 studied RR Lyrae variables in M33 in a Hubble ACS field located at $R_{dp} \sim 15'$, finding two populations which they identify as disk and halo components. They found the RR Lyrae metallicity distribution exhibited a pronounced peak at [Fe/H] $\sim$ -1.3 which was interpreted as corresponding to the field halo population. A previous study, Sarajedini et al. 2000 had focused on halo clusters for which they derived a metallicity of $<$[Fe/H]$>$ = -1.27 $\pm$ 0.11, with no evidence for a gradient. The peak of the metallicity distribution of the supposed field halo RR Lyrae stars is consistent with this. Brooks et al. 2004 constructed a radial stellar density profile out to 1 degree from the centre of M33, corresponding to a projected distance of 16 kpc. They determine a peak metallicity for the halo of M33 of [Fe/H] = -1.24 $\pm$ 0.04.

McConnachie et al. 2006 presented initial spectroscopic work in this galaxy finding 11 candidate halo stars which exhibited an average [Fe/H] $\sim$ -1.5, distinct in both velocity and colour from the strongly peaked disk populations in the same spectroscopic fields. Ibata et al. 2007 and McConnachie et al. 2009 present wide field photometry of this galaxy taken with the CFHT-MegaCam, showing faint extended emission and possible tidal tails dominating the radial profile of M33 at large radius, implying the presence of an extended stellar component in M33. McConnachie et al. 2010 show the presence of a large substrcture around M33, which they take as evidence that the Triangulum galaxy has interacted with Andromeda, and this substructure has its origin in tidal interactions. It is possible that the original halo of Triangulum may have been stripped off entirely, and studies of the "halo" of Triangulum are sampling this substructure population. See section 4.4 for a discussion of this hypothesis.

Our photometric and spectroscopic results both show a negative gradient in the "halo" population. For the 5% halo prior, the photometric "halo" metallicity trend is [Fe/H] = -0.80 - 0.044 and the spectroscopic is [Fe/H] = -0.35 - 0.137r. The photometric trend is indeed larger in magnitude (although not significantly so in a statistical sense) than those we observed in the "disk" population. However because of the greater uncertainties (a smaller number of stars), the photometric trend is not significant at the 2σ level, although the spectroscopic one is. This result, that there is a trend in the spectroscopic metallicity significant at 2σ level, is in disagreement with that found for the "disk" population. The overall median photometric [Fe/H] for the "halo" sample in all fields is -1.06 (at 5% Bayesian prior - quality cut data). The weighted mean of the (CaT2 only) stacked spectra [Fe/H]s is -1.37 for the same prior.

4.4 Modelling of a possible interaction between M31 and M33

In this section, the possibility that some interaction has taken place between M33 and M31 is examined. Such an interaction may have been the origin of the substructure population discovered in McConnachie et al. 2009 and examined in McConnachie et al. 2010. Much of what has been characterised in this work as the "halo" sample may in fact have its origin in this substructure.

Putman et al. 2009 discuss M33's spatial and kinematic structure in neutral hydrogen gas (H I). They observe that the H I gas extends well beyond the edge of the star-forming disk as traced in far-ultraviolet (FUV) observations. They observe warps, an arc from the northern warp to the disk, diffuse gas surrounding the galaxy, and a southern cloud with a filament back to the galaxy. These features are observed to extend 22 kpc from the galaxy centre. (they assume M33 is $\sim$ 730 kpc from the Milky Way). They hypothesise that these features of M33's gaseous structure originate from tidal disruption of M33 by M31 1-3 Gyr ago.

The usual assumption is that M31 and M33 are gravitationally bound, and that M33 can be considered as M31's largest satellite galaxy. Loeb et al. 2005 constrain M31's proper motion based on the observation that M33's disk has not been disrupted within the past 10 Gyr. van der Marel & Guhathakurta 2008 estimate the M31 transverse velocity by constraints from line-of-sight velocities of M31 satellites, proper motions of M31 satellites (M33 and IC10), and line-of-sight velocities of other Local Group galaxies. They find the probability distribution for V_{tan} has a median value of 42 km s^{-1}, and a 1 σ confidence interval $V_{tan} < 56$ km s^{-1}. Combining their estimate of the tangential velocity with likely mass estimates of the Local Group, they conclude the Local Group is gravitationally bound, and that M31 and M33 are also tightly bound. They conclude that some tidal disruption of M33 by M31 is likely to have occured.

A significant tidal interaction between M31 and M33 that could have produced the gaseous features observed is only possible if past orbits brought the two galaxies closer to each other. M33's orbital history may be constrained by integrating the motion of M33 backwards in time through M31's evolving potential. The proper motion of M33 has been measured (Brunthaler et al., 2005) and the radial velocities of both galaxies are well known, the tangential velocity of M31 is however unknown. Putman et al. 2009 calculated a large set of orbits using tangential velocity components for M31 ranging from -200 to +200 km s^{-1}. Since the Local Group is a relatively poor group, higher velocities are unlikely, and would violate the timing argument.

M33 is treated as a point mass orbiting in the combined gravitational potential of M31 and the Milky Way. The mass distribution of M31 is modelled as the sum of a disk and dark matter halo with a total virial mass of $M_{vir}(0) = 2 \times 10^{12} M_\odot$ at redshift $z = 0$. A disk mass of $M_d(0) = 4 \times 10^{10} M_\odot$ was adopted. The halo, which was shown to play the larger role in determining the orbits of M33 was modelled as a Navarro-Frenk-White profile with concetration parameter $c = 12$ at $z = 0$, in line with expectations from Λ Cold Dark Matter (ΛCDM) simulations. This results in a scale radius of $r_s \approx 25$ kpc. The outer mass distribution of M31 is not particularly well constrained and best estimates differ by a factor of a few (Loeb et al., 2005; van der Marel & Guhathakurta, 2008; Fardal et al., 2007; Seigar et al., 2008). Fardal et al. 2007 find a concentration $c \sim 30$.

Putman et al. 2009 found no plausible orbits for M33 coming closer than 60 kpc, therefore the size of the baryon contribution in the disk was relatively unimportant. It is assumed the disk mass of M31 scales linearly with cosmic time and the halo mass grows exponentially. Most orbits find the last close passage between M33 and M31 in the last 3 Gyr, which means the evolution of gravitational potential with redshift is relatively unimportant. The Milky Way's potential is treated as point mass of $10^{12} M_\odot$ and turns out to

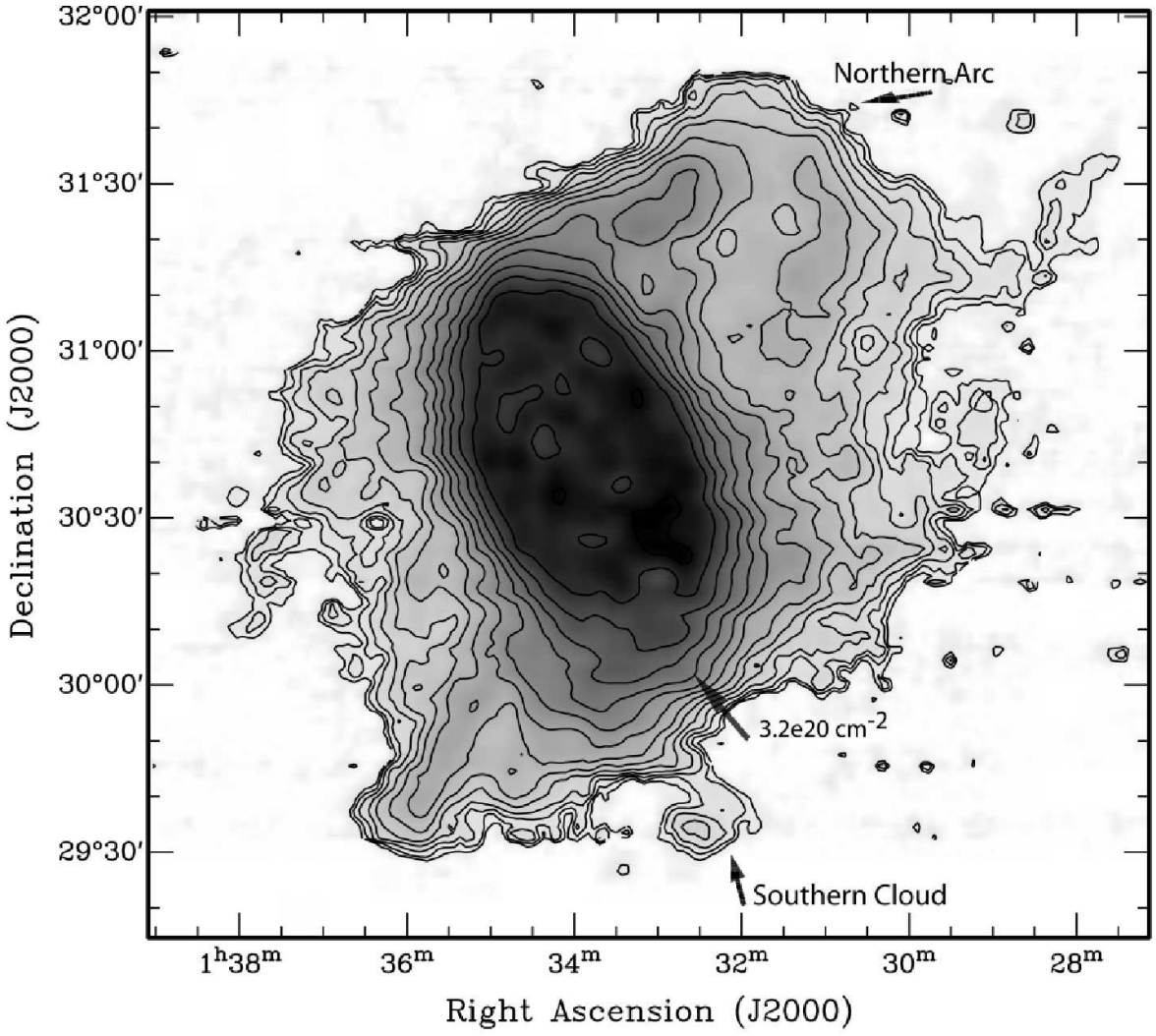

Figure 4.4: A figure reproduced from Putman et al. 2009 (their Figure 1) showing the H I column density in M33. Contours are $8.3 \times 1.5^n \times 10^{18}$ cm^{-2} where n = 0...13 and 8.3×10^{18}cm^{-2} being 5σ to a 25 km s^{-1} feature. The maximum contour is at 1.6×10^{21}cm^{-2}. The beam is 3′.4 which is (according to their distance assumption) 720 pc at the M33 distance

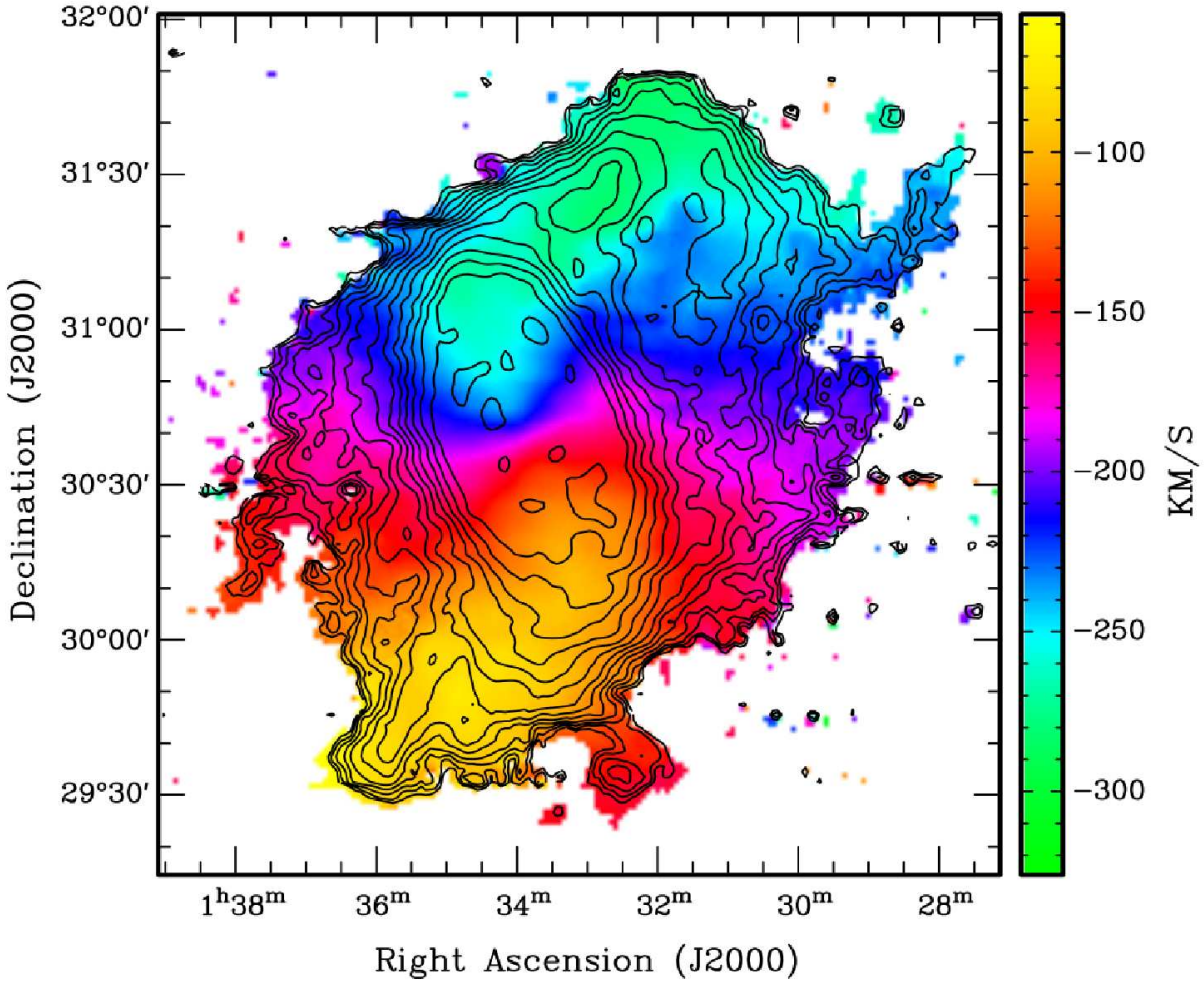

Figure 4.5: A figure reproduced from Putman et al. 2009 (their Figure 4) showing the intensity weighted velocity (LSR) of the M33 gas with the H I column density contours from figure 4.4 overlaid.

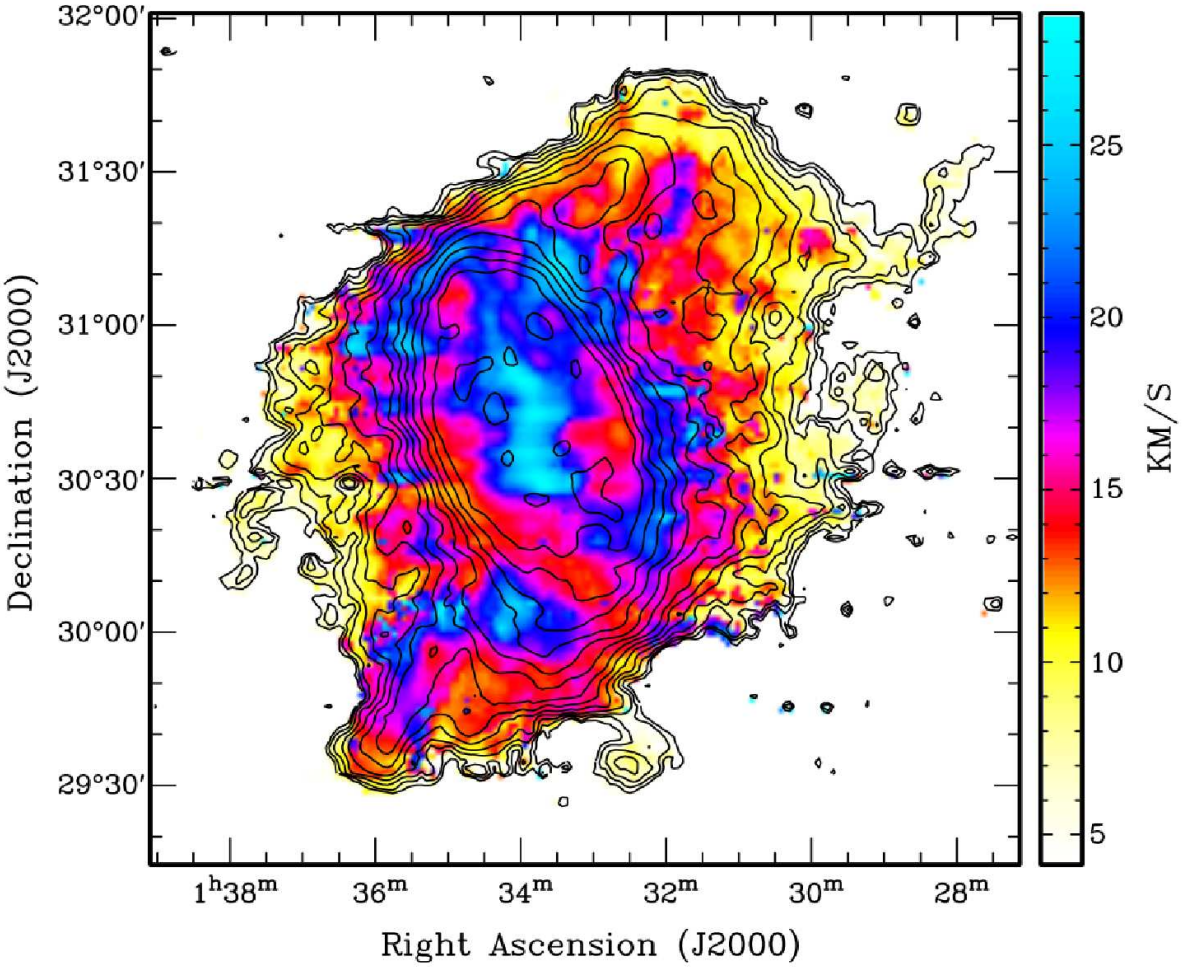

Figure 4.6: A figure reproduced from Putman et al. 2009 (their Figure 5) showing the intensity weighted velocity dispersion map of M33 with H I column density contours from 4.4 overlaid.

have negligible effect due to its large distance. Dynamical friction is included although in the Putman et al. 2009 model this effect is also small since M33 does not get close enough to M31 for it to play a large role. The tidal radius of M33 is estimated at $r_t \approx 0.15 R_p$ where R_p is the perigalactic distance between M31 and M33.

It is shown that there is a 60% probability of the galaxies being once closer than 100 kpc to each other, implying a tidal radius of M33 below 15 kpc. A couple of figures from Putman et al. 2009 describing the possible orbits of M33 with respect to M31 are reproduced in Figures 4.7 and 4.8.

To compare these two hypotheses, it is worth examining the consequences of each being true, and the likely impact this would have on what should be observed in terms of metallicity and kinematics of the stellar populations.

Given the likelihood of an approach between M31 and M33 resulting in a tidal radius of M33 $<$ 15 kpc, the extensive gaseous features observed around M33 are likely to have been pulled from the outer disk during this passage. the gaseous disks of spiral and dwarf galaxies are commonly found to extend beyond the stellar components (Meurer et al., 1996; Begum et al., 2005) and will be the first thing stripped. Depending on the closeness of the interaction, it is also possible that stellar components will also be stripped.

Cockcroft et al. 2011 study the M33 area using the PAndAS data, searching an area of more than 40 square degrees of the halo of M33 in a search for outer halo clusters using both automated search and visual inspection. Only one new cluster was found in this work, which is smaller, fainter and slightly redder than the three INT clusters found by Huxor et al. 2009 and the Stonkutė et al. 2008 cluster. Although it lies within the INT area of Huxor et al. 2009 it was not recognised due to its small size and low luminosity. It lies at a projected radius of 22 kpc, close to the feature observed in the stellar substructure (McConnachie et al. 2010). This brings the total outer halo clusters in M33 (between projected radii of 9 kpc $\leq$ r $\leq$ 50 kpc and to $g'_{lim} \approx 20$ to six. There are 2440 cluster candidates of various degrees of confidence identified in this paper of which the vast majority are expected to be background contaminants.

In contrast M31 has 67 known outer halo clusters which are located at projected radius 30 kpc $\leq r \leq$ 130 kpc (Mackey et al., 2010). Huxor et al. 2009 found a GC surface density in M33 of ~ 0.4 deg^{-2} in their 12 deg^2 study, which they noted was about half that derived for M31 over 30 kpc $\leq r \leq$ 130 kpc. An even lower figure of 0.15 deg^{-2} is derived in Cockcroft et al. 2011.

One of the hypotheses put forward for the relative lack of outer halo clusters is that some of M33's outer halo clusters were stripped off in a previous dynamical interaction with M31. Huxor et al. 2009 noted the apparent asymmetry in the distribution of the outer clusters in M33, venturing the hypothesis that tidal interactions with M31 may have produced this asymmetry. (Huxor et al., 2009; San Roman et al., 2010)

4.5 The "halo" population - genuine stellar halo or stripped disk material?

It may be asked therefore, if the "halo" sample we have detected spectroscopically is a genuine M33 halo population. If the M33 disk has been stripped to a certain extent in interaction with M31, then what we are observing as "halo" may in fact be derived from the M33 disk.

Based on the observation that the halo and disk exponential fits contribute rather a greater halo/disk ratio than would be expected from previous photometric surveys (see table 4.1), it appears to be the case

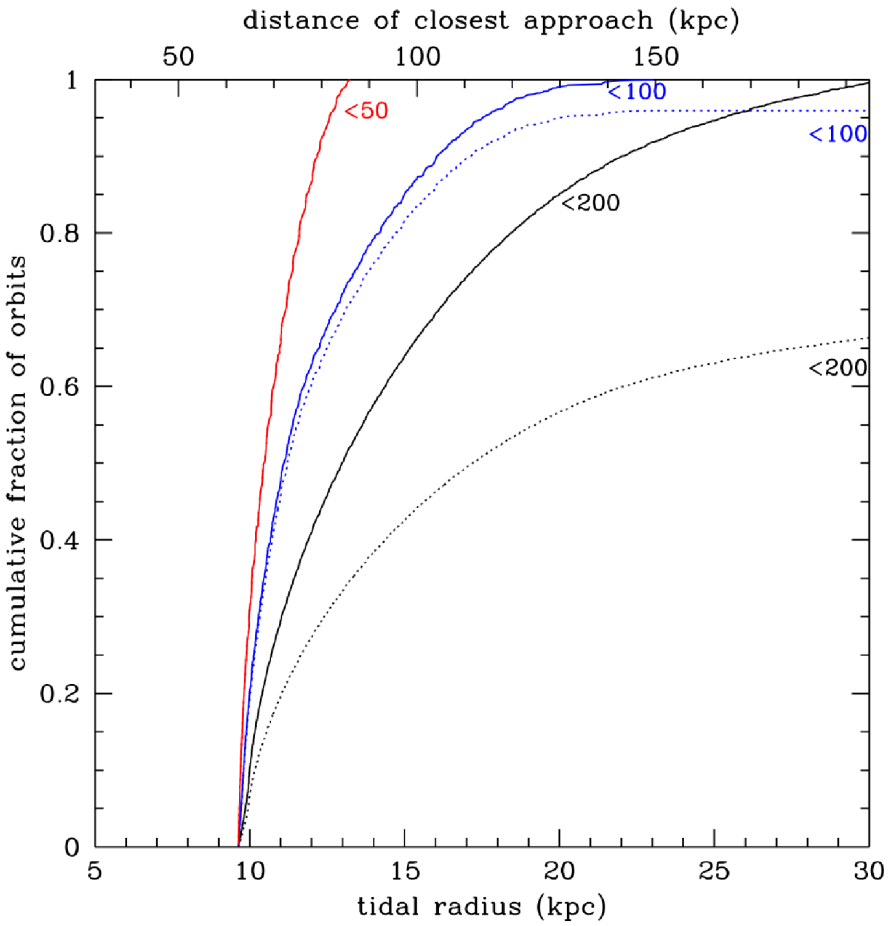

Figure 4.7: A figure reproduced from Putman et al. 2009 (their Figure 10) showing the cumulative fraction of orbits that result in the tidal radius for M33 noted on the bottom x-axis and the distance of closest approach between M31 and M33 (perigalacticon) noted on the top x-axis. The three different pairs of lines show subsets of orbits with the maximum tangential velocity of M31 restricted to be below 50, 100 and 200 km s^{-1}, respectively. The solid lines are for orbits that had a perigalacticon closer than M33's current separation ($\sim$ 200 kpc) and the dashed lines represent the total grid of orbits.

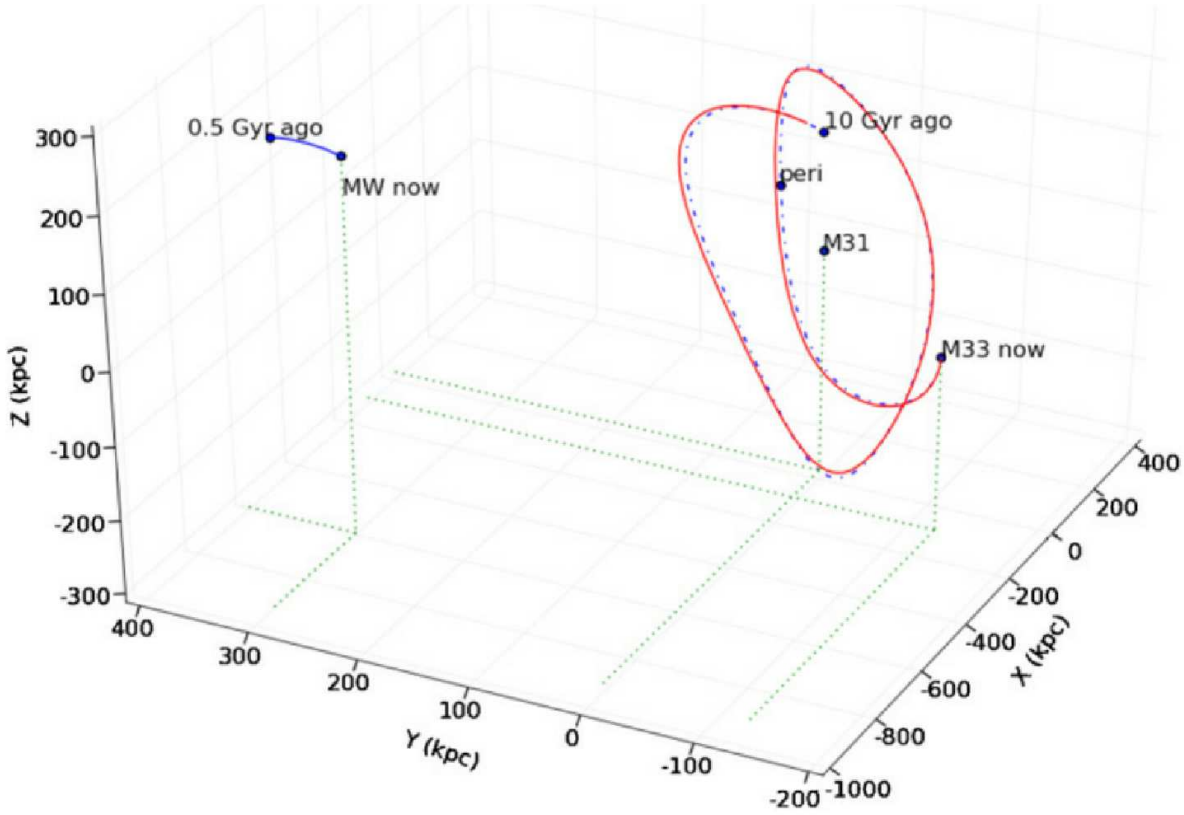

Figure 4.8: A figure reproduced from Putman et al. 2009 (their Figure 11) showing a three-dimensional representation of a typical possible orbit of M33 shown in the M31 reference frame. The solid line shows M33's orbit when the Milky Way potential is included and the dashed line shows the orbit when it is excluded. "peri" marks the closest approach of M33 to M31 ($\sim$ 10 kpc) on this orbit 1.6 Gyr ago. The Milky Way moves outside the plotted box after only $\approx$ 0.5 Gyr in the past and has little influence on the orbit.

that what is being observed in our "halo" sample is not a true, primordial halo but some other population. The "halo" metallicity gradient, significant at 2σ in the spectroscopic analysis, may also be evidence that we are not observing a "true" halo population.

Another possibility to consider is that the substructure could have originated from the disruption of a dwarf satellite galaxy. However, this is not likely if M33 has indeed interacted closely with M31 with a tidal radius < 15 kpc, since it is unlikely such a satellite would have remained bound. The work by Cockcroft et al. 2011 indicating a relative lack of outer halo clusters in M33 indicates that the interaction would have tidally stripped any dwarf satellites that may have been found around M33.

Therefore the overall conclusion is that the substructure we observe is likely to be a tidal substructure, i.e. the material is likely to have been stripped from the M33 disk. This is supported by its relatively high overall metallicity, (median of [Fe/H] = -1.06, "halo" sample 5% Bayesian prior), not much different from the "disk" sample (median of [Fe/H] = -0.96), compared to what might be expected from a metal poor halo. See figure 3.29 where the metallicity distribution functions of the "disk" and "halo" are presented.

Appendix A

Summary of M31 DEIMOS Fields

Field	Median RA	Median Dec	Total N targets	Observing run
04Disk	$00^h47^m30^s.7$	$42°32^m04^s.5$	154	2003 Sep
06Disk	$00^h50^m29^s.7$	$42°42^m18^s.1$	133	2003 Sep
101Dis	$00^h38^m01^s.7$	$39°54^m36^s.7$	276	2004 Sep
102Dis	$00^h37^m58^s.9$	$40°01^m11^s.3$	269	2004 Sep
104Dis	$00^h38^m43^s.4$	$40°20^m33^s.2$	272	2004 Sep
105Dis	$00^h38^m58^s.8$	$40°28^m44^s.8$	272	2004 Sep
106Dis	$00^h39^m03^s.7$	$40°39^m37^s.0$	258	2004 Sep
107Ext	$00^h35^m26^s.7$	$39°36^m44^s.7$	266	2004 Sep
108Ext	$00^h39^m58^s.5$	$39°22^m34^s.4$	257	2004 Sep
109Ext	$00^h40^m01^s.5$	$39°47^m49^s.6$	251	2004 Sep
110Hal	$00^h31^m41^s.7$	$38°50^m22^s.0$	132	2004 Sep
111Hal	$00^h31^m55^s.4$	$39°02^m33^s.6$	119	2004 Sep
123Glo	$00^h58^m20^s.8$	$38°02^m57^s.5$	100	2005 Oct
124Glo	$00^h58^m11^s.8$	$38°05^m00^s.4$	104	2005 Sep
131Dis	$00^h46^m15^s.5$	$42°07^m05^s.2$	287	2005 Oct
134Dis	$00^h47^m25^s.7$	$42°22^m37^s.0$	276	2005 Oct
135Dis	$00^h49^m11^s.4$	$42°33^m25^s.9$	213	2005 Oct
137Dis	$00^h50^m02^s.2$	$42°50^m05^s.4$	259	2005 Oct
138Dis	$00^h50^m07^s.0$	$42°54^m32^s.6$	264	2005 Oct
148Ext	$00^h37^m10^s.2$	$39°13^m02^s.5$	212	2005 Sep
14Disk	$00^h48^m34^s.3$	$43°04^m05^s.4$	60	2004 Sep
150Ext	$00^h49^m19^s.3$	$43°27^m40^s.3$	229	2005 Sep
151Ext	$00^h52^m05^s.8$	$43°38^m24^s.0$	197	2005 Sep
152Ext	$00^h52^m01^s.9$	$43°46^m51^s.0$	209	2005 Sep
153Ext	$00^h43^m48^s.8$	$40°24^m21^s.8$	179	2005 Sep
165Dis	$00^h46^m46^s.2$	$42°12^m44^s.4$	268	2005 Oct
166Dis	$00^h39^m15^s.5$	$40°42^m41^s.6$	210	2005 Oct
167Hal	$00^h34^m26^s.9$	$39°24^m57^s.9$	205	2005 Oct
168Hal	$00^h34^m28^s.6$	$39°04^m20^s.3$	167	2005 Oct
17Disk	$00^h45^m33^s.1$	$41°26^m18^s.9$	146	2004 Sep
18Disk	$00^h46^m36^s.1$	$42°00^m26^s.5$	214	2004 Sep
50Disk	$00^h37^m45^s.7$	$39°34^m46^s.8$	217	2004 Sep
51Disk	$00^h47^m32^s.6$	$42°20^m56^s.9$	173	2004 Sep
52Disk	$00^h46^m35^s.2$	$42°09^m40^s.3$	199	2004 Sep
53Blob	$00^h53^m26^s.3$	$43°14^m06^s.5$	138	2004 Sep

54Blob	$00^h39^m54^s.9$	$42°19^m39^s.3$	178	2004 Sep
55Blob	$00^h52^m20^s.2$	$44°07^m21^s.2$	126	2004 Sep
56Blob	$00^h50^m17^s.0$	$41°26^m21^s.5$	163	2004 Sep
57Halo	$00^h48^m29^s.7$	$40°20^m24^s.6$	94	2004 Sep
59Halo	$00^h55^m01^s.7$	$39°44^m22^s.4$	86	2004 Sep
s01old	$00^h52^m44^s.0$	$37°18^m12^s.2$	69	2002 Sep
s02old	$00^h51^m33^s.4$	$37°44^m29^s.1$	68	2002 Sep
s06old	$00^h46^m26^s.3$	$39°31^m20^s.6$	78	2002 Sep
s08old	$00^h43^m50^s.2$	$40°23^m41^s.3$	89	2002 Sep
s24old	$00^h49^m31^s.9$	$36°18^m48^s.5$	129	2003 Sep
s26old	$00^h45^m48^s.9$	$38°27^m37^s.7$	144	2003 Sep
s27old	$00^h48^m32^s.8$	$38°41^m45^s.4$	145	2003 Sep
w11old	$00^h35^m30^s.7$	$39°35^m57^s.9$	96	2002 Sep
w42old	$00^h50^m07^s.5$	$41°38^m38^s.5$	78	2002 Sep
w72old	$00^h35^m04^s.2$	$40°16^m47^s.9$	89	2002 Sep
w80old	$00^h36^m46^s.5$	$41°17^m03^s.7$	77	2002 Sep
w91old	$00^h41^m08^s.6$	$42°34^m13^s.6$	87	2002 Sep
w95old	$00^h45^m40^s.7$	$43°00^m12^s.9$	97	2002 Sep
213Dis	$00^h37^m49^s.2$	$40°07^m08^s.5$	156	2006 Sep
220Dis	$00^h37^m58^s.0$	$40°06^m59^s.3$	323	2006 Sep
221Dis	$00^h37^m12^s.2$	$39°45^m40^s.8$	304	2006 Sep
222Dis	$00^h37^m14^s.6$	$39°48^m55^s.1$	299	2006 Sep
223Dis	$00^h37^m13^s.6$	$39°57^m37^s.2$	305	2006 Sep
224Dis	$00^h38^m48^s.3$	$40°20^m59^s.0$	266	2006 Sep
227Dis	$00^h39^m36^s.2$	$40°51^m14^s.6$	313	2006 Sep
228Dis	$00^h40^m53^s.8$	$40°44^m22^s.1$	302	2006 Sep
230Dis	$00^h46^m47^s.1$	$42°12^m32^s.2$	280	2006 Sep
231Dis	$00^h38^m00^s.0$	$40°01^m02^s.2$	186	2006 Sep
232DiS	$00^h38^m49^s.2$	$40°20^m28^s.3$	185	2006 Sep
233Blo	$00^h46^m33^s.6$	$33°47^m04^s.4$	29	2006 Sep
234Blo	$00^h47^m33^s.9$	$34°23^m22^s.8$	47	2006 Sep
235Blo	$00^h52^m16^s.5$	$32°59^m55^s.1$	42	2006 Sep
305Tan	$01^h00^m33^s.7$	$38°46^m15^s.7$	103	2007 Oct
306Tan	$00^h57^m34^s.6$	$39°50^m08^s.3$	101	2007 Oct
402TaS	$00^h58^m58^s.1$	$40°21^m07^s.4$	108	2008 Sep
405HaS	$01^h13^m20^s.0$	$37°04^m21^s.2$	76	2008 Sep
406HaS	$01^h13^m23^s.9$	$37°09^m34^s.9$	75	2008 Sep
407HaS	$01^h13^m32^s.1$	$37°17^m00^s.0$	137	2008 Sep
415DiS	$00^h38^m08^s.9$	$40°05^m48^s.2$	189	2008 Oct
416DiS	$00^h40^m06^s.3$	$40°46^m17^s.2$	205	2008 Oct
418DiS	$00^h40^m06^s.9$	$40°33^m22^s.0$	218	2008 Oct
503HaS	$00^h23^m58^s.4$	$37°31^m12^s.7$	70	2009 Oct
504HaS	$00^h24^m01^s.5$	$37°21^m05^s.6$	72	2009 Oct
505HaS	$00^h12^m56^s.6$	$45°00^m59^s.4$	99	2009 Oct
506HaS	$00^h15^m58^s.7$	$43°58^m37^s.2$	97	2009 Oct
507HaS	$00^h18^m01^s.3$	$43°07^m04^s.7$	93	2009 Oct
515DiS	$00^h40^m07^s.8$	$40°33^m24^s.0$	216	2009 Oct
Total			14067	

Table A.1: The DEIMOS fields around M31 that have been reduced.

Appendix B

[Fe/H] results for various combinations of CaT lines

Halo prior (%)	Sub-population	Method	Fit for [Fe/H](r)	Lower 2σ confidence	Upper 2σ confidence	(Weighted) mean [Fe/H]
5	halo	photometric	-0.8 - 0.044r	-0.131	0.043	-1.07
5	halo	spec (CaT2)	-0.35 - 0.137r	-0.234	-0.039	-1.37
5	halo	spec (CaT23)	-0.22 - 0.118r	-0.277	0.041	-1.1
5	halo	spec (CaT12)	-0.71 - 0.108r	-0.213	-0.004	-1.53
5	halo	spec (CaT123)	-0.24 - 0.125r	-0.263	0.012	-1.23
5	disk	photometric	-0.8 - 0.024r	-0.038	-0.010	-0.97
5	disk	spec (CaT2)	-0.63 - 0.038r	-0.092	0.015	-0.93
5	disk	spec (CaT23)	-0.84 - 0.017r	-0.171	0.138	-0.96
5	disk	spec (CaT12)	-0.88 - 0.029r	-0.117	0.059	-1.17
5	disk	spec (CaT123)	-0.78 - 0.022r	-0.137	0.093	-0.96
3	halo	photometric	-0.75 - 0.042r	-0.133	0.049	-1.06
3	halo	spec (CaT2)	-0.37 - 0.136r	-0.231	-0.041	-1.40
3	halo	spec (CaT23)	-0.25 - 0.114r	-0.262	0.033	-1.13
3	halo	spec (CaT12)	-0.74 - 0.108r	-0.203	-0.012	-1.60
3	halo	spec (CaT123)	-0.28 - 0.122r	-0.254	0.010	-1.27
3	disk	photometric	-0.8 - 0.024r	-0.039	-0.009	-0.97
3	disk	spec (CaT2)	-0.64 - 0.038r	-0.092	0.015	-0.93
3	disk	spec (CaT23)	-0.83 - 0.018r	-0.174	0.138	-0.96
3	disk	spec (CaT12)	-0.88 - 0.029r	-0.116	0.059	-1.17
3	disk	spec (CaT123)	-0.77 - 0.023r	-0.139	0.093	-0.96
1	halo	photometric	-0.82 - 0.048r	-0.128	0.032	-1.11
1	halo	spec (CaT2)	-0.45 - 0.128r	-0.216	-0.041	-1.46
1	halo	spec (CaT23)	-0.42 - 0.096r	-0.215	0.023	-1.22
1	halo	spec (CaT12)	-0.80 - 0.103r	-0.202	-0.004	-1.66
1	halo	spec (CaT123)	-0.43 - 0.106r	-0.223	0.011	-1.37
1	disk	photometric	-0.78 - 0.026r	-0.042	-0.011	-0.97
1	disk	spec (CaT2)	-0.64 - 0.039r	-0.092	0.014	-0.93
1	disk	spec (CaT23)	-0.82 - 0.021r	-0.180	0.137	-0.96
1	disk	spec (CaT12)	-0.88 - 0.029r	-0.115	0.057	-1.17
1	disk	spec (CaT123)	-0.76 - 0.026r	-0.143	0.091	-0.96
0.5	halo	photometric	-0.87 - 0.045r	-0.120	0.030	-1.14
0.5	halo	spec (CaT2)	-0.5 - 0.122r	-0.204	-0.039	-1.49

0.5	halo	spec (CaT23)	-0.53 - 0.082r	-0.188	0.024	-1.28
0.5	halo	spec (CaT12)	-0.84 - 0.099r	-0.198	0.000	-1.70
0.5	halo	spec (CaT123)	-0.87 - 0.045r	-0.120	0.030	-1.42
0.5	disk	photometric	-0.77 - 0.028r	-0.046	-0.010	-0.97
0.5	disk	spec (CaT2)	-0.64 - 0.039r	-0.092	0.014	-0.94
0.5	disk	spec (CaT23)	-0.87 - 0.004r	-0.153	0.145	-0.93
0.5	disk	spec (CaT12)	-0.89 - 0.029r	-0.114	0.056	-1.18
0.5	disk	spec (CaT123)	-0.77 - 0.015r	-0.133	0.103	-0.94
0.1	halo	photometric	-0.82 - 0.053r	-0.103	-0.002	-1.16
0.1	halo	spec (CaT2)	-0.56 - 0.110r	-0.181	-0.038	-1.55
0.1	halo	spec (CaT23)	-0.70 - 0.062r	-0.167	0.044	-1.42
0.1	halo	spec (CaT12)	-0.96 - 0.099r	-0.208	0.009	-1.85
0.1	halo	spec (CaT123)	-1.02 - 0.068r	-0.158	0.022	-1.57
0.1	disk	photometric	-0.76 - 0.029r	-0.047	-0.011	-0.97
0.1	disk	spec (CaT2)	-0.65 - 0.040r	-0.092	0.013	-0.94
0.1	disk	spec (CaT23)	-0.87 - 0.005r	-0.154	0.144	-0.93
0.1	disk	spec (CaT12)	-0.89 - 0.029r	-0.112	0.054	-1.18
0.1	disk	spec (CaT123)	-0.77 - 0.016r	-0.134	0.102	-0.94
simple	halo	photometric	-0.89 -0.039r	-0.128	0.049	-1.14
simple	halo	spec (CaT2)	-0.36 - 0.128r	-0.230	-0.025	-1.45
simple	halo	spec (CaT23)	-0.87 - 0.059r	-0.165	0.047	-1.27
simple	halo	spec (CaT12)	-0.99 -0.102r	-0.226	0.023	-1.78
simple	halo	spec (CaT123)	-1.08 - 0.060r	-0.162	0.042	-1.45
simple	disk	photometric	-0.72 - 0.033r	-0.055	-0.011	-0.96
simple	disk	spec (CaT2)	-0.79 - 0.019r	-0.077	0.038	-0.95
simple	disk	spec (CaT23)	-0.93 - 0.0002r	-0.166	0.166	-0.93
simple	disk	spec (CaT12)	-0.89 - 0.024r	-0.112	0.065	-1.15
simple	disk	spec (CaT123)	-0.76 - 0.018r	-0.150	0.114	-0.91

Table B.1: The 2σ confidence intervals for the gradients in [Fe/H]. In this table, the spectroscopic metallicities derived from stacked spectra using various combinations of the CaT lines (calibrations described in the text) are presented.

Appendix C

Tables of the individual stars

field	starnum	velocity	velerr	CCmax	$\frac{Signal}{Noise}$	TD	I mag	$V-I$ colour	NaEW
237Tri	7	-210.25	3.23	0.057	2.16	2.84	20.941	1.079	0.42
237Tri	70	-238.16	6.22	0.174	4.45	7.66	20.766	1.507	1.409
237Tri	78	-188.03	4.13	0.155	4.07	6.47	21.128	1.185	1.596
237Tri	92	-182.28	8.92	0.125	5.53	4.52	20.795	1.557	4.223
237Tri	97	-189.25	11.2	0.093	4.03	7.14	21.04	1.316	1.566
237Tri	109	-217.27	9.45	0.127	5.28	8.35	20.865	1.522	3.071
237Tri	125	-236.3	9.93	0.077	4.17	3.59	20.664	1.775	1.734
237Tri	126	-183.88	14.01	0.079	4.06	5.72	20.979	1.461	0.393
237Tri	129	-201.16	3.67	0.117	3.37	9.7	21.058	1.398	1.027
237Tri	142	-223.66	11.35	0.096	3.68	4.06	20.902	1.607	2.913
237Tri	164	-257.92	4.27	0.094	2.48	5.01	20.985	1.621	0.731
237Tri	172	-259.75	4.47	0.135	3.0	6.87	21.224	1.416	3.015
237Tri	193	-231.77	11.05	0.079	3.19	5.32	21.192	1.577	2.483
237Tri	246	-242.42	6.06	0.196	5.55	7.27	20.796	2.289	3.909
237Tri	336	-239.42	15.57	0.056	3.11	3.34	20.752	1.063	1.129

Table C.1: All candidate halo stars from field 237Tri passing the quality cut.

field	starnum	velocity	velerr	CCmax	$\frac{Signal}{Noise}$	TD	I mag	$V-I$ colour	NaEW
237Tri	15	-207.52	29.89	0.057	3.55	3.3	20.678	1.383	0.055
237Tri	90	-227.86	17.3	0.033	1.67	1.84	21.172	1.172	0.843
237Tri	99	-206.09	13.13	0.021	2.14	1.78	20.863	1.497	3.491
237Tri	218	-256.14	12.41	0.028	3.01	1.39	21.047	1.872	5.014
237Tri	230	-194.46	26.38	0.015	1.68	1.11	21.179	1.79	4.165
237Tri	272	-205.93	16.56	0.074	1.95	3.2	21.072	2.158	2.779
237Tri	318	-256.42	3.71	0.049	1.73	3.09	20.621	2.996	2.225

Table C.2: All candidate halo stars from field 237Tri failing the quality cut.

field	starnum	velocity	velerr	CCmax	$\frac{Signal}{Noise}$	TD	I mag	$V-I$ colour	NaEW
237Tri	9	-102.51	4.11	0.171	5.47	12.25	20.623	1.4	4.087
237Tri	14	-105.82	6.8	0.158	4.28	8.89	20.832	1.224	3.985
237Tri	16	-148.97	18.55	0.086	5.42	4.28	20.656	1.413	3.469
237Tri	17	-114.81	10.85	0.105	5.05	5.24	20.838	1.236	4.313
237Tri	20	-109.94	7.6	0.068	2.89	3.62	20.836	1.25	1.082
237Tri	26	-134.9	10.13	0.123	3.86	7.79	20.585	1.548	6.981
237Tri	30	-136.82	9.78	0.154	4.53	4.83	20.618	1.54	5.196
237Tri	37	-101.93	20.42	0.06	3.42	4.77	21.039	1.147	0.647
237Tri	39	-128.57	3.26	0.153	3.97	8.73	20.695	1.494	3.976
237Tri	42	-117.69	7.92	0.188	5.4	8.11	20.749	1.457	4.755
237Tri	45	-140.75	8.45	0.158	4.24	8.32	20.652	1.559	3.659
237Tri	48	-112.84	14.05	0.14	4.12	6.84	20.708	1.51	4.059
237Tri	51	-118.33	1.98	0.053	4.68	4.17	20.935	1.289	3.775
237Tri	53	-132.04	13.65	0.129	4.57	7.16	20.852	1.378	4.196
237Tri	58	-143.23	6.43	0.087	3.58	4.79	20.672	1.561	4.446
237Tri	60	-141.01	9.83	0.11	5.67	5.71	20.736	1.505	0.374
237Tri	63	-119.72	6.08	0.157	3.87	6.44	20.871	1.386	3.305
237Tri	65	-110.14	2.12	0.1	3.16	6.08	21.033	1.225	3.922
237Tri	71	-111.82	17.09	0.075	2.43	4.91	21.022	1.252	0.363
237Tri	72	-103.72	4.65	0.215	4.31	9.88	20.842	1.437	8.175
237Tri	73	-107.16	8.44	0.069	3.01	2.8	20.949	1.333	4.328
237Tri	75	-105.31	8.59	0.086	3.51	4.3	20.718	1.58	2.529
237Tri	80	-128.92	3.01	0.074	3.63	3.53	21.088	1.229	3.2
237Tri	85	-156.14	10.55	0.078	2.92	3.21	21.045	1.286	5.227
237Tri	89	-100.48	2.78	0.052	2.05	2.59	20.957	1.387	0.42
237Tri	91	-100.63	7.58	0.254	7.33	12.7	20.653	1.695	5.082
237Tri	93	-140.63	16.32	0.105	5.71	6.74	20.527	1.827	2.783
237Tri	94	-101.48	2.61	0.223	3.5	9.02	20.7	1.655	5.944
237Tri	96	-130.95	11.86	0.145	3.81	6.25	20.894	1.462	3.394
237Tri	98	-105.63	16.82	0.137	4.39	6.5	21.03	1.328	3.498
237Tri	100	-105.39	15.27	0.103	3.59	6.35	20.591	1.769	4.933
237Tri	106	-103.98	2.62	0.073	3.16	3.9	20.686	1.69	4.23
237Tri	110	-107.23	4.62	0.211	5.96	13.08	20.804	1.585	4.31
237Tri	116	-125.31	8.97	0.276	6.3	9.98	20.966	1.444	4.999
237Tri	119	-136.87	15.44	0.243	6.22	8.29	20.794	1.628	5.624
237Tri	120	-110.51	11.11	0.15	3.76	11.12	21.054	1.369	5.349
237Tri	127	-159.76	16.2	0.068	2.33	5.62	21.193	1.252	5.022
237Tri	130	-109.65	21.53	0.061	2.78	5.93	21.212	1.253	4.693
237Tri	131	-120.61	9.64	0.177	5.04	9.34	20.601	1.864	4.568
237Tri	136	-100.12	8.1	0.11	3.24	5.21	21.141	1.344	4.839
237Tri	141	-131.09	19.16	0.093	2.76	3.9	21.065	1.442	4.184
237Tri	149	-154.09	11.08	0.088	3.91	6.59	20.872	1.682	3.545
237Tri	153	-134.16	9.12	0.108	3.56	4.18	21.106	1.458	1.286
237Tri	155	-134.35	8.41	0.086	3.33	6.85	21.239	1.337	2.826
237Tri	157	-125.65	6.96	0.167	4.6	12.59	20.534	2.052	4.579
237Tri	160	-119.29	14.55	0.102	4.31	3.09	20.963	1.63	3.545
237Tri	168	-114.53	22.97	0.093	3.7	5.95	20.984	1.637	11.122
237Tri	170	-143.07	2.16	0.084	2.45	5.9	20.943	1.682	6.274
237Tri	171	-126.15	16.97	0.071	3.61	5.83	20.95	1.689	1.936
237Tri	173	-106.68	3.8	0.068	3.89	4.56	20.843	1.8	2.634

237Tri	174	-100.13	5.9	0.098	3.23	5.47	21.23	1.414	4.916
237Tri	175	-110.21	6.03	0.116	4.53	5.51	21.231	1.415	3.51
237Tri	177	-107.43	11.46	0.205	6.31	6.73	20.655	2.0	4.894
237Tri	178	-113.38	7.41	0.218	7.09	11.25	20.621	2.048	3.994
237Tri	179	-135.92	13.88	0.077	3.35	5.75	20.804	1.874	2.562
237Tri	180	-114.46	10.07	0.237	5.06	10.59	20.569	2.126	5.29
237Tri	181	-112.65	22.51	0.1	4.63	3.35	20.977	1.719	3.356
237Tri	185	-105.89	1.68	0.129	3.81	6.48	20.922	1.812	5.674
237Tri	187	-156.12	13.8	0.116	2.75	7.62	21.06	1.683	9.843
237Tri	188	-100.56	4.41	0.17	3.33	7.06	21.159	1.586	2.504
237Tri	191	-125.57	13.13	0.161	7.82	6.45	20.54	2.215	3.571
237Tri	200	-104.77	12.29	0.085	5.12	7.92	20.973	1.82	0.669
237Tri	201	-137.93	10.42	0.101	3.1	8.47	21.222	1.572	3.427
237Tri	206	-113.13	3.88	0.181	4.57	10.03	21.049	1.765	4.882
237Tri	207	-178.03	11.99	0.107	3.14	5.89	20.992	1.83	3.11
237Tri	210	-111.67	4.07	0.176	4.2	8.35	20.928	1.93	2.765
237Tri	212	-108.12	3.11	0.15	4.38	4.31	20.634	2.244	2.671
237Tri	213	-133.8	17.89	0.126	3.61	7.59	21.01	1.879	0.07
237Tri	214	-150.73	1.91	0.111	3.94	5.85	21.045	1.861	3.17
237Tri	220	-112.45	1.89	0.117	4.85	4.77	20.773	2.155	1.126
237Tri	223	-101.05	16.64	0.053	2.25	4.36	20.725	2.216	3.635
237Tri	224	-103.78	2.35	0.125	5.4	5.87	21.119	1.831	3.344
237Tri	225	-108.25	4.73	0.138	4.94	8.26	21.147	1.803	4.241
237Tri	227	-130.59	9.47	0.141	5.76	7.73	20.578	2.377	2.612
237Tri	228	-149.13	5.85	0.082	2.33	5.44	21.123	1.833	4.768
237Tri	231	-101.67	3.39	0.227	6.46	10.01	20.793	2.178	4.73
237Tri	232	-123.44	16.34	0.089	4.14	5.83	21.18	1.795	4.825
237Tri	234	-126.48	22.89	0.047	3.59	3.0	21.15	1.868	3.029
237Tri	236	-101.85	4.47	0.051	2.8	4.62	21.675	1.37	1.252
237Tri	237	-142.39	15.9	0.079	3.65	5.26	21.009	2.037	3.391
237Tri	238	-109.85	22.83	0.12	3.24	9.15	21.08	1.968	4.244
237Tri	241	-138.47	6.17	0.135	2.8	5.02	21.31	1.751	5.17
237Tri	247	-106.86	4.47	0.114	3.47	5.53	21.135	1.953	1.596
237Tri	251	-148.38	4.27	0.152	4.25	7.88	21.173	1.956	3.137
237Tri	254	-109.33	7.97	0.107	3.1	4.81	21.674	1.475	4.035
237Tri	256	-111.77	7.35	0.179	4.6	11.83	21.066	2.098	3.751
237Tri	257	-112.07	12.48	0.23	6.81	11.31	20.689	2.479	3.942
237Tri	260	-117.96	15.37	0.109	4.46	6.04	21.149	2.034	4.103
237Tri	263	-139.36	10.19	0.134	5.51	7.79	20.749	2.455	2.105
237Tri	264	-152.9	20.79	0.077	5.09	6.07	21.078	2.126	2.05
237Tri	266	-141.65	4.63	0.112	6.42	5.29	20.574	2.638	3.69
237Tri	271	-100.73	10.21	0.128	4.51	9.24	20.639	2.59	1.944
237Tri	276	-104.03	4.51	0.067	5.1	6.76	21.106	2.133	3.06
237Tri	277	-105.26	3.43	0.057	3.26	3.22	20.553	2.689	0.647
237Tri	278	-109.64	5.91	0.11	3.74	7.13	21.046	2.199	1.587
237Tri	285	-149.99	4.45	0.155	3.55	7.45	21.036	2.257	5.089
237Tri	288	-113.48	9.47	0.085	5.25	4.91	20.85	2.496	3.085
237Tri	289	-119.83	17.97	0.076	3.06	3.26	21.131	2.226	3.63
237Tri	293	-110.63	5.74	0.093	5.06	3.96	20.892	2.479	3.286
237Tri	296	-128.06	17.49	0.096	3.29	3.88	20.965	2.436	2.769
237Tri	297	-112.46	4.05	0.097	4.89	6.72	21.052	2.368	3.178
237Tri	300	-105.97	6.44	0.123	4.86	5.78	21.113	2.321	3.417

237Tri	303	-104.44	5.07	0.262	5.53	8.73	20.847	2.612	5.328
237Tri	309	-112.48	19.77	0.104	4.69	5.66	20.977	2.535	3.498
237Tri	310	-118.6	13.85	0.124	3.74	6.53	21.161	2.352	4.901
237Tri	314	-130.66	14.9	0.086	4.33	4.87	21.211	2.324	3.289
237Tri	320	-106.32	6.44	0.112	2.4	5.43	21.846	1.795	6.352
237Tri	321	-101.15	3.27	0.142	6.36	11.17	20.75	2.933	2.931
237Tri	324	-103.32	7.62	0.217	4.33	13.79	20.863	2.849	6.587
237Tri	325	-104.15	2.26	0.303	6.13	13.73	20.746	2.966	4.574

Table C.3: All candidate disk stars from field 237Tri passing the quality cut.

field	starnum	velocity	velerr	CCmax	$\frac{Signal}{Noise}$	TD	I mag	$V-I$ colour	NaEW
237Tri	22	-170.25	12.66	0.033	1.82	2.7	20.773	1.34	4.569
237Tri	66	-116.33	54.76	0.014	1.51	1.13	21.188	1.07	8.021
237Tri	101	-141.61	13.49	0.067	1.4	2.45	21.163	1.199	4.164
237Tri	103	-160.62	5.9	0.053	3.72	1.61	21.223	1.145	4.09
237Tri	111	-107.27	6.49	0.021	1.61	1.94	21.235	1.154	1.444
237Tri	115	-102.94	10.51	0.028	1.29	2.13	20.821	1.589	2.578
237Tri	146	-148.86	8.96	0.003	3.91	5.73	20.792	1.734	6.725
237Tri	183	-158.41	37.95	0.04	3.3	2.41	21.202	1.525	0.517
237Tri	215	-102.93	6.11	0.03	4.06	1.88	20.676	2.233	0.966
237Tri	298	-151.8	3.43	0.078	1.18	5.05	21.045	2.377	4.91
237Tri	333	-116.08	3.8	0.454	9.93	12.95	19.244	1.385	5.794

Table C.4: All candidate disk stars from field 237Tri failing the quality cut.

field	starnum	velocity	velerr	CCmax	$\frac{Signal}{Noise}$	TD	I mag	$V-I$ colour	NaEW
237Tri	31	201.45	11.8	0.062	4.26	3.34	20.587	1.58	0.202
237Tri	35	129.7	4.85	0.042	2.27	2.31	21.089	1.095	11.087
237Tri	52	225.99	3.69	0.058	3.38	4.13	20.759	1.466	0.27
237Tri	79	76.84	4.21	0.06	4.95	4.83	20.753	1.562	2.265
237Tri	163	432.2	5.91	0.078	2.9	3.99	20.929	1.675	3.587
237Tri	233	265.1	13.18	0.106	2.34	5.96	21.222	1.783	2.341
237Tri	245	248.01	7.98	0.137	3.52	4.78	21.982	1.094	4.606

Table C.5: All stars with v_{hel} > -100 km s^{-1} from field 237Tri passing the quality cut.

field	starnum	velocity	velerr	CCmax	$\frac{Signal}{Noise}$	TD	I mag	$V-I$ colour	NaEW
237Tri	1	614.58	20.75	-0.006	7.0	-0.18	18.415	1.649	1.184
237Tri	25	236.46	48.15	0.048	1.65	5.4	20.801	1.321	25.691
237Tri	34	341.54	41.8	0.027	1.26	1.86	20.934	1.249	0.522

237Tri	40	295.18	19.12	0.058	1.78	2.96	20.88	1.32	15.692
237Tri	44	359.54	76.18	0.03	2.1	2.04	20.946	1.262	19.843
237Tri	55	391.07	97.81	0.028	1.75	1.98	20.674	1.558	7.393
237Tri	74	18.98	34.66	0.044	3.12	2.09	21.045	1.248	1.875
237Tri	77	307.59	31.16	0.021	1.28	2.05	20.687	1.614	17.289
237Tri	145	574.71	24.03	0.028	1.58	1.43	21.178	1.341	1.472
237Tri	147	311.74	8.25	0.032	1.33	1.41	20.994	1.539	0.877
237Tri	156	80.29	5.47	0.034	1.73	1.93	21.047	1.534	2.666
237Tri	162	385.28	13.13	0.041	1.23	3.26	21.248	1.35	8.202
237Tri	192	489.47	14.92	0.047	1.48	1.34	21.164	1.595	3.031
237Tri	243	259.58	21.44	0.027	1.21	6.66	21.052	2.012	43.991
237Tri	244	65.09	20.09	0.004	1.24	0.21	21.189	1.881	0.085
237Tri	262	69.04	104.46	0.022	1.52	1.48	20.689	2.513	24.855
237Tri	273	460.09	63.14	0.01	1.14	0.74	21.073	2.159	3.019
237Tri	279	248.05	2.91	0.006	1.3	0.67	21.165	2.106	3.284
237Tri	287	18.13	16.06	0.022	1.51	1.52	21.042	2.275	0.237
237Tri	294	6.06	6.13	0.003	4.2	2.05	21.193	2.184	2.6
237Tri	305	278.68	11.52	0.034	1.05	1.85	20.801	2.681	11.775
237Tri	307	429.66	28.05	0.024	1.75	1.76	21.019	2.477	0.399
237Tri	311	450.29	114.93	0.019	1.42	1.45	21.106	2.414	8.509
237Tri	339	556.44	13.45	0.013	2.17	1.02	21.911	0.864	1.995

Table C.6: All stars with v_{hel} > -100 km s^{-1} from field 237Tri failing the quality cut.

field	starnum	velocity	velerr	CCmax	$\frac{Signal}{Noise}$	TD	I mag	$V-I$ colour	NaEW
236Tri	12	-218.68	17.03	0.089	4.3	5.44	20.662	1.47	4.431
236Tri	89	-190.87	11.0	0.104	4.36	3.62	21.168	1.322	1.355
236Tri	90	-185.88	2.94	0.157	5.42	13.4	20.909	1.582	4.642
236Tri	111	-239.32	5.23	0.133	7.13	11.09	20.751	1.817	3.746
236Tri	114	-207.31	20.46	0.126	4.57	4.91	20.8	1.783	3.116
236Tri	117	-200.91	8.25	0.117	4.43	4.69	21.123	1.472	3.665
236Tri	142	-179.92	12.45	0.048	4.49	3.46	21.08	1.574	3.736
236Tri	170	-194.51	7.38	0.073	2.39	6.43	21.205	1.565	3.312
236Tri	182	-236.2	18.38	0.05	4.49	4.51	21.227	1.57	3.688
236Tri	195	-207.27	7.57	0.073	5.29	4.74	21.113	1.707	1.993
236Tri	263	-258.2	2.94	0.096	3.77	10.72	21.127	2.075	2.8
236Tri	285	-212.49	18.35	0.085	7.25	4.12	20.971	2.375	1.532

Table C.7: All candidate halo stars from field 236Tri passing the quality cut.

field	starnum	velocity	velerr	CCmax	$\frac{Signal}{Noise}$	TD	I mag	$V-I$ colour	NaEW
236Tri	72	-298.72	12.51	0.03	2.38	1.02	20.569	1.868	4.347
236Tri	91	-261.67	6.1	0.017	2.8	1.89	21.057	1.434	2.177
236Tri	98	-270.64	32.92	0.018	2.94	1.67	21.157	1.363	1.529
236Tri	158	-260.73	21.83	0.013	0.89	1.38	21.125	1.609	10.048

236Tri	333	-190.62	11.22	0.148	7.32	6.45	20.442	1.853	3.013

Table C.8: All candidate halo stars from field 236Tri failing the quality cut.

field	starnum	velocity	velerr	CCmax	$\frac{Signal}{Noise}$	TD	I mag	$V-I$ colour	NaEW
236Tri	7	-112.2	13.53	0.104	5.96	12.35	20.904	1.175	4.031
236Tri	11	-101.46	2.73	0.224	7.89	13.84	20.668	1.459	3.354
236Tri	14	-147.08	6.03	0.108	5.57	6.76	20.523	1.613	4.528
236Tri	16	-105.85	10.13	0.181	4.45	10.92	20.613	1.539	7.372
236Tri	20	-122.25	15.41	0.075	3.85	3.41	20.968	1.193	2.91
236Tri	21	-105.15	7.67	0.043	2.88	4.81	21.131	1.032	1.324
236Tri	24	-135.28	5.59	0.116	3.39	4.81	21.089	1.095	4.747
236Tri	30	-126.19	4.4	0.16	4.09	12.03	20.784	1.432	6.633
236Tri	31	-115.11	7.57	0.136	6.26	12.9	20.522	1.694	3.923
236Tri	32	-135.8	12.15	0.076	7.63	4.46	20.723	1.522	4.565
236Tri	33	-127.23	8.83	0.189	4.05	10.71	20.714	1.535	5.63
236Tri	34	-104.52	5.04	0.117	3.74	8.25	20.874	1.382	4.398
236Tri	35	-115.89	12.27	0.059	3.07	2.53	20.73	1.531	0.288
236Tri	36	-115.72	13.19	0.045	2.7	3.03	20.987	1.275	4.032
236Tri	37	-127.46	22.91	0.067	3.91	3.81	20.911	1.355	4.19
236Tri	38	-167.39	21.66	0.044	3.61	3.26	20.847	1.422	12.217
236Tri	39	-111.32	10.75	0.129	4.13	4.94	20.942	1.33	7.581
236Tri	40	-119.41	17.8	0.146	2.51	10.64	21.096	1.193	7.468
236Tri	41	-137.3	4.75	0.225	6.99	13.21	20.733	1.559	1.549
236Tri	42	-110.68	3.08	0.046	4.66	5.36	21.037	1.256	2.117
236Tri	45	-110.48	11.22	0.302	9.63	18.25	20.525	1.781	5.905
236Tri	46	-106.8	5.6	0.095	3.67	4.36	21.197	1.121	4.133
236Tri	48	-111.79	7.08	0.21	6.36	6.13	20.78	1.55	6.187
236Tri	49	-118.0	13.7	0.141	6.08	5.44	21.014	1.321	3.156
236Tri	51	-158.15	18.72	0.085	3.13	5.65	20.759	1.577	4.641
236Tri	52	-121.65	17.07	0.069	2.59	3.04	21.208	1.133	5.023
236Tri	53	-166.07	8.86	0.05	3.31	4.07	20.728	1.613	1.363
236Tri	55	-108.07	9.82	0.075	4.27	5.91	20.929	1.416	4.581
236Tri	56	-136.18	15.38	0.13	3.23	6.47	21.053	1.293	6.612
236Tri	57	-148.84	10.48	0.086	3.36	3.9	21.055	1.312	5.791
236Tri	58	-105.36	8.38	0.084	5.4	8.17	20.803	1.571	4.675
236Tri	61	-112.22	22.52	0.081	2.88	4.75	21.133	1.254	5.009
236Tri	62	-126.62	13.69	0.195	4.28	8.04	21.017	1.378	4.989
236Tri	63	-102.66	5.81	0.156	5.67	7.43	20.81	1.586	1.086
236Tri	64	-149.69	1.66	0.076	4.12	6.99	21.034	1.367	5.487
236Tri	66	-107.2	6.24	0.287	6.33	12.5	20.659	1.746	4.641
236Tri	67	-119.51	7.73	0.152	5.04	7.49	21.09	1.32	4.959
236Tri	69	-122.85	13.48	0.084	5.93	7.45	20.737	1.679	4.095
236Tri	70	-114.63	4.75	0.047	4.85	2.09	21.16	1.26	3.284
236Tri	71	-113.8	7.99	0.055	3.71	2.25	20.893	1.538	3.847
236Tri	73	-108.58	18.68	0.09	3.52	9.96	21.13	1.314	5.727
236Tri	74	-126.95	9.04	0.219	5.69	9.12	20.685	1.763	5.387
236Tri	75	-119.5	10.77	0.141	3.03	5.91	21.081	1.367	6.805

236Tri	78	-106.55	4.1	0.193	6.33	9.95	20.791	1.666	4.08
236Tri	79	-100.76	6.37	0.105	4.61	6.19	21.017	1.446	12.931
236Tri	80	-145.31	10.34	0.128	4.02	7.13	20.93	1.539	0.813
236Tri	83	-107.89	5.64	0.12	3.27	2.93	20.784	1.693	0.602
236Tri	87	-121.54	9.59	0.204	7.35	16.5	20.555	1.931	4.899
236Tri	88	-100.36	5.61	0.188	2.59	7.61	20.886	1.603	4.282
236Tri	93	-118.52	8.13	0.086	4.92	4.37	20.782	1.715	4.531
236Tri	95	-131.1	11.41	0.078	5.8	6.32	20.894	1.617	2.723
236Tri	96	-109.36	16.1	0.179	8.01	8.5	20.504	2.01	4.167
236Tri	99	-123.28	11.89	0.138	4.82	9.8	20.932	1.59	4.369
236Tri	100	-115.82	11.73	0.075	3.48	5.55	20.917	1.607	5.936
236Tri	102	-102.26	10.85	0.114	4.26	6.83	21.185	1.347	1.964
236Tri	103	-118.04	15.94	0.081	3.09	11.71	21.138	1.396	5.25
236Tri	106	-156.33	11.4	0.124	7.73	12.1	20.525	2.027	6.999
236Tri	113	-124.9	8.0	0.231	6.27	16.78	20.597	1.984	5.567
236Tri	115	-102.12	5.28	0.297	8.23	13.98	20.621	1.964	4.066
236Tri	116	-111.83	5.94	0.143	3.98	5.86	20.675	1.913	5.807
236Tri	121	-108.97	10.58	0.168	4.81	10.35	20.985	1.632	5.03
236Tri	123	-171.12	12.6	0.068	4.63	4.29	20.762	1.858	4.778
236Tri	127	-118.52	8.76	0.059	2.83	3.98	21.058	1.569	1.372
236Tri	130	-129.7	8.09	0.066	2.96	5.49	20.979	1.653	3.129
236Tri	135	-178.73	10.09	0.03	4.55	6.25	20.95	1.689	1.801
236Tri	136	-111.61	9.5	0.112	4.12	6.59	21.533	1.108	2.58
236Tri	137	-118.15	16.08	0.05	5.61	5.29	21.046	1.595	3.37
236Tri	138	-125.03	2.47	0.061	3.43	4.17	21.109	1.537	3.832
236Tri	139	-110.34	2.92	0.115	3.81	9.62	21.21	1.437	4.824
236Tri	141	-108.34	6.24	0.089	4.24	6.43	21.065	1.587	3.925
236Tri	144	-135.68	10.94	0.103	3.8	9.79	21.115	1.563	5.452
236Tri	145	-151.66	9.36	0.044	3.69	2.89	21.047	1.633	5.588
236Tri	147	-142.67	11.96	0.119	3.87	7.12	21.089	1.604	5.928
236Tri	152	-133.65	13.8	0.077	3.61	8.42	21.086	1.626	3.528
236Tri	153	-175.82	13.69	0.062	3.38	3.48	21.141	1.572	3.935
236Tri	155	-122.5	13.91	0.043	2.51	2.44	20.967	1.758	0.899
236Tri	156	-136.69	7.38	0.166	5.0	8.11	20.944	1.784	0.734
236Tri	159	-144.98	5.73	0.101	5.49	4.18	20.976	1.761	2.268
236Tri	163	-112.63	4.53	0.192	6.95	8.22	20.753	1.998	4.965
236Tri	165	-102.54	3.43	0.044	3.6	6.92	21.222	1.535	3.224
236Tri	168	-114.99	4.45	0.073	4.22	5.17	21.087	1.678	4.942
236Tri	169	-112.4	7.22	0.14	4.59	9.2	21.07	1.696	4.742
236Tri	171	-114.77	11.12	0.138	4.23	9.7	21.233	1.538	6.806
236Tri	173	-113.67	4.79	0.152	4.69	5.36	21.244	1.533	3.374
236Tri	175	-103.89	13.89	0.065	7.87	3.62	20.64	2.144	0.265
236Tri	176	-103.55	13.07	0.112	4.44	5.13	21.013	1.773	4.143
236Tri	178	-106.65	8.66	0.1	3.65	3.42	21.076	1.718	1.818
236Tri	180	-126.39	14.64	0.149	5.42	8.43	21.184	1.612	6.313
236Tri	183	-119.28	14.59	0.049	5.1	5.13	20.674	2.126	1.343
236Tri	184	-130.91	16.69	0.207	3.72	13.35	21.183	1.618	6.842
236Tri	186	-118.17	14.4	0.11	3.03	5.99	21.033	1.77	5.797
236Tri	188	-104.7	4.68	0.221	5.4	7.39	21.217	1.59	2.919
236Tri	190	-106.87	10.1	0.242	4.74	10.55	20.941	1.869	6.733
236Tri	191	-129.97	7.75	0.184	6.73	10.29	20.667	2.146	3.364
236Tri	194	-124.33	7.43	0.224	4.95	12.04	21.059	1.758	6.041

236Tri	197	-170.68	4.15	0.03	4.97	4.79	21.174	1.672	2.85
236Tri	199	-121.43	15.62	0.065	5.26	2.08	20.811	2.042	0.667
236Tri	201	-107.27	6.66	0.182	4.02	10.1	21.245	1.612	3.172
236Tri	203	-111.34	6.94	0.141	4.9	9.31	20.984	1.881	3.993
236Tri	206	-142.65	4.58	0.089	3.71	4.09	21.193	1.687	4.336
236Tri	207	-112.27	12.32	0.046	5.59	2.68	20.958	1.937	1.331
236Tri	209	-140.63	8.07	0.058	4.93	3.89	21.183	1.717	3.001
236Tri	210	-150.95	4.54	0.145	3.96	8.38	20.638	2.266	3.317
236Tri	214	-110.3	12.45	0.16	5.11	9.57	20.952	1.982	3.873
236Tri	216	-123.0	10.91	0.201	6.88	10.54	20.733	2.224	4.888
236Tri	218	-129.31	9.8	0.122	5.32	7.37	21.089	1.877	4.234
236Tri	219	-115.13	5.17	0.28	6.14	13.79	21.002	1.973	5.836
236Tri	221	-108.35	12.97	0.119	4.85	10.31	20.82	2.158	4.91
236Tri	223	-123.83	14.53	0.209	5.64	9.15	20.988	2.0	4.861
236Tri	227	-170.9	19.63	0.068	3.77	7.01	21.013	1.99	4.019
236Tri	230	-142.45	8.66	0.064	5.92	6.0	21.212	1.802	2.513
236Tri	232	-110.84	6.36	0.229	9.67	12.03	20.913	2.106	3.483
236Tri	233	-112.23	5.83	0.112	3.48	11.32	21.248	1.773	6.549
236Tri	235	-155.74	5.21	0.194	5.95	8.98	21.007	2.042	2.626
236Tri	237	-111.66	3.7	0.331	6.46	12.52	20.903	2.147	5.054
236Tri	239	-168.27	12.25	0.127	5.12	9.54	21.058	2.009	4.261
236Tri	241	-103.09	22.12	0.047	3.33	3.72	21.197	1.876	5.871
236Tri	245	-131.57	7.03	0.222	6.63	9.79	20.762	2.326	5.768
236Tri	246	-126.21	2.58	0.135	6.03	10.76	20.778	2.312	2.276
236Tri	250	-119.44	3.26	0.188	4.47	3.84	20.708	2.395	2.396
236Tri	252	-115.33	8.69	0.259	10.91	14.5	20.539	2.566	3.625
236Tri	254	-143.06	23.95	0.088	6.13	11.26	20.528	2.618	4.101
236Tri	257	-167.7	11.82	0.064	5.41	7.46	21.167	1.999	3.817
236Tri	258	-108.24	23.22	0.021	9.38	2.36	20.771	2.402	5.9
236Tri	261	-151.87	9.7	0.178	5.52	7.41	21.155	2.034	5.738
236Tri	268	-118.69	3.2	0.124	4.99	8.49	21.156	2.069	3.703
236Tri	269	-100.9	6.43	0.131	5.12	4.38	20.623	2.62	0.453
236Tri	271	-150.85	6.67	0.147	7.12	10.92	20.623	2.638	2.386
236Tri	274	-122.07	13.61	0.156	6.0	8.32	21.216	2.066	2.34
236Tri	281	-101.4	4.27	0.089	5.33	7.25	21.09	2.241	4.208
236Tri	286	-119.75	8.25	0.031	2.92	3.77	21.66	1.686	2.861
236Tri	289	-107.5	1.97	0.142	4.17	9.59	21.146	2.225	4.113
236Tri	290	-111.59	3.7	0.158	5.85	12.76	20.87	2.502	4.857
236Tri	295	-124.49	13.55	0.107	3.83	9.78	21.121	2.27	5.272
236Tri	302	-102.79	10.58	0.091	5.95	10.38	21.099	2.358	2.603
236Tri	305	-116.33	4.63	0.047	3.33	3.01	20.54	2.934	3.485
236Tri	310	-101.11	6.77	0.048	4.7	2.18	21.074	2.462	0.424
236Tri	312	-145.26	3.5	0.196	7.85	8.54	20.783	2.781	4.288
236Tri	319	-108.23	4.7	0.128	3.96	4.09	20.608	3.107	1.466
236Tri	321	-121.57	21.77	0.112	5.75	5.53	20.797	3.001	3.494
236Tri	323	-100.03	6.74	0.129	5.49	7.47	20.967	2.888	3.404
236Tri	326	-154.34	3.88	0.248	7.69	10.37	20.713	3.252	3.089
236Tri	327	-167.95	12.9	0.039	6.19	6.16	21.041	2.948	2.76
236Tri	335	-117.26	8.12	0.082	3.66	4.95	21.866	2.146	5.431

Table C.9: All candidate disk stars from field 236Tri passing the quality cut.

field	starnum	velocity	velerr	CCmax	$\frac{Signal}{Noise}$	TD	I mag	$V-I$ colour	NaEW
236Tri	5	-136.35	10.96	0.002	3.88	6.45	20.809	1.213	5.499
236Tri	13	-109.14	53.64	0.01	4.13	0.53	20.773	1.362	143.833
236Tri	59	-164.28	44.99	0.01	1.12	2.52	20.803	1.571	16.594
236Tri	60	-102.17	6.89	0.027	4.58	1.4	21.246	1.135	1.151
236Tri	81	-175.38	14.25	0.013	2.09	1.59	21.048	1.422	2.166
236Tri	97	-129.48	28.67	0.056	4.01	5.06	21.075	1.444	2.365
236Tri	112	-149.88	60.67	0.039	2.78	3.79	20.963	1.61	11.672
236Tri	120	-112.34	25.41	0.025	5.22	5.39	20.922	1.688	1.168
236Tri	134	-108.48	11.43	0.034	1.92	2.87	20.818	1.821	1.293
236Tri	154	-118.95	26.46	0.084	8.18	5.28	20.543	2.178	3.41
236Tri	225	-125.01	28.63	0.04	4.74	2.39	21.17	1.829	7.011
236Tri	229	-160.5	14.3	0.011	3.74	6.68	21.132	1.876	4.517
236Tri	234	-160.74	42.55	0.012	4.82	1.24	21.2	1.842	0.421
236Tri	253	-162.82	10.71	0.028	1.81	1.8	20.539	2.6	2.333
236Tri	255	-117.07	2.49	0.051	1.69	4.11	21.14	2.013	5.743
236Tri	278	-127.58	17.39	0.066	1.78	4.84	21.649	1.664	18.476
236Tri	283	-117.96	10.77	0.098	1.39	6.66	21.582	1.749	14.343
236Tri	288	-101.29	2.74	0.033	0.87	4.01	20.84	2.528	0.668
236Tri	314	-113.07	39.27	0.012	0.1	2.39	21.163	2.462	377.835
236Tri	316	-113.03	16.93	0.05	1.09	2.85	21.663	1.991	4.335
236Tri	331	-168.48	11.06	0.132	7.81	5.74	20.305	1.757	3.524
236Tri	332	-137.04	11.3	0.065	4.75	4.62	20.412	1.791	4.879

Table C.10: All candidate disk stars from field 236Tri failing the quality cut.

field	starnum	velocity	velerr	CCmax	$\frac{Signal}{Noise}$	TD	I mag	$V-I$ colour	NaEW
236Tri	109	268.43	19.38	0.043	3.58	2.96	21.068	1.488	3.743
236Tri	149	216.18	5.71	0.064	2.64	3.8	20.513	2.189	5.313
236Tri	166	219.89	5.92	0.066	2.63	3.12	21.28	1.478	3.051
236Tri	172	265.9	13.37	0.052	3.27	2.64	21.078	1.693	9.167
236Tri	189	233.44	8.33	0.105	2.11	6.56	21.7	1.109	1.95
236Tri	244	268.99	10.99	0.077	2.59	5.14	21.479	1.607	11.177
236Tri	256	464.31	18.86	0.037	2.57	2.59	21.104	2.059	5.863
236Tri	293	249.66	20.98	0.063	10.72	3.35	20.53	2.853	1.323
236Tri	311	269.59	8.41	0.04	3.95	5.17	21.269	2.29	3.284
236Tri	315	244.99	7.21	0.061	2.11	5.6	21.773	1.879	0.939

Table C.11: All stars with v_{hel} > -100 km s^{-1} from field 236Tri passing the quality cut.

field	starnum	velocity	velerr	CCmax	$\frac{Signal}{Noise}$	TD	I mag	$V-I$ colour	NaEW

236Tri	1	604.32	10.03	-0.007	5.07	-0.18	18.526	1.572	1.045
236Tri	76	260.16	6.03	0.055	1.33	3.94	20.932	1.519	2.113
236Tri	86	217.9	54.73	0.03	3.16	9.52	21.247	1.235	14.3
236Tri	92	51.59	36.39	0.05	5.98	2.8	20.734	1.761	1.495
236Tri	129	221.51	3.39	0.071	1.8	6.19	21.54	1.089	4.565
236Tri	132	251.19	25.06	0.07	1.76	6.66	21.174	1.459	17.12
236Tri	146	136.48	41.24	0.036	2.65	2.42	20.668	2.021	2.756
236Tri	185	10.92	10.31	0.024	1.64	2.54	21.01	1.793	7.306
236Tri	204	250.66	28.16	0.086	3.73	4.85	21.238	1.638	2.822
236Tri	215	400.96	11.43	0.033	1.75	1.92	21.076	1.864	5.141
236Tri	226	104.54	57.8	0.022	2.89	1.64	21.209	1.792	14.595
236Tri	236	584.41	45.14	0.011	3.43	0.81	21.585	1.465	2.099
236Tri	248	220.81	8.72	0.052	1.96	1.8	21.726	1.37	2.067
236Tri	259	211.01	2.64	0.062	1.68	6.09	20.854	2.33	13.391
236Tri	260	219.93	6.81	0.07	0.74	4.91	20.663	2.524	5.976
236Tri	267	602.44	5.77	0.029	1.56	2.8	21.061	2.143	2.677
236Tri	291	209.59	3.44	0.119	1.3	5.99	20.557	2.817	3.04
236Tri	309	521.96	6.7	0.013	0.98	2.54	20.904	2.622	0.302
236Tri	313	613.5	12.32	0.033	2.54	1.68	21.034	2.54	2.686
236Tri	322	439.58	13.15	0.037	1.48	1.55	20.834	2.973	3.787
236Tri	340	301.58	19.73	0.129	1.66	4.08	25.0	0.0	34.713

Table C.12: All stars with v_{hel} > -100 km s^{-1} from field 236Tri failing the quality cut.

field	starnum	velocity	velerr	CCmax	$\frac{Signal}{Noise}$	TD	I mag	$V-I$ colour	NaEW
408TrS	16	-196.58	6.36	0.203	6.38	8.0	20.51	1.718	2.128
408TrS	32	-232.98	18.19	0.232	5.0	6.51	21.147	1.297	4.481
408TrS	88	-207.14	17.81	0.259	3.54	8.95	21.293	1.527	7.098
408TrS	113	-259.96	8.33	0.28	5.01	7.67	21.431	1.549	4.859
408TrS	121	-183.25	4.7	0.305	6.56	10.64	20.982	2.05	4.949
408TrS	123	-186.12	22.37	0.291	5.56	11.63	21.072	1.973	4.606
408TrS	140	-207.41	4.5	0.18	2.8	6.13	21.599	1.543	2.894
408TrS	141	-284.73	21.27	0.223	4.55	9.45	21.31	1.855	8.476
408TrS	194	-181.05	9.1	0.174	3.28	5.27	21.536	2.076	4.772

Table C.13: All candidate halo stars from field 408TrS passing the quality cut.

field	starnum	velocity	velerr	CCmax	$\frac{Signal}{Noise}$	TD	I mag	$V-I$ colour	NaEW
408TrS	47	-250.39	33.77	0.176	3.22	5.19	21.394	1.202	6.456
408TrS	84	-239.61	56.45	0.193	4.54	6.1	21.048	1.755	5.108
408TrS	124	-183.0	17.78	0.203	1.89	7.15	21.593	1.455	9.049
408TrS	188	-204.11	15.99	0.211	1.33	6.71	20.515	3.011	6.247

Table C.14: All candidate halo stars from field 408TrS failing the quality cut.

field	starnum	velocity	velerr	CCmax	$\frac{Signal}{Noise}$	TD	I mag	$V-I$ colour	NaEW
408TrS	5	-137.55	10.8	0.42	7.59	12.2	20.771	1.258	4.687
408TrS	6	-128.2	12.61	0.275	6.18	8.38	20.846	1.189	4.772
408TrS	7	-113.81	14.1	0.264	4.17	9.01	20.873	1.174	4.082
408TrS	9	-120.71	9.5	0.225	6.13	11.07	20.657	1.462	6.231
408TrS	11	-151.12	14.63	0.309	5.31	11.07	20.773	1.362	4.529
408TrS	15	-162.41	15.46	0.308	9.03	9.43	20.784	1.415	5.256
408TrS	17	-125.26	7.16	0.304	2.78	7.04	20.73	1.531	7.729
408TrS	19	-124.4	12.27	0.425	7.97	11.42	20.525	1.781	6.242
408TrS	20	-111.12	8.65	0.408	6.8	13.04	20.769	1.556	3.832
408TrS	22	-156.12	12.51	0.176	4.38	6.19	20.803	1.538	6.817
408TrS	23	-139.9	3.91	0.344	7.23	10.54	20.651	1.698	5.856
408TrS	24	-163.01	9.04	0.257	3.09	8.67	21.096	1.254	4.407
408TrS	26	-144.92	15.53	0.277	6.05	9.56	21.079	1.292	3.772
408TrS	27	-128.23	20.58	0.272	3.63	9.84	20.906	1.466	8.192
408TrS	33	-116.97	15.58	0.21	5.77	6.95	20.879	1.612	3.573
408TrS	36	-128.07	14.71	0.182	3.34	5.67	21.05	1.458	3.508
408TrS	39	-128.97	7.03	0.255	3.74	8.85	21.096	1.451	6.687
408TrS	40	-145.45	11.59	0.31	4.77	11.81	21.237	1.311	5.624
408TrS	41	-115.48	3.21	0.207	5.22	6.18	20.868	1.68	4.729
408TrS	42	-163.2	14.06	0.243	5.96	6.69	20.811	1.745	2.254
408TrS	43	-154.52	12.72	0.243	3.87	8.74	21.12	1.44	4.229
408TrS	44	-138.21	22.45	0.249	4.95	6.46	20.95	1.62	3.345
408TrS	49	-164.07	3.83	0.324	5.16	12.34	20.984	1.627	8.624
408TrS	50	-106.31	22.77	0.192	5.09	6.84	21.029	1.6	5.459
408TrS	51	-118.11	4.03	0.243	3.91	8.66	20.794	1.838	7.707
408TrS	54	-165.98	15.01	0.221	6.8	7.35	21.131	1.511	4.836
408TrS	57	-131.85	11.77	0.237	3.76	7.26	21.21	1.437	5.997
408TrS	59	-167.07	15.77	0.241	4.26	6.49	21.115	1.563	5.23
408TrS	63	-120.12	17.79	0.389	6.2	10.54	20.941	1.753	6.702
408TrS	65	-164.43	10.61	0.302	4.58	9.71	21.154	1.55	7.439
408TrS	69	-125.91	16.75	0.202	2.7	7.91	21.205	1.513	6.539
408TrS	70	-112.74	10.33	0.244	4.04	8.99	21.472	1.251	4.327
408TrS	71	-122.84	7.57	0.246	4.23	8.74	21.181	1.552	4.336
408TrS	75	-101.23	12.1	0.277	3.25	9.73	21.391	1.385	7.728
408TrS	76	-133.68	7.63	0.339	4.44	10.54	21.216	1.566	7.042
408TrS	77	-157.68	12.16	0.221	2.24	7.87	21.409	1.374	9.543
408TrS	78	-131.81	8.52	0.298	5.27	9.2	21.002	1.783	4.782
408TrS	86	-107.48	15.9	0.205	3.72	6.98	21.206	1.605	4.887
408TrS	87	-132.46	8.8	0.276	4.08	8.24	21.289	1.524	7.988
408TrS	89	-140.93	9.59	0.226	3.73	7.04	21.395	1.437	4.425
408TrS	90	-153.07	13.45	0.3	6.19	13.38	20.861	1.98	5.138
408TrS	94	-138.61	11.43	0.233	2.4	8.26	21.763	1.088	13.598
408TrS	95	-116.66	8.84	0.25	4.32	8.37	21.245	1.612	2.269
408TrS	96	-114.02	14.37	0.346	6.52	12.13	20.568	2.295	7.179
408TrS	100	-123.16	13.27	0.322	5.18	10.88	20.974	1.914	7.513
408TrS	101	-145.59	5.52	0.265	4.89	9.43	21.129	1.765	4.946
408TrS	103	-171.97	8.48	0.317	5.54	11.96	20.638	2.266	4.826
408TrS	104	-170.98	8.63	0.291	2.72	9.31	21.512	1.395	7.195
408TrS	105	-171.03	8.1	0.348	4.88	11.55	21.08	1.827	9.785

408TrS	106	-171.53	13.01	0.257	3.4	8.76	21.511	1.398	7.412
408TrS	108	-149.13	24.5	0.197	5.75	6.27	21.152	1.768	5.535
408TrS	110	-165.59	21.44	0.178	4.28	7.88	21.301	1.638	2.103
408TrS	112	-119.64	9.23	0.226	2.23	8.87	21.222	1.729	8.149
408TrS	114	-125.54	17.84	0.378	5.41	14.63	20.993	1.989	5.968
408TrS	122	-112.98	12.8	0.239	2.43	7.89	21.957	1.084	4.976
408TrS	128	-141.61	7.65	0.294	5.18	9.45	20.931	2.147	5.125
408TrS	130	-102.69	18.24	0.342	8.87	11.91	20.526	2.566	4.058
408TrS	131	-166.82	5.36	0.25	2.8	9.27	21.525	1.567	4.598
408TrS	132	-139.66	17.19	0.284	3.07	9.51	21.239	1.854	6.885
408TrS	135	-102.28	8.8	0.286	3.83	9.35	21.544	1.567	4.721
408TrS	137	-140.72	10.02	0.32	3.48	11.31	21.554	1.564	5.77
408TrS	149	-164.51	21.67	0.152	4.47	5.71	21.77	1.454	3.214
408TrS	153	-164.22	3.88	0.279	4.97	7.66	21.15	2.088	5.278
408TrS	155	-176.15	11.48	0.147	3.66	5.82	21.481	1.765	4.092
408TrS	162	-112.3	18.19	0.238	2.55	8.44	21.631	1.677	8.359
408TrS	164	-152.7	13.63	0.166	2.56	5.7	21.649	1.664	6.695
408TrS	165	-125.63	22.87	0.184	3.52	5.37	21.602	1.738	1.774
408TrS	167	-114.53	13.15	0.216	5.09	7.75	21.329	2.028	7.233
408TrS	173	-128.27	11.91	0.298	5.01	9.37	21.121	2.27	5.819
408TrS	174	-149.41	5.12	0.239	3.0	8.44	21.757	1.635	0.087
408TrS	176	-133.63	6.8	0.208	5.57	7.96	21.079	2.328	4.514
408TrS	179	-132.14	22.51	0.241	2.44	8.68	21.863	1.575	5.856
408TrS	190	-135.6	4.87	0.356	4.33	12.0	21.485	2.094	7.923
408TrS	196	-127.95	17.82	0.277	7.21	9.92	21.171	2.772	4.618
408TrS	197	-131.69	3.23	0.3	4.37	11.5	21.132	2.82	3.885
408TrS	207	-108.09	8.19	0.268	5.49	9.29	20.539	1.253	4.422
408TrS	209	-132.45	13.5	0.297	3.91	10.16	20.801	1.158	4.403
408TrS	211	-153.91	23.64	0.235	5.31	8.19	20.836	1.153	5.431
408TrS	225	-110.35	14.72	0.204	3.57	8.12	21.669	2.727	6.864

Table C.15: All candidate disk stars from field 408TrS passing the quality cut.

field	starnum	velocity	velerr	CCmax	$\frac{Signal}{Noise}$	TD	I mag	$V-I$ colour	NaEW
408TrS	30	-121.5	5.99	0.233	1.75	7.52	20.991	1.4	10.436
408TrS	60	-102.46	11.15	0.233	1.93	7.56	21.272	1.406	4.41
408TrS	66	-170.2	37.03	0.182	3.99	6.09	21.039	1.666	3.44
408TrS	74	-104.77	27.19	0.215	3.83	8.63	21.298	1.466	6.948
408TrS	125	-130.41	31.59	0.132	1.94	4.78	21.611	1.444	4.445
408TrS	133	-105.82	31.79	0.176	2.35	6.55	21.755	1.339	8.217
408TrS	138	-150.73	26.45	0.164	2.44	4.73	21.699	1.43	7.328
408TrS	152	-142.95	19.51	0.157	0.96	5.05	21.894	1.342	10.879
408TrS	157	-129.57	25.37	0.26	8.91	9.24	20.623	2.638	2.612
408TrS	166	-122.32	9.0	0.314	1.83	8.88	21.921	1.427	12.791
408TrS	177	-145.48	29.89	0.15	0.82	4.35	20.808	2.604	6.716
408TrS	180	-112.64	26.51	0.225	4.63	8.11	21.48	1.97	3.575
408TrS	210	-114.67	27.69	0.246	4.77	8.65	20.719	1.263	4.49
408TrS	215	-162.69	8.94	0.111	5.07	3.79	20.321	1.904	0.463

408TrS	218	-116.35	5.6	0.463	10.59	12.18	20.052	2.419	4.34
408TrS	219	-132.2	13.1	0.238	7.37	4.06	20.301	2.19	3.129

Table C.16: All candidate disk stars from field 408TrS failing the quality cut.

field	starnum	velocity	velerr	CCmax	$\frac{Signal}{Noise}$	TD	I mag	$V-I$ colour	NaEW
408TrS	25	267.17	6.35	0.237	4.18	7.14	21.171	1.186	8.196
408TrS	72	247.66	19.15	0.323	3.44	11.14	21.56	1.174	11.62
408TrS	158	353.67	20.29	0.093	2.9	3.46	21.703	1.58	2.501
408TrS	163	254.03	6.41	0.231	2.18	7.88	21.718	1.592	9.028
408TrS	169	225.24	14.19	0.119	6.35	4.19	20.637	2.723	0.071
408TrS	178	222.47	13.26	0.201	2.01	6.97	21.208	2.218	9.023
408TrS	181	254.99	10.31	0.213	3.4	8.35	21.79	1.667	0.905
408TrS	212	237.14	6.96	0.304	2.2	10.92	21.73	0.276	8.035

Table C.17: All stars with v_{hel} > -100 km s^{-1} from field 408TrS passing the quality cut.

field	starnum	velocity	velerr	CCmax	$\frac{Signal}{Noise}$	TD	I mag	$V-I$ colour	NaEW
408TrS	38	289.94	26.71	0.128	1.14	4.27	21.498	1.015	8.559
408TrS	55	1888.79	239.76	0.019	2.54	0.31	21.546	1.1	0.197
408TrS	64	230.28	3.04	0.263	1.71	3.44	20.676	2.027	43.131
408TrS	81	252.93	6.31	0.218	0.56	6.17	21.184	1.606	9.839
408TrS	111	282.61	7.44	0.186	1.54	6.61	21.643	1.297	7.153
408TrS	150	184.6	5.52	0.277	1.24	6.04	21.734	1.492	32.721
408TrS	151	203.17	6.42	0.263	0.48	8.11	21.296	1.931	25.035
408TrS	161	271.67	10.42	0.192	1.98	5.86	21.896	1.39	7.09
408TrS	222	277.38	9.36	0.172	0.53	5.79	21.986	0.629	27.159

Table C.18: All stars with v_{hel} > -100 km s^{-1} from field 408TrS failing the quality cut.

field	starnum	velocity	velerr	CCmax	$\frac{Signal}{Noise}$	TD	I mag	$V-I$ colour	NaEW
157Tri	13	-224.41	8.83	0.149	4.26	7.09	21.49	1.246	4.267
157Tri	84	-264.28	13.81	0.054	3.15	4.19	21.409	1.243	5.2
157Tri	109	-225.92	7.42	0.156	3.97	15.92	21.2	1.574	2.832
157Tri	177	-207.38	2.32	0.036	2.07	4.01	21.761	1.352	1.091

Table C.19: All candidate halo stars from field 157Tri passing the quality cut.

field	starnum	velocity	velerr	CCmax	$\frac{Signal}{Noise}$	TD	I mag	$V-I$ colour	NaEW
157Tri	26	-263.49	26.38	0.043	1.39	3.4	21.837	1.152	6.477
157Tri	242	-197.56	6.83	0.136	9.58	11.81	19.831	1.258	1.533
157Tri	245	-248.48	7.22	0.203	9.95	8.18	20.433	1.561	1.843

Table C.20: All candidate halo stars from field 157Tri failing the quality cut.

field	starnum	velocity	velerr	CCmax	$\frac{Signal}{Noise}$	TD	I mag	$V-I$ colour	NaEW
157Tri	7	-138.27	9.68	0.06	4.76	4.29	20.747	1.743	1.922
157Tri	8	-130.05	11.59	0.168	7.56	12.71	20.879	1.63	4.86
157Tri	10	-119.08	10.45	0.152	5.82	7.59	20.974	1.684	3.749
157Tri	14	-155.29	6.01	0.1	6.08	8.71	21.006	1.766	4.122
157Tri	18	-135.01	9.31	0.091	4.54	5.8	21.313	1.574	3.336
157Tri	20	-109.1	5.42	0.112	5.23	5.5	20.855	2.049	2.827
157Tri	21	-153.85	8.8	0.091	5.61	6.44	21.3	1.632	3.573
157Tri	24	-135.32	11.71	0.095	3.9	4.02	21.544	1.415	3.751
157Tri	25	-103.58	9.67	0.103	2.42	3.53	21.61	1.376	3.714
157Tri	27	-164.09	8.96	0.136	3.27	7.4	21.631	1.377	3.5
157Tri	29	-156.47	3.41	0.083	2.82	6.07	21.518	1.508	4.404
157Tri	31	-150.85	3.51	0.087	3.12	3.54	21.447	1.619	3.882
157Tri	33	-133.06	7.76	0.036	3.44	2.01	21.677	1.429	1.507
157Tri	34	-122.53	12.84	0.063	2.71	5.43	21.818	1.324	0.583
157Tri	38	-132.83	7.25	0.061	2.49	6.16	21.89	1.42	1.908
157Tri	47	-113.21	7.48	0.095	4.83	5.21	20.79	1.315	3.592
157Tri	52	-141.74	10.46	0.122	4.83	6.76	21.086	1.119	8.764
157Tri	55	-140.83	15.34	0.081	3.17	7.23	21.107	1.15	6.61
157Tri	58	-174.49	6.72	0.116	4.67	9.42	20.793	1.507	3.809
157Tri	61	-108.47	1.43	0.154	4.37	7.06	20.883	1.529	5.315
157Tri	62	-106.01	1.34	0.055	3.03	7.15	21.06	1.367	4.08
157Tri	63	-104.8	4.99	0.182	5.82	12.55	20.597	1.832	3.086
157Tri	64	-109.71	21.02	0.173	4.72	7.96	20.991	1.471	6.808
157Tri	66	-105.21	12.79	0.144	4.13	8.55	20.958	1.512	5.891
157Tri	71	-121.01	8.99	0.127	4.47	10.61	21.192	1.354	5.25
157Tri	72	-101.23	18.06	0.126	4.95	7.95	20.935	1.615	5.838
157Tri	74	-103.32	12.4	0.178	4.23	5.43	20.602	1.958	5.038
157Tri	75	-104.08	4.17	0.137	6.2	11.66	20.964	1.601	3.277
157Tri	77	-110.1	6.64	0.161	4.92	7.96	20.9	1.684	4.345
157Tri	79	-117.79	14.17	0.08	3.48	4.16	21.056	1.53	8.273
157Tri	83	-155.82	2.86	0.041	3.57	4.16	21.196	1.417	2.944
157Tri	85	-119.62	3.47	0.086	4.71	5.66	21.011	1.644	2.864
157Tri	89	-111.54	9.74	0.133	5.02	8.01	20.87	1.827	4.249
157Tri	92	-166.61	9.67	0.084	5.07	5.53	21.249	1.453	3.914
157Tri	93	-127.33	8.92	0.081	3.9	8.58	21.117	1.591	4.163
157Tri	94	-149.14	10.66	0.033	3.81	4.54	21.087	1.63	2.25
157Tri	97	-107.89	4.68	0.116	5.65	7.88	20.738	1.982	2.992
157Tri	99	-145.01	11.26	0.141	4.55	7.35	21.034	1.695	6.896
157Tri	101	-105.53	3.21	0.141	7.29	8.34	21.002	1.742	3.544
157Tri	103	-112.25	21.74	0.069	4.14	5.61	21.155	1.595	4.94

157Tri	104	-155.29	3.21	0.043	2.9	3.1	21.683	1.069	2.302
157Tri	105	-106.52	1.1	0.079	4.06	5.86	21.065	1.696	4.033
157Tri	110	-111.92	8.23	0.123	5.0	5.77	21.108	1.669	4.229
157Tri	112	-157.86	9.16	0.078	3.31	5.78	21.079	1.708	2.613
157Tri	113	-109.09	2.07	0.082	3.25	5.45	21.13	1.668	3.045
157Tri	115	-142.22	8.68	0.119	4.56	11.82	21.016	1.801	3.704
157Tri	119	-106.0	20.26	0.034	2.16	2.62	21.24	1.604	5.407
157Tri	120	-103.13	9.07	0.149	3.6	11.46	21.213	1.637	4.402
157Tri	126	-148.55	3.89	0.07	3.91	3.76	21.218	1.664	4.674
157Tri	127	-100.78	12.53	0.106	4.25	6.89	21.015	1.868	6.254
157Tri	129	-119.62	10.46	0.037	6.13	3.13	20.587	2.3	2.593
157Tri	134	-114.57	11.4	0.069	3.56	5.79	21.206	1.708	0.573
157Tri	135	-112.11	12.59	0.089	3.79	6.14	21.313	1.608	0.736
157Tri	136	-150.99	8.53	0.102	2.69	7.81	21.441	1.48	7.35
157Tri	137	-128.82	11.06	0.138	4.58	5.33	21.214	1.71	6.743
157Tri	138	-105.98	3.09	0.109	4.11	8.88	21.168	1.775	3.62
157Tri	139	-144.13	13.14	0.084	3.93	6.97	21.243	1.704	1.331
157Tri	140	-147.98	7.86	0.107	3.49	5.8	21.393	1.555	13.72
157Tri	142	-124.67	18.09	0.042	3.61	3.77	21.334	1.626	3.674
157Tri	143	-109.22	6.84	0.094	4.31	7.04	21.12	1.843	4.306
157Tri	145	-109.15	6.28	0.101	4.47	7.07	21.107	1.859	2.626
157Tri	146	-157.62	16.37	0.114	2.51	7.73	21.511	1.465	8.068
157Tri	152	-106.23	4.26	0.086	4.4	5.84	21.131	1.863	1.048
157Tri	155	-108.65	20.37	0.048	3.25	5.5	21.238	1.766	4.409
157Tri	158	-138.23	14.01	0.074	5.1	2.4	21.087	1.929	2.446
157Tri	163	-134.47	3.5	0.057	6.23	2.14	20.81	2.236	0.648
157Tri	165	-153.38	5.76	0.096	2.7	4.93	21.654	1.402	5.744
157Tri	167	-106.28	5.33	0.079	2.65	9.34	21.654	1.412	4.169
157Tri	171	-155.28	3.18	0.068	2.1	7.38	21.771	1.312	6.102
157Tri	172	-124.66	14.11	0.05	2.38	4.83	21.798	1.289	3.564
157Tri	173	-102.24	4.39	0.097	4.08	6.85	20.988	2.109	3.761
157Tri	175	-148.85	2.7	0.091	3.23	6.71	21.487	1.618	3.93
157Tri	178	-110.67	3.25	0.081	4.2	4.25	21.096	2.017	2.631
157Tri	180	-112.91	3.5	0.049	2.33	7.4	21.773	1.344	5.446
157Tri	183	-115.73	15.73	0.038	3.48	2.25	21.171	1.962	0.223
157Tri	184	-113.39	2.3	0.045	2.54	3.13	21.561	1.574	3.17
157Tri	185	-118.36	1.96	0.051	2.55	2.67	21.661	1.479	1.461
157Tri	192	-111.83	9.42	0.141	3.88	9.18	21.143	2.023	8.9
157Tri	197	-112.38	14.37	0.1	4.34	4.17	20.942	2.261	3.124
157Tri	207	-120.72	16.67	0.039	2.03	3.75	21.823	1.464	2.56
157Tri	209	-127.98	13.39	0.093	2.69	5.45	21.921	1.388	1.281
157Tri	213	-118.64	11.12	0.055	2.97	3.42	21.711	1.63	4.327
157Tri	224	-106.58	2.85	0.041	2.01	3.79	21.903	1.532	5.865
157Tri	225	-144.61	21.17	0.109	4.35	4.44	20.83	2.615	1.662
157Tri	229	-125.84	10.96	0.159	2.43	9.89	21.986	1.513	7.52
157Tri	232	-157.09	12.76	0.123	5.3	8.28	21.211	2.325	9.028
157Tri	234	-149.4	5.53	0.276	7.44	10.5	20.618	2.957	5.981
157Tri	239	-125.93	11.72	0.249	11.08	10.8	20.574	3.337	3.682
157Tri	241	-117.6	2.3	0.087	5.32	7.33	21.301	2.697	1.479

Table C.21: All candidate disk stars from field 157Tri passing the quality cut.

field	starnum	velocity	velerr	CCmax	$\frac{Signal}{Noise}$	TD	I mag	$V-I$ colour	NaEW
157Tri	28	-141.38	27.39	0.105	5.55	7.31	21.135	1.875	3.64
157Tri	70	-157.87	4.73	0.006	2.89	0.45	21.313	1.222	0.415
157Tri	117	-167.47	16.84	0.008	3.47	0.51	21.277	1.559	1.769
157Tri	123	-130.16	28.11	0.043	3.21	1.91	21.446	1.426	3.645
157Tri	131	-132.92	29.37	0.071	3.18	5.46	21.431	1.469	4.148
157Tri	133	-146.26	4.79	0.034	2.78	1.96	21.321	1.587	0.866
157Tri	153	-127.45	22.63	0.034	2.09	1.93	21.65	1.344	2.682
157Tri	157	-122.72	4.51	0.043	1.44	3.17	21.782	1.229	1.238
157Tri	169	-116.63	83.05	0.013	1.67	0.96	21.977	1.097	1.124
157Tri	174	-102.81	14.13	0.093	1.93	6.13	21.805	1.298	1.874
157Tri	199	-111.11	6.14	0.03	2.4	1.85	21.898	1.317	3.736
157Tri	200	-141.28	16.16	0.029	2.64	1.66	21.757	1.469	1.198
157Tri	223	-108.18	7.89	0.021	1.47	1.93	21.966	1.462	1.796
157Tri	251	-161.26	6.66	0.019	2.0	1.84	21.856	0.932	2.418
157Tri	252	-115.15	7.89	0.298	12.05	17.3	20.233	2.931	3.767

Table C.22: All candidate disk stars from field 157Tri failing the quality cut.

field	starnum	velocity	velerr	CCmax	$\frac{Signal}{Noise}$	TD	I mag	$V-I$ colour	NaEW
157Tri	11	193.62	6.87	0.092	2.18	7.31	21.614	1.061	0.961
157Tri	15	195.7	13.29	0.081	3.38	5.57	21.45	1.356	0.199
157Tri	16	228.2	22.26	0.07	4.38	5.16	21.117	1.705	1.024
157Tri	17	59.68	6.21	0.047	4.44	3.46	21.394	1.468	1.536
157Tri	23	195.89	9.49	0.073	6.55	5.24	20.706	2.239	0.799
157Tri	30	211.91	12.86	0.068	4.16	3.57	21.638	1.406	2.172
157Tri	40	235.07	13.25	0.063	2.46	5.15	21.958	1.508	4.43
157Tri	42	209.09	12.18	0.059	8.84	4.65	20.708	2.89	0.992
157Tri	50	37.52	16.36	0.102	5.22	6.01	20.687	1.463	0.172
157Tri	78	12.22	5.97	0.053	3.11	4.59	21.374	1.211	1.752
157Tri	87	303.98	18.56	0.067	3.7	2.99	21.195	1.488	1.52
157Tri	88	250.88	4.41	0.08	4.3	5.87	21.125	1.567	6.137
157Tri	108	236.75	7.8	0.031	2.48	2.7	21.506	1.264	7.273
157Tri	144	249.16	1.67	0.1	2.6	7.87	21.723	1.243	10.304
157Tri	149	581.95	7.03	0.032	2.32	2.35	21.565	1.423	0.197
157Tri	151	372.77	11.97	0.047	2.38	2.56	21.89	1.102	0.912
157Tri	168	215.55	5.78	0.163	2.52	6.38	21.664	1.402	8.138
157Tri	170	515.83	10.36	0.046	2.3	2.79	21.888	1.189	6.43
157Tri	179	399.02	14.29	0.047	3.67	2.44	21.407	1.708	6.542
157Tri	201	22.41	10.71	0.096	4.39	6.49	21.139	2.093	0.501
157Tri	211	132.69	7.44	0.057	3.86	3.97	20.954	2.384	3.922
157Tri	221	0.59	22.9	0.111	3.34	5.61	21.52	1.906	0.125
157Tri	226	232.52	12.54	0.088	4.5	3.27	21.117	2.337	1.599

Table C.23: All stars with v_{hel} > -100 km s^{-1} from field 157Tri passing the quality cut.

field	starnum	velocity	velerr	CCmax	$\frac{Signal}{Noise}$	TD	I mag	$V-I$ colour	NaEW
157Tri	22	247.72	17.36	0.029	2.94	1.68	21.72	1.218	6.48
157Tri	32	274.83	14.03	0.044	1.16	5.72	21.782	1.292	16.156
157Tri	36	193.94	12.82	0.042	1.96	2.98	21.894	1.327	11.016
157Tri	37	323.76	9.55	0.04	1.26	4.27	21.987	1.3	40.515
157Tri	39	227.49	10.03	0.114	1.82	9.17	21.905	1.425	1.875
157Tri	43	498.17	21.41	0.034	1.55	2.51	21.865	1.74	5.662
157Tri	44	52.19	11.04	0.025	2.04	1.28	20.504	3.142	3.511
157Tri	45	223.71	21.28	0.056	1.85	4.67	21.519	2.306	1.185
157Tri	128	244.06	6.64	0.047	1.73	3.92	21.696	1.187	1.904
157Tri	132	494.73	21.58	0.005	0.88	0.53	21.871	1.032	46.009
157Tri	156	11.5	131.11	0.02	2.07	2.41	21.903	1.102	5.374
157Tri	160	538.14	27.67	0.058	1.98	2.28	21.753	1.274	3.384
157Tri	162	85.15	73.4	0.031	2.27	2.46	21.73	1.312	1.312
157Tri	164	237.67	41.01	0.042	5.39	2.75	20.925	2.126	3.75
157Tri	181	256.61	9.16	0.042	1.03	3.02	21.839	1.281	14.723
157Tri	196	609.27	153.79	0.007	1.56	0.93	21.9	1.292	2.791
157Tri	202	267.1	18.47	0.038	1.56	3.41	21.794	1.44	0.185
157Tri	205	549.38	24.24	0.008	1.59	0.63	21.989	1.279	0.173
157Tri	210	239.53	191.86	0.02	2.47	2.0	21.618	1.692	4.173
157Tri	216	575.85	11.18	0.009	1.45	0.82	21.706	1.652	0.373
157Tri	231	399.1	290.81	0.022	2.56	3.02	21.329	2.2	2.971
157Tri	237	236.17	31.02	0.021	2.37	3.08	21.214	2.631	2.124
157Tri	243	29.88	4.11	0.341	19.15	19.29	19.017	2.134	1.904
157Tri	244	5.88	6.06	0.208	17.45	11.16	19.538	2.448	1.892

Table C.24: All stars with v_{hel} > -100 km s^{-1} from field 157Tri failing the quality cut.

field	starnum	velocity	velerr	CCmax	$\frac{Signal}{Noise}$	TD	I mag	$V-I$ colour	NaEW
158Tri	7	-180.93	10.42	0.082	3.03	5.74	21.186	1.599	2.928
158Tri	13	-184.45	12.82	0.061	2.59	3.08	21.392	1.514	3.984
158Tri	35	-205.32	2.65	0.085	4.23	5.24	21.137	1.123	1.852
158Tri	38	-235.1	14.67	0.049	2.32	2.67	20.782	1.572	2.908
158Tri	42	-219.46	5.39	0.153	3.1	6.14	21.128	1.368	2.118
158Tri	50	-221.68	9.04	0.091	4.85	3.4	21.086	1.505	0.107

Table C.25: All candidate halo stars from field 158Tri passing the quality cut.

field	starnum	velocity	velerr	CCmax	$\frac{Signal}{Noise}$	TD	I mag	$V-I$ colour	NaEW
158Tri	40	-191.16	6.49	0.03	3.73	1.93	21.226	1.156	1.633
158Tri	137	-221.29	19.73	0.058	1.44	4.93	21.979	1.253	3.484
158Tri	146	-179.74	8.28	0.024	1.48	1.97	21.874	1.418	3.715

158Tri	183	-262.68	11.37	0.04	5.07	2.92	20.116	0.821	1.874
158Tri	184	-218.09	14.69	0.136	10.21	5.07	19.854	1.282	0.568
158Tri	196	-224.49	16.55	0.06	5.59	1.05	20.078	0.883	1.404

Table C.26: All candidate halo stars from field 158Tri failing the quality cut.

field	starnum	velocity	velerr	CCmax	$\frac{Signal}{Noise}$	TD	I mag	$V-I$ colour	NaEW
158Tri	5	-115.42	13.51	0.183	5.0	5.47	20.944	1.537	2.706
158Tri	8	-165.32	7.67	0.055	2.75	4.64	21.272	1.517	3.424
158Tri	9	-116.3	4.89	0.085	2.98	4.03	21.401	1.391	3.673
158Tri	10	-143.87	10.16	0.08	3.0	7.85	21.146	1.721	3.541
158Tri	15	-151.9	17.15	0.041	3.22	2.31	21.655	1.284	3.256
158Tri	17	-138.11	4.34	0.056	2.73	3.16	21.391	1.601	4.214
158Tri	30	-172.52	13.14	0.109	5.55	5.32	21.128	2.836	1.312
158Tri	33	-102.73	8.98	0.057	3.11	3.97	20.99	1.22	0.062
158Tri	34	-103.89	7.61	0.167	4.43	14.51	20.568	1.667	9.38
158Tri	36	-107.5	4.95	0.15	3.75	9.17	20.634	1.663	8.24
158Tri	39	-104.92	17.17	0.103	2.46	5.47	21.259	1.114	0.654
158Tri	46	-134.96	8.91	0.098	3.49	4.14	20.901	1.641	2.46
158Tri	47	-101.53	10.05	0.12	2.4	7.21	21.063	1.5	0.934
158Tri	48	-117.47	6.61	0.153	3.24	10.02	20.823	1.741	11.973
158Tri	51	-126.76	6.62	0.171	5.31	7.93	20.661	1.932	3.885
158Tri	52	-143.51	6.29	0.109	2.02	6.76	21.217	1.38	5.228
158Tri	53	-108.51	7.67	0.216	5.2	10.61	20.774	1.833	6.78
158Tri	55	-110.25	7.72	0.24	7.39	9.56	20.579	2.052	4.156
158Tri	60	-158.37	3.43	0.063	2.64	5.58	21.055	1.646	2.916
158Tri	61	-109.22	3.14	0.113	3.29	10.16	21.167	1.54	1.148
158Tri	62	-116.46	3.46	0.057	2.39	3.77	21.372	1.349	4.114
158Tri	66	-154.04	5.36	0.114	4.16	4.82	20.963	1.776	4.312
158Tri	72	-121.25	12.9	0.06	3.94	2.73	21.023	1.761	0.886
158Tri	76	-151.33	5.73	0.121	3.08	6.29	21.121	1.674	5.988
158Tri	81	-123.64	2.48	0.184	2.19	13.43	21.425	1.41	10.435
158Tri	83	-113.22	6.16	0.179	5.54	10.62	20.961	1.923	2.781
158Tri	86	-133.18	7.91	0.109	2.96	5.11	21.515	1.379	3.413
158Tri	96	-122.04	6.37	0.164	3.82	7.17	21.143	1.8	4.726
158Tri	99	-110.49	8.48	0.216	4.25	10.8	21.047	1.906	4.344
158Tri	100	-116.61	6.62	0.14	3.62	8.06	21.013	1.95	9.216
158Tri	101	-160.19	5.47	0.079	4.1	4.06	21.243	1.74	2.08
158Tri	104	-118.59	9.47	0.104	3.12	4.15	21.218	1.787	5.921
158Tri	105	-118.96	2.96	0.212	3.45	5.85	21.194	1.822	2.478
158Tri	116	-139.97	7.3	0.072	2.32	3.95	21.483	1.589	6.362
158Tri	118	-118.0	6.84	0.059	3.09	3.59	21.229	1.852	4.64
158Tri	119	-165.36	23.36	0.094	3.06	4.09	21.033	2.051	4.989
158Tri	122	-124.97	6.64	0.057	2.33	2.85	21.622	1.521	1.135
158Tri	124	-107.06	17.34	0.064	2.09	4.71	21.504	1.642	5.511
158Tri	127	-157.73	23.32	0.102	2.57	4.7	21.614	1.54	5.087
158Tri	140	-107.27	11.55	0.076	2.44	4.0	21.713	1.543	3.891
158Tri	164	-129.27	21.0	0.081	2.13	5.12	21.705	1.738	2.084

158Tri	170	-150.47	6.35	0.072	2.48	11.3	20.949	2.541	19.182

Table C.27: All candidate disk stars from field 158Tri passing the quality cut.

field	starnum	velocity	velerr	CCmax	$\frac{Signal}{Noise}$	TD	I mag	$V-I$ colour	NaEW
158Tri	63	-144.09	17.05	0.028	2.82	1.9	21.64	1.085	2.393
158Tri	73	-127.91	13.12	0.042	1.5	2.61	21.5	1.285	0.431
158Tri	103	-137.39	28.21	0.045	2.45	2.67	21.672	1.329	0.439
158Tri	150	-174.31	12.27	0.086	1.92	3.11	21.562	1.747	3.046
158Tri	160	-153.56	10.75	0.042	1.52	3.25	21.996	1.387	1.201
158Tri	186	-104.14	4.52	0.134	11.23	8.06	19.199	2.429	1.247
158Tri	193	-107.75	6.48	0.242	10.57	10.58	19.316	0.932	2.22
158Tri	205	-121.76	3.59	0.163	4.5	4.56	20.287	2.188	1.309
158Tri	206	-110.64	14.98	0.069	5.04	5.42	20.495	1.991	2.085
158Tri	209	-129.91	6.0	0.151	2.41	9.41	20.452	2.356	7.522
158Tri	210	-112.48	4.05	0.118	5.92	5.9	20.45	2.476	1.377
158Tri	211	-121.06	12.5	0.211	6.0	13.48	20.481	2.505	4.247

Table C.28: All candidate disk stars from field 158Tri failing the quality cut.

field	starnum	velocity	velerr	CCmax	$\frac{Signal}{Noise}$	TD	I mag	$V-I$ colour	NaEW
158Tri	6	254.77	14.37	0.079	2.4	5.96	21.187	1.322	6.825
158Tri	11	5.57	18.56	0.076	4.28	3.62	20.963	1.914	0.23
158Tri	23	219.49	1.89	0.192	2.13	9.95	21.845	1.465	20.683
158Tri	26	69.34	7.85	0.053	3.72	2.38	21.254	2.188	1.767
158Tri	41	289.06	3.92	0.098	2.89	4.78	20.562	1.914	2.154
158Tri	45	58.33	10.62	0.069	3.53	2.74	20.97	1.547	1.235
158Tri	64	210.49	14.18	0.074	2.95	4.58	21.192	1.544	3.268
158Tri	68	206.99	2.85	0.16	2.46	9.6	21.321	1.429	13.266
158Tri	70	259.71	9.58	0.059	2.37	3.33	21.591	1.192	0.702
158Tri	78	270.54	18.11	0.077	2.91	4.23	21.365	1.439	0.463
158Tri	79	116.63	8.59	0.058	2.22	3.55	21.493	1.325	0.847
158Tri	88	76.42	21.58	0.047	2.01	4.26	21.439	1.46	5.409
158Tri	102	203.64	12.9	0.09	3.03	5.29	21.201	1.785	2.138
158Tri	106	96.51	16.99	0.099	2.38	3.82	20.611	2.411	7.372
158Tri	154	236.89	2.44	0.067	2.21	2.23	21.851	1.49	0.684
158Tri	157	284.02	6.47	0.1	3.44	5.3	20.568	2.786	0.491
158Tri	163	300.18	5.23	0.054	2.36	3.06	21.212	2.225	2.0
158Tri	187	210.7	12.61	0.192	2.44	8.87	21.218	0.434	19.045
158Tri	189	225.83	5.69	0.09	2.14	8.39	21.418	0.58	1.692
158Tri	199	228.53	14.63	0.109	2.27	6.27	20.743	1.094	0.665
158Tri	200	238.27	3.32	0.035	2.72	2.89	20.923	0.98	0.708

Table C.29: All stars with v_{hel} > -100 km s^{-1} from field 158Tri passing the quality cut.

field	starnum	velocity	velerr	CCmax	$\frac{Signal}{Noise}$	TD	I mag	$V-I$ colour	NaEW
158Tri	1	605.62	20.0	-0.008	7.64	-0.2	18.115	1.605	1.164
158Tri	12	241.22	22.11	0.023	2.38	1.72	21.833	1.057	22.367
158Tri	16	431.96	25.84	0.042	2.18	1.46	21.758	1.183	11.309
158Tri	21	239.33	14.1	0.079	1.16	3.74	21.965	1.288	14.929
158Tri	22	192.0	179.62	0.07	2.16	2.59	21.68	1.627	2.957
158Tri	28	245.87	56.55	0.044	3.91	3.05	20.994	2.584	13.725
158Tri	37	545.59	14.02	0.02	3.0	1.17	21.164	1.18	2.946
158Tri	84	43.49	52.24	0.044	2.36	2.41	21.377	1.509	0.647
158Tri	120	406.13	24.84	0.037	3.42	1.51	21.564	1.529	4.882
158Tri	121	274.01	6.23	0.101	1.6	5.57	21.714	1.388	1.039
158Tri	135	373.27	407.55	0.055	1.85	3.61	21.918	1.304	5.815
158Tri	145	441.66	6.16	0.074	1.94	5.11	21.619	1.67	6.211
158Tri	161	165.74	18.86	0.032	2.35	1.31	21.966	1.442	1.289
158Tri	165	273.65	15.65	0.043	1.93	3.66	21.703	1.745	1.546
158Tri	167	635.76	37.42	0.032	3.83	1.41	21.113	2.341	1.897
158Tri	173	200.15	30.6	0.03	4.38	1.09	21.189	2.393	2.07
158Tri	175	35.77	56.02	0.069	4.62	3.0	20.804	2.848	0.309
158Tri	191	214.1	7.72	0.049	7.99	2.96	19.73	2.473	0.143
158Tri	202	9.75	9.15	0.245	9.55	6.54	19.617	2.458	0.92
158Tri	207	228.26	30.49	0.087	4.1	3.66	20.317	2.18	2.74
158Tri	274	236.67	6.47	0.224	1.79	7.79	25.0	0.0	28.345

Table C.30: All stars with v_{hel} > -100 km s^{-1} from field 158Tri failing the quality cut.

field	starnum	velocity	velerr	CCmax	$\frac{Signal}{Noise}$	TD	I mag	$V-I$ colour	NaEW
ec1	6	-249.63	9.8	0.198	2.96	9.22	22.382	1.042	6.349
ec1	7	-194.32	7.36	0.2	3.65	10.22	21.721	1.332	5.346
ec1	13	-203.92	3.49	0.168	3.57	6.88	22.221	1.142	1.453
ec1	15	-272.7	8.69	0.315	6.88	10.51	21.388	1.41	4.86
ec1	30	-180.67	2.99	0.212	4.02	9.27	22.116	1.06	3.009
ec1	69	-243.35	5.35	0.277	6.13	9.61	21.422	1.463	3.568
ec1	74	-197.79	3.33	0.613	13.12	21.47	20.849	1.626	4.968
ec1	77	-247.78	3.04	0.467	11.53	20.73	20.773	1.617	3.835
ec1	94	-229.84	3.0	0.459	8.74	19.71	21.128	1.368	3.5
ec1	175	-223.37	6.45	0.282	8.34	9.68	21.086	1.313	3.515

Table C.31: All candidate halo stars from field ec1 passing the quality cut.

field	starnum	velocity	velerr	CCmax	$\frac{Signal}{Noise}$	TD	I mag	$V-I$ colour	NaEW
ec1	154	-191.73	2.02	0.035	1.74	3.61	22.152	1.274	14.585

Table C.32: All candidate halo stars from field ec1 failing the quality cut.

field	starnum	velocity	velerr	CCmax	$\frac{Signal}{Noise}$	TD	I mag	$V-I$ colour	NaEW
ec1	9	-125.72	10.26	0.116	3.18	4.33	22.173	1.078	0.146
ec1	20	-149.28	7.18	0.092	4.85	10.93	21.151	1.227	2.163
ec1	26	-115.29	5.11	0.501	8.43	18.38	21.341	1.59	4.445
ec1	32	-103.98	2.16	0.636	13.62	24.7	20.711	1.751	5.248
ec1	34	-122.53	8.16	0.459	9.07	14.87	20.998	1.465	4.516
ec1	35	-123.71	3.51	0.305	5.06	16.65	21.768	1.435	5.772
ec1	43	-100.9	7.03	0.264	4.58	14.29	22.046	1.257	5.769
ec1	50	-120.03	5.52	0.132	2.14	5.22	22.347	1.528	3.393
ec1	52	-135.78	4.19	0.466	9.2	17.84	21.261	1.813	6.283
ec1	58	-140.42	4.43	0.22	4.64	11.46	21.705	1.448	6.882
ec1	59	-121.82	10.36	0.308	3.62	9.47	21.903	1.473	8.069
ec1	62	-115.52	4.12	0.37	6.78	14.73	21.473	1.031	3.821
ec1	80	-128.21	6.43	0.166	3.1	10.37	22.22	1.395	5.304
ec1	86	-171.19	11.17	0.193	2.73	15.98	22.19	1.268	9.492
ec1	91	-130.21	6.89	0.283	6.28	11.66	21.532	1.808	3.17
ec1	96	-103.42	4.24	0.283	3.45	9.5	21.987	1.116	4.844
ec1	98	-121.06	4.63	0.254	4.77	13.04	21.823	1.35	4.562
ec1	105	-113.87	5.9	0.272	5.81	9.16	21.619	1.67	4.504
ec1	106	-104.13	4.4	0.289	4.92	12.38	21.674	1.456	3.654
ec1	108	-108.0	6.96	0.43	6.99	21.18	21.523	1.545	5.582
ec1	109	-124.52	21.52	0.169	3.32	8.42	21.69	1.266	8.258
ec1	112	-116.86	9.37	0.41	8.07	19.83	21.428	1.516	5.377
ec1	113	-135.02	4.83	0.289	4.71	9.62	21.907	1.387	5.032
ec1	114	-112.13	7.51	0.468	8.46	25.31	21.217	1.628	5.767
ec1	117	-116.06	8.22	0.266	5.36	17.39	21.53	1.694	5.351
ec1	118	-113.2	17.02	0.291	5.38	13.32	21.415	1.421	2.136
ec1	123	-102.95	10.37	0.27	3.58	9.43	22.349	1.213	2.753
ec1	124	-152.94	10.47	0.132	2.59	8.57	22.26	1.445	4.979
ec1	137	-116.03	11.78	0.174	7.97	3.89	20.765	1.991	1.941
ec1	138	-116.42	6.34	0.297	4.15	14.09	21.973	1.365	7.116
ec1	143	-117.83	5.31	0.132	3.87	6.68	22.029	1.27	1.33
ec1	144	-103.77	18.08	0.081	5.13	4.34	21.552	1.505	0.682
ec1	147	-112.73	3.08	0.247	3.63	9.64	22.082	1.394	7.712
ec1	150	-117.94	5.25	0.356	6.95	12.28	21.35	1.439	5.655
ec1	151	-109.76	2.97	0.175	2.68	8.03	22.271	1.344	5.956
ec1	152	-118.29	2.27	0.19	3.64	9.12	22.018	1.43	4.719
ec1	153	-114.86	4.09	0.228	2.97	7.81	22.376	1.37	5.517
ec1	155	-107.62	4.78	0.249	3.94	8.89	21.99	1.165	4.409
ec1	156	-108.21	1.9	0.379	4.69	21.04	21.795	1.535	6.301
ec1	160	-114.22	13.13	0.394	7.47	14.3	21.335	1.982	5.936
ec1	162	-164.8	4.93	0.192	3.1	8.75	22.037	1.269	4.149
ec1	164	-111.85	3.81	0.457	7.37	20.95	21.126	1.515	5.386
ec1	166	-104.11	4.64	0.169	7.57	4.03	20.724	2.39	1.878
ec1	167	-100.23	6.81	0.333	4.71	13.45	21.809	1.605	5.351

ec1	168	-138.98	3.72	0.066	3.46	5.4	21.677	0.933	3.287
ec1	170	-110.26	2.74	0.494	7.17	19.3	21.321	1.429	5.501
ec1	174	-107.03	5.05	0.28	4.95	11.13	21.765	1.639	5.012
ec1	180	-114.81	6.67	0.253	7.77	8.83	21.548	1.528	5.739

Table C.33: All candidate disk stars from field ec1 passing the quality cut.

field	starnum	velocity	velerr	CCmax	$\frac{Signal}{Noise}$	TD	I mag	$V-I$ colour	NaEW
ec1	4	-166.46	31.92	0.009	5.67	1.56	22.288	1.138	0.945
ec1	127	-152.04	4.51	0.15	3.51	5.81	20.419	0.84	1.894

Table C.34: All candidate disk stars from field ec1 failing the quality cut.

field	starnum	velocity	velerr	CCmax	$\frac{Signal}{Noise}$	TD	I mag	$V-I$ colour	NaEW
ec1	23	256.75	11.14	0.146	2.89	5.31	21.679	1.652	3.352
ec1	27	993.19	3.14	0.055	13.12	6.23	20.727	1.113	0.475
ec1	36	394.34	16.53	0.071	6.79	3.74	21.573	1.869	0.257
ec1	49	9.09	14.46	0.116	3.39	5.32	21.127	2.584	0.303
ec1	51	396.04	12.87	0.089	8.33	5.87	21.163	1.882	0.362
ec1	57	670.74	20.39	0.081	13.08	2.77	20.641	2.118	0.074
ec1	67	228.87	19.05	0.162	3.63	11.8	21.909	1.16	3.828
ec1	72	219.57	2.57	0.057	2.25	2.38	22.149	1.238	1.797
ec1	83	243.95	7.87	0.162	4.18	6.94	21.673	0.97	3.337
ec1	121	254.16	10.72	0.121	3.46	5.83	21.67	1.586	2.495
ec1	135	207.53	12.86	0.111	9.87	3.78	20.741	0.782	0.543
ec1	178	240.12	5.32	0.113	31.5	4.66	21.713	1.514	1.389

Table C.35: All stars with $v_{hel} >$ -100 km s^{-1} from field ec1 passing the quality cut.

field	starnum	velocity	velerr	CCmax	$\frac{Signal}{Noise}$	TD	I mag	$V-I$ colour	NaEW
ec1	107	262.58	5.75	0.054	1.6	7.11	22.448	1.184	7.135

Table C.36: All stars with $v_{hel} >$ -100 km s^{-1} from field ec1 failing the quality cut.

field	starnum	velocity	velerr	CCmax	$\frac{Signal}{Noise}$	TD	I mag	$V-I$ colour	NaEW
ec2	5	-236.18	3.59	0.516	14.86	15.77	0.0	0.0	2.684
ec2	37	-242.59	16.15	0.146	3.28	7.61	0.0	0.0	1.186

Table C.37: All candidate halo stars from field ec2 failing the quality cut.

field	starnum	velocity	velerr	CCmax	$\frac{Signal}{Noise}$	TD	I mag	$V-I$ colour	NaEW
ec2	12	-116.13	4.68	0.36	4.02	14.49	0.0	0.0	8.157
ec2	18	-160.5	4.97	0.114	3.42	5.43	0.0	0.0	1.196
ec2	21	-152.39	4.19	0.129	2.87	5.61	0.0	0.0	3.471
ec2	28	-118.14	17.8	0.163	4.06	6.12	0.0	0.0	1.121
ec2	30	-107.37	15.72	0.116	3.64	4.43	0.0	0.0	1.649
ec2	49	-129.45	7.21	0.256	3.79	10.19	0.0	0.0	2.516
ec2	55	-135.97	7.42	0.101	2.66	4.85	0.0	0.0	1.615
ec2	80	-101.41	4.18	0.292	4.41	13.77	0.0	0.0	6.49

Table C.38: All candidate disk stars from field ec2 failing the quality cut.

field	starnum	velocity	velerr	CCmax	$\frac{Signal}{Noise}$	TD	I mag	$V-I$ colour	NaEW
ec2	7	254.37	1.65	0.059	-0.31	2.18	0.0	0.0	0.0
ec2	9	261.69	20.18	0.124	2.3	5.24	0.0	0.0	0.44
ec2	20	474.34	14.73	0.06	1.44	2.7	0.0	0.0	3.493
ec2	24	270.84	9.34	0.136	2.32	5.24	0.0	0.0	3.613
ec2	38	95.06	11.19	0.057	1.13	3.51	0.0	0.0	0.339
ec2	40	105.66	10.28	0.176	4.04	8.19	0.0	0.0	2.419
ec2	43	908.04	8.74	0.083	2.27	3.19	0.0	0.0	0.764
ec2	47	277.62	16.0	0.092	2.61	3.52	0.0	0.0	3.833
ec2	48	231.53	10.55	0.179	7.27	5.61	0.0	0.0	2.458
ec2	52	259.34	8.75	0.126	3.33	6.63	0.0	0.0	0.924
ec2	60	128.86	30.34	0.093	1.85	3.69	0.0	0.0	2.354
ec2	66	168.53	4.01	0.082	5.13	3.3	0.0	0.0	1.225
ec2	70	233.02	24.49	0.071	4.17	3.34	0.0	0.0	1.458

Table C.39: All stars with $v_{hel} >$ -100 km s^{-1} from field ec2 failing the quality cut.

field	starnum	velocity	velerr	CCmax	$\frac{Signal}{Noise}$	TD	I mag	$V-I$ colour	NaEW
409TrS	5	-161.85	8.27	0.27	4.73	9.52	20.846	1.196	6.437
409TrS	60	-115.24	9.25	0.241	4.29	9.96	21.0	1.597	5.416
409TrS	81	-156.41	19.45	0.175	4.48	5.81	21.026	1.718	5.601
409TrS	83	-175.63	10.9	0.225	2.73	5.61	21.189	1.557	6.803
409TrS	93	-115.0	14.71	0.234	3.83	7.04	21.201	1.611	6.126
409TrS	106	-149.07	8.58	0.29	2.4	9.54	21.381	1.501	9.901
409TrS	123	-139.18	22.84	0.203	2.18	5.59	21.211	1.775	7.372

409TrS	132	-155.27	5.77	0.344	4.79	10.2	20.984	2.063	6.038
409TrS	148	-106.45	9.46	0.187	2.62	6.69	21.723	1.425	7.167
409TrS	150	-150.88	23.2	0.237	2.47	7.13	21.617	1.573	9.331
409TrS	166	-154.14	15.02	0.202	2.97	6.3	21.711	1.627	7.056
409TrS	172	-116.77	8.93	0.214	2.26	6.09	21.623	1.851	8.954
409TrS	186	-167.76	14.82	0.192	4.35	5.45	21.249	2.596	7.572

Table C.40: All candidate halo stars from field 409TrS passing the quality cut.

field	starnum	velocity	velerr	CCmax	$\frac{Signal}{Noise}$	TD	I mag	$V-I$ colour	NaEW
409TrS	74	-166.51	51.28	0.195	3.11	7.33	21.189	1.507	6.377
409TrS	76	-126.02	37.94	0.171	3.99	4.02	20.82	1.886	3.828
409TrS	114	-104.96	10.91	0.209	1.13	6.38	21.833	1.094	9.775
409TrS	168	-155.49	13.78	0.168	1.28	4.55	21.79	1.556	6.127
409TrS	171	-148.49	11.53	0.214	1.71	6.61	21.783	1.68	6.072
409TrS	193	-154.95	30.56	0.225	7.85	5.34	20.215	0.297	4.559

Table C.41: All candidate halo stars from field 409TrS failing the quality cut.

field	starnum	velocity	velerr	CCmax	$\frac{Signal}{Noise}$	TD	I mag	$V-I$ colour	NaEW
409TrS	9	-240.08	15.86	0.303	3.17	12.26	21.034	1.11	7.119
409TrS	10	-267.7	15.17	0.226	4.37	8.57	20.937	1.224	6.316
409TrS	11	-209.95	15.77	0.198	4.18	7.13	20.982	1.206	4.319
409TrS	12	-269.59	23.09	0.247	3.78	9.34	20.963	1.227	4.823
409TrS	14	-191.13	7.35	0.233	5.61	5.89	20.949	1.251	5.201
409TrS	15	-217.63	11.4	0.213	3.52	7.27	20.945	1.271	7.031
409TrS	18	-242.03	5.97	0.237	3.37	8.21	21.133	1.115	7.366
409TrS	21	-231.65	15.1	0.244	6.19	8.31	20.739	1.561	4.138
409TrS	22	-288.74	13.68	0.237	4.19	8.51	20.9	1.409	4.494
409TrS	23	-229.23	14.18	0.301	4.97	8.7	20.968	1.351	4.632
409TrS	24	-186.8	5.11	0.267	4.98	11.2	21.109	1.215	5.411
409TrS	27	-243.57	7.49	0.313	4.86	9.51	20.865	1.473	4.638
409TrS	28	-195.45	5.78	0.233	3.36	6.66	21.121	1.217	5.924
409TrS	32	-241.6	8.7	0.269	4.88	8.1	20.977	1.415	3.983
409TrS	34	-248.82	18.47	0.236	4.32	8.49	21.037	1.364	6.347
409TrS	35	-227.7	7.43	0.366	7.45	11.16	20.604	1.808	4.999
409TrS	40	-248.82	13.26	0.294	6.68	8.79	20.764	1.675	5.503
409TrS	41	-299.33	19.35	0.189	2.84	5.49	20.994	1.459	7.959
409TrS	43	-220.69	17.55	0.205	4.98	6.74	20.909	1.545	6.205
409TrS	44	-213.18	8.14	0.415	5.84	16.87	20.976	1.511	4.308
409TrS	45	-293.08	15.47	0.331	7.18	12.89	20.708	1.79	3.393
409TrS	46	-282.4	13.01	0.228	5.36	6.46	20.953	1.551	3.453
409TrS	47	-224.76	16.03	0.273	4.07	7.84	20.899	1.605	7.001
409TrS	48	-195.07	20.98	0.226	3.87	5.98	20.629	1.879	9.969
409TrS	51	-223.22	13.83	0.223	3.07	5.95	20.989	1.546	5.263

409TrS	52	-238.99	23.34	0.209	4.34	6.79	21.045	1.498	4.515
409TrS	53	-271.72	11.23	0.398	6.68	12.27	20.844	1.701	6.917
409TrS	57	-260.91	18.85	0.191	2.12	5.88	21.259	1.325	8.704
409TrS	61	-272.05	21.07	0.2	4.52	6.93	21.046	1.569	5.162
409TrS	62	-233.88	20.27	0.306	3.65	10.7	20.916	1.701	7.992
409TrS	63	-274.09	5.9	0.347	5.27	10.56	21.012	1.612	4.168
409TrS	64	-254.68	18.88	0.197	6.48	5.93	20.757	1.867	1.199
409TrS	65	-226.77	16.49	0.294	4.65	10.65	20.998	1.627	6.781
409TrS	69	-230.2	10.37	0.254	4.91	7.96	21.118	1.528	7.471
409TrS	71	-228.06	12.35	0.265	3.11	7.78	21.174	1.51	6.107
409TrS	72	-231.55	21.96	0.252	3.32	10.3	20.858	1.834	7.194
409TrS	75	-236.69	15.16	0.224	4.05	6.77	21.086	1.61	5.2
409TrS	77	-262.73	17.62	0.293	3.95	9.55	21.013	1.693	5.248
409TrS	78	-258.98	7.55	0.168	2.23	5.05	21.435	1.272	3.607
409TrS	79	-227.7	13.55	0.22	5.27	7.33	21.033	1.682	6.626
409TrS	82	-226.69	8.33	0.225	5.12	7.9	21.145	1.599	3.739
409TrS	85	-198.89	6.33	0.324	4.41	10.67	20.911	1.855	6.558
409TrS	86	-299.2	13.93	0.238	4.69	8.03	21.249	1.536	4.539
409TrS	87	-258.61	10.62	0.205	3.28	6.42	21.199	1.587	4.205
409TrS	90	-195.14	9.91	0.257	5.43	6.8	20.661	2.131	6.358
409TrS	91	-262.8	4.58	0.231	2.49	8.82	21.363	1.441	11.952
409TrS	96	-210.19	9.07	0.262	4.37	7.5	21.146	1.679	6.667
409TrS	98	-254.45	13.71	0.358	4.75	11.23	21.069	1.763	5.471
409TrS	99	-179.77	7.34	0.356	7.49	12.36	20.693	2.148	5.756
409TrS	102	-216.87	4.8	0.224	5.99	5.72	20.909	1.957	5.241
409TrS	103	-231.06	21.48	0.272	5.95	8.72	21.08	1.787	5.716
409TrS	104	-292.1	20.34	0.231	5.83	8.88	20.74	2.128	2.711
409TrS	105	-252.33	7.58	0.216	4.18	7.87	20.98	1.902	3.52
409TrS	109	-231.85	10.35	0.159	2.8	6.12	21.511	1.39	2.705
409TrS	111	-181.42	19.6	0.223	5.61	6.91	21.13	1.775	3.316
409TrS	113	-249.79	13.9	0.309	7.47	11.56	20.623	2.3	4.654
409TrS	115	-261.79	11.62	0.216	2.83	7.0	21.462	1.471	7.749
409TrS	117	-296.87	9.95	0.268	3.93	8.42	21.103	1.838	4.286
409TrS	118	-222.87	4.79	0.495	9.58	15.08	20.594	2.349	4.604
409TrS	120	-254.94	18.18	0.401	8.95	10.38	20.579	2.373	4.972
409TrS	126	-232.28	10.96	0.252	2.6	7.75	21.448	1.541	8.509
409TrS	133	-266.47	24.93	0.166	3.76	5.05	21.496	1.568	2.229
409TrS	136	-180.07	12.71	0.29	5.2	9.24	21.055	2.02	5.909
409TrS	137	-234.57	8.0	0.287	4.35	9.82	21.177	1.91	5.647
409TrS	141	-195.8	7.91	0.272	3.38	9.22	21.247	1.867	7.884
409TrS	143	-240.25	6.89	0.369	5.61	10.36	20.677	2.444	4.559
409TrS	144	-253.63	17.6	0.224	2.81	6.7	21.359	1.763	13.255
409TrS	145	-278.41	5.54	0.346	5.21	12.3	21.206	1.919	7.242
409TrS	149	-225.19	18.59	0.294	6.4	8.79	20.551	2.611	4.93
409TrS	151	-179.2	4.96	0.309	5.67	9.13	21.089	2.105	4.823
409TrS	155	-243.48	17.05	0.133	4.6	4.91	21.156	2.056	2.979
409TrS	158	-267.11	8.06	0.345	7.14	10.31	20.737	2.483	3.838
409TrS	159	-208.7	11.57	0.289	5.09	9.09	21.038	2.196	6.233
409TrS	160	-254.95	13.84	0.204	2.56	6.54	21.562	1.689	6.788
409TrS	161	-274.53	19.9	0.235	3.25	7.48	21.47	1.802	6.286
409TrS	163	-266.13	9.81	0.238	5.45	6.95	21.123	2.158	5.861
409TrS	165	-237.76	6.62	0.232	2.86	8.36	21.888	1.445	10.784

409TrS	167	-210.12	7.7	0.303	4.19	9.98	21.443	1.902	6.896
409TrS	170	-264.95	13.21	0.206	2.29	7.42	21.593	1.812	5.287
409TrS	175	-251.38	9.73	0.378	8.11	10.75	20.679	2.817	4.321
409TrS	178	-267.22	9.23	0.325	6.12	10.68	21.177	2.375	3.767
409TrS	181	-228.43	23.92	0.135	2.95	4.46	21.753	1.92	5.113
409TrS	183	-239.92	8.78	0.323	6.18	9.69	20.953	2.775	4.266
409TrS	184	-233.26	16.91	0.167	3.05	4.43	21.703	2.04	1.292
409TrS	185	-245.58	7.8	0.369	7.15	12.35	20.87	2.911	3.423
409TrS	189	-197.1	14.55	0.269	3.1	10.16	21.686	2.217	8.724
409TrS	190	-196.04	5.81	0.242	2.66	8.01	21.774	2.22	2.113
409TrS	212	-242.32	23.14	0.24	3.51	8.77	21.349	1.014	0.478
409TrS	216	-185.9	4.48	0.227	3.26	7.02	21.35	2.669	6.672

Table C.42: All candidate disk stars from field 409TrS passing the quality cut.

field	starnum	velocity	velerr	CCmax	$\frac{Signal}{Noise}$	TD	I mag	$V-I$ colour	NaEW
409TrS	7	-234.77	27.54	0.254	5.38	8.52	20.817	1.294	5.82
409TrS	13	-192.64	44.05	0.165	2.9	5.31	20.979	1.217	2.453
409TrS	42	-206.23	26.45	0.219	2.47	7.93	21.097	1.357	5.132
409TrS	50	-186.23	8.71	0.185	5.25	7.74	20.497	2.038	1.792
409TrS	80	-234.98	26.61	0.171	4.05	5.69	21.128	1.597	6.913
409TrS	84	-297.71	45.9	0.161	2.59	4.84	21.355	1.392	6.059
409TrS	116	-232.38	35.67	0.186	5.91	6.02	20.738	2.197	3.06
409TrS	127	-216.31	38.66	0.141	0.96	4.09	21.788	1.209	7.436
409TrS	138	-291.91	21.24	0.179	1.36	5.85	21.956	1.145	13.215
409TrS	146	-274.16	4.99	0.475	10.29	15.64	20.464	2.682	5.062
409TrS	152	-213.46	35.23	0.207	2.73	5.98	21.771	1.424	3.979
409TrS	180	-205.7	35.54	0.237	3.07	6.97	21.128	2.526	5.373
409TrS	195	-216.4	10.42	0.327	7.99	14.75	19.953	0.691	3.788
409TrS	196	-248.48	3.94	0.654	17.29	20.56	19.301	1.381	6.18
409TrS	202	-277.06	14.55	0.265	9.21	6.37	19.857	1.467	4.385
409TrS	204	-258.22	5.2	0.542	11.2	19.0	19.889	1.632	6.121
409TrS	205	-264.39	10.64	0.566	12.46	16.66	19.997	1.565	5.162
409TrS	206	-260.22	7.05	0.415	8.79	13.82	20.061	1.521	4.228
409TrS	214	-275.17	8.22	0.39	9.76	11.69	20.351	2.135	4.082
409TrS	215	-261.96	8.13	0.426	8.97	10.92	20.408	2.404	4.613
409TrS	219	-274.89	7.54	0.124	7.06	2.85	20.455	3.683	2.704

Table C.43: All candidate disk stars from field 409TrS failing the quality cut.

field	starnum	velocity	velerr	CCmax	$\frac{Signal}{Noise}$	TD	I mag	$V-I$ colour	NaEW
409TrS	38	250.74	19.56	0.158	2.65	5.33	21.002	1.422	1.696
409TrS	59	261.96	23.47	0.166	4.51	5.95	20.862	1.732	5.057
409TrS	67	2138.15	20.9	0.307	6.02	13.54	20.82	1.808	0.558
409TrS	97	246.23	12.35	0.302	2.34	8.45	21.521	1.306	7.082

409TrS	139	200.33	19.47	0.152	2.08	5.67	21.616	1.492	6.382
409TrS	154	205.51	4.1	0.225	3.22	5.58	21.644	1.568	9.549
409TrS	169	234.98	7.5	0.226	6.4	5.84	20.812	2.547	0.585

Table C.44: All stars with v_{hel} > -100 km s^{-1} from field 409TrS passing the quality cut.

field	starnum	velocity	velerr	CCmax	$\frac{Signal}{Noise}$	TD	I mag	$V-I$ colour	NaEW
409TrS	17	265.46	39.13	0.208	3.52	7.83	21.079	1.149	4.466
409TrS	73	2344.79	26.69	0.035	5.47	1.15	20.978	1.717	1.088
409TrS	107	224.15	23.3	0.18	1.1	5.26	21.258	1.638	10.582
409TrS	134	207.44	6.37	0.219	1.77	7.95	21.902	1.169	5.881
409TrS	142	377.65	25.43	0.162	2.97	5.68	21.697	1.417	1.753
409TrS	156	213.95	19.8	0.266	1.53	6.03	21.046	2.169	28.762
409TrS	162	281.28	4.93	0.185	1.23	7.26	21.882	1.399	9.146
409TrS	194	222.04	43.26	0.079	6.17	2.92	20.376	0.194	0.5
409TrS	201	137.85	27.49	0.207	5.88	5.08	20.665	0.6	3.441
409TrS	203	9.31	7.18	0.297	14.41	10.17	19.644	1.828	1.332
409TrS	217	332.33	10.16	0.154	0.89	4.84	20.439	3.664	3.987

Table C.45: All stars with v_{hel} > -100 km s^{-1} from field 409TrS failing the quality cut.

field	starnum	velocity	velerr	CCmax	$\frac{Signal}{Noise}$	TD	I mag	$V-I$ colour	NaEW
412TrS	12	-160.77	11.03	0.291	5.93	9.53	20.835	1.439	1.67
412TrS	43	-158.86	16.17	0.22	4.75	8.38	21.225	1.489	4.269
412TrS	100	-177.5	11.98	0.229	2.65	8.08	21.908	1.169	4.378
412TrS	103	-138.42	9.93	0.227	2.5	6.07	21.915	1.186	9.613

Table C.46: All candidate halo stars from field 412TrS passing the quality cut.

field	starnum	velocity	velerr	CCmax	$\frac{Signal}{Noise}$	TD	I mag	$V-I$ colour	NaEW
412TrS	25	-117.04	13.12	0.202	8.61	5.34	20.495	1.999	2.184
412TrS	85	-152.55	13.93	0.259	1.97	7.97	21.952	1.064	9.472
412TrS	112	-159.84	44.29	0.197	3.05	7.76	21.907	1.333	4.094
412TrS	132	-178.04	9.51	0.416	21.25	8.17	19.236	0.062	5.474

Table C.47: All candidate halo stars from field 412TrS failing the quality cut.

field	starnum	velocity	velerr	CCmax	$\frac{Signal}{Noise}$	TD	I mag	$V-I$ colour	NaEW
412TrS	5	-258.18	18.14	0.306	4.48	10.31	21.128	1.548	4.771
412TrS	6	-268.06	21.96	0.24	5.3	7.36	21.128	1.549	7.747
412TrS	7	-253.6	23.18	0.287	4.44	9.15	21.207	1.535	4.305
412TrS	8	-242.94	9.18	0.372	5.93	13.21	21.104	1.712	4.645
412TrS	11	-245.85	5.28	0.531	10.46	17.95	20.508	1.685	4.734
412TrS	14	-248.93	21.2	0.43	6.9	14.2	21.036	1.306	4.48
412TrS	15	-248.92	3.65	0.34	6.31	9.93	21.149	1.215	5.073
412TrS	16	-249.73	4.31	0.26	5.72	8.26	21.098	1.31	4.008
412TrS	17	-291.16	5.98	0.362	6.87	12.33	20.871	1.547	6.715
412TrS	18	-248.1	24.68	0.191	4.87	7.02	20.952	1.477	4.104
412TrS	19	-250.76	23.14	0.333	6.25	11.13	20.97	1.473	3.343
412TrS	20	-275.39	9.16	0.375	7.21	13.53	20.83	1.613	5.231
412TrS	21	-250.67	12.89	0.513	10.67	16.18	20.669	1.781	5.667
412TrS	22	-263.49	14.11	0.324	6.28	8.87	21.06	1.413	5.922
412TrS	23	-271.8	7.47	0.254	4.99	9.51	21.189	1.289	3.207
412TrS	24	-238.19	11.94	0.354	6.03	9.42	20.902	1.584	5.957
412TrS	26	-294.97	4.97	0.448	7.58	12.03	20.8	1.699	4.888
412TrS	27	-214.83	11.0	0.324	5.71	12.02	21.002	1.51	4.504
412TrS	28	-234.16	6.32	0.524	10.85	15.29	20.663	1.855	5.688
412TrS	29	-193.88	14.77	0.275	6.67	9.07	21.158	1.392	2.763
412TrS	30	-254.93	15.11	0.397	6.92	12.92	20.887	1.669	4.265
412TrS	31	-229.14	10.42	0.352	5.32	13.11	21.003	1.561	4.119
412TrS	32	-274.01	16.62	0.377	6.59	12.13	21.061	1.514	5.054
412TrS	36	-249.19	11.56	0.208	5.71	8.18	21.111	1.516	3.556
412TrS	37	-245.09	6.68	0.435	10.05	14.2	20.694	1.95	5.422
412TrS	38	-224.69	4.37	0.375	6.11	12.61	21.183	1.479	5.014
412TrS	39	-259.32	11.98	0.35	6.18	12.65	21.091	1.602	3.437
412TrS	40	-192.8	22.95	0.331	5.03	12.79	21.096	1.599	4.21
412TrS	41	-245.81	9.73	0.365	6.33	10.74	21.16	1.536	5.691
412TrS	42	-229.68	12.19	0.257	6.71	7.48	21.17	1.532	5.081
412TrS	44	-272.21	7.71	0.313	7.05	8.48	21.012	1.703	5.112
412TrS	45	-250.31	14.52	0.191	4.46	5.62	21.083	1.634	4.124
412TrS	47	-284.04	8.79	0.28	4.86	10.46	21.19	1.535	6.65
412TrS	48	-231.81	18.8	0.339	5.56	11.39	21.297	1.446	4.903
412TrS	49	-199.98	17.53	0.34	6.38	9.16	21.15	1.596	6.667
412TrS	50	-271.82	17.33	0.316	6.97	9.88	20.93	1.816	4.925
412TrS	51	-209.78	14.73	0.514	9.48	18.03	20.95	1.8	6.482
412TrS	53	-297.36	17.61	0.269	4.65	8.7	21.258	1.503	6.792
412TrS	54	-246.81	13.76	0.367	4.96	11.5	21.245	1.526	5.599
412TrS	55	-216.52	15.61	0.216	4.24	5.74	21.314	1.465	5.167
412TrS	56	-237.33	21.45	0.238	4.41	8.69	21.411	1.374	5.049
412TrS	59	-257.8	10.54	0.258	5.14	9.12	21.226	1.588	4.069
412TrS	61	-272.88	17.84	0.282	4.87	8.93	21.061	1.76	6.817
412TrS	62	-235.47	18.82	0.211	4.62	6.83	21.405	1.429	2.2
412TrS	63	-225.3	15.41	0.181	4.12	6.14	21.529	1.306	4.385
412TrS	64	-235.55	11.43	0.197	6.0	6.49	20.946	1.897	3.564
412TrS	66	-212.35	9.31	0.31	6.92	10.99	21.062	1.788	3.51
412TrS	67	-252.48	18.8	0.22	4.38	7.17	21.607	1.252	5.339
412TrS	68	-265.09	17.44	0.218	5.27	6.62	21.123	1.736	5.542
412TrS	69	-263.77	13.88	0.322	6.37	9.73	21.154	1.733	3.914

412TrS	71	-278.2	15.47	0.306	6.82	10.81	21.093	1.814	5.854
412TrS	72	-271.43	13.35	0.185	5.47	7.06	21.107	1.815	3.597
412TrS	73	-247.11	7.5	0.305	6.84	8.31	21.142	1.781	6.427
412TrS	74	-205.52	8.67	0.243	4.96	7.18	21.247	1.676	6.977
412TrS	76	-259.25	5.68	0.343	6.51	12.29	21.198	1.748	5.297
412TrS	77	-219.51	23.37	0.278	5.99	7.55	21.33	1.621	3.966
412TrS	78	-245.98	21.02	0.186	2.85	5.4	21.798	1.161	5.711
412TrS	80	-219.31	11.06	0.274	6.42	7.96	21.072	1.905	3.706
412TrS	81	-263.12	16.73	0.159	3.58	6.41	21.726	1.255	5.454
412TrS	83	-251.94	15.58	0.324	3.5	9.17	21.501	1.49	7.952
412TrS	84	-236.49	10.97	0.245	4.72	7.26	21.591	1.416	4.597
412TrS	86	-233.28	12.7	0.226	4.37	7.82	21.516	1.501	5.731
412TrS	87	-231.14	3.87	0.322	3.03	11.61	21.735	1.295	9.945
412TrS	88	-248.49	6.02	0.457	6.0	14.29	21.133	1.9	6.43
412TrS	89	-214.56	8.21	0.273	4.15	6.81	21.563	1.473	6.339
412TrS	90	-238.82	6.21	0.255	4.08	9.47	21.388	1.653	5.804
412TrS	91	-238.81	6.8	0.325	6.47	10.9	21.115	1.93	5.461
412TrS	96	-233.75	21.26	0.195	2.57	7.09	21.958	1.108	4.588
412TrS	97	-254.59	16.33	0.213	4.09	7.44	21.313	1.753	4.176
412TrS	101	-242.28	10.46	0.133	5.74	12.56	21.136	1.957	5.692
412TrS	102	-224.4	7.61	0.227	3.17	6.77	21.659	1.438	4.849
412TrS	104	-249.73	17.4	0.298	3.31	11.16	21.9	1.206	6.486
412TrS	107	-281.42	19.31	0.148	2.39	5.07	21.821	1.316	5.958
412TrS	108	-220.89	7.24	0.201	3.3	4.42	21.694	1.482	2.342
412TrS	109	-230.95	10.64	0.486	13.1	15.57	20.624	2.56	5.354
412TrS	114	-264.22	18.73	0.165	3.01	5.04	21.892	1.375	3.837
412TrS	116	-207.01	12.08	0.202	3.93	6.34	21.765	1.509	4.743
412TrS	117	-252.74	14.76	0.338	4.7	11.37	21.671	1.628	4.383
412TrS	122	-247.54	16.89	0.185	2.33	6.8	21.946	1.509	10.586
412TrS	123	-209.18	21.38	0.147	7.64	2.85	20.968	2.552	3.681
412TrS	141	-221.33	12.18	0.266	6.9	8.78	20.587	1.042	4.11
412TrS	143	-246.55	8.62	0.327	5.04	9.83	20.77	1.052	5.809
412TrS	145	-225.53	10.63	0.349	9.21	11.37	20.503	1.45	4.802

Table C.48: All candidate disk stars from field 412TrS passing the quality cut.

field	starnum	velocity	velerr	CCmax	$\frac{Signal}{Noise}$	TD	I mag	$V-I$ colour	NaEW
412TrS	46	-214.82	35.96	0.254	5.99	6.89	21.114	1.605	4.431
412TrS	58	-292.81	36.16	0.297	5.27	9.56	21.186	1.62	6.329
412TrS	60	-252.62	36.29	0.212	4.55	6.17	21.195	1.623	4.437
412TrS	65	-235.19	54.2	0.178	3.71	6.21	21.508	1.341	7.165
412TrS	70	-196.83	37.85	0.262	3.73	7.39	21.251	1.644	5.857
412TrS	79	-263.61	11.86	0.272	8.29	4.53	20.493	2.475	3.881
412TrS	133	-253.62	6.67	0.62	22.79	18.61	19.038	0.509	5.376
412TrS	139	-268.0	6.11	0.552	12.86	15.03	20.131	1.254	4.496
412TrS	140	-247.27	4.36	0.73	25.57	22.52	19.309	2.271	5.293
412TrS	144	-239.14	8.86	0.269	10.66	4.04	19.604	2.264	3.836
412TrS	146	-261.64	5.94	0.591	15.04	20.95	20.176	1.821	6.066

412TrS	149	-248.28	17.02	0.273	7.48	5.02	20.261	1.858	5.489
412TrS	150	-252.95	4.63	0.587	14.49	19.97	19.941	2.293	5.733
412TrS	153	-272.7	12.87	0.483	9.45	14.26	20.383	2.031	5.019
412TrS	156	-259.06	15.02	0.192	8.91	2.96	19.881	2.835	2.59
412TrS	157	-258.35	11.33	0.365	10.63	10.16	20.429	2.299	4.664

Table C.49: All candidate disk stars from field 412TrS failing the quality cut.

field	starnum	velocity	velerr	CCmax	$\frac{Signal}{Noise}$	TD	I mag	$V-I$ colour	NaEW
412TrS	9	2140.68	16.05	0.14	9.63	2.7	20.612	2.476	0.176
412TrS	10	274.09	3.66	0.27	2.33	10.17	21.496	1.846	10.326
412TrS	57	304.96	7.98	0.191	3.49	6.01	21.607	1.187	3.666
412TrS	95	159.86	8.06	0.165	2.6	5.39	21.921	1.139	3.838
412TrS	128	10.72	18.93	0.206	8.54	5.85	20.916	2.932	1.662
412TrS	129	512.15	11.17	0.164	2.69	5.62	21.553	2.353	0.23
412TrS	152	242.97	6.33	0.087	3.03	5.37	21.353	0.943	2.931
412TrS	155	261.77	8.41	0.199	2.57	6.07	21.714	0.809	1.935

Table C.50: All stars with v_{hel} > -100 km s^{-1} from field 412TrS passing the quality cut.

field	starnum	velocity	velerr	CCmax	$\frac{Signal}{Noise}$	TD	I mag	$V-I$ colour	NaEW
412TrS	99	47.12	28.2	0.222	9.12	5.94	20.872	2.204	1.895
412TrS	120	1515.22	35.13	0.089	5.02	3.1	21.08	2.277	1.656
412TrS	125	10.43	50.27	0.171	7.16	5.32	20.894	2.724	0.616
412TrS	130	23.54	20.99	0.167	1.68	4.43	21.955	1.985	3.191

Table C.51: All stars with v_{hel} > -100 km s^{-1} from field 412TrS failing the quality cut.

field	starnum	velocity	velerr	CCmax	$\frac{Signal}{Noise}$	TD	I mag	$V-I$ colour	NaEW
156Tri	13	-121.53	9.46	0.159	5.28	8.83	20.673	1.976	3.128
156Tri	26	-118.38	7.14	0.129	3.1	7.99	21.043	1.977	2.164
156Tri	30	-112.8	13.26	0.114	4.11	4.97	20.863	2.217	2.502
156Tri	53	-133.53	6.63	0.064	3.66	3.78	21.101	2.407	0.999

Table C.52: All candidate halo stars from field 156Tri passing the quality cut.

field	starnum	velocity	velerr	CCmax	$\frac{Signal}{Noise}$	TD	I mag	$V-I$ colour	NaEW

156Tri	4	-106.08	11.45	0.155	12.06	10.01	18.738	2.037	1.203
156Tri	34	-129.08	10.85	0.073	1.9	2.98	21.234	1.878	2.71
156Tri	37	-168.08	28.0	0.073	0.64	2.9	20.993	2.155	2.992
156Tri	45	-116.89	11.44	0.045	0.82	3.08	21.867	1.418	2.879
156Tri	47	-135.14	11.53	0.113	0.8	6.1	21.41	1.944	6.319
156Tri	51	-164.74	18.97	0.058	1.92	3.3	20.535	2.894	0.23
156Tri	55	-107.94	14.49	0.155	1.71	8.41	21.931	1.596	6.545
156Tri	58	-104.2	9.91	0.044	2.94	1.78	21.221	2.351	0.89
156Tri	67	-127.08	3.58	0.036	1.68	2.38	21.508	2.308	4.374
156Tri	100	-146.15	9.25	0.075	1.55	4.91	21.487	0.846	7.494
156Tri	109	-102.86	7.18	0.108	0.95	5.73	21.755	2.3	7.104

Table C.53: All candidate halo stars from field 156Tri failing the quality cut.

field	starnum	velocity	velerr	CCmax	$\frac{Signal}{Noise}$	TD	I mag	$V-I$ colour	NaEW
156Tri	5	-206.66	4.71	0.124	2.67	9.81	20.773	1.26	4.261
156Tri	7	-227.03	10.49	0.066	3.22	2.83	21.124	1.281	2.424
156Tri	10	-248.58	7.64	0.23	3.52	15.1	21.106	1.448	5.8
156Tri	14	-231.22	5.14	0.078	2.18	4.0	21.283	1.401	0.114
156Tri	15	-241.51	7.72	0.262	4.81	11.99	20.788	1.95	4.903
156Tri	16	-260.35	9.45	0.153	2.88	6.59	21.103	1.687	4.739
156Tri	18	-246.7	11.6	0.098	2.04	4.65	21.449	1.407	0.309
156Tri	57	-217.95	5.08	0.179	7.01	7.68	20.525	3.012	1.816
156Tri	113	-180.84	8.59	0.056	2.34	3.04	21.76	2.835	1.452

Table C.54: All candidate disk stars from field 156Tri passing the quality cut.

field	starnum	velocity	velerr	CCmax	$\frac{Signal}{Noise}$	TD	I mag	$V-I$ colour	NaEW
156Tri	12	-183.9	9.32	0.059	0.92	4.02	21.563	1.028	6.368
156Tri	17	-262.46	27.11	0.079	1.17	1.75	21.682	1.136	10.198
156Tri	24	-266.13	9.81	0.1	1.84	3.77	21.582	1.423	5.645
156Tri	25	-245.71	9.83	0.064	0.73	4.36	21.337	1.671	2.06
156Tri	39	-262.97	16.54	0.072	1.82	3.83	21.736	1.454	0.83
156Tri	75	-297.53	18.51	0.134	5.33	7.81	19.722	0.566	1.493
156Tri	97	-229.87	6.98	0.165	4.99	6.36	20.327	1.934	1.727

Table C.55: All candidate disk stars from field 156Tri failing the quality cut.

field	starnum	velocity	velerr	CCmax	$\frac{Signal}{Noise}$	TD	I mag	$V-I$ colour	NaEW

156Tri	9	303.35	13.9	0.058	3.6	3.09	20.712	1.817	1.234
156Tri	11	226.58	8.98	0.085	4.41	5.23	20.689	1.881	0.683
156Tri	19	123.49	12.81	0.048	2.54	3.43	21.138	1.746	4.079
156Tri	35	503.24	6.06	0.042	2.13	3.93	21.189	1.925	0.648
156Tri	41	122.3	12.55	0.147	2.82	5.61	21.41	1.844	3.619
156Tri	52	82.5	11.24	0.064	2.39	3.4	21.279	2.221	0.258
156Tri	59	108.38	12.65	0.053	2.85	3.45	21.286	2.317	1.672
156Tri	61	481.31	13.38	0.053	2.72	2.2	21.364	2.299	0.343
156Tri	64	13.69	8.49	0.071	2.59	3.12	21.573	2.102	5.846
156Tri	68	402.29	23.09	0.064	3.17	2.17	21.418	2.412	5.616
156Tri	101	279.18	6.77	0.082	2.02	4.94	21.488	0.847	6.092

Table C.56: All stars with v_{hel} > -100 km s^{-1} from field 156Tri passing the quality cut.

field	starnum	velocity	velerr	CCmax	$\frac{Signal}{Noise}$	TD	I mag	$V-I$ colour	NaEW
156Tri	3	23.68	8.01	0.224	9.31	13.71	18.988	1.593	1.667
156Tri	6	168.57	41.55	0.032	3.69	1.55	20.931	1.162	1.199
156Tri	8	514.53	50.3	-0.002	3.18	-0.06	20.73	1.797	0.63
156Tri	20	175.62	37.13	0.066	1.25	3.75	21.697	1.194	3.896
156Tri	21	131.01	17.43	0.064	0.86	4.59	21.144	1.787	0.282
156Tri	23	273.05	12.66	0.054	0.65	3.94	21.892	1.055	0.638
156Tri	27	137.71	12.23	0.031	1.52	2.4	21.695	1.332	3.268
156Tri	28	508.23	7.27	0.026	0.69	1.42	21.509	1.555	13.353
156Tri	36	78.76	15.93	0.063	1.6	3.3	20.985	2.14	4.425
156Tri	38	295.26	9.85	0.028	1.04	2.06	21.818	1.362	3.849
156Tri	46	74.08	43.16	0.073	4.4	3.52	20.732	2.619	0.162
156Tri	54	500.06	4.22	0.057	1.02	1.81	21.889	1.627	8.205
156Tri	56	264.95	11.7	0.044	1.5	2.57	21.791	1.744	6.581
156Tri	65	262.11	2.33	0.121	1.15	6.73	21.69	2.034	6.395
156Tri	66	513.06	12.82	0.029	2.98	1.48	21.152	2.579	1.048
156Tri	86	0.92	6.15	0.188	15.03	7.14	19.266	2.604	0.014
156Tri	90	97.97	24.44	0.036	0.49	1.33	21.614	0.375	17.18
156Tri	94	251.98	1.34	0.062	0.6	2.9	21.203	0.929	5.963
156Tri	96	14.43	11.24	0.137	4.51	6.97	20.405	1.793	3.288
156Tri	102	333.51	9.45	0.037	1.41	1.85	21.361	0.983	2.129
156Tri	106	263.79	4.67	0.075	0.75	4.43	21.652	0.926	2.22
156Tri	107	6.27	3.59	0.127	11.92	6.45	19.728	2.851	0.131
156Tri	111	57.14	53.85	0.016	5.05	1.01	20.826	3.268	1.438

Table C.57: All stars with v_{hel} > -100 km s^{-1} from field 156Tri failing the quality cut.

field	starnum	velocity	velerr	CCmax	$\frac{Signal}{Noise}$	TD	I mag	$V-I$ colour	NaEW
511TrS	57	-110.72	6.26	0.108	7.09	4.46	20.341	0.633	0.799
511TrS	58	-132.8	6.44	0.413	6.99	18.43	20.226	1.085	4.443

511TrS	67	-140.76	8.24	0.193	11.71	8.8	20.098	2.323	1.568

Table C.58: All candidate halo stars from field 511TrS failing the quality cut.

field	starnum	velocity	velerr	CCmax	$\frac{Signal}{Noise}$	TD	I mag	$V-I$ colour	NaEW
511TrS	45	-197.7	2.59	0.339	15.1	15.01	19.276	0.623	1.22
511TrS	47	-199.5	4.77	0.407	11.98	18.96	19.655	1.01	2.73

Table C.59: All candidate disk stars from field 511TrS failing the quality cut.

field	starnum	velocity	velerr	CCmax	$\frac{Signal}{Noise}$	TD	I mag	$V-I$ colour	NaEW
511TrS	5	151.19	7.74	0.145	2.53	6.17	21.021	1.302	4.33
511TrS	15	0.18	16.87	0.103	4.97	4.42	21.056	2.288	1.27
511TrS	22	28.05	17.86	0.158	4.87	8.38	21.419	2.661	0.904
511TrS	30	20.0	9.64	0.184	7.64	8.73	20.711	2.391	0.882
511TrS	33	1090.03	14.28	0.192	4.83	17.42	20.937	2.352	1.148
511TrS	36	4.13	3.66	0.183	6.19	7.37	21.114	2.348	1.983

Table C.60: All stars with v_{hel} > -100 km s^{-1} from field 511TrS passing the quality cut.

field	starnum	velocity	velerr	CCmax	$\frac{Signal}{Noise}$	TD	I mag	$V-I$ colour	NaEW
511TrS	20	52.91	33.88	0.134	4.95	6.14	21.236	2.628	0.535
511TrS	52	9.14	4.06	0.356	16.09	13.21	19.571	2.381	1.364
511TrS	61	23.16	4.16	0.361	11.18	19.03	19.935	2.024	0.811
511TrS	65	5.86	4.17	0.41	16.28	14.86	19.62	2.512	1.477
511TrS	66	2.6	4.63	0.339	11.5	9.52	20.058	2.214	2.52

Table C.61: All stars with v_{hel} > -100 km s^{-1} from field 511TrS failing the quality cut.

Bibliography

Babusiaux, C. & Gilmore, G. 2005, *MNRAS*, 358, 1309

Barker, M. K. 2007, PhD thesis, University of Florida

Barker, M. K., Ferguson, A. M. N., Cole, A. A., Ibata, R., Irwin, M., Lewis, G. F., Smecker-Hane, T. A., & Tanvir, N. R. 2010, *MNRAS*, 1591

Barker, M. K. & Sarajedini, A. 2008, *MNRAS*, 390, 863

Barker, M. K., Sarajedini, A., Geisler, D., Harding, P., & Schommer, R. 2007a, *AJ*, 133, 1125

—. 2007b, *AJ*, 133, 1138

Battaglia, G., Irwin, M., Tolstoy, E., Hill, V., Helmi, A., Letarte, B., & Jablonka, P. 2008, *MNRAS*, 383, 183

Beers, T. C., Lee, Y. S., & Carollo, D. 2008, in IAU Symposium, Vol. 255, IAU Symposium, ed. L. K. Hunt, S. Madden, & R. Schneider, 323–329

Begum, A., Chengalur, J. N., & Karachentsev, I. D. 2005, *A&A*, 433, L1

Bekki, K., Couch, W. J., Drinkwater, M. J., & Gregg, M. D. 2001, *ApJ*, 557, L39

Belokurov, V., Evans, N. W., Irwin, M. J., Lynden-Bell, D., Yanny, B., Vidrih, S., Gilmore, G., Seabroke, G., Zucker, D. B., Wilkinson, M. I., Hewett, P. C., Bramich, D. M., Fellhauer, M., Newberg, H. J., Wyse, R. F. G., Beers, T. C., Bell, E. F., Barentine, J. C., Brinkmann, J., Cole, N., Pan, K., & York, D. G. 2007a, *ApJ*, 658, 337

Belokurov, V., Zucker, D. B., Evans, N. W., Gilmore, G., Vidrih, S., Bramich, D. M., Newberg, H. J., Wyse, R. F. G., Irwin, M. J., Fellhauer, M., Hewett, P. C., Walton, N. A., Wilkinson, M. I., Cole, N., Yanny, B., Rockosi, C. M., Beers, T. C., Bell, E. F., Brinkmann, J., Ivezić, Ž., & Lupton, R. 2006a, *ApJ*, 642, L137

Belokurov, V., Zucker, D. B., Evans, N. W., Kleyna, J. T., Koposov, S., Hodgkin, S. T., Irwin, M. J., Gilmore, G., Wilkinson, M. I., Fellhauer, M., Bramich, D. M., Hewett, P. C., Vidrih, S., De Jong, J. T. A., Smith, J. A., Rix, H.-W., Bell, E. F., Wyse, R. F. G., Newberg, H. J., Mayeur, P. A., Yanny, B., Rockosi, C. M., Gnedin, O. Y., Schneider, D. P., Beers, T. C., Barentine, J. C., Brewington, H., Brinkmann, J., Harvanek, M., Kleinman, S. J., Krzesinski, J., Long, D., Nitta, A., & Snedden, S. A. 2007b, *ApJ*, 654, 897

Belokurov, V., Zucker, D. B., Evans, N. W., Wilkinson, M. I., Irwin, M. J., Hodgkin, S., Bramich, D. M., Irwin, J. M., Gilmore, G., Willman, B., Vidrih, S., Newberg, H. J., Wyse, R. F. G., Fellhauer, M., Hewett, P. C., Cole, N., Bell, E. F., Beers, T. C., Rockosi, C. M., Yanny, B., Grebel, E. K., Schneider, D. P., Lupton, R., Barentine, J. C., Brewington, H., Brinkmann, J., Harvanek, M., Kleinman, S. J., Krzesinski, J., Long, D., Nitta, A., Smith, J. A., & Snedden, S. A. 2006b, *ApJ*, 647, L111

Binney, J. & Merrifield, M. 1998, Galactic astronomy, ed. Binney, J. & Merrifield, M.

Binney, J. & Tremaine, S. 2008, Galactic Dynamics: Second Edition, ed. Binney, J. & Tremaine, S. (Princeton University Press)

Bonanos, A. Z., Stanek, K. Z., Kudritzki, R. P., Macri, L., Sasselov, D. D., Kaluzny, J., Bersier, D., Bresolin, F., Matheson, T., Mochejska, B. J., Przybilla, N., Szentgyorgyi, A. H., Tonry, J., & Torres, G. 2006, *Ap&SS*, 304, 207

Bothun, G. D. 1992, *AJ*, 103, 104

Brooks, R. S., Wilson, C. D., & Harris, W. E. 2004, *AJ*, 128, 237

Brown, T. M. 2009, in Astronomical Society of the Pacific Conference Series, Vol. 419, Astronomical Society of the Pacific Conference Series, ed. S. Jogee, I. Marinova, L. Hao, & G. A. Blanc, 110–+

Brown, T. M., Beaton, R., Chiba, M., Ferguson, H. C., Gilbert, K. M., Guhathakurta, P., Iye, M., Kalirai, J. S., Koch, A., Komiyama, Y., Majewski, S. R., Reitzel, D. B., Renzini, A., Rich, R. M., Smith, E., Sweigart, A. V., & Tanaka, M. 2008, *ApJ*, 685, L121

Brown, T. M., Smith, E., Ferguson, H. C., Guhathakurta, P., Kalirai, J. S., Kimble, R. A., Renzini, A., Rich, R. M., Sweigart, A. V., & Vanden Berg, D. A. 2009, *ApJS*, 184, 152

Brown, T. M., Smith, E., Ferguson, H. C., Guhathakurta, P., Kalirai, J. S., Rich, R. M., Renzini, A., Sweigart, A. V., Reitzel, D., Gilbert, K. M., & Geha, M. 2007, *ApJ*, 658, L95

Brunthaler, A., Reid, M. J., Falcke, H., Greenhill, L. J., & Henkel, C. 2005, Science, 307, 1440

Cabrera-Lavers, A., González-Fernández, C., Garzón, F., Hammersley, P. L., & López-Corredoira, M. 2008, *A&A*, 491, 781

Carollo, D., Beers, T. C., Chiba, M., Norris, J. E., Freeman, K. C., Lee, Y. S., Ivezić, Ž., Rockosi, C. M., & Yanny, B. 2010, *ApJ*, 712, 692

Carollo, D., Beers, T. C., Lee, Y. S., Chiba, M., Norris, J. E., Wilhelm, R., Sivarani, T., Marsteller, B., Munn, J. A., Bailer-Jones, C. A. L., Fiorentin, P. R., & York, D. G. 2007, *Nature*, 450, 1020

Chandar, R., Bianchi, L., Ford, H. C., & Sarajedini, A. 2002, *ApJ*, 564, 712

Chapman, S. C., Ibata, R., Irwin, M., Koch, A., Letarte, B., Martin, N., Collins, M., Lewis, G. F., McConnachie, A., Peñarrubia, J., Rich, R. M., Trethewey, D., Ferguson, A., Huxor, A., & Tanvir, N. 2008, *MNRAS*, 390, 1437

Chapman, S. C., Ibata, R., Lewis, G. F., Ferguson, A. M. N., Irwin, M., McConnachie, A., & Tanvir, N. 2006, *ApJ*, 653, 255

Chiba, M. & Beers, T. C. 2000, *AJ*, 119, 2843

Ciardullo, R., Durrell, P. R., Laychak, M. B., Herrmann, K. A., Moody, K., Jacoby, G. H., & Feldmeier, J. J. 2004, *ApJ*, 614, 167

Cioni, M., Irwin, M., Ferguson, A. M. N., McConnachie, A., Conn, B. C., Huxor, A., Ibata, R., Lewis, G., & Tanvir, N. 2008, *A&A*, 487, 131

Cockcroft, R., Harris, W. E., Ferguson, A. M. N., Huxor, A., Ibata, R., Irwin, M. J., McConnachie, A. W., Woodley, K. A., Chapman, S. C., Lewis, G. F., & Puzia, T. H. 2011, *ApJ*, 730, 112

Collins, M. L. M., Chapman, S. C., Ibata, R. A., Irwin, M. J., Rich, R. M., Ferguson, A. M. N., Lewis, G. F., Tanvir, N., & Koch, A. 2011, *MNRAS*, 248

Collins, M. L. M., Chapman, S. C., Irwin, M., Ibata, R., Martin, N. F., Ferguson, A. M. N., Huxor, A., Lewis, G. F., Mackey, A. D., McConnachie, A. W., & Tanvir, N. 2009, *MNRAS*, 396, 1619

Collins, M. L. M., Chapman, S. C., Irwin, M. J., Martin, N. F., Ibata, R. A., Zucker, D. B., Blain, A., Ferguson, A. M. N., Lewis, G. F., McConnachie, A. W., & Peñarrubia, J. 2010, *MNRAS*, 407, 2411

Corbelli, E. & Salucci, P. 2000, *MNRAS*, 311, 441

Davidge, T. J. 2003, *AJ*, 125, 3046

Davidge, T. J., Olsen, K. A. G., Blum, R., Stephens, A. W., & Rigaut, F. 2005, *AJ*, 129, 201

Davis, M., Faber, S. M., Newman, J., Phillips, A. C., Ellis, R. S., Steidel, C. C., Conselice, C., Coil, A. L., Finkbeiner, D. P., Koo, D. C., Guhathakurta, P., Weiner, B., Schiavon, R., Willmer, C., Kaiser, N., Luppino, G. A., Wirth, G., Connolly, A., Eisenhardt, P., Cooper, M., & Gerke, B. 2003, in Society of Photo-Optical Instrumentation Engineers (SPIE) Conference Series, Vol. 4834, Society of Photo-Optical Instrumentation Engineers (SPIE) Conference Series, ed. P. Guhathakurta, 161–172

de Jong, R. S. 1996, *A&AS*, 118, 557

de Vaucouleurs, G. 1959, *ApJ*, 130, 728

Deason, A. J., Belokurov, V., & Evans, N. W. 2010, *MNRAS*, 1761

Dotter, A., Chaboyer, B., Jevremović, D., Kostov, V., Baron, E., & Ferguson, J. W. 2008, *ApJS*, 178, 89

Dressler, A. 1980a, *ApJS*, 42, 565

—. 1980b, *ApJ*, 236, 351

Durrell, P. R., Harris, W. E., & Pritchet, C. J. 2004, *AJ*, 128, 260

Eggen, O. J. 1961, Royal Greenwich Observatory Bulletin, 41, 245

—. 1964, Royal Greenwich Observatory Bulletin, 84, 111

Eggen, O. J., Lynden-Bell, D., & Sandage, A. R. 1962, *ApJ*, 136, 748

Eke, V. R., Baugh, C. M., Cole, S., Frenk, C. S., Norberg, P., Peacock, J. A., Baldry, I. K., Bland-Hawthorn, J., Bridges, T., Cannon, R., Colless, M., Collins, C., Couch, W., Dalton, G., de Propris, R., Driver, S. P., Efstathiou, G., Ellis, R. S., Glazebrook, K., Jackson, C., Lahav, O., Lewis, I., Lumsden, S., Maddox, S., Madgwick, D., Peterson, B. A., Sutherland, W., & Taylor, K. 2004, *MNRAS*, 348, 866

Faber, S. M., Tremaine, S., Ajhar, E. A., Byun, Y., Dressler, A., Gebhardt, K., Grillmair, C., Kormendy, J., Lauer, T. R., & Richstone, D. 1997, *AJ*, 114, 1771

Faber et al. 2000, DEEP Survey Brochure

Fardal, M. A., Babul, A., Geehan, J. J., & Guhathakurta, P. 2006, *MNRAS*, 366, 1012

Fardal, M. A., Guhathakurta, P., Babul, A., & McConnachie, A. W. 2007, *MNRAS*, 380, 15

Fellhauer, M., Belokurov, V., Evans, N. W., Wilkinson, M. I., Zucker, D. B., Gilmore, G., Irwin, M. J., Bramich, D. M., Vidrih, S., Wyse, R. F. G., Beers, T. C., & Brinkmann, J. 2006, *ApJ*, 651, 167

Ferguson, A., Irwin, M., Chapman, S., Ibata, R., Lewis, G., & Tanvir, N. Resolving the Stellar Outskirts of M31 and M33, ed. de Jong, R. S., 239–+

Ferguson, A. M. N., Irwin, M. J., Ibata, R. A., Lewis, G. F., & Tanvir, N. R. 2002, *AJ*, 124, 1452

Freedman, W. L., Madore, B. F., Gibson, B. K., Ferrarese, L., Kelson, D. D., Sakai, S., Mould, J. R., Kennicutt, Jr., R. C., Ford, H. C., Graham, J. A., Huchra, J. P., Hughes, S. M. G., Illingworth, G. D., Macri, L. M., & Stetson, P. B. 2001, *ApJ*, 553, 47

Freeman, K. C. 1970, *ApJ*, 160, 811

Freudenreich, H. T. 1998, *ApJ*, 492, 495

Galleti, S., Bellazzini, M., & Ferraro, F. R. 2004, *A&A*, 423, 925

Geehan, J. J., Fardal, M. A., Babul, A., & Guhathakurta, P. 2006, *MNRAS*, 366, 996

Gilbert, K. M., Guhathakurta, P., Kalirai, J. S., Rich, R. M., Majewski, S. R., Ostheimer, J. C., Reitzel, D. B., Cenarro, A. J., Cooper, M. C., Luine, C., & Patterson, R. J. 2006, *ApJ*, 652, 1188

Gilbert, K. M., Guhathakurta, P., Kollipara, P., Beaton, R. L., Geha, M. C., Kalirai, J. S., Kirby, E. N., Majewski, S. R., & Patterson, R. J. 2009, *ApJ*, 705, 1275

Gilmore, G., Wyse, R. F. G., & Kuijken, K. 1989, *ARA&A*, 27, 555

Giovanelli, R., Haynes, M. P., & Chincarini, G. L. 1986, *ApJ*, 300, 77

Girardi, L., Bressan, A., Bertelli, G., & Chiosi, C. 2000, *A&AS*, 141, 371

Guhathakurta, P., Rich, R. M., Reitzel, D. B., Cooper, M. C., Gilbert, K. M., Majewski, S. R., Ostheimer, J. C., Geha, M. C., Johnston, K. V., & Patterson, R. J. 2006, *AJ*, 131, 2497

Hammer, F., Puech, M., Chemin, L., Flores, H., & Lehnert, M. D. 2007, *ApJ*, 662, 322

Helmi, A. 2004, *MNRAS*, 351, 643

—. 2008, *A&A Rev.*, 15, 145

Herschel, W. 1785, Royal Society of London Philosophical Transactions Series I, 75, 213

Hippelein, H., Haas, M., Tuffs, R. J., Lemke, D., Stickel, M., Klaas, U., & Völk, H. J. 2003, *A&A*, 407, 137

Hogg, D. W. 1999, ArXiv Astrophysics e-prints, astro-ph/9905116

Hood, M., Smecker-Hane, T., Teig, M., Ferguson, A. M. N., & Irwin, M. J. 2007, in Astronomical Society of the Pacific Conference Series, Vol. 374, From Stars to Galaxies: Building the Pieces to Build Up the Universe, ed. A. Vallenari, R. Tantalo, L. Portinari, & A. Moretti, 281–+

Hubble, E. P. 1925, The Observatory, 48, 139

Huggins, W. & Miller, W. A. 1864, Royal Society of London Philosophical Transactions Series I, 154, 437

Huxor, A., Ferguson, A. M. N., Barker, M. K., Tanvir, N. R., Irwin, M. J., Chapman, S. C., Ibata, R., & Lewis, G. 2009, *ApJ*, 698, L77

Ibata, R., Chapman, S., Ferguson, A. M. N., Lewis, G., Irwin, M., & Tanvir, N. 2005, *ApJ*, 634, 287

Ibata, R., Irwin, M., Lewis, G., Ferguson, A. M. N., & Tanvir, N. 2001, *Nature*, 412, 49

Ibata, R., Martin, N. F., Irwin, M., Chapman, S., Ferguson, A. M. N., Lewis, G. F., & McConnachie, A. W. 2007, *ApJ*, 671, 1591

Ibata, R. A., Gilmore, G., & Irwin, M. J. 1994, *Nature*, 370, 194

Impey, C. & Bothun, G. 1997, *ARA&A*, 35, 267

Irwin, M. J., Ferguson, A. M. N., Ibata, R. A., Lewis, G. F., & Tanvir, N. R. 2005, *ApJ*, 628, L105

Johnston, K. V., Law, D. R., & Majewski, S. R. 2005, *ApJ*, 619, 800

Kahn, F. D. & Woltjer, L. 1959, *ApJ*, 130, 705

Kalirai, J. S., Beaton, R. L., Geha, M. C., Gilbert, K. M., Guhathakurta, P., Kirby, E. N., Majewski, S. R., Ostheimer, J. C., Patterson, R. J., & Wolf, J. 2010, *ApJ*, 711, 671

Kalirai, J. S., Zucker, D. B., Guhathakurta, P., Geha, M., Kniazev, A. Y., Martínez-Delgado, D., Bell, E. F., Grebel, E. K., & Gilbert, K. M. 2009, *ApJ*, 705, 1043

Keeler, J. E. 1908, Publications of Lick Observatory, 8, 1

Kim, M., Kim, E., Lee, M. G., Sarajedini, A., & Geisler, D. 2002, *AJ*, 123, 244

Kippenhahn, R. & Weigert, A. 1994, Stellar Structure and Evolution, ed. Kippenhahn, R. & Weigert, A.

Kormendy, J., Fisher, D. B., Cornell, M. E., & Bender, R. 2009, *ApJS*, 182, 216

Kormendy, J. & McClure, R. D. 1993, *AJ*, 105, 1793

Lauer, T. R., Faber, S. M., Ajhar, E. A., Grillmair, C. J., & Scowen, P. A. 1998, *AJ*, 116, 2263

Law, D. R., Majewski, S. R., & Johnston, K. V. 2009, *ApJ*, 703, L67

Lee, M. G., Kim, M., Sarajedini, A., Geisler, D., & Gieren, W. 2002, *ApJ*, 565, 959

Li, Y. & White, S. D. M. 2008, *MNRAS*, 384, 1459

Loeb, A., Reid, M. J., Brunthaler, A., & Falcke, H. 2005, *ApJ*, 633, 894

Mackey, A. D., Huxor, A. P., Ferguson, A. M. N., Irwin, M. J., Tanvir, N. R., McConnachie, A. W., Ibata, R. A., Chapman, S. C., & Lewis, G. F. 2010, *ApJ*, 717, L11

Martin, N. F., Ibata, R. A., Irwin, M. J., Chapman, S., Lewis, G. F., Ferguson, A. M. N., Tanvir, N., & McConnachie, A. W. 2006, *MNRAS*, 371, 1983

Martin, N. F., McConnachie, A. W., Irwin, M., Widrow, L. M., Ferguson, A. M. N., Ibata, R. A., Dubinski, J., Babul, A., Chapman, S., Fardal, M., Lewis, G. F., Navarro, J., & Rich, R. M. 2009, *ApJ*, 705, 758

Mateo, M. L. 1998, *ARA&A*, 36, 435

McConnachie, A. W., Chapman, S. C., Ibata, R. A., Ferguson, A. M. N., Irwin, M. J., Lewis, G. F., Tanvir, N. R., & Martin, N. 2006, *ApJ*, 647, L25

McConnachie, A. W., Ferguson, A. M. N., Irwin, M. J., Dubinski, J., Widrow, L. M., Dotter, A., Ibata, R., & Lewis, G. F. 2010, *ApJ*, 723, 1038

McConnachie, A. W., Irwin, M. J., Ferguson, A. M. N., Ibata, R. A., Lewis, G. F., & Tanvir, N. 2005, *MNRAS*, 356, 979

McConnachie, A. W., Irwin, M. J., Ibata, R. A., Dubinski, J., Widrow, L. M., Martin, N. F., Côté, P., Dotter, A. L., Navarro, J. F., Ferguson, A. M. N., Puzia, T. H., Lewis, G. F., Babul, A., Barmby, P., Bienaymé, O., Chapman, S. C., Cockcroft, R., Collins, M. L. M., Fardal, M. A., Harris, W. E., Huxor, A., Mackey, A. D., Peñarrubia, J., Rich, R. M., Richer, H. B., Siebert, A., Tanvir, N., Valls-Gabaud, D., & Venn, K. A. 2009, *Nature*, 461, 66

McLean, I. S. & Liu, T. 1996, *ApJ*, 456, 499

McWilliam, A. & Rich, R. M. 1994, *ApJS*, 91, 749

Mellinger, A. 2009, *PASP*, 121, 1180

Melnick, J. & Sargent, W. L. W. 1977, *ApJ*, 215, 401

Meurer, G. R., Carignan, C., Beaulieu, S. F., & Freeman, K. C. 1996, *AJ*, 111, 1551

Minniti, D., Olszewski, E. W., & Rieke, M. 1993, *ApJ*, 410, L79

Mo, H. J., Mao, S., & White, S. D. M. 1998, *MNRAS*, 295, 319

Mould, J. & Kristian, J. 1986, *ApJ*, 305, 591

NASA/IPAC Extragalactic Database. 2011, NASA/IPAC Extragalactic Database (NED)

Newberg, H. J., Yanny, B., Rockosi, C., Grebel, E. K., Rix, H., Brinkmann, J., Csabai, I., Hennessy, G., Hindsley, R. B., Ibata, R., Ivezić, Z., Lamb, D., Nash, E. T., Odenkirchen, M., Rave, H. A., Schneider, D. P., Smith, J. A., Stolte, A., & York, D. G. 2002, *ApJ*, 569, 245

Oemler, Jr., A. 1974, *ApJ*, 194, 1

Peñarrubia, J., Belokurov, V., Evans, N. W., Martínez-Delgado, D., Gilmore, G., Irwin, M., Niederste-Ostholt, M., & Zucker, D. B. 2010, *MNRAS*, 408, L26

Pierce, M. J., Jurcevic, J. S., & Crabtree, D. 2000, *MNRAS*, 313, 271

Purcell, C. W., Bullock, J. S., & Zentner, A. R. 2007, *ApJ*, 666, 20

Putman, M. E., Peek, J. E. G., Muratov, A., Gnedin, O. Y., Hsu, W., Douglas, K. A., Heiles, C., Stanimirovic, S., Korpela, E. J., & Gibson, S. J. 2009, *ApJ*, 703, 1486

Regan, M. W. & Vogel, S. N. 1994, *ApJ*, 434, 536

Richardson, J. C., Irwin, M., McConnachie, A. W., Martin, N. F., Dotter, A., Ferguson, A. M. N., Ibata, R. A., Chapman, S., Lewis, G. F., Tanvir, N. R., & Rich, R. M. 2011, ArXiv e-prints, 1102.2902

Roberts, I. 1893, The Universal Press, London

—. 1899, The Universal Press, London

Robin, A. C., Reylé, C., Derrière, S., & Picaud, S. 2003, *A&A*, 409, 523

Rogstad, D. H., Wright, M. C. H., & Lockhart, I. A. 1976, *ApJ*, 204, 703

Roman, N. G., de Vaucouleurs, G., de Vaucouleurs, A., Corwin, Jr., H. G., Buta, R. J., Paturel, G., & Fouqué, P. 1991, Third Reference Catalogue of Bright Galaxies (de Vaucouleurs, de Vaucouleurs, Corwin, Buta, Paturel, and Fouqué 1991). Documentation for the machine-readable version., ed. Roman, N. G., de Vaucouleurs, G., de Vaucouleurs, A., Corwin, H. G., Jr., Buta, R. J., Paturel, G., & Fouqué, P.

Rosse. 1850, Philosophical Transactions of the Royal Society of London, 140, 499

Roškar, R., Debattista, V. P., Quinn, T. R., Stinson, G. S., & Wadsley, J. 2008a, *ApJ*, 684, L79

Roškar, R., Debattista, V. P., Stinson, G. S., Quinn, T. R., Kaufmann, T., & Wadsley, J. 2008b, *ApJ*, 675, L65

Rowe, J. F., Richer, H. B., Brewer, J. P., & Crabtree, D. R. 2005, *AJ*, 129, 729

Saglia, R. P., Fabricius, M., Bender, R., Montalto, M., Lee, C., Riffeser, A., Seitz, S., Morganti, L., Gerhard, O., & Hopp, U. 2010, *A&A*, 509, A61+

San Roman, I., Sarajedini, A., & Aparicio, A. 2010, *ApJ*, 720, 1674

Sandage, A. & Bedke, J. 1994, The Carnegie atlas of galaxies, ed. Sandage, A. & Bedke, J.

Sarajedini, A., Barker, M. K., Geisler, D., Harding, P., & Schommer, R. 2006, *AJ*, 132, 1361

Sarajedini, A., Geisler, D., Schommer, R., & Harding, P. 2000, *AJ*, 120, 2437

Scheiner, J. 1899, *ApJ*, 9, 149

Schlegel, D. J., Finkbeiner, D. P., & Davis, M. 1998, *ApJ*, 500, 525

Scowcroft, V., Bersier, D., Mould, J. R., & Wood, P. R. 2009, *MNRAS*, 396, 1287

Searle, L. & Zinn, R. 1978, *ApJ*, 225, 357

Seigar, M. S., Barth, A. J., & Bullock, J. S. 2008, *MNRAS*, 389, 1911

Simpson, R. 2010, Types of Galaxies, http://blogs.zooniverse.org/galaxyzoo/2010/05/12/types-of-galaxies/

Skrutskie, M. F., Cutri, R. M., Stiening, R., Weinberg, M. D., Schneider, S., Carpenter, J. M., Beichman, C., Capps, R., Chester, T., Elias, J., Huchra, J., Liebert, J., Lonsdale, C., Monet, D. G., Price, S., Seitzer, P., Jarrett, T., Kirkpatrick, J. D., Gizis, J. E., Howard, E., Evans, T., Fowler, J., Fullmer, L., Hurt, R., Light, R., Kopan, E. L., Marsh, K. A., McCallon, H. L., Tam, R., Van Dyk, S., & Wheelock, S. 2006, *AJ*, 131, 1163

Spergel, D. N., Bean, R., Doré, O., Nolta, M. R., Bennett, C. L., Dunkley, J., Hinshaw, G., Jarosik, N., Komatsu, E., Page, L., Peiris, H. V., Verde, L., Halpern, M., Hill, R. S., Kogut, A., Limon, M., Meyer, S. S., Odegard, N., Tucker, G. S., Weiland, J. L., Wollack, E., & Wright, E. L. 2007, *ApJS*, 170, 377

Starkenburg, E., Hill, V., Tolstoy, E., González Hernández, J. I., Irwin, M., Helmi, A., Battaglia, G., Jablonka, P., Tafelmeyer, M., Shetrone, M., Venn, K., & de Boer, T. 2010, *A&A*, 513, A34+

Stephens, A. W. & Frogel, J. A. 2002, *AJ*, 124, 2023

Stonkutė, R., Vansevičius, V., Arimoto, N., Hasegawa, T., Narbutis, D., Tamura, N., Jablonka, P., Ohta, K., & Yamada, Y. 2008, *AJ*, 135, 1482

Teig, M. 2008, *PASP*, 120, 474

Teig, M. J. 2007, PhD thesis, University of California, Irvine

Tiede, G. P., Sarajedini, A., & Barker, M. K. 2004, *AJ*, 128, 224

Tolstoy, E., Hill, V., & Tosi, M. 2009, *ARA&A*, 47, 371

Tonry, J. & Davis, M. 1979, *AJ*, 84, 1511

U, V., Urbaneja, M. A., Kudritzki, R., Jacobs, B. A., Bresolin, F., & Przybilla, N. 2009, *ApJ*, 704, 1120

Vale Asari, N., Stasińska, G., Cid Fernandes, R., Gomes, J. M., Schlickmann, M., Mateus, A., & Schoenell, W. 2009, *MNRAS*, 396, L71

van den Bergh, S. 1999, *JRASC*, 93, 175

van der Marel, R. P. & Guhathakurta, P. 2008, *ApJ*, 678, 187

van Gorkom, J. 2003, Carnegie Observatory Astrophysics Series, Vol. 3: Clusters of Galaxies: Probes of Cosmological Structure and Galaxy Evolution ed. JS Mulchaey, A. Dressler, and A. Oemler

Verley, S., Corbelli, E., Giovanardi, C., & Hunt, L. K. 2009, *A&A*, 493, 453

Walterbos, R. A. M. & Kennicutt, Jr., R. C. 1988, *A&A*, 198, 61

Watkins, L. L., Evans, N. W., & An, J. H. 2010, *MNRAS*, 406, 264

Westerlund, B. E. 1997, Cambridge Astrophysics Series, 29

Widrow, L. M., Perrett, K. M., & Suyu, S. H. 2003, *ApJ*, 588, 311

Wilkinson, M. I. & Evans, N. W. 1999, *MNRAS*, 310, 645

Williams, B. F., Dalcanton, J. J., Dolphin, A. E., Holtzman, J., & Sarajedini, A. 2009, *ApJ*, 695, L15

Wilson, C. D., Madore, B. F., & Freedman, W. L. 1990, *AJ*, 99, 149

Zwicky, F. 1933, Helvetica Physica Acta, 6, 110

—. 1937, *ApJ*, 86, 217